5-2-2022

Methods for High Resolution Study of the Geometry of Active Galactic Nuclei with Applications of Reverberation Mapping and Optical Interferometry

Matthew D. Anderson
Georgia State University

Methods for High Resolution Study of the Geometry of Active Galactic Nuclei with Applications of Reverberation Mapping and Optical Interferometry

by

Matthew David Anderson

Under the Direction of Fabien Baron, PhD

A Dissertation Submitted in Partial Fulfillment of the Requirements of

Doctor of Philosophy

in the College of Arts and Sciences

Georgia State University

2022

ABSTRACT

All but a few Active Galactic Nuclei are too distant for any single aperture telescope to resolve, yet the geometry of these objects is key to our understanding of the evolution of galaxies in the universe. To study the geometry of Active Galactic Nuclei, methods are leveraged using smaller telescopes to gain resolution rather than relying on larger and larger single aperture telescopes. Principally, these are via reverberation mapping which utilizes temporal and spectral resolution to gain spatial resolution and interferometry which sacrifices the light gathering power of large aperture telescopes for high angular resolution. To provide a tool for recovering geometric indicators of AGNs from reverberation mapping data, an image reconstructing algorithm is developed utilizing the alternating direction method of multipliers with compressed sensing regularization. This new algorithm is applied to the Arp 151 dataset from the Lick AGN Monitoring Project 2008. In addition to the reverberation mapping algorithm, the first calibrated extragalactic results for the CHARA Array are presented for NGC 4151. At the extreme detection limit for the instruments of the CHARA Array, the observational strategies utilized for successful observations and the results obtained are discussed.

INDEX WORDS: Astronomy software, Active Galactic Nuclei, Seyfert Galaxies, Reverberation Mapping, Long baseline interferometry, Observational astronomy, Optical interferometry

Methods for High Resolution Study of the Geometry of Active Galactic Nuclei with Applications of Reverberation Mapping and Optical Interferometry

by

Matthew David Anderson

Committee Chair:	Fabien Baron
Committee:	Theo ten Brummelaar
	D. Michael Crenshaw
	Stuart Jefferies
	John Monnier

Electronic Version Approved:

Office of Graduate Studies

College of Arts and Sciences

Georgia State University

May 2022

DEDICATION

I dedicate this dissertation to my family and friends for supporting me and my endless shenanigans throughout this arduous endeavor. Without all of you, this would not have been possible.

ACKNOWLEDGEMENTS

There are a great many people who deserve a whole lot of credit.

Without the CHARA staff on Mount Wilson, none of this would have been possible.

Many thanks to Steve Golden, Larry Webster, and Craig Woods for CO_2-ing, burnishing, washing telescope mirrors, and everything else you do to get every possible photon into the lab.

Many thanks to Theo ten Brummelear and Gail Schaefer for their expertise and assistance in tracking down bugs, developing new sequences, and assisting in the data reduction for the CLASSIC beam combiner at the hairy edge of the noise limit for the detector.

To the Sturmanns, Laszlo and Judit. Thank you for your unending encouragement and dedication to keeping the CHARA array running. May your retirement spare you the unending stream of Tech Reports.

Many thanks to the observing staff. Olli Majoinen and Norm Vargas, your patience with getting this program running, and dedication to keeping the data flowing at CHARA does not go unnoticed.

Many and more thanks to Christopher Farrington. Without the sharing of your extensive knowledge of the array's functionality and foibles I'd still be beating my head against the wall without a data file to show for it.

Thanks to anyone and everyone who has contributed to the CHARA Array Adaptive Optics program. Without your efforts, there would be no results on AGN at CHARA.

Thanks to Keith Horne for many valuable discussions about reverberation mapping and instructions for the PREPSPEC software package.

To the folks at SoCal Herding, Ted Ondrak and Chandra David thank you so much for watching Stella during my observing runs. You have saved me from madness.

A very special thanks to John Monnier. Without your introduction to real astronomy, I would not be where I am today. Your support and encouragement through the years has been invaluable.

Many thanks to Misty Bentz, your expertise in reverberation mapping made this whole process much smoother than it could have been.

Many thanks to my thesis advisor Fabien Baron.

To my parents and siblings, thank you for all the support for so many years!

Lastly, all the thanks in the world to Stella the Border Collie. A day at Mount Wilson Observatory cannot properly begin without your happy face, fluffy tail, and a bark report for good measure.

TABLE OF CONTENTS

LIST OF TABLES

LIST OF FIGURES

List of Abbreviations

ADMM	Alternating Direction Method of Multipliers
AGN	Active Galactic Nucleus
AO	Adaptive Optics
BCL	Beam Combination Laboratory
BIC	Bayesian Information Criterion
BLR	Broad Line Region
BRT	Beam Reducing Telescope
CCF	Cross correlation function
CHARA	Center for High Angular Resolution Astronomy
CPU	Central Processing Unit
DEC	Declination
DM	Deformable Mirror
FFT	Fast Fourier Transform
FWHM	Full Width at Half Maximum
GP	Gaussian Process
GPU	Graphics Processing Unit
GVCO	General Variable Consensus Optimization
HJD	Heliocentric Julian Date
KI	Keck Interferometer

L-BFGS-B	Bounded, Memory Limited Broyden-Fletcher-Goldfarb-Shanno Algorithm
LABAO	Laboratory-based AO
LAMP	Lick AGN Monitoring Project
μm	Microns
MAP	Maximum A Posteriori
mas	Milliarcsecond
MEM	Maximum Entropy Method
MIR	Mid Infrared
MLE	Maximum Likelihood Estimation
mm	Millimeters
NIR	Near Infrared
NLR	Narrow Line Region
nm	Nanometers
NPOI	Navy Precision Optical Interferometer
OI	Optical Interferometry
OITOOLS	Optical Interferometry Tools
OPLE	Optical Path Length Equalization system
P.A.	Position Angle
PoPs	Pipes of Pan
PSNR	Peak Signal-to-Noise Ratio

RA Right Ascension

RLI Regularized Linear Inversion

RM Reverberation Mapping

RMS Root Mean Square

SHOT Stocastically-Driven Damped Harmonic Oscillator

SMBH Super-Massive Black Hole

TAO Telescope AO

TLDR Time-Lag Delay Reconstructor

TV Total Variation

VDM Velocity Delay Map

VLA Very Large Array

VLBA Very Long Baseline Array

VLTI Very Large Telescope Interferometer

WFS Wavefront Sensor

CHAPTER 1
ACTIVE GALACTIC NUCLEI

1.1 Definition

Since the very beginning of modern astronomy, the idea of an Active Galactic Nucleus (AGN) has been an amorphous and evolving concept. Before considering some of the historical framework behind the modern understanding of AGN, a modern definition of AGN will be posed. As it is where many astronomy students begin their exploration of AGNs, it is prudent to adopt the definition put forth in Bradley Peterson's "An Introduction to Active Galactic Nuclei" (Peterson 1997).

> "The term 'active galactic nucleus', or AGN, refers to the existence of energetic phenomena in the nuclei or central regions of galaxies which cannot be attributed clearly and directly to stars."

Nonstellar emission from these objects can be incredibly bright and is created by matter accreting onto a super massive black hole (SMBH) (Sparke & Gallagher 2007). Although it is now believed that all galaxies have a super massive black hole laying at their center, most nearby galaxies, including our own, do not have active nuclei. Given that nearby galaxies do not have active nuclei and that more distant (and therefore younger) galaxies do have active nuclei, it is generally believed that AGN arise as a phase in the development of galaxies. Studying AGN is therefore critical to our understanding of galaxy evolution.

1.2 Historical Perspective

1.2.1 Seyfert Galaxies

During the first part of the twentieth century, the arrival of the first modern large aperture telescopes facilitated the study of the so-called nebulae. The large apertures provided by the 60 inch and 100 inch reflecting telescopes at Mount Wilson Observatory, followed shortly after by the 200 inch telescope at Palomar Observatory, provided enough light-gathering power to make spectroscopic studies of nebulae possible.

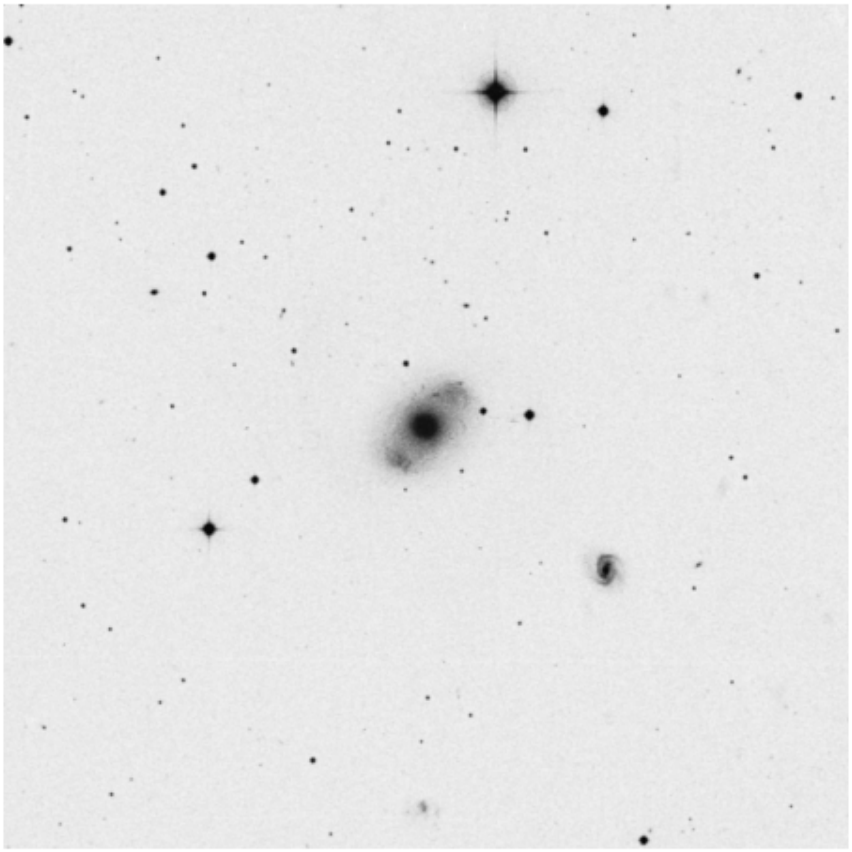

Figure 1.1 Image of the classic Seyfert galaxy NGC 4151 and surrounding field taken with the 48 inch Schmidt at Palomar Observatory accessed from the NASA/IPAC Extragalactic Database. The bright star-like nucleus superimposed on the faint, fuzzy structure of the galaxy shows an original indicator of the class under its early morphological definition.

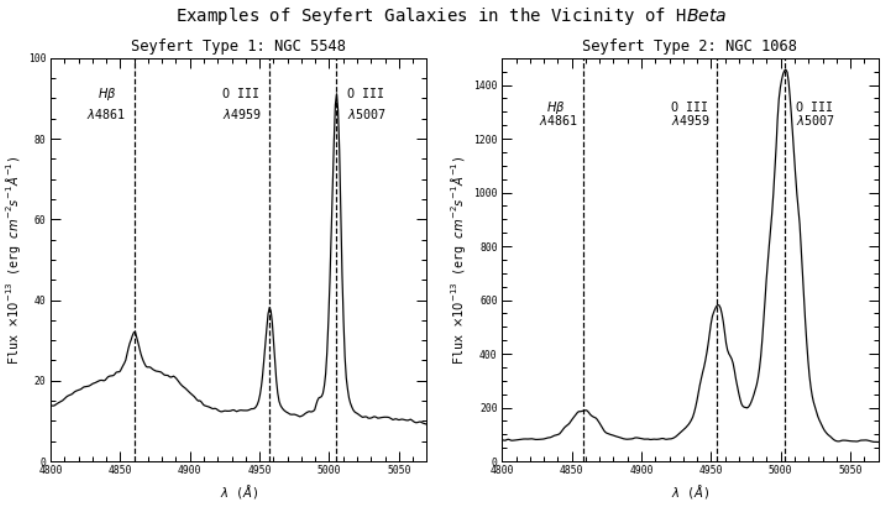

Figure 1.2 Examples of spectra of Seyfert Type 1 and Type 2 galaxies. On the left, NGC 5548 a typical Type 1 Seyfert AGN, with both the strong forbidden narrow Oxygen III lines and the very broad Hβ feature. On the right, the Type 2 Seyfert AGN NGC 1068 with similar strong forbidden Oxygen III spectral lines and an un-broadened Hβ feature. Both sets of spectra come from Ho et al. (1995) and were accessed via the NASA/IPAC Extragalactic Database (NED).

For a number of years, spectroscopic studies of galaxies were carried out, and anomalies were noted. It would not be until 1943 that Carl Seyfert would group together twelve galaxies with spectra exhibiting

> "many high-excitation emission lines localized in the nuclei" and having "exceedingly luminous stellar or semi-stellar nucleus" (Seyfert 1943).

Some years later, this class of objects known as "Seyfert Galaxies" would be split into two distinct categories based on the appearance of broad emission lines, where those with broad Balmer lines in evidence would be known as Type 1 and those without would be known as Type 2 (Khachikian & Weedman 1974). In figure 1.2, a prototypical example of each Type 1 and Type 2 is shown near the Hβ (λ=4861Å) feature. On the left, NGC 5548, a Type 1 Seyfert with strong forbidden Oxygen lines (O [III] (λ=4959Å and 5007Å) as well as the very broad Hβ feature. On the right, NGC 1068, a Type 2 Seyfert with the same strong forbidden oxygen lines, but with only a small unbroadened Hβ feature.

Within a decade of the original categorical split of Seyfert galaxies into two distinct categories, it was suggested that the two groups existed at opposite ends of a continuous spectrum (Osterbrock & Koski 1976). The space between Seyfert Type 1s and Seyfert Type 2s would soon be filled with a number of intermediary types 1.2, 1.5, 1.8, 1.9 (Osterbrock 1977, 1981). Further complicating the picture, in 1968 polarimetric observations of NGC 1068 revealed polarized broad Hydrogen features (Walker 1968). Myriad follow-up observations confirmed the finding and NGC 1068 became the target of much study for many years as astronomers worked to understand the relationship between Type 1 and Type 2 Seyfert Galaxies (Miller et al. 1991). The idea that Seyfert Type 1s and Type 2s exist on a spectrum has long fed speculation that the two types of objects share a common structure. The revelation that some Type 2 Seyferts hide Type 1 features in their polarized spectra gave a final hint that led to the modern understanding of Seyferts and of AGNs in general.

1.2.2 Quasi-stellar Objects

While investigating interference for Bell Telephone Laboratories in the 1920s and early 1930s, Karl Jansky discovered that a source of radio interference moved across the sky in step with the apparent motion of the stars launching the field of radio astronomy (Jansky 1933). By the end of the 1950s the field was mature enough to facilitate the first large scale radio surveys of the sky (Edge et al. 1959; Bennett 1962). Such surveys were soon followed by the co-location of radio sources with optical counterparts (Matthews & Sandage 1962, 1963).

In some cases, radio sources coincided with point-like optical sources. These objects exhibited spectra showing some evidence of a stellar contribution but also strong nonstellar features. These quasistellar radioloud sources and their radioquiet brethren would later become collectively known as quasars (Sparke & Gallagher 2007). The nature of quasars was a mystery until it was discovered in 1963 that these objects have significant redshift. In 1963 using the 200" reflecting telescope at Palomar, M. Schmidt found that the spectra

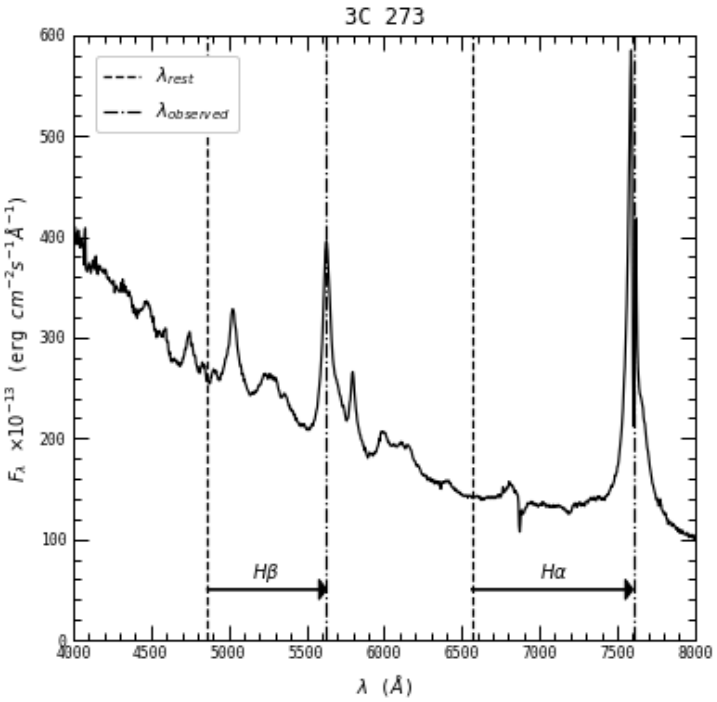

Figure 1.3 The spectrum of the quasar 3C 273, in the optical showing the rest frame positions of the $H\alpha$ and $H\beta$ emission lines and the observed locations of these features. This spectrum comes from Torrealba et al. (2012) and was accessed via the NASA/IPAC Extragalactic Database (NED).

for the optical component of 3C 273 were significantly redshifted (Schmidt 1963). Schmidt measured a redshift of $z = 0.158$, determined by the ~ 770Å shift in the $H\beta$ spectral line by

$$\lambda_{observed} = \lambda_{rest}\,(z + 1)\,. \tag{1.1}$$

Schmidt concluded that 3C 273 is the nuclear region of a galaxy subject to cosmological redshift and not a star. The redshifted optical spectrum of 3C 273 is shown in figure 1.3 with the hydrogen α and β features denoted by a dashed line at their rest wavelength and dash-dotted line at their observed wavelength.

1.2.3 Other Types of AGNs

While Seyferts and quasars are the most recognizable AGNs, there are numerous additional AGN types. Identified by the presence or absence of certain spectral features, variability features, or their overall luminosity, there is a veritable zoo of AGN types. While not relevant to the remainder of this dissertation, a few additional categories of AGNs are:

- BL Lacs and optically violent variables: Highly polarized radio loud rapidly variable AGNs (Peterson 1997)
- LINERS: Low ionization nuclear emission line regions appear similar to Seyfert 2s but with strong low ionization lines (Heckman 1980)
- Radio Galaxies: Radio loud AGNs which can be seen to exhibit broad lines, or just narrow lines (Peterson 1997).

1.3 The Modern View of AGN

It is generally accepted that at the heart of all AGNs lies a super massive black hole. This conclusion arises largely due to the staggering luminosity of AGNs. According to Peterson (1997) a typical luminosity for Seyfert galaxies is $\sim 10^{44}$ ergs s^{-1} and 10^{46} ergs s^{-1} for quasars. Assuming that AGNs are fueled by matter accreting onto the SMBH, an argument for the mass of the SMBH can be made. The theoretical limit for the luminosity of an object accreting pure hydrogen where the radiation pressure is balanced by the force of gravity, is known as the Eddington Luminosity (Eddington 1921; Joss et al. 1973). In the form presented by Peterson (1997), the Eddington Luminosity is

$$L_{Edd} = \frac{4\pi G c m_p}{\sigma_T} M, \tag{1.2}$$

where G is the gravitational constant, c is the speed of light, m_p is a proton mass, σ_T is the Thompson cross-section, and M is the mass of the accreting object. From the Eddington

Luminosity and the measured luminosity's of AGNs, it is simple to calculate that Seyferts must have masses of $\sim 10^6\ M_\odot$ and quasars $\sim 10^8\ M_\odot$. An alternative definition for AGN found in the literature classifies AGNs as those with an Eddington Ratio $L_{AGN}/L_{Edd} \geq 10^{-5}$ (Netzer 2015).

1.3.1 AGN Unification

It has been the goal of the community to lump all AGNs into a single group described by a single unifying phenomenological model. The original scheme for AGN unification consists of a SMBH surrounded by an accretion disk which gives way to an optically thick obscuring torus. In this model, the broad line emitting region lies close to the SMBH and accretion disk, but above the plane of the disk. The narrow line emitting region lies farther out along the polar axis within the cone shape defined by the opening in the torus (Urry & Padovani 1995; Antonucci 1993). The system may or may not have a jet and may or may not be radio loud. A commonly seen cartoon of the phenomenological model for AGN unification for radio loud objects is shown in figure 1.4 from Urry & Padovani (1995). In its most basic form, the goal of the unification model is to describe the difference between Type 1 and Type 2 AGN as a function of viewing angle. If the 'line-of-sight between the SMBH and the viewer passes through the obscuring torus, the broadline region is obscured and a Type 2 AGN is seen, but if the line-of-sight does not pass through the obscuring torus, then a Type 1 AGN is seen.

More recently, AGN Unification has sought to bring all AGNs together across different luminosity regimes. With the various selection effects in our observational data and the likelihood that some apparent AGNs are not what they seem, unification is challenging. It is clear that two major things should be kept in mind; first, an evolutionary path between Type 1 and Type 2 AGN has not been ruled out and second that there may be misidentified objects included in the AGN sample (Spinoglio & Fernández-Ontiveros 2021). While the simple unification model first presented is a good starting point, significant adjustments need

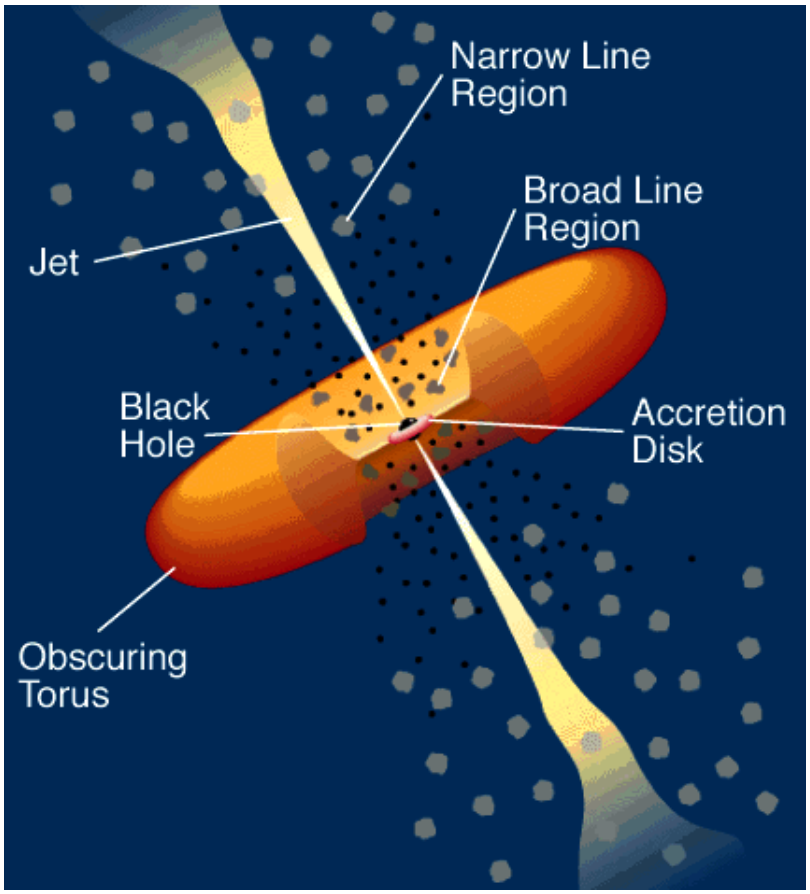

Figure 1.4 From Urry & Padovani (1995). Unification cartoon for AGN.

to be made due to our increased understanding of AGN. A recent review of AGN science Netzer (2015), describes several important points in revision of the original phenomenological model as:

- The torus is probably clumpy and axisymmetric.
- Disk winds are the likely cause of clumpiness and some outflows.
- The inconsistency in observed tori is not understood.
- Ionization cones exist along the polar axis of AGN separate from the central disk.
- There may be a population of objects included with AGNs that do not belong.
- Unification likely cannot describe SMBHs in galaxy mergers.

It is clear that most of the issues with the original model are refinements adding explanations of physical processes to our understanding of AGN rather than directly arguing against unification. The major sticking point is that of the obscuring torus, which has only become more complicated. It does not come as a surprise that these massive systems covering parsecs in scale are more complicated than a simple phenomenological model can describe. Despite the challenges in pursuing a fully satisfying unification model, it is still a worthy goal and tool providing a framework which the community can use to drive the study of AGN.

1.4 This Study of AGN

This dissertation is comprised of two parts, each an application of a different method for studying AGNs at the highest resolutions possible with today's technology. While both methods could be applied to any bright AGN, due to brightness constraints and data available at present, they are applied to Seyfert galaxies exclusively in this dissertation.

The first part of this dissertation, comprising chapter 2 through chapter 5 discusses the Reverberation Mapping technique. It includes an overview of the technique, as well

as the development of an image reconstruction algorithm for Reverberation Mapping, and an application of the algorithm to the Arp 151 dataset from the Lick AGN Monitoring Project data release from 2008. This well studied dataset allows for the comparison VDMs reconstructed with different methods.

The second part of this dissertation, from chapter 6 to the end is an application of long baseline optical interferometry to the study of AGN. This includes a brief introduction to optical interferometry, a description of the Center for High Angular Resolution Astronomy (CHARA) Array, first results for an extragalactic source observed by the CHARA Array on the AGN NGC 4151.

CHAPTER 2
REVERBERATION MAPPING

2.1 Introduction to Reverberation Mapping

In an AGN, clouds of photoionized gas near the SMBH at the galaxy's center emit highly broadened emission lines due to the extreme kinematics of the region. The area in which these broad lines are emitted is known as the broad-line region (BLR). Rapid variation of the broad line emission in response to variations in the continuum emission has long been observed for both radio quiet and radio loud AGN (Sandage 1967; Cromwell & Weymann 1970; Penston et al. 1974; Peterson 1988; Ulrich et al. 1997).

While the precise mechanism behind the observed variability is unknown, a number of viable theories exist, including, but not limited to, simple accretion onto the SMBH, magnetic field interactions within the accretion disk, or some combination of processes varying in contribution over various timescales (Czerny 2006). Regardless of the mechanism at play, the release of energy is observed as continuum light which propagates outward from the central region of the AGN. During the process, clouds of gas are ionized at different times depending on their distance from the accretion disk. As the photoionized gas recombines, it reemits the light as an emission line feature subject to the kinematics of the cloud. This is to say that any observed change above the noise level in the continuum emission from the AGN will be followed by a change in emission lines in the BLR separated by a delay corresponding to the difference in path length between the directly observed continuum emission, the resulting emission line feature, and the observer.

The classic example is that of a thin ring as described in Peterson (1993), shown in schematic form in Fig. 2.1, where the observer lies in plane of the figure at a sufficient distance along the horizontal line that light traveling from the thin ring to the observer arrives in effectively flat wavefronts. The thin ring of gas at a radius of one light-day from the central black hole is ionized by a pulse of light described by a δ-function. The ionizing pulse reaches the gas that comprises the shell at the same time. The gas is ionized and the

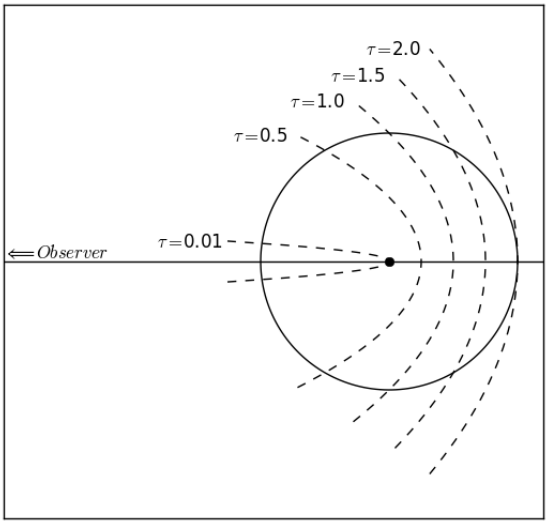

Figure 2.1 Classic isodelay surface schematic of an AGN showing how the various delays sample the entire area of the AGN consisting of a thin ring of spectral emitting material about the central SMBH. Recreated from Peterson (1993).

energy is then reemitted by the gas, subject to Doppler effects due to the kinematics of the region. Some of this reemitted light is along the line of sight to the observer. Light that is reemitted at the far side of the ring must travel back across the region, a distance of twice the ring's radius, such that it arrives at the observer with a delay of $2r/c$. Following the arc of the ring from the near side to the far side, the observer will see the reemitted light arrive with delay times covering the range from 0 to $2r/c$ with a bulk average delay of r/c. In Fig. 2.1 the dashed lines show lines of constant delay, known as isodelay surfaces, across the thin ring at varying delay times τ.

Moving from the thin ring to a more realistic distribution of gas around the SMBH results in more complex patterns in the observed response. Reverberation mapping (RM) is the tomographic method used to study the arrangement of photoionized gas near accreting black holes (Blandford & McKee 1982). At present, RM is primarily used to measure the masses of the SMBH at the heart of AGNs (Peterson & Wandel 2000; Bentz et al. 2009; De Rosa et al. 2015; Shen et al. 2015; Bentz & Katz 2015a). RM results also establish the radius-luminosity relationship (Bentz 2009; Bentz et al. 2013), which allows us to estimate

SMBH masses across all redshifts and consequently consider their influence on the evolution of galaxies across cosmological time (Booth & Schaye 2009).

Studying the kinematics of AGNs at the geometric scale provided by RM represents a substantial impetus behind RM campaigns (Peterson 1993; Horne et al. 2004). By providing complementary information on scales smaller than may be probed via Integral Field Spectroscopy (Storchi-Bergmann & Schnorr-Müller 2019) or Interferometry (Gravity Collaboration et al. 2020b), RM has the potential to bridge the gap in spatial scale between inflows and outflows and the central engine of AGNs.

One goal of RM in the inverse problem approach is to recover the velocity delay map (VDM), of an observed AGN. The VDM is a representation of the BLR where the geometry is encoded in the observed delay time and line-of-sight velocity of the re-emitting gas. Mathematical recovery of the VDM results from solving an ill-posed inverse problem, meaning that the number of degrees of freedom to reconstruct in the VDM is greater than the effective number of data points (flux-varying spectra). A conventional solution to this problem is regularized maximum likelihood or Maximum A Posteriori (MAP) in a Bayesian framework. Most software packages for RM rely on this formalism (Horne 1994; Krolik 1994; Skielboe et al. 2015), where the χ^2 of the reconstructed map is minimized along a set of regularizers that enforce the prior expectations on the model, the exception being a direct modeling approach (Pancoast et al. 2014a).

Classic examples of regularizers are positivity and maximum entropy (to enforce smoothness). Note that without these priors, the reconstruction algorithm would over-fit the χ^2, giving rise to spurious artifacts which would make the VDM un-interpretable. On the other hand, regularizers must remain generic, i.e., as non-committal as possible, so as not to bias the reconstruction towards a nonphysical solution. As shown in other fields of study such as interferometry (Schutz et al. 2015; Thiebaut & Giovannelli 2010), and medical imaging (Li et al. 2016b; Cao et al. 2007; Yao et al. 2015), it is the quality of the regularization and its strength that determine the actual mapping fidelity of a given piece of software.

Unfortunately, currently available software packages for RM offer little to no flexibility in terms of regularizers, and are mostly centered on smoothing, which *de facto* limit the interpretation of the data. From recent advances in the theory of Compressed Sensing, we now know that the key to optimally regularize such inverse problems is tapping into the sparsity of the reconstructed signals (Candes & Wakin 2008). In image reconstruction, sparsity is the idea that a signal may be represented by a number of non-zero coefficients that is small relative to the total number of coefficients in the signal (Davenport et al. 2011; Bryan & Leise 2013). RM is a poster example for Compressed Sensing, in that the VDMs that have been previously recovered for various AGNs are sparse.

The Time Lag/Delay Reconstruction algorithm (TLDR) presented here utilizes the Alternating Direction Method of Multipliers (ADMM), as well as two-dimensional regularization across the temporal and spectral axes of RM data, to reconstruct VDMs for RM.

2.2 Reverberation Mapping Mathematical Formulation

Reverberation mapping is a tomographic imaging process in which rapid changes in continuum emission from the center of an AGN are used to map the kinematics and geometry of the gas that reemits the continuum emission as line emission. While the precise relationship between the ionizing and emitted radiation is unknown, a number of assumptions serve as the backbone of reverberation mapping. These assumptions as laid down in Peterson (1993) are:

1. The continuum emission originates from a compact isotropically emitting central source.

2. The light-travel time between the central source and the clouds of the BLR is the primary source of delay.

3. A simple relationship between the ionizing emission of the central source and the response observed in BLR exists. This relationship need not be strictly linear in nature.

In reality, continuum emission does not appear in δ-function pulses, but rather as continuous variations. Both the spectral line and continuum emission must be treated as continuous functions. Doing so, the observed line emission $\mathbf{L}(t, \lambda)$ and continuum emission $\mathbf{C}(t)$ are functions of time which are related by the VDM $\mathbf{x}$ (Peterson 1994). Mathematically, the emission line response is the result of the continuum being convolved with the VDM, also called the transfer function (Blandford & McKee 1982),

$$\mathbf{L}\left(t, \lambda\right) = \int_0^\infty \mathbf{x}\left(\tau, \lambda\right) \mathbf{C}\left(t - \tau\right) d\tau. \tag{2.1}$$

Due to the discrete nature of observations, the convolution is not continuous, but discrete which appears as:

$$\mathbf{L}[t, \lambda] = \sum_{\tau=0}^{N} \mathbf{x}[\tau, \lambda]\mathbf{C}[t - \tau]. \tag{2.2}$$

The nature of the element-wise convolution allows the construction of a mapping matrix $\mathbf{H}$ comprised of elements from the continuum so that equation 2.2 can be represented purely as a linear relation

$$\mathbf{L} = \mathbf{H}\mathbf{x}. \tag{2.3}$$

The matrix $\mathbf{H}$ is constructed with rows corresponding to the number of observations in the spectra taken at time t and columns corresponding to the delay times τ such that each element in the matrix is a value of the continuum flux measured at time $t - \tau$, as shown in equation 2.4. The resulting mapping matrix $\mathbf{H}$ is a Toeplitz matrix representing the 1-dimensional convolution. Since the entire problem is linear, recovering the VDM is a straightforward inverse problem.

$$\mathbf{H} = \begin{array}{c} \\ t_{\rm time} \downarrow \end{array} \overset{\tau_{\rm delay} \longrightarrow}{\begin{pmatrix} C_{\mathrm{t}_1-\tau_1} & C_{\mathrm{t}_1-\tau_2} & C_{\mathrm{t}_1-\tau_3} & \cdots \\ C_{\mathrm{t}_2-\tau_1} & C_{\mathrm{t}_2-\tau_2} & C_{\mathrm{t}_2-\tau_3} & \cdots \\ C_{\mathrm{t}_3-\tau_1} & C_{\mathrm{t}_3-\tau_2} & C_{\mathrm{t}_3-\tau_3} & \cdots \\ \vdots & \vdots & \vdots & \ddots \end{pmatrix}}. \tag{2.4}$$

It is evident in Eqn. 2.3 that this method requires that the continuum data must exist at the proper sample times $t - \tau$ for all spectral sample dates t and all delay times τ. The required high cadence represents a serious challenge for all RM observational campaigns. In earlier work on RM, the requirement that continuum observations exist on a grid has been met by linearly interpolating the continuum data (Horne 1994; Krolik 1994). Recently, it has become common to model the continuum data in some way where both Damped Random Walk (Zu et al. 2011; Kelly et al. 2009) and Gaussian Process (Pancoast et al. 2011) models have been used to interpolate continuum observations.

2.3 The Velocity Delay Map

The VDM is a two-dimensional representation of the distribution of reverberating gas in the BLR, where the geometry is represented by line-of-sight velocity and delay time. The brief explanation of a thin ring orbiting a SMBH is an excellent place to develop an understanding of how the VDM relates to the physical geometry of the BLR, before expanding to more complicated geometries and their VDMs. The two bases for the VDM are velocity and delay. While velocity is relatively easy to understand with little explanation, the delay warrants some consideration.

Consider a cloud of gas in a circular orbit around a super massive black hole and its continuum creating source. A pulse of continuum light propagates outward at the speed of light in all directions, including towards the cloud of gas and an observer located very far

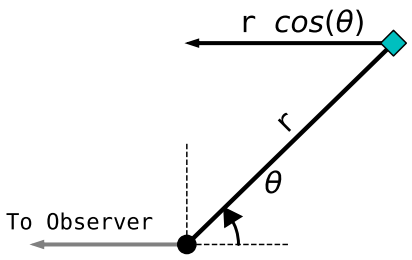

Figure 2.2 Schematic showing a geometric explanation for delay seen in reverberating BLR clouds relative to continuum emission in AGN.

away. The light propagating outward will encounter the cloud of gas after an amount of time corresponding to the cloud's orbital distance. The gas will absorb, reprocess, and emit the energy from the continuum as spectral emission, some of which will be along the line of sight to the observer. This pulse of continuum light, seen as a change in brightness of the continuum by the observer, will be followed by a change in brightness of the spectral emission at a later time, where the difference in time is the delay considered in RM. A more mathematical definition of delay is the amount of time it takes for light to travel the extra distance between the continuum emitting system and the gas cloud that reprocesses the continuum.

Light seen as a reprocessed continuum pulse from a cloud of gas orbiting at a distance r from the continuum emitting SMBH system at an angle θ has to travel an extra distance of

$$\text{extra distance} = r + r\cos(\theta) \tag{2.5}$$

where θ is defined with respect to the line passing through the SMBH system along the line of sight from the observer. The geometric layout for the extra distance is shown in figure 2.2, where the distance travelled from the SMBH system, shown as a black circle, to the gas

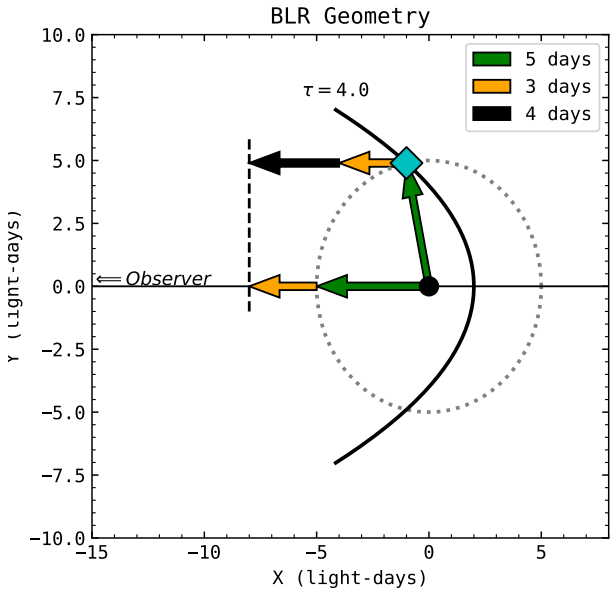

Figure 2.3 Schematic showing the delay arising from a cloud on a circular orbit as it intersects with a 4 day isodelay surface relative to continuum emission from the central source.

cloud, shown as a cyan diamond, and back to the position of the SMBH system along the x-axis is shown as a black arrow with the distance traveled in each segment labelled. Since the extra distance travelled is travelled at the speed of light, this extra distance corresponds to the delay time labelled τ, between emission from the central source and the emitting gas cloud. The standard form for the delay imposed by a cloud of gas at radius r, and angle θ relative to a continuum emitting SMBH system is

$$\tau = \frac{r}{c}\left(1 + \cos\left(\theta\right)\right). \tag{2.6}$$

It is common to rearrange equation 2.6 to show lines of constant delay, called isodelay surfaces. In which case the equation becomes

$$r = \frac{\tau c}{1 + \cos\left(\theta\right)}. \tag{2.7}$$

It may be more intuitive to describe the delay using a more complete schematic. A more physical example of this is shown in figure 2.3, where a cloud of gas lies on an orbit 5 light-days from the continuum emitting SMBH system with the center seen edge-on by an observer a very long way away along the labelled line. The orbiting gas is represented by the cyan diamond, its orbit as the dashed gray line, and the SMBH system as a black circle at 0,0. A solid black line represents an isodelay surface with a delay time of 4 days. This expected delay arises as follows. A continuum pulse propagates outward from the SMBH system at the speed of light. The pulse of light reaches the orbital distance of the cloud after 5 days, a time represented by the green arrows. One arrow shows the propagation of the continuum pulse along the line of sight to the observer, and the other to the position of the cloud of gas lying on the intersection of the orbit and the isodelay line representing a delay of 4 days. The cloud of gas absorbs the continuum pulse, reprocesses it, and emits the energy as spectral emission, which happens instantaneously relative to the light travel time from the central source.

The reemitted light includes some along the line of sight to the observer. After a few more days, the continuum pulse and the spectrally reprocessed pulse have moved towards the observer. The yellow arrows in figure 2.3 show the signals' progress after 3 days. Yet, the finite speed of light means that the spectrally reprocessed pulse is still behind the continuum pulse by the expected 4 days.

The velocity component of the VDM can be easily understood by considering the physical properties of the gas orbiting the SMBH system. For this, the single gas cloud becomes a large number of clouds on circular orbits creating a ring. Each gas cloud in the ring orbits the SMBH system with a velocity of

$$V = \sqrt{\frac{GM_{BH}}{r}} \tag{2.8}$$

Where G is the gravitational constant, M_{BH} is the mass of the central black hole, and R is the radius of the orbit. A schematic of the same geometry described in figure 2.3, is shown

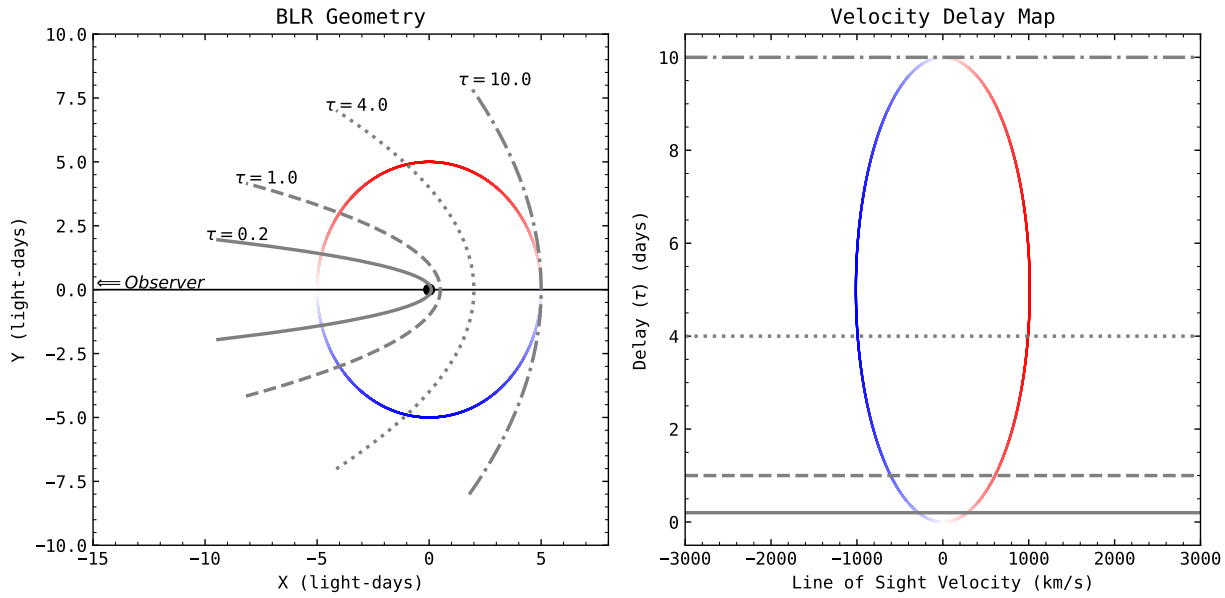

Figure 2.4 Example of a Keplerian ring orbiting about a SMBH and continuum emitting accretion disk. Left, the geometric layout with color indicating line-of-sight velocity and superimposed isodelay surfaces. Right, the VDM for the Keplerian ring with the same color scheme and matching isodelay surfaces from the geometric layout where velocity comes from the circular velocity of gas clouds in the ring.

in figure 2.4 on the left, where the single gas cloud is now a continuous ring of emitting gas clouds rotating clockwise as viewed from above. The ring's color represents the Doppler-shifted line-of-sight velocity as seen by the observer, where the gas moving away from the observer is red and the gas moving toward the observer is blue following with the comfortable convention of red-shift and blue-shift. The line-of-sight velocity is calculated as

$$V_{l.o.s.} = V\cos(\theta) \tag{2.9}$$

using the same definition for θ as in figure 2.3. The delay time τ for a particle can be calculated as in equation 2.6. This figure also has additional isodelay surfaces added at delays of 0.2, 1.0, and 10.0 days generated according to equation 2.7.

The VDM is then constructed by displaying the delay as a function of the line-of-sight velocity as shown in figure 2.4 on the right hand side. The circular ring is shown stretched

out in delay with the same color scheme corresponding to the velocity. The right plot also shows the same isodelay surfaces as the left plot where each is displayed as a matched solid, dashed, or dotted line between the two plots.

2.4 Velocity Delay Maps for Simple Geometries

With an understanding of the VDM, it is relatively simple to create VDMs for various geometries of the BLR in AGN. A spherical distribution of gas clouds around an AGN core with different velocity profiles, a Keplerian disk, and a spiral disk are classic examples of geometry and their VDMs used in the literature to show the expected VDM features in real RM programs.

First, a spherical distribution of gas clouds in a state of free fall as described in Welsh & Horne (1991) with an inner radius of 0.1 light-days and an outer radius of 4.0 light-days with an initial velocity of 250 km/s and an outward scaling of

$$V(r) = V_0 \left(\frac{r}{r_{min}} \right) \tag{2.10}$$

is adopted in which V_0 is the outflow velocity, and r_{min} is the inner velocity. Equations 2.9 and 2.6 for line-of-sight velocity and delay apply.

The overall geometry for a spherical distribution of gas clouds with an outflow is shown on the left in figure 2.5a where the observer lies very far away along the x-axis in the negative direction as indicated by the arrow and the gas clouds are colored according to their line-of-sight velocity. On the right side of figure 2.5b, the VDM for this distribution and velocity profile is shown, again with the color indicating the line-of-sight velocity. Taking the VDM and binning it down into pixels allows the VDM to be presented more as it would be seen in a VDM image reconstruction from real data. The diagonal response sweeping towards longer delays and higher line-of-sight velocity values is characteristic of outflows and would be expected from a VDM extracted from RM data on an AGN with strong outflow in the

BLR. To the right of the VDM in figure 2.5b the mean delay taken across all velocities is displayed. Below the VDM in the same figure, the mean velocity in each delay time pixel is displayed.

Second, the case of gas clouds in a spherical distribution in free fall. The same equations for delay and line-of-sight velocity are at play. In this case, the velocity is free-fall, where the gravitational potential energy is equal to the kinetic energy of the gas cloud.

$$V(r) = \sqrt{\frac{2GM_{BH}}{r}} \tag{2.11}$$

The characteristic evidence for free-fall in a VDM can be seen in figure 2.6a on the left, with the overall geometry shown on the right. An AGN with a significant free-fall signature could be identified by the straight edge starting near zero extending to longer delay times with a significant redshift as the delay time gets longer. A binned version of the free-fall VDM is shown in figure 2.6b with the mean profiles along the axes are also shown.

Another classic geometry for RM is that of a Keplerian disk orbiting about the central SMBH system. By populating a planar region from 0.1 light-days to 4.0 light-days and using equation 2.8 to calculate the velocity, a simple disk model can be made. The geometric model is shown in figure 2.7a on the left, with the VDM on the right. Once again, a binned version of the VDM is shown below the geometry and VDM. For the Keplerian disk, this is shown in figure 2.7b with the mean profiles projected below and next to the image.

Things get a bit more interesting when more complex geometry comes into play. One possible geometry for the BLR region could have clouds of gas orbiting in a spiral pattern. Utilizing the spiral model from Horne et al. (2004), where gas clouds on circular orbits are advanced logarithmically in azimuth as the radius increases.

$$\theta = \theta_{initial} + \log\left(\frac{r_0 - r}{\delta r}\right) \tag{2.12}$$

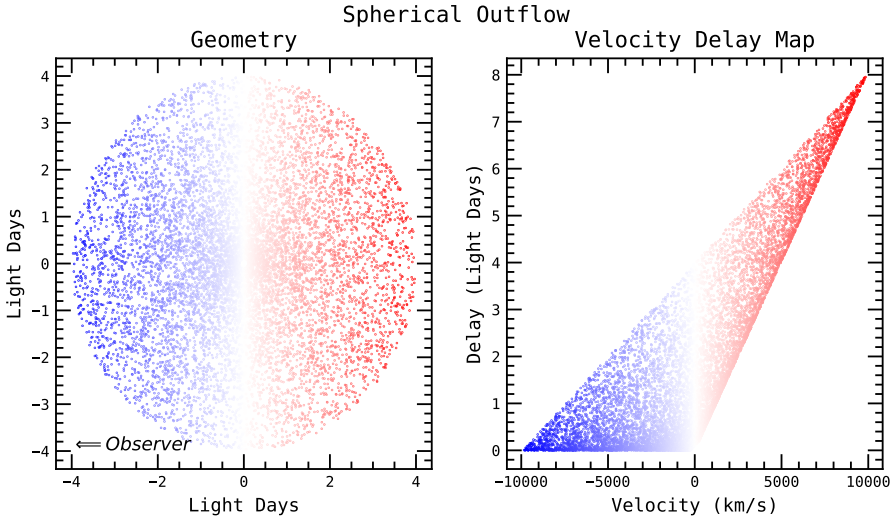

(a)

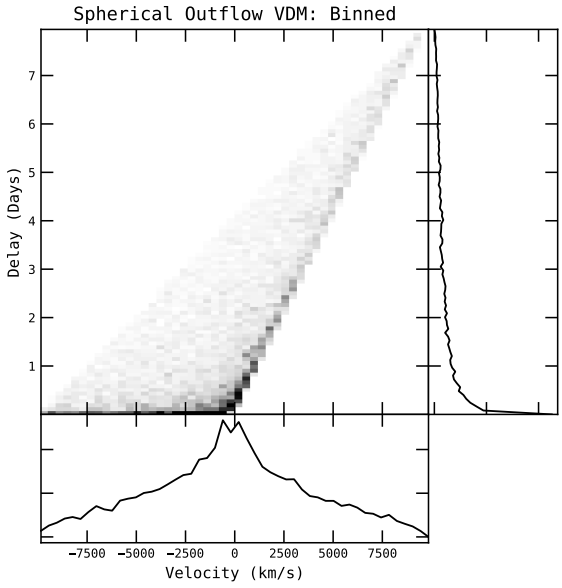

(b)

Figure 2.5 Simulated VDM for spherical outflow in AGN. (a) Simulated particle geometry, left, and velocity delay map, right. (b) Binned VDM for the simulated spherical outflow with mean cross-section responses below and to the right of the VDM. The characteristic evidence for outflow is the red-shifted response at longer delays.

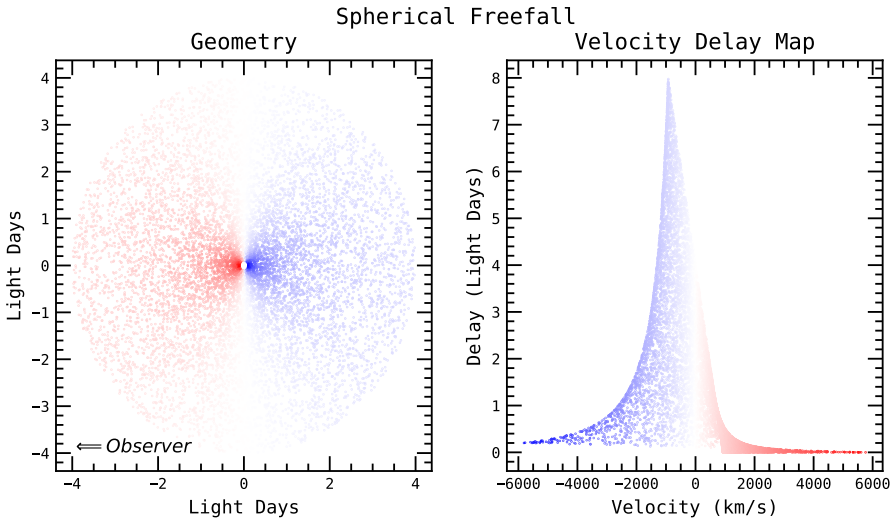

(a)

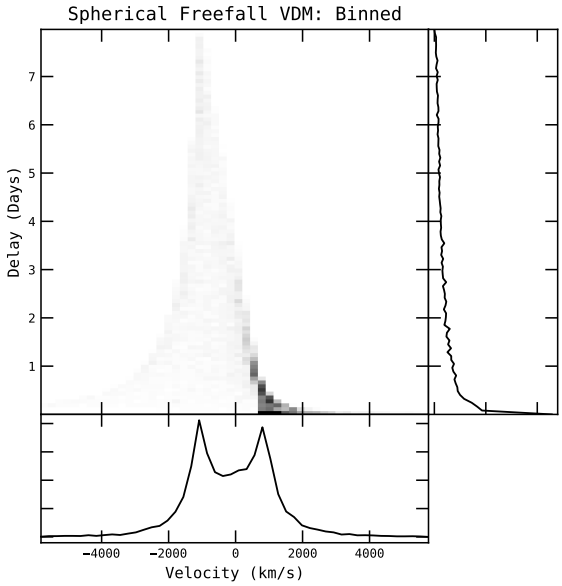

(b)

Figure 2.6 Simulated VDM for spherical free-fall in AGN. (a) Simulated particle geometry, left, and velocity delay map, right. (b) Binned VDM for the simulated spherical free-fall with mean cross-section responses below and to the right of the VDM. The characteristic evidence for inflow is the blue-shifted response at longer delays.

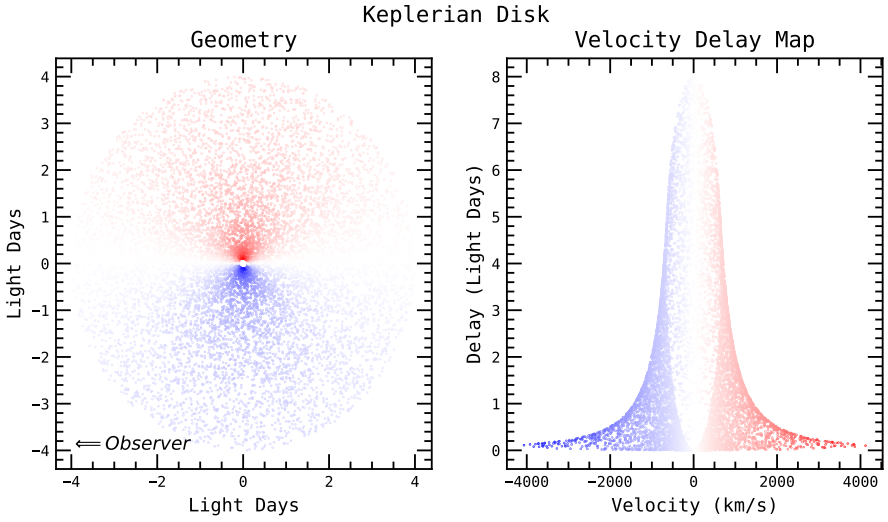

(a)

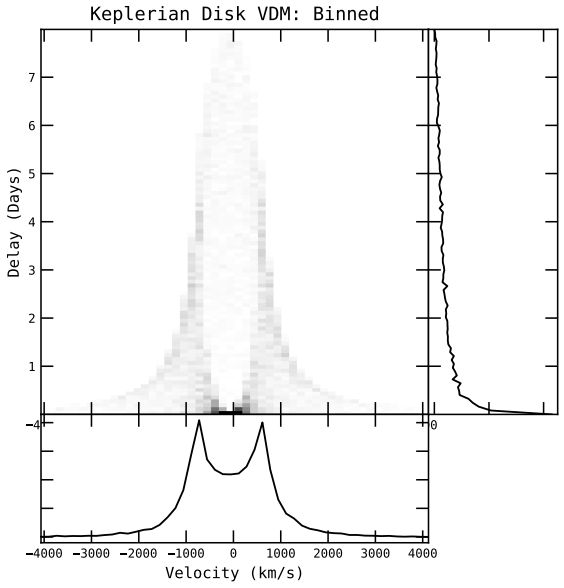

(b)

Figure 2.7 Simulated VDM for a Keplerian Disk about an AGN. (a) Simulated particle geometry, left, and velocity delay map, right. (b) Binned VDM for the simulated Keplerian Disk with mean cross-section responses below and to the right of the VDM. The characteristic evidence for disk geometry is the symmetric response and overall shape of the response.

Where r_0 is the inner radius of the spiral and δr is the average step in radius used in the model. As with the other models, the geometry, VDM, and binned VDM are shown in figure 2.8. Unsurprisingly, the filament structure of the spiral geometry results in filament structure in the VDM. These filaments are characteristic of a spiral geometry in a recovered VDM.

Before discussing some of the more exotic geometries proposed in the literature, it is important to note that all geometries discussed in section 2.4 were either planar and/or centrosymmetric. Of course, reality is not often planar or centrosymmetric, so any VDM is a two-dimensional representation of a three-dimensional space. Moving into three dimensions requires that the equations for delay and velocity must be updated to include the inclination of the system in question. Including the inclination, the line-of-sight velocity(equation 2.9) becomes

$$V_{l.o.s.} = V \cos(\theta) \sin(i), \tag{2.13}$$

and the delay(equation 2.6) becomes

$$\tau = \frac{r}{c} (1 + \cos(\theta) \sin(i)). \tag{2.14}$$

To consider the three-dimensional case, going back to a simple ring makes sense. With an inclination of 45 degrees, a mean radius of 10 light-days, and some noise added to the simulated gas cloud positions in both radius and height, a slightly fuzzy ring model is formed. The model is shown in figure 2.9a on the right with the coordinate axes for the ring and the coordinate axes for the observer denoted by the black and magenta arrows. The magenta arrow points to the observer, denoting line-of-sight. On the left, the same model is shown rotated so that the z axis corresponds to the observer's line of sight to object. In both plots shown in figure 2.9a, the 5 day isodelay surface is shown in green, and the 10 day isodelay surface is shown in yellow. In figure 2.9b on the right, the line-of-sight projection in the coordinate frame of the observer is shown, although in reality, these objects are too distant

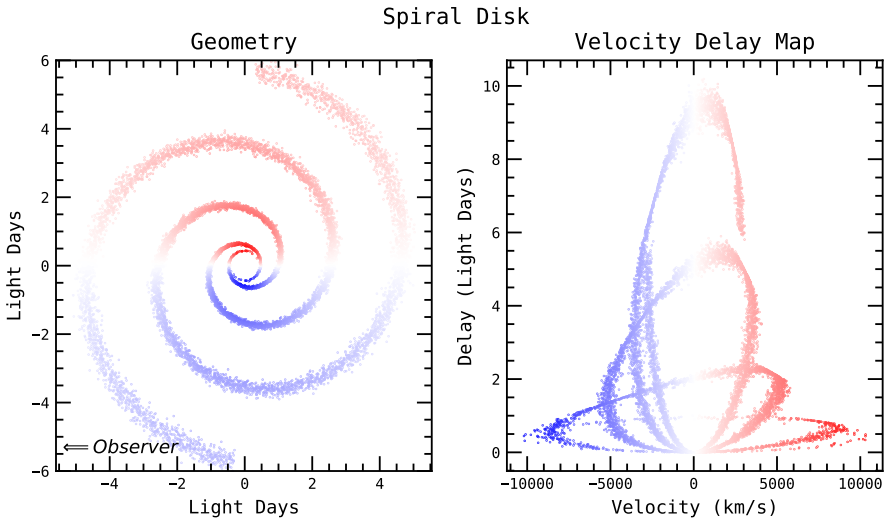

(a)

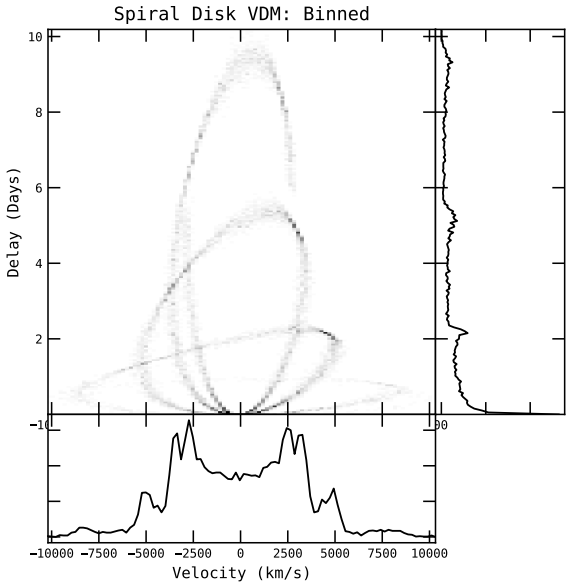

(b)

Figure 2.8 Simulated VDM for spiral geometry in AGN. (a) Simulated particle geometry, left, and velocity delay map, right. (b) Binned VDM for the simulated spiral with mean cross-section responses below and to the right of the VDM. The characteristic evidence for spiral geometry is the filaments in the response.

to be resolved like this using single aperture astronomy. On the left, the velocity delay map is shown with the same 5 day and 10 day isodelay surfaces represented again by green and yellow, respectively.

Despite the fact that geometrically the ring is consistent in its dimensions, the inclination angle has the effect of changing how much of the geometry coincides with a particular isodelay surface. This means that where an isodelay surface intersects with more of the ring, the expected signal in the VDM is enhanced. Similarly, projection effects cause some parts of the VDM to appear broader than others, again due to the amount of intersection between the ring and the isodelay surface. All of this is to point out that the three-dimensional geometry can confuse what would otherwise be expected to be relatively straightforward evidence of one geometric model over another in real RM data.

2.5 Velocity Delay maps for Complex Geometries

Of course, simple geometries are not always the best at explaining natural phenomena and a variety of more complicated theories exist on what may actually be happening in the BLR of AGNs. It is essential to consider how and why more complicated geometries might arise and how they might appear in recovered VDMs.

A common theory with wide spread acceptance for the origin of the BLR emitting clouds in AGN is a disk-driven wind. Arising out of the accretion disk around the SMBH, gas rises above the disk until the radiation pressure from the central engine dominates, where it begins to be pushed outward (Chiang & Murray 1996). The disk-wind model solves a few problems with traditional disk models, such as the "confinement problem" for outflows, as well as the lack of double-peaked emission-line profiles seen in observational AGN data (Murray et al. 1995). Mangham et al. (2019) has even shown that it is possible for RM to uncover response values less than zero, a counter-intuitive expectation that seems to break causality in the standard linearized echo model for RM. An example of a disk-wind model with negative response values is shown in figure 2.10. Furthermore, the disk-wind model can

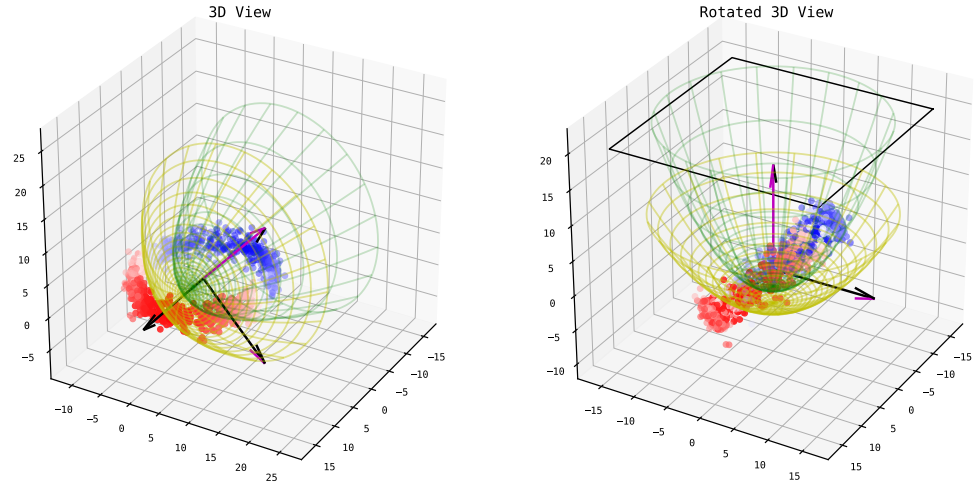

(a)

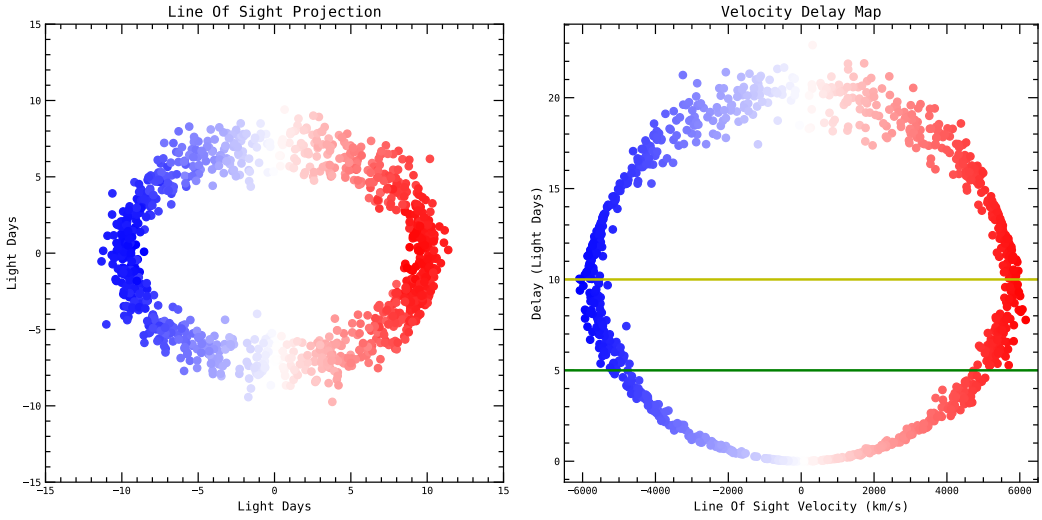

(b)

Figure 2.9 Simple model in three-dimensions of a ring of clouds on Keplerian orbits in an AGN. (a) left and right show the same geometry where the magenta arrow points to the observer along the line-of-sight and the green and yellow meshes are isodelay surfaces at 5 and 10 days respectively. On the left is represented the model where the x-y plane is the plane defined by the ring and on the right is the model rotated so that the x-y plane represents the projected view of the observer. (b) The same model as above, but shown as the two-dimensional projection into the line-of-sight on the left, and the corresponding VDM on the right with the same green and yellow lines showing the 5 and 10 day isodelay surfaces as above.

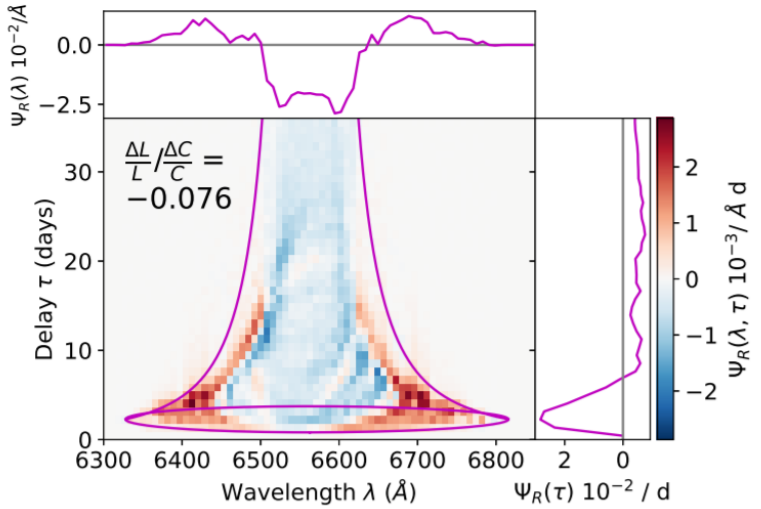

Figure 2.10 From Mangham et al. (2019). VDM for a disk-wind driven BLR where much of the VDM response is less than zero in direct opposition to discussions of causality in the linearized echo model.

give rise to many diverse shapes in VDMs, a selection of possible VDM signatures arising from disk-wind geometries from Waters et al. (2016) are shown in figure 2.11.

Regardless of the precise location and processes behind the BLR, AGNs are a likely place for binary black hole interactions to occur(McKernan et al. 2012; Ford & McKernan 2021). One possible scenario for binary black hole interactions is that of a binary black hole system embedded in the disk of an AGN. Li et al. (2021b) found that the material surrounding an AGN is a good location for binary black holes to contract towards a merger. Geometrically, binary black holes could have a profound effect on the geometry of the BLR, including the introduction of a localized spiral structure and clearing a gap in the accreting material.

Another plausible binary black hole interaction which might be expected in AGNs is that of a binary SMBH resulting from the merging of two galaxies. Two SMBHs could result in two distinct AGNs orbiting one another in close proximity. Depending on the state of each AGN and the characteristics of their orbit relative to line-of-sight, a binary AGN could appear as a superposition of any two AGN geometries as shown by Wang et al. (2018b), Songsheng et al. (2020), and Kovačević et al. (2020). An example, including combinations

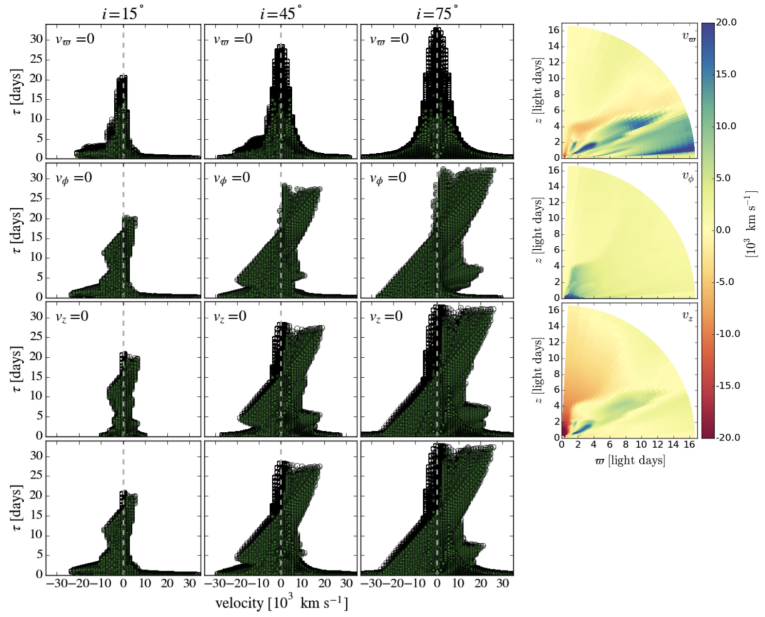

Figure 2.11 From Waters et al. (2016). A series of possible VDM geometries arising from disk-driven BLRs. Note that these VDMs have features indicative of both disk geometries and outflows. Additionally, some of these possibilities have unique features at low delay with velocities both positive and negative.

of simple BLR geometries in binary is shown in figure 2.12 from Wang et al. (2018b). While spectroscopic indications for binary SMBH have been detected, specifically for NGC 5548 (Li et al. 2016a), evidence for superimposed AGNs has not been found in recovered VDMs.

2.6 Reverberation Mapping Algorithms

Recovering VDMs from RM data is of significant interest in the RM community. As such, there exist a number of algorithms which have been developed to accomplish this goal. Each approaches the problem differently and results in VDMs of different qualities and focus. It has been shown in the field of optical interferometry, that multiple algorithms in friendly competition benefit the field by driving innovation and fostering community through a biennial imaging competition (Lawson et al. 2004; Cotton et al. 2008; Baron et al. 2012; Monnier et al. 2014; Sanchez-Bermudez et al. 2016; Mérand et al. 2018). In this regard, the development of another algorithm for VDM reconstruction in RM should not be viewed in

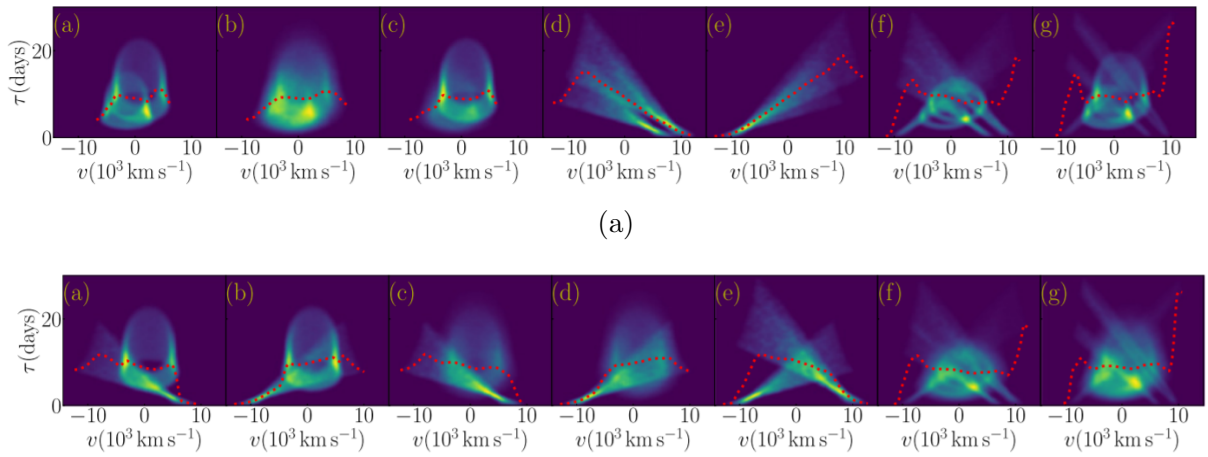

(a)

(b)

Figure 2.12 From Wang et al. (2018b); Songsheng et al. (2020). Composite VDMs arising from binary AGNs resulting from galaxy mergers using simple geometries, e.g. Disk, Inflow, Outflow. (a) Combinations of binary AGNs where each is of the same simple geometry. (b) Combinations of binary AGNs where each is of a different simple geometry.

a negative light, but as an additional tool driving the community towards consensus in our study of AGNs.

The first significant effort for recovering VDMs from RM data is regularized linear inversion (RLI). RLI is a relatively simple deconvolution method, which in its applied form focuses on smoothness of recovered VDMs (Krolik 1994; Krolik & Done 1995; Skielboe et al. 2015). A similar method and the one most widely used for recovering VDMs is the Maximum Entropy Method (MEM) applied via Keith Horne's MEMEcho algorithm (Horne 1994) as well as Xiao et al. (2018a). The MEM works by favoring the "simplest" solution to the RM problem, which favors very smooth VDMs and strictly enforces positivity. The Maximum Entropy Method has been applied with great success to many RM data sets (Bentz et al. 2010b; Grier et al. 2013a; Xiao et al. 2018b; Horne et al. 2021).

Recently, a Pixon-based VDM reconstruction algorithm has been developed by Li et al. (2021a). In the Pixon method, the pixels are transformed in to an array of information cells called "Pixons" which are intended to reflect the information from the source, rather than the interpretation of the information imposed by the detecting instrument (Pina & Puetter

1993). In the Pixon method, the pixons are allowed to change size and number, based on the SNR of the data, so that the information is represented by the fewest number of pixons. While the results presented in Li et al. (2021a) on simulated data are promising, results on real RM data have yet to be published.

A final method for obtaining VDMs from RM data comes in the form of dynamical modelling of the BLR . The dynamical modelling method uses a Gaussian Process (GP) interpolation of the RM continuum data and a simulated three-dimensional distribution of gas clouds, it then seeks the geometric layout of gas clouds which most nearly fits the observed spectral data (Pancoast et al. 2014a).

CHAPTER 3
DEVELOPING A REVERBERATION MAPPING ALGORITHM

As described in Anderson et al. (2021), this chapter explains the development of the TLDR algorithm version 1.

3.1 Inverse Problem Approach

As seen in chapter 2, there are many diverse signatures which may be present in RM data indicating the geometry and behavior of the BLR in an AGN. Due to the possible diversity in VDM signatures, it is imperative that any reconstruction not favor any particular geometric indicators. Rather, reconstructions should favor only characteristics common to all known indicators. In order to recover a VDM from RM data, the general framework for MAP is adopted. Common characteristics of geometric indicators in VDMs are applied as prior knowledge, such as positivity, smoothness, etc. Such prior knowledge is introduced in the form of regularization terms (Thiébaut 2005) that are minimized alongside the neg-log-likelihood of the data. The VDM solution $\mathbf{x}_{\text{opt}}$ is given by:

$$\mathbf{x}_{\text{opt}} = \underset{\mathbf{x}\in\mathbb{R}^{M\times N}}{\arg\min} \left\{ f_{data}\left(\mathbf{x}\right) + f_{prior}\left(\mathbf{x}\right) \right\} \tag{3.1}$$

Assuming Gaussian statistics based on flux levels, exposure times, and the Central Limit Theorem, the f_{data} term is commonly known as the χ^2 of the model relative to the data. In the case that Gaussian statistics do not hold and Poisson noise dominates, ADMM could still be used, albeit with some modifications. Here, construction of the χ^2 involves combining the discrete convolution of equation 2.3 with knowledge of the uncertainty in the data,

$$f_{data}(\mathbf{x}) = \frac{1}{2}\chi^2(\mathbf{x}) = \frac{1}{2}\left\|\mathbf{L}-\mathbf{H}\mathbf{x}\right\|_W^2 = \frac{1}{2}\left(\mathbf{H}\mathbf{x}-\mathbf{L}\right)^\top \mathbf{W}\left(\mathbf{H}\mathbf{x}-\mathbf{L}\right), \tag{3.2}$$

where $\mathbf{W}$ is the inverse covariance matrix of the emission line data $\mathbf{L}$ having the form

$$\mathbf{W}_\lambda = \begin{pmatrix} \frac{1}{\sigma_0^2} & 0 & 0 & \cdots \\ 0 & \frac{1}{\sigma_1^2} & 0 & \cdots \\ 0 & 0 & \frac{1}{\sigma_2^2} & \cdots \\ \vdots & \vdots & \vdots & \ddots \end{pmatrix}. \tag{3.3}$$

The second term in equation 3.1, $f_{prior}\,(x)$, is the prior or regularization term where the prior knowledge and expectations of the problem are enforced. The regularization term consists of the weighted sum of all regularizers, so that $f_{\rm prior}$ can be written:

$$f_{prior}(\mathbf{x}) = \sum_i \mu_i R_i(\mathbf{x}). \tag{3.4}$$

The combination of each regularizer $R_{\rm i}$ and its associated regularization hyper-parameter $\mu_{\rm i}$ allows each regularization term to be weighted individually allowing for flexibility in the reconstruction process. These functions serve to penalize the likelihood term in the minimization equation (equation 3.1). The effect of these penalties is to increase the value of the function within the minimization engine, making these solutions less probable in the Bayesian framework. Selection of regularizers for a reconstruction is an important step in setting up the reconstruction. Aside from being important to the eventual solution the use of different regularization strategies may impact the problem to be fed into the minimization algorithm.

For the RM problem, there are a number of regularizations that are natural choices. Tradiaionally, foremost among these would be positivity. Due to the nature of the AGN system creating the continuum pulses and the linear relationship between the pulses and the re-emission from the reverberating medium, only positive delays have any physical meaning. The traditional view is that negative values can only arise in the reconstruction where the linear model does not hold. In which case, the positivity regularizer works as a filter where negative values are simply projected to zero. Recently, it has been shown that under the disk-wind model, it is possible for negative values to arise naturally (Mangham et al. 2017). The

argument for causality has resulted in strict positivity enforcement in other VDM recovering algorithms which renders them incapable of recovering responses less than zero (Mangham et al. 2019). In order to allow for the case of negative responses, it is important that positivity be enforced optionally.

Since previously reconstructed VDMs are visibly sparse in the spectral axis (Bentz et al. 2010b; Grier et al. 2013a), another obvious regularizer choice is that of the ℓ_1-norm. More specifically, in the spectrum of an AGN at wavelengths where no broad emission lines are present, the VDM is expected to be zero for all delay times. As previously mentioned, this sparsity makes the RM problem a particularly good example for compressed sensing. As such, the so called ℓ_1-norm is well suited for reconstructing VDMs. Mathematically appearing as

$$\|x\|_1 \coloneqq \sum_{i=1}^{n} |x_i|, \tag{3.5}$$

the ℓ_1-norm favors the fewest number of nonzero terms in $\mathbf{x}$. In the case of RM this means that solutions with more zero-valued VDMs will be favored over any other solutions, matching with the expected sparsity in the VDM. Regularization by the ℓ_1-norm is accomplished according to the Soft Thresholding scheme of Donoho (1995).

As an alternative to the ℓ_1-norm, the square of the ℓ_2-norm favors images with many zero valued coefficients. It is however, slightly different mathematically with the ℓ_2-norm itself appearing as

$$\|x\|_1 \coloneqq \left(\sum_{i=1}^{n} |x_i|^2 \right)^{\frac{1}{2}}. \tag{3.6}$$

Its primary purpose is to promote smoothness in the image. The ℓ_2-norm penalizes larger pixel values more than small ones due to the square of the values seen in equation. Reducing the value of the ℓ_2-norm-squared drives the total amount of flux in the image down and brings the maximum and minimum flux values closer together, promoting smoother images.

Perhaps most importantly, the VDM is expected to be smooth both along the temporal axis and the spectral axis. The temporal axis is expected to be smooth due to the relationship

between absorbed and emitted light from the gas clouds being mapped in the BLR. The spectral axis will be smooth due to the kinematics of the region and the Doppler broadening of the emission lines themselves. Compressed sensing theory prescribes to enforce smoothness based on sparsity, either that of the gradient of the solution, or even more generally that of its wavelet transform. In both cases, regularization along the different axes is better treated as two individual regularization steps, allowing the regularization along each axis to be weighted differently.

In the case of gradient sparsity, the regularizer is known as anisotropic total variation (TV) and given by the ℓ_1-norm of the gradient of the image (Rudin et al. 1992).

$$\|x\|_{TV} \coloneqq \sum_{i=1}^{n} |\nabla x_i|. \tag{3.7}$$

Minimizing this regularization term favors $\mathbf{x}$ such that the sum over the gradient is as small as possible, which is to say the solutions with the least variations are favored. TV in this case is constructed using a finite difference matrix operator to represent the gradient, and the TV regularization term can be easily calculated and minimized using the same Soft Thresholding scheme as the standard ℓ_1-norm.

3.2 ADMM

In order to solve the problem posed by equation 3.13, ADMM is used. ADMM was developed as a combination of the method of multipliers and the dual ascent method (Boyd et al. 2011; Eckstein & Yao 2012). The convergence behavior of ADMM is well documented in general (Wang et al. 2018a; Nishihara et al. 2015) and for linear and quadratic problems specifically (Boley 2013; Han & Yuan 2013). This section is comprised of a discussion of ADMM for Global Variable Consensus Optimization (GVCO) and how it solves problems of the form of equation 3.13.

GVCO ADMM seeks to find the solution to the general GVCO problem,

$$\begin{aligned} \underset{\mathbf{x_i}}{\arg\min} \quad & \sum_{i=1}^{N} f_i\left(\mathbf{x}_i\right) \\ \text{subject to} \quad & \mathbf{x}_i - \mathbf{z} = 0, i = 1, ..., N. \end{aligned} \tag{3.8}$$

While having a different form than the general equation for solving an inverse problem in the MAP framework (equation 3.1), equation 3.8 represents the same problem. The differences lie in the construction of the ADMM algorithm. Key in the construction of ADMM is a variable splitting. In ADMM, the problem must be separable so that the general function can be split into two groups of functions, $f_{\mathrm{i}}(\mathbf{x}_{\mathrm{i}})$ and $g(\mathbf{z})$. ADMM will then seek to bring these two functions into consensus so that at convergence $\mathbf{x}_{\mathrm{i}} = \mathbf{z}$.

The ADMM algorithm is an augmented Lagrangian method, so the algorithm relies on the augmented Lagrangian in its minimization steps. The augmented Lagrangian takes the general form,

$$\begin{aligned} &\mathcal{L}\left(\ \mathbf{x}_{\mathrm{i}}, \mathbf{z}, \mathbf{y}_{\mathrm{i}}\right) = \\ &\quad \sum_{i=1}^{N} \left(f_i\left(\mathbf{x}_i\right) + \mathbf{y}_i^{\top}\left(\mathbf{x}_i - \mathbf{z}\right) + \frac{\rho_i}{2}\left\|\mathbf{x}_i - \mathbf{z}\right\|_2^2 \right) \end{aligned} \tag{3.9}$$

where $\mathbf{y}_i$ represents the Lagrange multipliers and ρ_i the penalty parameter. ADMM then proceeds iterating and following three steps, where the current iteration number is denoted by a superscript k:

1. Minimize each term, subscript i, of the augmented Lagrangian with respect to the corresponding $\mathbf{x}_{\mathrm{i}}$,

$$\mathbf{x}_i^{k+1} = \underset{\mathbf{x}_i}{\arg\min} \left(f_i\left(\mathbf{x}_i^k\right) + \mathbf{y}_i^{\top,k}\left(\mathbf{x}_i^k - \mathbf{z}^k\right) + \frac{\rho_i}{2}\left\|\mathbf{x}_i^k - \mathbf{z}^k\right\|_2^2 \right). \tag{3.10}$$

2. Minimize the augmented Lagrangian with respect to $\mathbf{z}$,

$$\mathbf{z}^{k+1} = \underset{\mathbf{z}}{\arg\min} \left(\sum_{i=1}^{N} -\mathbf{y}_i^{\top,k}\mathbf{z}^k + \frac{\rho_i}{2}\left\|\mathbf{x}_i^{k+1} - \mathbf{z}^k\right\|_2^2 \right). \tag{3.11}$$

3. Update the Lagrange Multipliers,

$$\mathbf{y}_i^{k+1} = \mathbf{y}_i^k + \rho_i \left(\mathbf{x}_i^{k+1} - \mathbf{z}^{k+1} \right). \tag{3.12}$$

This procedure repeats until the convergence parameters in place are satisfied. This method offers flexibility in that numerous regularization terms can be added with relatively little difficulty. The method also offers the potential for great computational speed because many steps and subroutines in the algorithm can be implemented in parallel.

3.3 TLDR Version 1

Inspired by recent implementations of ADMM in interferometry (Schutz et al. 2014; Ferrari et al. 2015; Thiébaut & Soulez 2012), the TLDR algorithm is built as an implementation of GVCO ADMM constructed to solve the RM problem given by equation 3.13. Through the assignment of new variable names, one for each regularization term used, the equations 3.10, 3.11, and 3.12 can be expanded to build the algorithm. Within TLDR, the χ^2 and ℓ_2-norm smoothing regularizations operate on $\mathbf{X}$, the positivity regularization operates on $\mathbf{P}$, the compressed sensing regularizer operates on $\mathbf{N}$, and the TV regularizer operates on $\mathbf{T}$. The new variables and their associated penalty parameters and Lagrange multipliers help to distinguish mathematical operations in the code, and are listed in Table 3.1. For convenience, the variable z is assigned to $\mathbf{Z}$.

With the new variables in place, the problem of equation 3.1 can be rewritten as follows,

$$\begin{aligned} \underset{\mathbf{X}}{\arg\min} \quad & \frac{1}{2} \left(\mathbf{HX} - \mathbf{L} \right)^\top \mathbf{W} \left(\mathbf{HX} - \mathbf{L} \right) + \frac{\mu_X}{2} \left\| \mathbf{X} \right\|_2^2 + \\ & \mu_N \left\| \mathbf{N} \right\|_1 + \mathbb{1}_{\mathbb{R}^+} (\mathbf{P}) + \mu_T \left\| \mathbf{T} \right\|_1 . \\ \text{subject to} \quad & \mathbf{X}, \mathbf{P}, \mathbf{N} = \mathbf{Z}; \mathbf{T} = \nabla \mathbf{Z} \end{aligned} \tag{3.13}$$

Expanding equation 3.9 using the new variables and the problem as written in equation 3.13 allows us to easily write the full Augmented Lagrangian.

Table 3.1. ADMM variable assignments within TLDR.

	Data $+\ell_2$-norm	Positivity	ℓ_1-norm	Total Variation
Original Term	$\|\mathbf{Hx}-\mathbf{L}\|_2^2+\frac{\mu_{\ell_2}}{2}\|\mathbf{x}\|_2^2$	$\mathbb{1}_{\mathbb{R}^+}(\mathbf{x})$	$\mu_{\ell_1}\|\mathbf{x}\|_1$	$\mu_{\mathrm{T}}\|\nabla\mathbf{x}\|_1$
Variable Assignment	$\mathbf{x}_0=\mathbf{X}$	$\mathbf{x}_1=\mathbf{P}$	$\mathbf{x}_2=\mathbf{N}$	$\mathbf{x}_3=\nabla\mathbf{Z}=\mathbf{T}$
New Term	$\|\mathbf{HX}-\mathbf{L}\|_F^2+\frac{\mu_{\ell_2}}{2}\|\mathbf{X}\|_2^2$	$\mathbb{1}_{\mathbb{R}^+}(\mathbf{P})$	$\mu_{\ell_1}\|\mathbf{N}\|_1$	$\mu_{\mathrm{T}}\|\mathbf{T}\|_1$
Penalty Parameter	$\mathbf{Y}_{\mathrm{X}}$	$\mathbf{Y}_{\mathrm{P}}$	$\mathbf{Y}_{\mathrm{N}}$	$\mathbf{Y}_{\mathrm{T}}$

$$
\begin{aligned}
\mathcal{L} = &(\mathbf{HX}-\mathbf{L})^\top\mathbf{W}(\mathbf{HX}-\mathbf{L})+\frac{\mu_{\ell_2}}{2}\|\mathbf{X}\|_2^2\\
&+\mathbf{Y_X}^\top(\mathbf{X}-\mathbf{Z})+\frac{\rho_X}{2}\|\mathbf{X}-\mathbf{Z}\|_2^2\\
&+\mathbb{1}_{\mathbb{R}^+}(\mathbf{P})+\mathbf{Y_P}^\top(\mathbf{P}-\mathbf{Z})+\frac{\rho_P}{2}\|\mathbf{P}-\mathbf{Z}\|_2^2\\
&+\mu_{\ell_1}\|\mathbf{N}\|_1+\mathbf{Y_N}^\top(\mathbf{N}-\mathbf{Z})+\frac{\rho_N}{2}\|\mathbf{N}-\mathbf{Z}\|_2^2\\
&+\mu_T\|\mathbf{T}\|_1+\mathbf{Y_T}^\top(\mathbf{T}-\nabla\mathbf{Z})+\frac{\rho_T}{2}\|\mathbf{T}-\nabla\mathbf{Z}\|_2^2
\end{aligned}
\tag{3.14}
$$

TLDR proceeds through the steps of ADMM outlined in Section 3.2 shown as pseudocode in algorithm 1.

Algorithm 1: Pseudocode for TLDR's ADMM block.

initialization $\mathbf{X},\mathbf{P},\mathbf{N}=\mathbf{Z}$; $\mathbf{T}=\nabla\mathbf{Z}$
calculate Initial VDM
while *converged == False* **do**
  minimization of Augmented Lagrangian w.r.t. $\mathbf{X}$
  minimization of Augmented Lagrangian w.r.t. regularization terms $\mathbf{P}$, $\mathbf{N}$, $\mathbf{T}$
  minimization of Augmented Lagrangian w.r.t. $\mathbf{Z}$
  update Lagrange Multipliers $\mathbf{Y}_{\mathrm{X}}$, $\mathbf{Y}_{\mathrm{P}}$, $\mathbf{Y}_{\mathrm{N}}$, $\mathbf{Y}_{\mathrm{T}}$
  check for convergence
end

Aside from the Lagrange multipliers update, which is performed exactly as equation 3.12, the steps in algorithm 1 are non-trivial and each warrants some discussion. Therefore, each will be discussed in order.

3.3.1 Initial VDM

The TLDR algorithm could begin from any initial VDM, but the optimal starting delay map should be as close to the final solution as possible. This reduces the amount of parameter space over which the pixel values in the delay map must move to find the best values. By starting near to the final solution, the number of iterations required by the algorithm is reduced, thereby reducing the amount of time required for the algorithm to find the final solution. However, care must be taken as it is possible to introduce artifacts into the initial VDM that will not easily be removed within the rest of the algorithm.

By isolating the first term in the augmented Lagrangian, a singly regularized least squares equation for the RM problem is found:

$$f\left(\mathbf{X}\right) = \left(\mathbf{HX} - \mathbf{L}\right)^{\top} \mathbf{W} \left(\mathbf{HX} - \mathbf{L}\right) + \frac{\mu_{\ell_2}}{2} \left\|\mathbf{X}\right\|_2^2 . \tag{3.15}$$

Minimizing, by taking the derivative of the function $f(\mathbf{X})$, setting it equal to zero, and solving for $\mathbf{X}$, yields the initial VDM:

$$\mathbf{X}^0 = \left(\mathbf{H}^{\top}\mathbf{WH} + \mu_{\ell_2}\mathbf{I}\right)^{-1} \left(\mathbf{H}^{\top}\mathbf{WL}\right) . \tag{3.16}$$

This method for analytically solving the ℓ_2-squared regularized least squares problem is known as Tikhonov Regularization (Tikhonov 1963) or Ridge Regression (Hoerl & Kennard 1970).

3.3.2 Minimization with respect to X

The minimization for $\mathbf{X}$ can be found analytically by solving the derivative of the full Augmented Lagrangian, equation 3.14, set equal to zero, for $\mathbf{X}$,

$$0 = \frac{\partial}{\partial \mathbf{x}} \mathcal{L}^*. \tag{3.17}$$

It is easy to begin by dropping all terms in the Augmented Lagrangian which do not include $\mathbf{x}$, leaving behind

$$\frac{\partial}{\partial \mathbf{X}} \left[\frac{1}{2} \left\| \mathbf{L} - \mathbf{H}\mathbf{X} \right\|_F^2 + \frac{\mu_{\ell_2}}{2} \left\| \mathbf{X} \right\|_2^2 + \mathbf{Y_X}^\top (\mathbf{X} - \mathbf{Z}) + \frac{\rho_{\mathbf{X}}}{\mathbf{2}} \left\| \mathbf{X} - \mathbf{Z} \right\|_{\mathbf{2}}^{\mathbf{2}} \right]. \tag{3.18}$$

What is left is easily separable allowing for the taking of the derivative term by term.

Term 1, using Eq. A.4

$$\frac{\partial}{\partial \mathbf{X}} \left[\frac{1}{2} \left\| \mathbf{L} - \mathbf{H}\mathbf{X} \right\|_F^2 \right] = \frac{1}{2} \frac{\partial}{\partial \mathbf{X}} \left[(\mathbf{L} - \mathbf{H}\mathbf{X})^\top \mathbf{W} (\mathbf{L} - \mathbf{H}\mathbf{X}) \right] = -\mathbf{H}^\top \mathbf{W} (\mathbf{L} - \mathbf{H}\mathbf{X}) \tag{3.19}$$

Term 2, using Eq. A.5

$$\frac{\partial}{\partial \mathbf{X}} \left[\frac{\mu_{\ell_2}}{2} \left\| \mathbf{X} \right\|_2^2 \right] = \mu_{\ell_2} \mathbf{X} \tag{3.20}$$

Term 3, using Eq. A.1

$$\frac{\partial}{\partial \mathbf{X}} \left[\mathbf{Y_X}^\top (\mathbf{X} - \mathbf{Z}) \right] = -\frac{\partial}{\partial \mathbf{X}} \left[\mathbf{Y_X}^\top \mathbf{X} \right] = \mathbf{Y_X} \tag{3.21}$$

Term 4, using Eq. A.3

$$\frac{\partial}{\partial \mathbf{X}} \left[\frac{\rho_X}{2} \left\| \mathbf{X} - \mathbf{Z} \right\|_2^2 \right] = \frac{\rho_X}{2} \frac{\partial}{\partial \mathbf{X}} \left[(\mathbf{X} - \mathbf{Z})^\top \mathbf{I} (\mathbf{X} - \mathbf{Z}) \right] = \rho_X (\mathbf{X} - \mathbf{Z}) \tag{3.22}$$

Now gather the terms for the derivative

$$\frac{\partial}{\partial \mathbf{X}}\mathcal{L}^* = -\mathbf{H}^\top \mathbf{W}\left(\mathbf{L} - \mathbf{H}\mathbf{X}\right) + \mu_{\ell_2}\mathbf{X} + \mathbf{Y}_\mathbf{Z} + \rho_\mathbf{Z}\left(\mathbf{X} - \mathbf{Z}\right) \tag{3.23}$$

Expand all terms

$$\frac{\partial}{\partial \mathbf{X}}\mathcal{L}^* = -\mathbf{H}^\top \mathbf{W}\mathbf{L} + \mathbf{H}^\top \mathbf{W}\mathbf{H}\mathbf{X} + \mu_{\ell_2}\mathbf{X} + \mathbf{Y}_\mathbf{Z} - \rho_\mathbf{Z}\mathbf{Z} + \rho_\mathbf{Z}\mathbf{X} \tag{3.24}$$

Group terms

$$\mathbf{H}^\top \mathbf{W}\mathbf{H}\mathbf{X} + \mu_{\ell_2}\mathbf{X} + \rho_X\mathbf{X} \quad -\mathbf{H}^\top \mathbf{W}\mathbf{L} + \mathbf{Y}_\mathbf{Z} - \rho_\mathbf{X}\mathbf{Z} \tag{3.25}$$

Separate $\mathbf{X}$ and simplify

$$\left(\mathbf{H}^\top \mathbf{W}\mathbf{H} + \left(\mu_{\ell_2} + \rho_\mathbf{X}\right)\mathbf{I}\right)\mathbf{X} = \mathbf{H}^\top \mathbf{W}\mathbf{L} - \mathbf{Y}_\mathbf{Z} + \rho_\mathbf{Z}\mathbf{Z} \tag{3.26}$$

Finally, solve for $\mathbf{X}$,

$$\mathbf{X}^{k+1} = \left(\mathbf{H}^\top \mathbf{W}\mathbf{H} + \left(\mu_X + \rho_X\right)\mathbf{I}\right)^{-1}\left(\mathbf{H}^\top \mathbf{W}\mathbf{L} + \rho_X\mathbf{Z} - \mathbf{Y}_X^k\right). \tag{3.27}$$

Due to the spectral dependence of $\mathbf{W}$, the minimization with respect to $\mathbf{X}$ must be carried out spectral line by spectral line so that equation 3.27 is used to find $\mathbf{X}$ by finding $\mathbf{X}_\lambda$ using each unique $\mathbf{W}_\lambda$, however, this step can be parallelized and the inversion step is constant. The pseudocode for solving equation 3.27 is shown in algorithm 2.

Algorithm 2: Pseudocode for TLDR's minimization of the Augmented Lagrangian with respect to $\mathbf{X}$.

for λ **do**
  $\mathbf{X}_\lambda = \left(H^\top W_\lambda H + \left(\mu_X + \rho_X\right) I\right)^{-1}\left(\mathbf{H}^\top W_\lambda L_\lambda + \rho_X Z_\lambda - Y_{X,\lambda}\right)$
end

3.3.3 Minimization w.r.t. Regularizers

The minimization of the augmented Lagrangian for each of the regularized variables involving the ℓ_1-norms of $\mathbf{N}$ and $\mathbf{T}$ is identical, though the input changes. The minimization problem can be written using a stand-in variable $\mathbf{r}_\mathrm{i}$,

$$\arg\min_{\mathbf{r_i}} f\left(\mathbf{r}_i\right) + \frac{\rho_{\mathbf{r}_i}}{2} \left\|\mathbf{r}_i - \tilde{\mathbf{r}}_i\right\|_2^2 . \tag{3.28}$$

when posing $\tilde{\mathbf{r}}_\mathrm{i} = \mathbf{Z} - \mathbf{Y}_{\mathbf{r}_\mathrm{i}}/\rho_{\mathbf{r}_\mathrm{i}}$. This is as a MAP problem, solvable by proximal operators. A proximal operator allows the minimization to be replaced with analytic functions that can be evaluated quickly within the ADMM loop, e.g. the proximal operator for the ℓ_1-norm is known as soft-thresholding (Donoho 1995). The solution to the minimization is the projection

$$\mathbf{r}_\mathbf{i}^+ = \mathrm{sgn}\left(\tilde{r}_i\right) \max\left(\left|\tilde{r}_i\right| - \frac{\mu_r}{\rho_r}, 0\right) . \tag{3.29}$$

Although the projection is identical, the input for the projected solution for $\mathbf{T}$ must include the gradient. So that for $\mathbf{T}$, $\tilde{\mathbf{r}}_\mathrm{T} = \nabla\mathbf{Z} - \mathbf{Y}_\mathbf{T}/\rho_\mathbf{T}$. In practice, the projection relating to negative values $\tilde{\mathbf{r}}_\mathbf{i} \leq -\mu_\mathbf{r}/\rho_\mathbf{r}$ in the VDM are rejected as an additional enforcement of positivity in TLDR version 1.

Similarly, for the positivity regularizer, equation 3.28 holds and only the projection changes. Where the projection is simply

$$\mathbf{P}^+ = \max\left(0, \mathbf{Z} - \frac{\mathbf{Y_P}}{\rho_P}\right) . \tag{3.30}$$

In effect, the proximal operator for positivity simply rejects values where $\mathbf{Z} < \frac{\mathbf{Y_P}}{\rho_\mathbf{P}}$.

3.3.4 Minimization w.r.t. Z

To find the analytical solution for $\mathbf{Z}$, the same procedure as used for the minimization of $\mathbf{X}$ is used. Begin by taking the derivative of the Augmented Lagrangian, equation 3.14, with respect to Z, set equal to zero and solve for $\mathbf{Z}$. Once again, step by step. The goal is to solve

$$0 = \frac{\partial}{\partial \mathbf{Z}} \mathcal{L}^* \tag{3.31}$$

We can immediately reduce the number of terms to deal with by dropping anything that does not include $\mathbf{Z}$,

$$\begin{aligned} \frac{\partial}{\partial \mathbf{Z}} [\ & \mathbf{Y_Z}^\top (\mathbf{X} - \mathbf{Z}) + \frac{\rho_\mathbf{X}}{\mathbf{2}} \|\mathbf{X} - \mathbf{Z}\|_\mathbf{2}^\mathbf{2} \\ & + \mathbf{Y_P}^\top (\mathbf{P} - \mathbf{Z}) + \frac{\rho_\mathbf{P}}{\mathbf{2}} \|\mathbf{P} - \mathbf{Z}\|_\mathbf{2}^\mathbf{2} \\ & + \mathbf{Y_N}^\top (\mathbf{N} - \mathbf{Z}) + \frac{\rho_\mathbf{N}}{\mathbf{2}} \|\mathbf{N} - \mathbf{Z}\|_\mathbf{2}^\mathbf{2} \\ & + \mathbf{Y_T}^\top (\mathbf{T} - \nabla \mathbf{Z}) + \frac{\rho_\mathbf{T}}{\mathbf{2}} \|\mathbf{T} - \nabla \mathbf{Z}\|_\mathbf{2}^\mathbf{2} \Big] \end{aligned} \tag{3.32}$$

To be thorough and reduce the chances for errors, the derivative for each term will be found independently.

Term 1, using Eq. A.1

$$\frac{\partial}{\partial \mathbf{Z}} \left[\mathbf{Y_X}^\top (\mathbf{X} - \mathbf{Z}) \right] = \frac{\partial}{\partial \mathbf{Z}} \left[\mathbf{Y_X}^\top \mathbf{Z} \right] = -\mathbf{Y_X} \tag{3.33}$$

The derivatives of terms 3 and 5 will be identical to those of term 1 with the $\mathbf{X}$ swapped for $\mathbf{P}$ and $\mathbf{N}$ respectively.

Term 2, using Eq. A.3

$$\frac{\partial}{\partial \mathbf{Z}} \left[\frac{\rho_X}{2} \|\mathbf{X} - \mathbf{Z}\|_2^2 \right] = \frac{\rho_X}{2} \frac{\partial}{\partial \mathbf{Z}} \left[(\mathbf{X} - \mathbf{Z})^\top I (\mathbf{X} - \mathbf{Z}) \right] = -\rho_X (\mathbf{X} - \mathbf{Z}) \tag{3.34}$$

Term 3, using Eq. A.1

$$\frac{\partial}{\partial \mathbf{Z}}\left[{\mathbf{Y_P}}^{\top}\left(\mathbf{P}-\mathbf{Z}\right)\right]=-\mathbf{Y_P} \tag{3.35}$$

Term 4, using Eq. A.3

$$\frac{\partial}{\partial \mathbf{Z}}\left[\frac{\rho_P}{2}\left\|\mathbf{P}-\mathbf{Z}\right\|_2^2\right]=-\rho_P\left(\mathbf{P}-\mathbf{Z}\right) \tag{3.36}$$

Term 5, using Eq. A.1

$$\frac{\partial}{\partial \mathbf{Z}}\left[{\mathbf{Y_N}}^{\top}\left(\mathbf{N}-\mathbf{Z}\right)\right]=-\frac{\partial}{\partial \mathbf{Z}}\left[{\mathbf{Y_N}}^{\top}\mathbf{Z}\right]=-\mathbf{Y_N} \tag{3.37}$$

Term 6, using Eq. A.3

$$\frac{\partial}{\partial \mathbf{Z}}\left[\frac{\rho_N}{2}\left\|\mathbf{N}-\mathbf{Z}\right\|_2^2\right]=\frac{\rho_N}{2}\frac{\partial}{\partial \mathbf{Z}}\left[\left(\mathbf{N}-\mathbf{Z}\right)^{\top}\mathbf{I}\left(\mathbf{N}-\mathbf{Z}\right)\right]=-\rho_N\left(\mathbf{N}-\mathbf{Z}\right) \tag{3.38}$$

Term 7, using Eq. A.1

$$\frac{\partial}{\partial \mathbf{Z}}\left[{\mathbf{Y_T}}^{\top}\left(\mathbf{T}-\nabla\mathbf{Z}\right)\right]=-\frac{\partial}{\partial \mathbf{Z}}\left[{\mathbf{Y_T}}^{\top}\nabla\mathbf{Z}\right]=-\nabla^{\top}\mathbf{Y_T} \tag{3.39}$$

Term 8, using Eq. A.3

$$\frac{\partial}{\partial \mathbf{Z}}\left[\frac{\rho_T}{2}\left\|\mathbf{T}-\nabla\mathbf{Z}\right\|_2^2\right]=\frac{\rho_T}{2}\frac{\partial}{\partial \mathbf{Z}}\left[\left(\mathbf{T}-\nabla\mathbf{Z}\right)^{\top}\mathbf{I}\left(\mathbf{T}-\nabla\mathbf{Z}\right)\right]=-\rho_T\nabla^{\top}\left(\mathbf{T}-\nabla\mathbf{Z}\right) \tag{3.40}$$

Now by assembling all terms, the derivative is constructed.

$$\begin{aligned}\frac{\partial}{\partial \mathbf{Z}}\mathcal{L}^{*}=&-\mathbf{Y_X}-\rho_{\mathbf{X}}\left(\mathbf{X}-\mathbf{Z}\right)\\&-\mathbf{Y_P}-\rho_{\mathbf{P}}\left(\mathbf{P}-\mathbf{Z}\right)\\&-\mathbf{Y_N}-\rho_{\mathbf{N}}\left(\mathbf{N}-\mathbf{Z}\right)\\&-\nabla^{\top}\mathbf{Y_T}-\rho_{\mathbf{T}}\nabla^{\top}\left(\mathbf{T}-\nabla\mathbf{Z}\right)\end{aligned} \tag{3.41}$$

First expand everything.

$$\begin{aligned}\frac{\partial}{\partial \mathbf{Z}}\mathcal{L}^* = &- \mathbf{Y_X} - \rho_{\mathbf{X}}\mathbf{X} + \rho_{\mathbf{X}}\mathbf{Z} \\ &- \mathbf{Y_P} - \rho_{\mathbf{P}}\mathbf{P} + \rho_{\mathbf{P}}\mathbf{Z} \\ &- \mathbf{Y_N} - \rho_{\mathbf{N}}\mathbf{N} + \rho_{\mathbf{N}}\mathbf{Z} \\ &- \nabla^\top \mathbf{Y_T} - \rho_{\mathbf{T}}\nabla^\top \mathbf{T} + \rho_{\mathbf{T}}\nabla^\top\nabla\mathbf{Z}\end{aligned} \tag{3.42}$$

Group terms

$$\rho_X\mathbf{Z} + \rho_{\mathbf{P}}\mathbf{Z} + \rho_{\mathbf{N}}\mathbf{Z} + \rho_{\mathbf{T}}\nabla^\top\nabla\mathbf{Z} - \mathbf{Y_X} - \rho_{\mathbf{X}}\mathbf{X} - \mathbf{Y_P} - \rho_{\mathbf{P}}\mathbf{P} - \mathbf{Y_N} - \rho_{\mathbf{N}}\mathbf{N} \tag{3.43}$$

Separate $\mathbf{Z}$

$$\left(\rho_X + \rho_P + \rho_N + \rho_T\nabla^\top\nabla\right)\mathbf{Z} - \mathbf{Y_X} - \rho_{\mathbf{X}}\mathbf{X} - \mathbf{Y_P} - \rho_{\mathbf{P}}\mathbf{P} - \mathbf{Y_N} - \rho_{\mathbf{N}}\mathbf{N} \tag{3.44}$$

Finally, solve for $\mathbf{Z}$

$$\begin{aligned}\mathbf{Z}^{k+1} = &\left(\left(\rho_X + \rho_P + \rho_N\right)\mathbf{I} + \rho_T\nabla^\top\nabla\right)^{-1} \\ &\left(\mathbf{Y}_X + \rho_X\mathbf{X} + \mathbf{Y}_P + \rho_P\mathbf{P} + \mathbf{Y}_N + \rho_N\mathbf{N} + \nabla^\top\mathbf{Y}_T + \rho_T\nabla^\top\mathbf{T}\right).\end{aligned} \tag{3.45}$$

The minimization w.r.t. $\mathbf{Z}$ benefits from the lack of spectral dependence in the solution. In its implemented form, $\mathbf{Z}$ is calculated very quickly as matrix multiplication using the Fast Fourier Transform (FFT) to handle the gradients. Implementing the the forward difference gradient operator as an implementation of the convolution theorem allows the Z update step to be calculated by only multiplication. Note also that the inversion used is constant, meaning that the Z update step is extremely fast.

3.3.5 Convergence Testing

In TLDR, convergence testing is carried out as outlined in Boyd et al. (2011) §3.3.1. At each iteration k, the primal residual $\mathbf{r}^k$, dual residual $\mathbf{s}^k$, and their tolerances ϵ^{pri} and ϵ^{dual} as:

$$\mathbf{r}^k = \left(\mathbf{X}^k - \mathbf{Z}^k, \mathbf{N}^k - \mathbf{Z}^k, \mathbf{P}^k - \mathbf{Z}^k, \frac{1}{2}\left(\mathbf{T}^k - \nabla \mathbf{Z}^k\right) \right) \tag{3.46}$$

$$\begin{aligned} \mathbf{s}^k = \big(&\rho_X \left(\mathbf{Z}^k - \mathbf{Z}^{k-1} \right), \rho_N \left(\mathbf{Z}^k - \mathbf{Z}^{k-1} \right), \\ &\rho_P \left(\mathbf{Z}^k - \mathbf{Z}^{k-1} \right), \rho_T \left(\mathbf{Z}^k - \mathbf{Z}^{k-1} \right) \big) \end{aligned} \tag{3.47}$$

$$\begin{aligned} \epsilon^{pri} = \epsilon^{abs} + \epsilon^{rel} \max \Big\{ &\left\| \mathbf{X}^k \right\|_2, \left\| \mathbf{N}^k \right\|_2, \left\| \mathbf{P}^k \right\|_2, \\ &\frac{1}{2} \left\| \mathbf{T}^k \right\|_2, \left\| \mathbf{Z}^k \right\|_2 \Big\}, \end{aligned} \tag{3.48}$$

and

$$\begin{aligned} \epsilon^{dual} = \epsilon^{abs} + \epsilon^{rel} \max \Big\{ &\left\| {\mathbf{Y}_\mathbf{X}}^k \right\|_2, \left\| {\mathbf{Y}_\mathbf{N}}^k \right\|_2, \left\| {\mathbf{Y}_\mathbf{P}}^k \right\|_2, \\ &\frac{1}{2} \left\| \nabla^\top {\mathbf{Y}_\mathbf{T}}^k \right\|_2, \Big\}, \end{aligned} \tag{3.49}$$

where ϵ^{pri} and ϵ^{dual} are the global tolerances of the primal and dual residuals, respectively.

TLDR is said to have converged when both the norm of the primal residual and norm of the dual residual have dropped below their respective tolerances ϵ^{pri} and ϵ^{dual}. Which is to say, TLDR has converged when $\left\| \mathbf{r}^k \right\|_2 \leq \epsilon^{pri}$ and $\left\| \mathbf{s}^k \right\|_2 \leq \epsilon^{dual}$. These parameters can be tuned to get the desired convergence behavior. Should the convergence criterion not be met, TLDR will terminate after a maximum number of iterations set by the user.

3.3.6 Input Data

Intended as a flexible method for reconstructing VDMs from RM data, TLDR makes minimal assumptions of the data provided to it. As mentioned in Section 2.2, the continuum data must exist on an appropriate grid of time corresponding to the sample times of the spectral data and the delay times of the VDM to be reconstructed. To guarantee the proper construction

of the convolution operator, TLDR applies a linear interpolation to the continuum data, but does not consider the uncertainty on the continuum. This is the only processing applied to continuum data by TLDR. Should the continuum data be modelled at the appropriate times before being passed to TLDR, this linear interpolation will not affect the data in any way. Additionally, TLDR makes no assumptions on the spectral data provided to it. The option to model either the continuum data or the spectra data is left to the user as a data preparation step.

While TLDR does not require modelled data to be provided to it, modelling of both continuum data and spectral data prior is strongly recommended prior to reconstructing a VDM. As TLDR does not consider uncertainties on continuum data, modelling the continuum allows these uncertainties and large gaps in observations to be considered before any VDM is reconstructed, as well as providing a reliable method for interpolating the light curve. Gaussian Process (GP) modelling, previously adopted for RLI (Skielboe et al. 2015), and Damped Random Walk models, as implemented in the JAVELIN code (Zu et al. 2011), have successfully been used for modelling continuum light curves for RM. For a fast Gaussian Process modelling method easily applied to RM data, see Foreman-Mackey et al. (2017). Similarly, modelling of spectral data with software such as PREPSPEC can isolate and remove constant spectral components, allowing TLDR to reconstruct a VDM based on only the broad line variations in the data. A recent discussion of the PREPSPEC software's spectral decomposition method can be found in Horne et al. (2020).

3.3.7 Additional TLDR Notes

To streamline the use of TLDR and ease the frustrations that arise due to the sensitivity of the algorithm to the selection of the penalty parameters, three strategies for automatically adapting the penalty parameters were tested. Unfortunately, the simple strategy in Boyd et al. (2011) §3.4.1, the more advanced residual balancing scheme described in Wohlberg (2017), and the Adaptive Consensus ADMM (ACADMM) strategy of Xu et al. (2017) re-

sulted in instability in the algorithm. These instabilities arise out of the proximal projections used in TLDR, although they worked quite well when these terms were not used. As such, TLDR does not have a method of automatically selecting penalty parameters. This means that TLDR contains seven individual parameters that must be tuned by the user, which can be an arduous process for the user.

Tuning can be broken down into two categories, the penalty parameters (ρ_X, ρ_P, ρ_N, ρ_T) and regularization hyper-parameters (μ_{ℓ_2}, μ_{ℓ_1}, μ_T). Increasing the magnitude of the penalty parameters reduces the number of iterations required before convergence. Varying the ratio between the various penalty parameters changes the relative importance of the different regularizers. Changing the regularization hyper-parameters increases the amount of smoothness or sparsity in the final VDM.

While tuning the various parameters for TLDR can be difficult, experience with the algorithm has revealed a general strategy. As a first step, set the penalty parameters to the same value and scale that value until TLDR converges in approximately 5000 iterations. Second, tune the regularization hyper-parameters. Beginning with each regularization parameter set to 1.0, tuning should be carried out one regularizer at a time with quadratic smoothing μ_{ℓ_2} first, sparsity μ_{ℓ_1} second, and TV μ_T last. Increase the value of the regularization parameter until the final reduced-χ^2 reaches an inflection point and repeats for the next regularizer. Third, tune the relative ratio of the penalty parameters to move the final reduced-χ^2 towards unity. Generally, this step has required increasing the penalty parameter for positivity more than anything else. It is likely that the user will need to iterate on the second and third steps to achieve a satisfactory result.

The TLDR algorithm is written in the Julia programming language (Bezanson et al. 2017). For ease and functionality, regularization variables exist as data structures within the algorithm's code. This allows the variables associated with each term to be stored and passed in the algorithm as a part of the regularization variable to which they belong.

3.4 TLDR Version 2

3.4.1 Motivations for Developing a Second Version

There are a number of reasons why developing a second version of the TLDR algorithm. Operating with a "first make it work, then make it work fast" philosophy, TLDR version 1 is not well optimized and its performance suffers due to a few specific problems. First, in TLDR version 1, the TV regularizer acting on both axes is implemented by FFT. Except at extreme resolutions, the RM data sets are not large enough to benefit from the application of FFT methods and are actually slower than direct convolution in the time domain. Second, TLDR version 1 is not compatible with the various automatic penalty parameter schemes in the literature. Having to optimize 4 penalty parameters along with 4 regularization parameters makes using TLDR on real data an arduous endeavor for the user. Finally, TLDR version 1 is a strictly single threaded central processing unit (CPU) code. There are a number of places where optimizations can be made.

TLDR version 2 seeks to remedy the problems with TLDR version 1. First, by implementing the TV regularizers with linear operators instead of FFTs, TLDR version 2 is faster at each step in the ADMM algorithm. Second, TLDR version 2 seeks to work with an automatic penalty parameter tuning sub-algorithm, cutting the number of parameters the user is responsible for in half. Automatic penalty parameter tuning has the additional benefit of reducing the number of iterations required for the ADMM algorithm to converge. Last, a number of other small changes are made to optimize the code, which do not rely on any changes to the mathematical formalism, but result in a much faster code. This includes the option for running TLDR on NVidia graphics processing units (GPU) using the Julia Programming Language's simple CUDA interface (Besard et al. 2019).

Table 3.2. ADMM variable assignments within TLDR version 2.

	Smoothing	ℓ_1-norm	Total Variation	Total Variation
Original Term	$\|\mathbf{Hx}-\mathbf{L}\|_2^2+\frac{\mu_{\ell_2}}{2}\|\mathbf{x}\|_2^2$	$\mu_{\ell_1}\|\mathbf{x}\|_1$	$\mu_{\mathrm{T}}\|\mathbf{D}_T\mathbf{x}\|_1$	$\mu_{\mathrm{V}}\|\mathbf{xD}_V\|_1$
Variable Assignment	$\mathbf{x}_0=\mathbf{X}$	$\mathbf{x}_2=\mathbf{N}$	$\mathbf{x}_3=\mathbf{D}_T\mathbf{Z}=\mathbf{T}$	$\mathbf{x}_4=\mathbf{ZD}_V=\mathbf{T}$
New Term	$\|\mathbf{HX}-\mathbf{L}\|_F^2+\frac{\mu_{\ell_2}}{2}\|\mathbf{X}\|_2^2$	$\mu_{\ell_1}\|\mathbf{N}\|_1$	$\mu_{\mathrm{T}}\|\mathbf{T}\|_1$	$\mu_{\mathrm{V}}\|\mathbf{V}\|_1$
Penalty Parameter	$\mathbf{Y}_{\mathrm{X}}$	$\mathbf{Y}_{\mathrm{N}}$	$\mathbf{Y}_{\mathrm{T}}$	$\mathbf{Y}_{\mathrm{V}}$

3.4.2 Mathematical Changes for TLDR Version 2

While much of the mathematical framework described for TLDR version 1 in section 3.3 is unchanged for TLDR version 2, there are a number of places where things change and must be re-derived or explained.

1. Positivity variables removed, but optionally applied to Z at each iteration.

2. Total Variation regularization changed to linear operation in the time domain.

3. Automatic penalty parameter selection implemented.

The most significant changes to the mathematics inside the TLDR algorithm arise from changing the TV regularizer to a linear operation in the time domain rather than relying on FFTs as in TLDR version 1. To make the TV regularization as a linear operation in the time domain, matrices of finite differences are used for both the temporal and spectral regularizers, which in general takes the form

$$\mathbf{D_{reg}} = \begin{pmatrix} -1.0 & 1.0 & 0 & 0 & \cdots & 0 \\ 0 & -1.0 & 1.0 & 0 & \cdots & 0 \\ 0 & 0 & -1.0 & 1.0 & \cdots & \vdots \\ \vdots & \vdots & \vdots & 0 & -1.0 & 1.0 \\ 0 & 0 & 0 & \cdots & 1.0 & -1.0 \end{pmatrix}. \tag{3.50}$$

Where D_T will denote the finite differences matrix for the temporal axis and D_V the finite differences matrix for the spectral axis. The two have the same form, but may have different dimensions due to being applied to the different axes of the VDM. To make the resulting equations easy to solve analytically, one of the TV steps is applied to $\mathbf{X}$ and the other to $\mathbf{Z}$. As with TLDR version 1, new variable names are applied for convenience, where X, N, and Z are the same as before, the positivity P is removed, and the newly split TV terms are T for the temporal axis and V for the spectral axis. The variable assignments for TLDR version 2 along with each term's penalty parameters are shown in table 3.2. With these changes in place, the equation for optimization can be written similarly to equation 3.13,

$$\begin{aligned} \arg\min_{\mathbf{X}} \quad & \frac{1}{2}\left(\mathbf{HX}-\mathbf{L}\right)^{\top}\mathbf{W}\left(\mathbf{HX}-\mathbf{L}\right)+\frac{\mu_X}{2}\left\|\mathbf{X}\right\|_2^2+ \\ & \qquad \mu_N\left\|\mathbf{N}\right\|_1+\mu_T\left\|\mathbf{T}\right\|_1+\mu_V\left\|\mathbf{V}\right\|_1. \\ \text{subject to} \quad & \mathbf{X}=\mathbf{N},\mathbf{Z};\mathbf{T}=\mathbf{D_T X};\mathbf{V}=\mathbf{Z D_V} \end{aligned} \tag{3.51}$$

Developing the full Augmented Lagrangian also proceeds similarly to equation 3.14 and appears as

$$\begin{aligned}\mathcal{L} = &\left(\mathbf{HX}-\mathbf{L}\right)^{\top}\mathbf{W}\left(\mathbf{HX}-\mathbf{L}\right)+\frac{\mu_{\ell_2}}{2}\left\|\mathbf{X}\right\|_2^2\\ &+\mathbf{Y}_X^{\top}\left(\mathbf{X}-\mathbf{Z}\right)+\frac{\rho_X}{2}\left\|\mathbf{X}-\mathbf{Z}\right\|_2^2\\ &+\mu_{\ell_1}\left\|\mathbf{N}\right\|_1+\mathbf{Y_N}^{\top}\left(\mathbf{N}-\mathbf{X}\right)+\frac{\rho_N}{2}\left\|\mathbf{N}-\mathbf{X}\right\|_2^2 \quad .\\ &+\mu_T\left\|\mathbf{T}\right\|_1+\mathbf{Y_T}^{\top}\left(\mathbf{T}-\mathbf{D}_T\mathbf{X}\right)+\frac{\rho_T}{2}\left\|\mathbf{T}-\mathbf{D}_T\mathbf{X}\right\|_2^2\\ &+\mu_V\left\|\mathbf{V}\right\|_1+\mathbf{Y_V}^{\top}\left(\mathbf{V}-\mathbf{Z}\mathbf{D}_V\right)+\frac{\rho_V}{2}\left\|\mathbf{T}-\mathbf{Z}\mathbf{D}_V\right\|_2^2\end{aligned} \tag{3.52}$$

Having just been through the derivation of TLDR version 1, it may be confusing why the different regularizers are now split between $\mathbf{X}$ and $\mathbf{Z}$. Knowing that an analytical solution for $\mathbf{X}$ and $\mathbf{Z}$ is sought, it is clear in equation 3.52 why the TV steps were split between $\mathbf{X}$ and $\mathbf{Z}$. It allows for the solution to each to be analytically solved. This has the effect of splitting the single ADMM problem of equation 3.13 into two nested ADMM problems. Fortunately, this still fits nicely in the established GVCO ADMM framework.

The same process as outlined in section 3.2 for ADMM can then be followed. The minimizations of equation 3.52 with respect to $\mathbf{X}$, the individual regularizes, and $\mathbf{Z}$ must be found. Fortunately, the minimizations for the individual regularizers $\mathbf{N}$,$\mathbf{T}$, and $\mathbf{V}$ are found exactly as in section 3.3.3 so no time need be spent on their account this time around. However, the minimzations with respect to $\mathbf{X}$ and $\mathbf{Z}$ are now different and must be found. Once again, an analytical solution is sought for each using the same strategies as in section 3.3.2 and section 3.3.4 can be used.

3.4.2.1 Minimization with respect to X

The minimization for $\mathbf{X}$ can be found analytically by solving the derivative of the full Augmented Lagrangian, equation 3.14, set equal to zero, for $\mathbf{X}$,

$$0 = \frac{\partial}{\partial \mathbf{X}}\mathcal{L}^*. \tag{3.53}$$

It is easy to begin by dropping all terms in the Augmented Lagrangian which do not include $\mathbf{X}$, leaving behind

$$\begin{aligned}\frac{\partial}{\partial \mathbf{X}}\Bigg[&\frac{1}{2}\left\|\mathbf{L}-\mathbf{H}\mathbf{X}\right\|_F^2+\frac{\mu_{\ell_2}}{2}\left\|\mathbf{X}\right\|_2^2+\mathbf{Y_X}^\top(\mathbf{X}-\mathbf{Z})+\frac{\rho_\mathbf{X}}{\mathbf{2}}\left\|\mathbf{X}-\mathbf{Z}\right\|_\mathbf{2}^\mathbf{2}\\&+\mu_{\ell_1}\left\|\mathbf{N}\right\|_1+\mathbf{Y_N}^\top(\mathbf{N}-\mathbf{X})+\frac{\rho_N}{2}\left\|\mathbf{N}-\mathbf{X}\right\|_2^2\\&+\mu_T\left\|\mathbf{T}\right\|_1+\mathbf{Y_T}^\top(\mathbf{T}-\mathbf{D}_T\mathbf{X})+\frac{\rho_T}{2}\left\|\mathbf{T}-\mathbf{D}_T\mathbf{X}\right\|_2^2\Bigg]\end{aligned}. \tag{3.54}$$

Using the matrix identities used previously in section 3.3.2 and section 3.3.4 the derivative can straightforwardly be written although special attention to the signs is needed.

$$\begin{aligned}0=\frac{\partial}{\partial \mathbf{X}}\mathcal{L}^*=&-\mathbf{H}^\top\mathbf{W}(\mathbf{L}-\mathbf{H}\mathbf{X})+\mu_{\ell_2}\mathbf{X}+\mathbf{Y}_X+\rho_X(\mathbf{X}-\mathbf{Z})\\&-\mathbf{Y}_N-\rho_N(\mathbf{N}-\mathbf{X})-\mathbf{D}_T^\top\mathbf{Y}_T-\rho_T\mathbf{D}_T^\top(\mathbf{T}-\mathbf{D}_T\mathbf{X})\end{aligned} \tag{3.55}$$

Which can be solved for $\mathbf{X}$ without any tricks,

$$\begin{aligned}\mathbf{X}=&\left(\mathbf{H}^\top\mathbf{W}\mathbf{H}+(\mu_{\ell_2}+\rho_X+\rho_N)\mathbf{I}+\rho_T\mathbf{D}_T^\top\mathbf{D}_T\mathbf{I}\right)^{-1}\\&\left(\mathbf{H}^\top\mathbf{W}\mathbf{L}-\mathbf{Y}_X+\rho_x\mathbf{Z}-\mathbf{Y}_N+\rho_N\mathbf{N}+\mathbf{D}_T^\top\mathbf{Y}_T+\rho_T\mathbf{D}_T^\top\mathbf{T}\right)\end{aligned}. \tag{3.56}$$

Once again, this must be carried out line by line as in algorithm 2.

3.4.2.2 Minimization with respect to Z

The minimization for $\mathbf{Z}$ can be found analytically by solving the derivative of the full Augmented Lagrangian, equation 3.14, set equal to zero, for $\mathbf{Z}$,

$$0=\frac{\partial}{\partial \mathbf{Z}}\mathcal{L}^*. \tag{3.57}$$

Once again, begin by dropping all terms in the Augmented Lagrangian which do not include $\mathbf{Z}$, leaving behind

$$\frac{\partial}{\partial \mathbf{Z}}\Bigg[\mathbf{Y_X}^\top(\mathbf{X}-\mathbf{Z})+\frac{\rho_\mathbf{X}}{\mathbf{2}}\|\mathbf{X}-\mathbf{Z}\|_\mathbf{2}^\mathbf{2} + \mathbf{Y_V}^\top(\mathbf{V}-\mathbf{Z}\mathbf{D}_V)+\frac{\rho_V}{2}\|\mathbf{V}-\mathbf{Z}\mathbf{D}_V\|_2^2\Bigg] \tag{3.58}$$

Using the matrix identities used previously in section 3.3.2 and section 3.3.4 the derivative can straightforwardly be written although special attention to the signs is needed.

$$0=\frac{\partial}{\partial \mathbf{X}}\mathcal{L}^* = -\mathbf{Y}_X-\rho_X(\mathbf{X}-\mathbf{Z}) - \mathbf{Y}_V\mathbf{D}_V^\top-\rho_V(\mathbf{V}-\mathbf{Z}\mathbf{D}_V)\mathbf{D}_V^\top \tag{3.59}$$

Which can be solved for $\mathbf{Z}$ which is,

$$\mathbf{Z}=\left(\rho_X\mathbf{I}+\rho_V\mathbf{I}\mathbf{D_V}\mathbf{D_V}^\top\right)^{-1}\left(\mathbf{Y}_X+\rho_X\mathbf{X}+\mathbf{Y}_V\mathbf{D}_V^\top+\rho_V\mathbf{V}\right) \tag{3.60}$$

Additionally, positivity is optionally enforced on $\mathbf{Z}$ rather than as a separate regularization term using equation 3.30,

$$\mathbf{Z}=\mathbb{1}_{\mathbb{R}^+}(\mathbf{Z}). \tag{3.61}$$

3.4.2.3 Automatic Penalty Parameter Tuning

A significant benefit of the changes made to the TV regularizers allows for a simple automatic penalty parameter tuning strategy to be implemented. TLDR version 2 utilizes the simple penalty parameter tuning scheme described by Boyd et al. (2011) §3.4.1:

$$\rho^{k+1}=\begin{cases} g\rho^k, & \text{if } \left\|r^k\right\|_2>\gamma\left\|s^k\right\|_2 \\ \rho^k/g, & \text{if } \left\|s^k\right\|_2>\gamma\left\|r^k\right\|_2 \\ \rho^k, & \text{otherwise}\end{cases}. \tag{3.62}$$

Where g and γ are constants hard-coded with values of 2.0 and 10.0 respectively as recommended in Boyd et al. (2011) §3.4.1. The primal residual is r^k which appears in TLDR version 2 as

$$\mathbf{r}^k = \left(\mathbf{X}^k - \mathbf{Z}^k, \mathbf{N}^k - \mathbf{Z}^k, \mathbf{T}^k - \mathbf{D}_T\mathbf{Z}^k, \mathbf{V}^k - \mathbf{Z}^k\mathbf{D}_V\right). \tag{3.63}$$

And the dual residual is s^k also changes if automatic penalty parameter tuning is active, where all penalty parameters become identical, making the equation simpler,

$$\mathbf{s}^k = 4\rho\left(\mathbf{Z}^k - \mathbf{Z}^{k-1}\right). \tag{3.64}$$

Note that TLDR version 2 allows the user to choose the number of iterations between each penalty parameter update. If the number of iterations between updates is longer than the total number of iterations, the penalty parameter is never updated and the user is free to use a unique fixed penalty parameter value for each of the individual regularization terms. For this reason, the individual term's penalty parameters are still shown in the preceding equations.

3.4.2.4 Convergence Testing in TLDR Version 2

Convergence testing in TLDR version 2 is largely unchanged from version 1 and TLDR is still said to have converged when both the norm of the primal residual and norm of the dual residual have dropped below their respective tolerances ϵ^{pri} and ϵ^{dual}. Because of the changes to the TV regularization, the equation for primal residual tolerance becomes

$$\epsilon^{pri} = \epsilon^{abs} + \epsilon^{rel}\max\left\{\left\|\mathbf{X}^k\right\|_2, \left\|\mathbf{N}^k\right\|_2, \left\|\mathbf{T}^k\right\|_2, \left\|\mathbf{V}^k\right\|_2\right\}, \tag{3.65}$$

and the equation for the dual residual tolerance is now

$$\epsilon^{dual} = \epsilon^{abs} + \epsilon^{rel}\max\left\{\left\|\mathbf{Y_X}^k\right\|_2, \left\|\mathbf{Y_N}^k\right\|_2, \left\|\mathbf{Y_T}^k\right\|_2, \left\|\mathbf{Y_V}^k\right\|_2\right\}. \tag{3.66}$$

The full ADMM block for TLDR version 2 can then proceed as shown in the pseudocode in algorithm 3.

Algorithm 3: Pseudocode for TLDR Version 2's ADMM block.

```
initialization X, N = Z; T = D_T X; V = Z D_V
calculate Initial VDM
while converged == False do
    minimization of Augmented Lagrangian w.r.t. X
    minimization of Augmented Lagrangian w.r.t. regularization terms N, T, V
    minimization of Augmented Lagrangian w.r.t. Z
    update Lagrange Multipliers Y_X, Y_N, Y_T, Y_V
    check for convergence by updating evaluating residuals r^k and s^k
    update penalty parameters using the residuals
end
```

3.5 Computational Performance Comparison of TLDR Versions 1 and 2

Since a major impetus for developing TLDR version 2 was to increase the speed of the algorithm, a series of tests were run on real RM data recovering VDMs with different resolutions on TLDR version 1 and on TLDR version 2's CPU and GPU implementations. For this comparison, only the dimensions of the recovered VDMs are important and the details of the real RM data can be ignored.

Two test scenarios were run on the versions of TLDR. The first represents a long reduction run of 5000 iterations on a small portion of the real data consisting of 52 spectral channels representing a single reverberating spectral feature. The second, a short run of 1000 iterations on the entire data set with 1369 spectral channels, far more than the first scenario. Each scenario was run with different resolutions on the VDM's delay axis with 10, 50, 100, 150, and 200 delay samples. In all cases, automatic penalty parameter tuning was disabled and the convergence criteria were set to zero so that the algorithm did not stop due to convergence. While the precise performance of each version of TLDR will vary across different computer hardware, this comparison was run on a single machine with no configuration changes between tests.

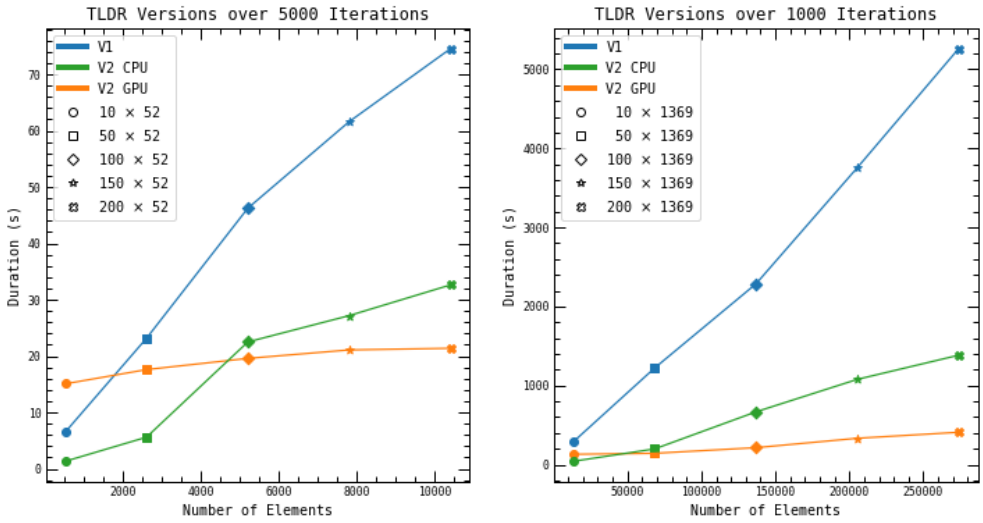

Figure 3.1 Numerical benchmark comparison between TLDR V1, TLDR V2 CPU-based, and TLDR V2 GPU-based. Left, average run time for the Hβ feature to run for 5000 iterations on each version of the code. Right, average run time for the full Arp 151 dataset to run for 1000 iterations on each version of the code. In each case, no convergence testing or automatic hyper-parameter tuning was used.

The results of the two test scenarios are shown in figure 3.1, with scenario 1, the long run on a single spectral feature on the left, and the short run on the entire data set on the right. In each plot, the overall number of elements in the reconstruction increases from left to right along the x axis and the duration of each run appears on the y axis. For only the very smallest reconstructed data set was TLDR version 2 faster than TLDR version 1 and that was only the case for the GPU implementation. This is not entirely unexpected as GPUs are specifically designed for operations on larger arrays. It is clearly obvious as VDMs are reconstructed with higher resolution in delay that TLDR version 2 is much faster. Additionally, it is clear that in most cases the GPU implementation of TLDR version 2 is preferable over the CPU implementation in all but the lowest resolution cases.

CHAPTER 4
TESTING TLDR

4.1 Testing

Described in Anderson et al. (2021) along with the development of TLDR version 1 testing of TLDR was accomplished using synthetic emission line data created using a number of model VDMs convolved with a continuum light curve. To generate the synthetic emission line data, the Johnson B band continuum light curve for Arp 151 from the Lick AGN Monitoring Project's 2008 data release is adopted, the complete discussion of the photometric observing campaign and data reduction can be found in Walsh et al. (2009). Observations of Arp 151 took place between February 10 and May 16 2008, and the resulting data were calibrated via differential photometry. The original continuum data have been reduced further by binning any observations made within 0.1 days. The resulting light curve consists of 66 observations with a median sampling frequency of 1.02 days, a mean sampling frequency of 1.5 days, a mean flux of $\langle f \rangle = 0.93$ mJy with a standard deviation of 0.15 mJy, and flux ratio $f_{max}/f_{min} = 1.8$. The light curve has an excess variance of $F_{var} = 0.16$ calculated as

$$F_{var} = \frac{\sqrt{\sigma^2 - \delta^2}}{\langle f \rangle}, \tag{4.1}$$

where σ^2 is the variance of the flux and δ^2 is the mean square of the uncertainties of the flux. The continuum light curve is linearly interpolated onto a grid based on the date of spectroscopic observation and delay sample times. The dates used for the spectroscopic observations are those of the spectroscopic monitoring of Arp 151 from the LAMP campaign, which ranged from March 25 to May 21 2008, with a median sampling of 1.02 days and a mean sampling of 1.4 days; the full description of the spectroscopic observations and data reduction are provided in Bentz et al. (2009). For all tests, a delay sampling time of 1.0 days was used for the reconstruction. From the interpolated continuum light curve, the convolution operator is created. Synthetic emission line data is then generated and Gaussian noise is added according to,

$$\mathbf{L}_{synthetic} = \mathbf{H}\mathbf{X}_{synthetic} + \mathbf{n}. \tag{4.2}$$

The continuum data used to generate all synthetic emission line data used for testing is shown in the top plot in figure 4.1 where the black circles represent the continuum observations of Arp 151 with error bars included. For comparison, the λ=4369Å spectral light curve from the spectra of the Arp 151 observations is also shown in figure 4.1. The x axis in both plots is heliocentric Julian date minus 2450000 days a space saving convention which can be confusing. By feeding the synthetic emission line data and the real continuum data into TLDR, the synthetic VDM is reconstructed. This provides a measure of the reconstructive efficacy of TLDR. Using continuum data and sampling dates from actual observations of Arp 151 in the creation of the artificial emission line data creates a dataset with realistic cadence, but none of the following tests are intended to be compared with any reconstruction of the VDM for the Arp 151 dataset.

4.1.1 Basic Tests

To test that the TLDR algorithm and each of its regularizers work properly, a number of simple VDMs were used. Each test VDM consists of a 10×10 pixel matrix with signal values that range between a minimum of 0.0 and a maximum of 1.0. The test data sets were prepared with emission line errors, yielding an SNR of 50.0. An example spectral line of each test VDM is shown in figure 4.2 where the noisy spectral light curve is shown as the blue circles with error bars and the noiseless spectral light curve is shown as the solid red line. In each case the 3rd spectral line is shown. Additionally, the same noise profile is maintained for each light curve scaled to achieve the desired SNR. It is difficult to discern much difference in the resulting light curves other than the overall level of the spectra flux.

The test VDMs and their reconstructions shown in figure 4.3 where the original VDM appears on the left of each pair with the reconstruction on the right. On the bottom is the colormap used for all test reconstructions, which in this case is a standard linear black

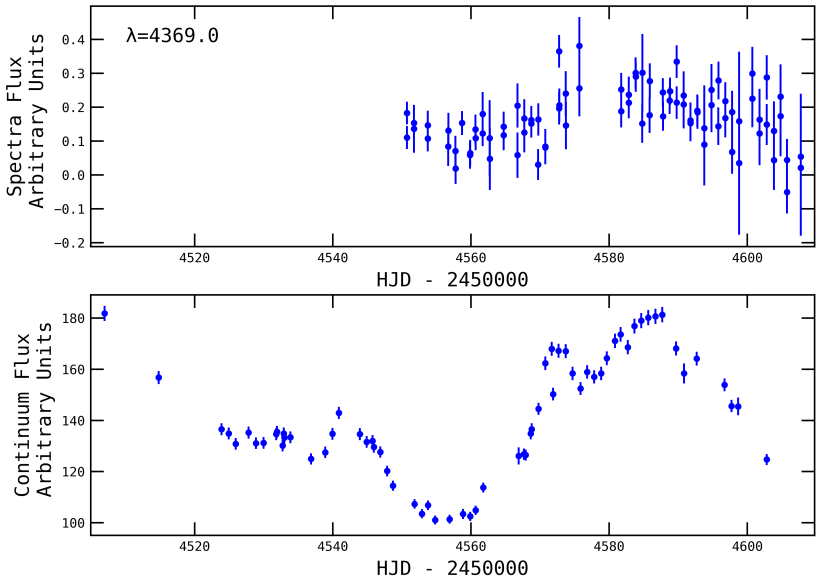

Figure 4.1 Light curve examples from the LAMP2008 Arp151 data. Top: λ=4369Å spectral light curve. Bottom: The Johnson B band continuum light curve.

and white colormap. Except for the random test swatch, it is very difficult to see the differences between the original and reconstructed VDM. To show the deviations between the reconstructed and original VDMs, a colormap that accentuates the variations but still maintains the black and white colors of the original VDMs is implemented. Figure 4.4 shows the same reconstructions as figure 4.3 except using the specialized colormap. In both figures, the peak signal-to-noise ratio (PSNR) of the reconstructed VDM is displayed below each image, providing a measure of the reconstruction fidelity. Where the PSNR is calculated in the usual way with

$$PSNR = 20 \cdot \log_{10}\left(\frac{1}{\sqrt{MSE}}\right) \tag{4.3}$$

in which MSE is the mean squared error,

$$MSE = \frac{1}{N}\sum_{i=1}^{N}\left(\mathbf{X}_i - \mathbf{X}_{true,i}\right)^2. \tag{4.4}$$

The geometries were chosen to test the ability of TLDR to recover characteristics that may be encountered in real data, specifically, the regularizers, smoothness, sparsity, etc . Clearly, the algorithm excels at reconstructions of smooth gradients and places where test VDMs have continuous values across their cross sections. This is unsurprising, as the majority of the regularizers used in TLDR promote smoothness. The algorithm has some difficulty when the VDM being reconstructed contains abrupt signal changes, as in the Checkerboard, Box, Circle, Ring, and Diagonal VDMs. Unsurprisingly, TLDR struggles the most when reconstructing a VDM consisting purely of random noise. The overall high quality of the reconstructions comes down to two factors. First the selection of test VDMs meant to test TLDR's regularizers inherently means that the algorithm should be able to reconstruct these VDMs well. Second, the relatively high SNR makes reconstructing these simple geometries even easier.

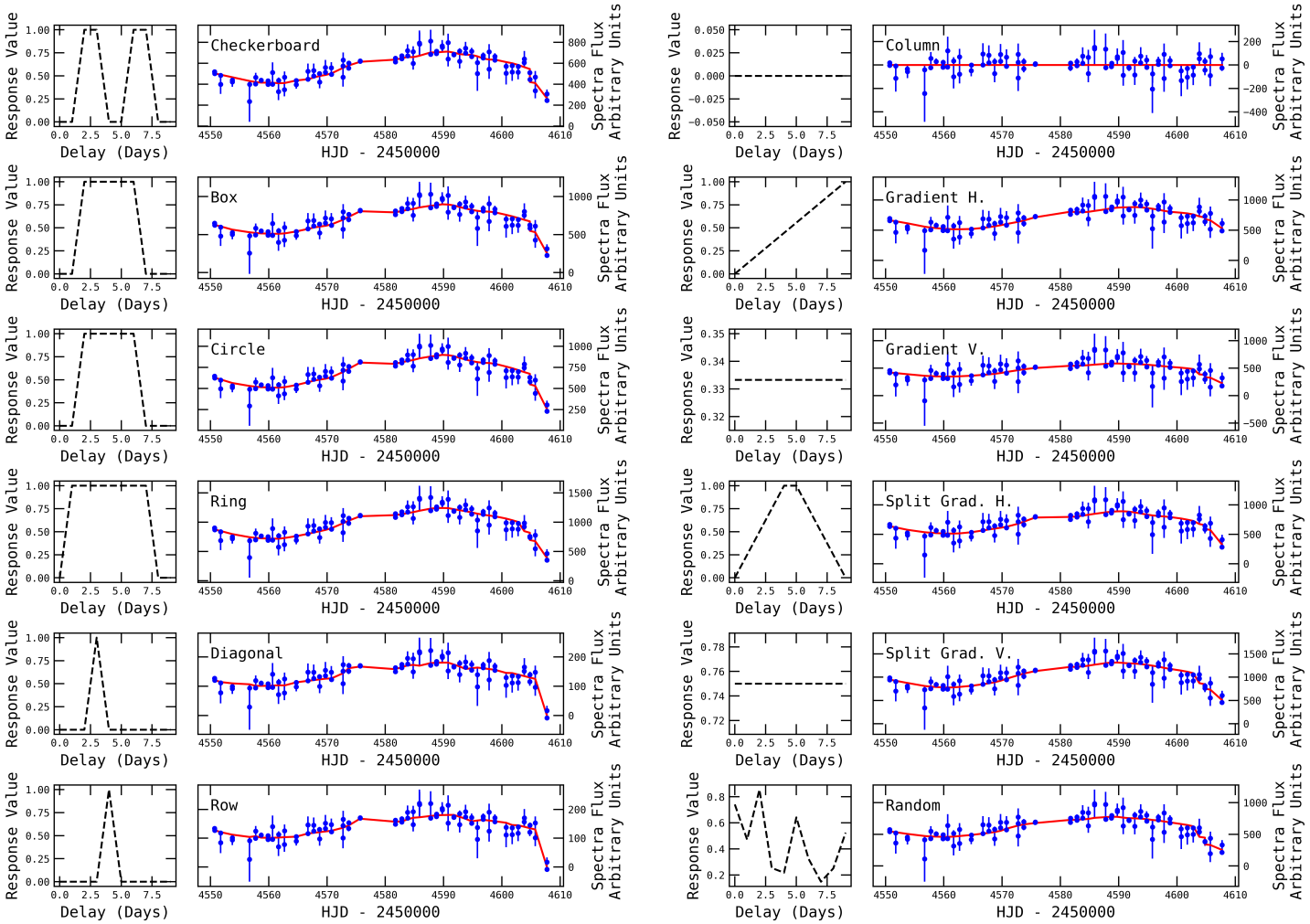

Figure 4.2 Example light curve from each 10x10 pixel test swatch. On the left of each pair of plots is the response curve of the VDM on the 4th spectral channel. On the right is the resulting synthetic light curve generated according to equation 4.2 with the noiseless curve shown as the solid red line and the resulting noisy curve as the blue circles with error bars shown. Note that the same noise profile was used, but scaled accordingly so that the SNR of the synthetic light curve matched the desired value.

4.1.2 Synthetic VDM of Keplerian disk

To test TLDR with a more complicated VDM than those used in Section 4.1.1, a synthetic VDM was created using a simple flat Keplerian disk toy model of the BLR described in section 2.4. This synthetic VDM was generated from an array of 1 million randomly situated points arranged in a flat disk about a central point corresponding to the location of a SMBH with mass $7 \times 10^6\ M_\odot$ with an inner radius of 1.0 and an outer radius of 5.0 light days shown in the top plot of figure 4.5.

After calculating the line-of-sight velocities (equations 2.8 and 2.14) and delays (equation 2.6) for all of the points in the simulated disk, the points are projected onto the VDM seen in figure 4.5 middle panel. The VDM is then binned along both delay time and velocity (figure 4.5 lower panel) with the delay times scaled to a maximum of 50.0 lightdays. The signal value of each pixel is normalized and scaled by counting the number of points that lie within a given pixel, normalizing to the maximum number of points found in a single pixel, and scaling the normalized array to the desired maximum value. Finally, each pixel is scaled by the ratio of its delay to the maximum delay to enhance the structure that appears in the VDM. In this case, the VDM was binned with 50 pixels of 1.0 light-day along the temporal axis and 20 pixels on the spectral axis, which happen to be 597 km/s wide, with a maximum signal value of 0.1.

This toy model is oversimplified in that the binned flux does not account for the relative flux difference in different delays corresponding to the light travel differences. Furthermore, the scaling and binning used for the reconstruction change the physicality of the model. Similarly, the use of a flat Keplerian disk is simplistic. The goal in generating this synthetic VDM is to provide a test case showing the algorithm's capability for recovering complicated signals that mimic those recovered by other methods. This synthetic VDM is not intended as a realistic model of the BLR. Furthermore, despite borrowing much from the Arp 151 dataset to create this synthetic line emission data, this toy model is not intended to provide any physical comparison to any reconstruction of a VDM for the Arp 151 dataset.

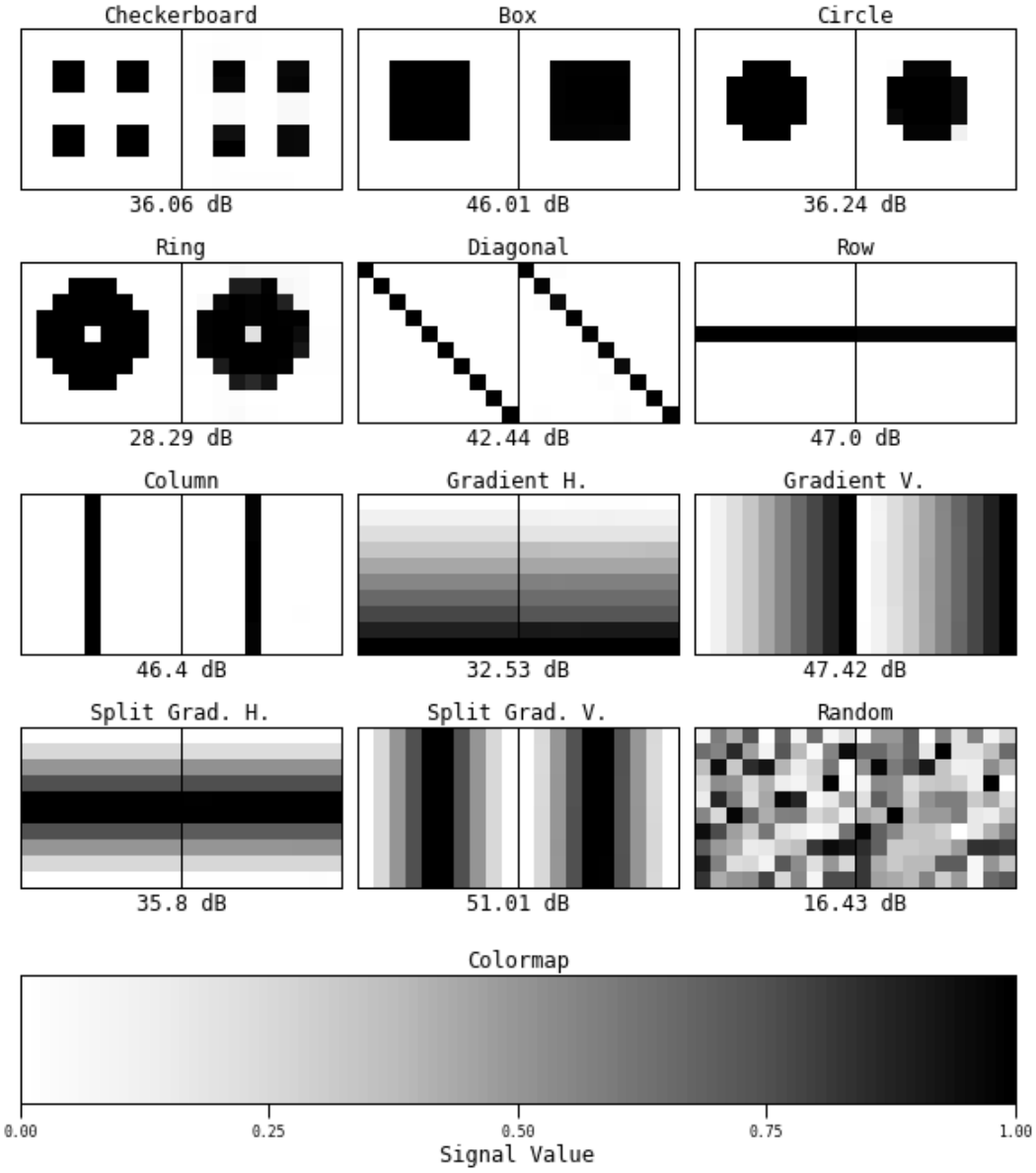

Figure 4.3 Reconstruction of 10x10 pixel test VDMs with signal values ranging from 0.0 to 1.0 and a signal to noise ratio of 50 in the synthetic emission lines. All plot's vertical axes represent the delay axis and the horizontal axes the wavelength axis. In both axes the units are inconsequential for these nonphysical tests. In each pair, the left plot shows the test VDM and the right plot shows the reconstructed VDM. Beneath each pair is the PSNR value of the reconstructed VDM in decibels. In this figure, a standard linear black and white colormap is used, shown on the bottom.

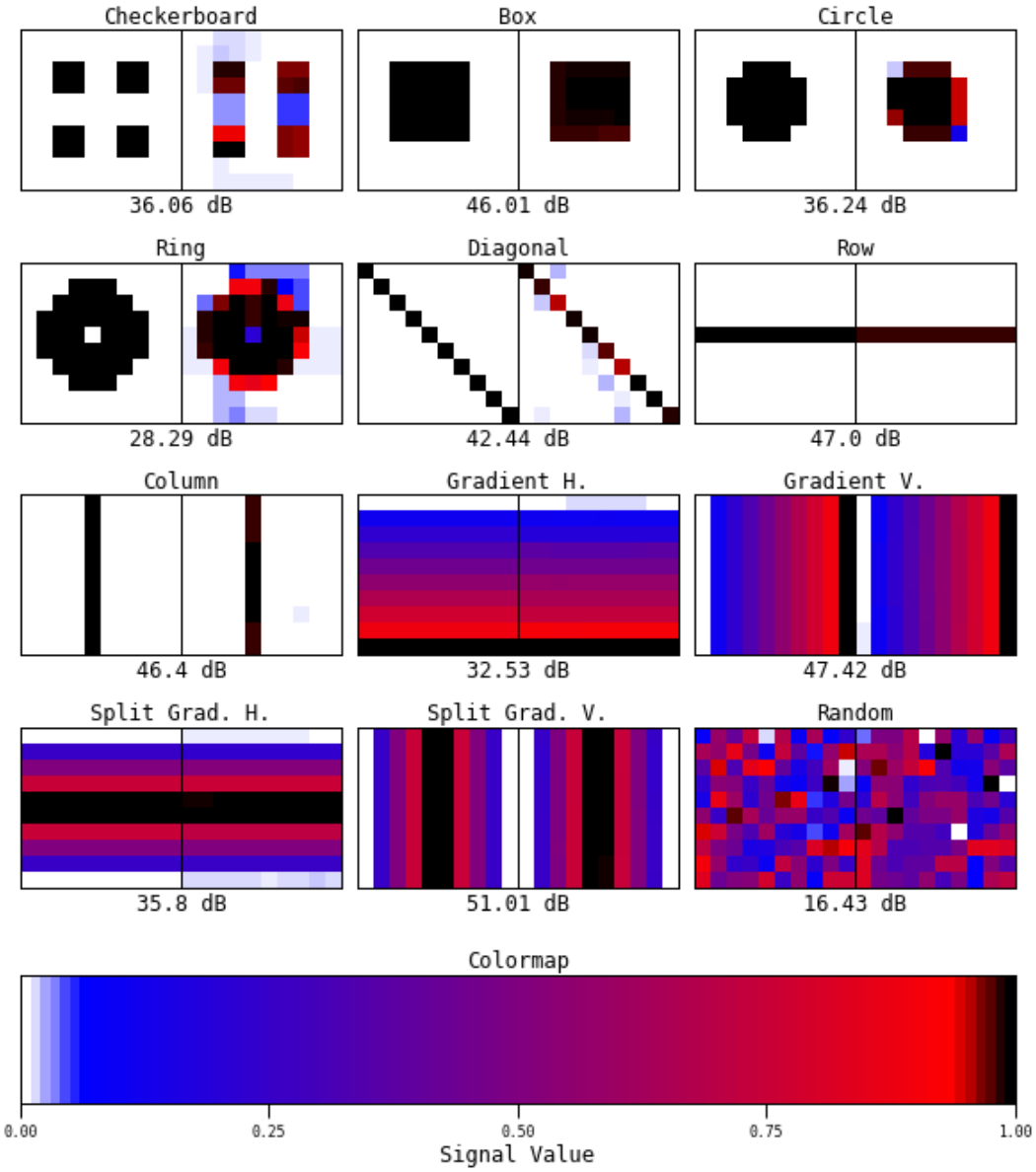

Figure 4.4 Reconstruction of 10x10 pixel test VDMs with signal values ranging from 0.0 to 1.0 and a signal to noise ratio of 50 in the synthetic emission lines. All plot's vertical axes represent the delay axis and the horizontal axes the wavelength axis. In both axes the units are inconsequential for these nonphysical tests. In each pair, the left plot shows the test VDM and the right plot shows the reconstructed VDM. Beneath each pair is the PSNR value of the reconstructed VDM in decibels. On the bottom is the colormap used for each inset plot which emphasizes deviations from the extrema of the test VDMs making problem areas in the reconstructed VDMs stand out.

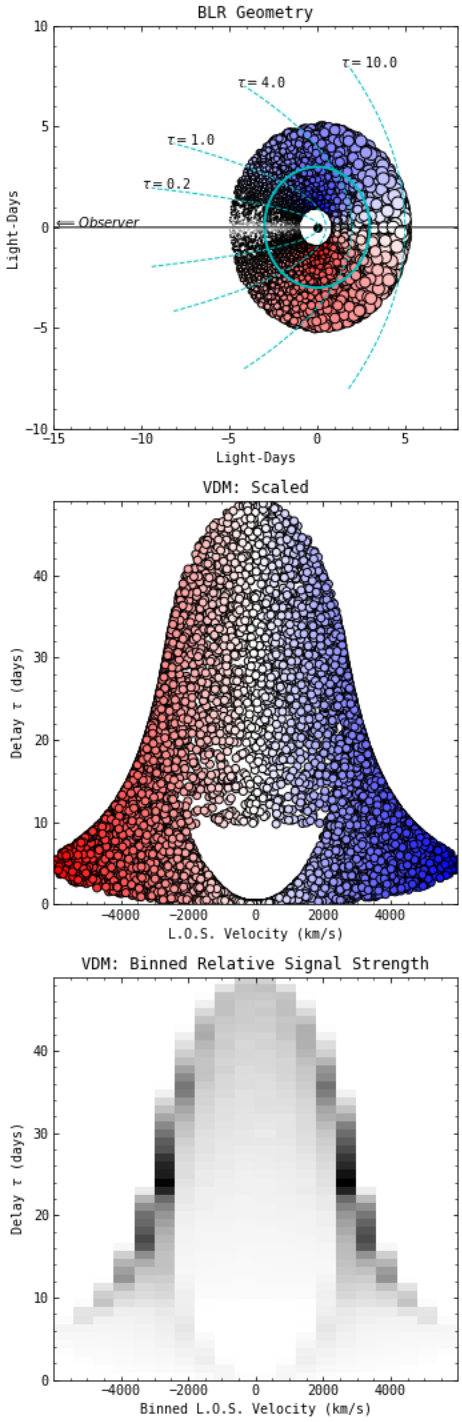

Figure 4.5 Top: Overview of the simulated flat Keplerian disk showing 1 million particles in the same two-dimensonal isodelay surface as figure 2.1. The size of the markers shows relative delay and color indicates Doppler shift due to rotational velocity. Middle: Projected VDM of the particles in the simulation, again color indicates Doppler shift. Bottom: Binned VDM of the simulated data.

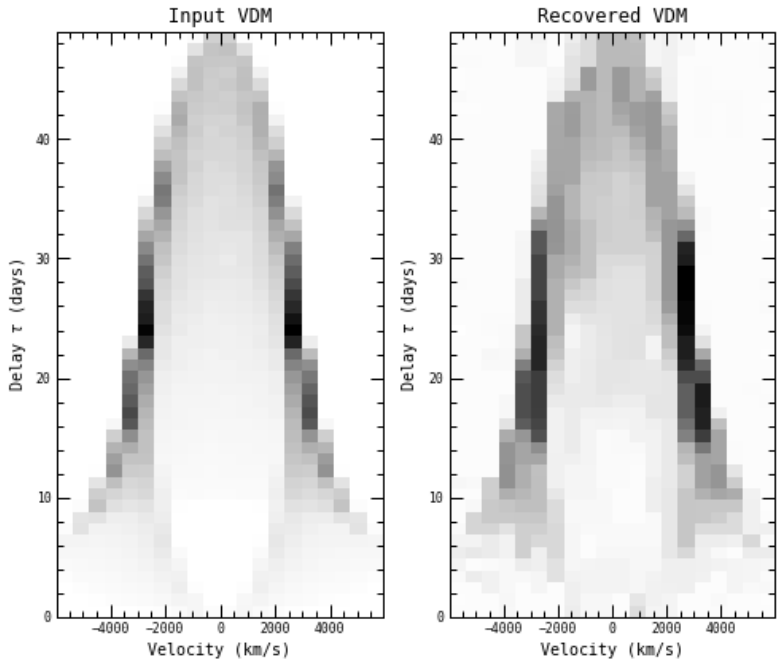

Figure 4.6 Synthetic VDM of a Keplerian disk (left) and the recovered VDM (right). Recovered VDM shows much of the detail of the synthetic VDM, with some artifacting visible.

The synthetic VDM was used to create synthetic spectra according to equation 4.2 with a fractional uncertainty of 1.5% matching the mean fractional error from the real Arp 151 dataset (Bentz et al. 2009) and then reconstructed using TLDR. The reconstructed synthetic VDM generated from the Keplerian disk model and Arp 151 continuum is shown alongside the original synthetic VDM in figure 4.6. Comparing the reconstructed Keplerian disk VDM with the original shows that the algorithm is providing an excellent reconstruction. There is some noisy distortion apparent at longer delay times and some loss of fine detail near the edges of the VDM, but with a PSNR of 45.0 dB the details of the VDM are well reconstructed.

The reconstruction can be further evaluated by looking at a sample of the light curves from the reconstruction shown in figure 4.7. The top plot is simply the continuum light curve used to generate the synthetic emission line data (i.e., the original Arp 151 continuum data) shown by black circles with error bars slightly larger than the markers and the interpolated data shown as the black solid line. The bottom four rows show the spectral light curves from

the data at 20% (-1196 km/s), 40% (-2394 km/s), 60% (-3591 km/s), and 80% (-4789 km/s) of the maximum line-of-sight rotational velocity of the model. Each shows the response function on the left with the true response as the grey dashed line and the reconstructed response as the green solid line. On the right, the spectral light curve is shown with the noiseless light curve shown as a black dashed line, the noisy spectral light curve input as the blue circles, and the recovered spectral light curve as the red solid line. Each also contains the line's reduced χ^2 value. While in each case, the recovered spectral line closely matches the noiseless true spectral line, they all show deviation from the true response function in the recovered response functions. The second row showing the curves for the -1196 km/s cross-section shows a very good recovery of the response function and spectral light curve. The bottom three rows, showing the -2394 km/s, -3591 km/s, and -4789 km/s lines contain oversmoothed responses where the signals assume the general shape expected but are suppressed in the regions of maximum response value. It would likely be possible to achieve a better fit across all lines by using a different set of regularization hyper-parameters for each line, but this would further complicate what can already be an arduous parameter selection process, a trade-off which must be considered for any image reconstruction process.

4.2 Preliminary Reconstruction of Arp 151 Hβ

As a final indication of the utility of TLDR, an initial reconstruction of the VDM for the $H\beta$ feature of Arp 151 from LAMP (Bentz et al. 2009) is provided. Using the continuum subtracted model spectra and the Johnson B continuum data used in the Maximum Entropy Method reconstruction presented in Bentz et al. (2010b), an initial VDM was calculated in accordance with Section 3.3.1 with a smoothing hyper-parameter of 2.0×10^6. The VDM was set up with the pixel spectral width matching the 2.0Å steps of the original spectral observations and a temporal width of 1.0 days matching the global average sampling frequency of the continuum and spectral observations. For this reconstruction, TLDR was run for 3.0×10^4 iterations with the parameters listed in table 4.1, selected from a grid of possible

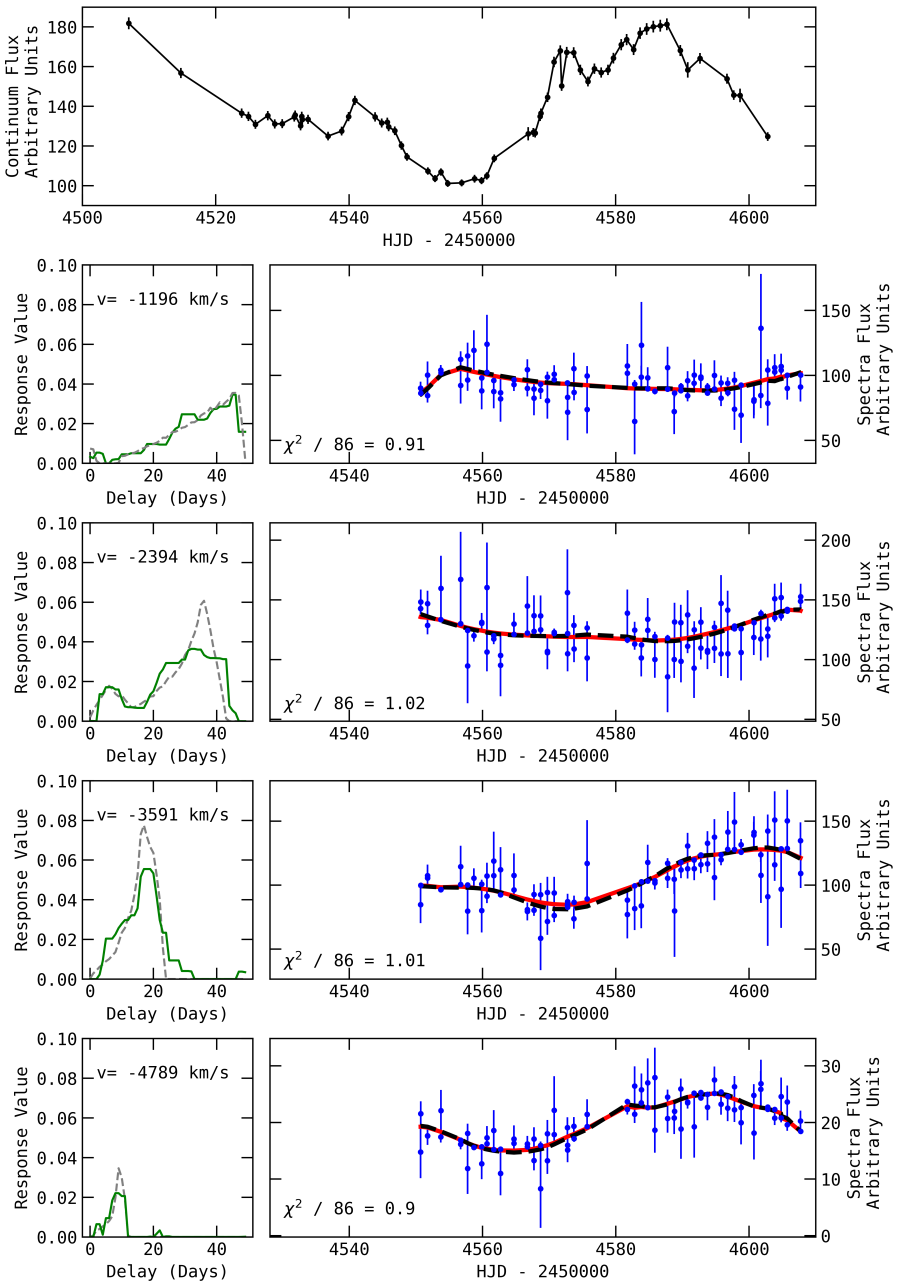

Figure 4.7 Sample light curves from the reconstruction of the Keplerian disk. Top: Continuum light curve where the black circles show the original sample data with error bar and the black solid line shows the linear interpolation of the original data. Bottom four rows: On the left, response function where the grey dashed line is the true function and the green solid line is the recovered function. On the right: Noiseless spectral light curve shown by the black dashed line, the noisy spectral light curve shown as the blue circles and the recovered spectral light curve as the red solid line. The lines shown represent 20% (-1196 km/s), 40% (-2394 km/s), 60% (-3591 km/s), and 80% (-4789 km/s) the maximum line of sight rotational velocity of the Keplerian disk model used to generate these emission line data.

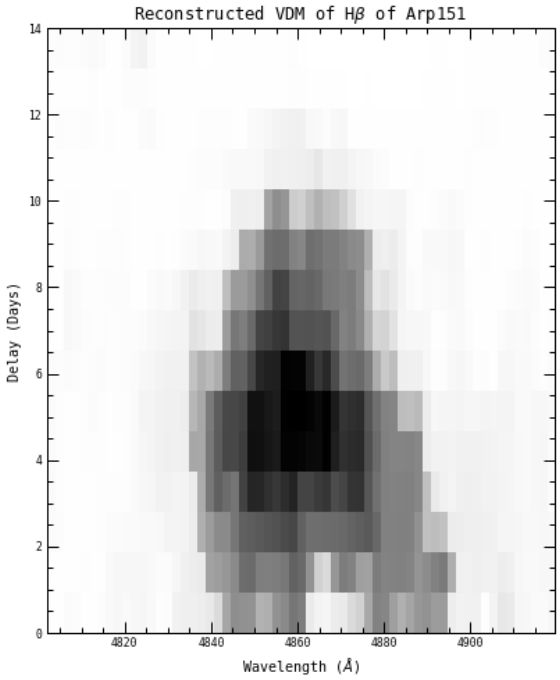

Figure 4.8 VDM of the $H\beta$ feature of Arp 151 from the LAMP RM project reconstructed with TLDR version 1.

regularization hyper-parameters by proximity to $\chi^2 = 1.0$. The reconstruction terminated with a reduced χ^2 of 1.02, yielding the VDM shown in figure 4.8. Visual comparison between the VDM reconstructed with TLDR and those recovered by the Maximum Entropy Method (Bentz et al. 2010b) and Regularized Linear Inversion (Skielboe et al. 2015) largely agree. In each case, the overall shape of the response in the VDM appears to match with asymmetries appearing in similar locations.

4.3 Remarks on the TLDR Algorithm

The TLDR algorithm provides an additional tool for RM that can be used in concert with existing tools or independently, to reconstruct VDMs from RM data. The regularization scheme implemented within TLDR provides a flexible platform for the reconstruction of

Table 4.1. Reconstruction parameters used in the reconstruction of the $H\beta$ feature of Arp 151.

Regularizer	Hyper-Parameter μ	Penalty-Parameter ρ
Smoothing **X**	2.0×10^6	1.0
Positivity **P**	N/A	100.0
Sparsity **N**	10.0	1.2
Total Variation **T**	1.75	1.2

VDMs. With numerous recent and ongoing RM campaigns (De Rosa et al. 2015; Shen et al. 2016; LAMP2016 Collaboration 2017), interest in using RM to study AGNs is high. With high interest and a growing number of data sets, TLDR should be able to make a sizable contribution to the RM field.

Future work on TLDR will include applying the algorithm to a number of well-studied data sets from the Lick AGN Monitoring Project (LAMP) (Bentz et al. 2009). The data contained in the LAMP data release has been studied by all of the reverberation mapping algorithms currently in use, including the Maximum Entropy Method (Bentz et al. 2010b), Regularized Linear Inversion (Skielboe et al. 2015), as well as direct modeling (Pancoast et al. 2014a). This will provide a way to directly evaluate the performance of TLDR and compare the different methods currently available.

CHAPTER 5
APPLYING TLDR

5.1 The LAMP Data

The Lick AGN Monitoring Project is an ongoing program to monitor AGNs with a daily cadence in order to have high quality data from which to estimate AGN masses. In this chapter, TLDR version 2.0 will be applied to the Arp 151 data from the LAMP 2008 data release, here after LAMP2008. The continuum monitoring campaign for the LAMP2008 data set ran from February 9 to June 1 2008, with daily monitoring beginning on March 16 utilizing a number of telescopes using differential photometry to measure the continuum light curves in Johnson B and V bands. The full details of the continuum monitoring campaign are discussed in Walsh et al. (2009). The spectroscopic monitoring campaign for the LAMP2008 data set ran from 2008 March 25 and June 1 using the red-side of the Kast dual spectrograph on the 3-meter Shane telescope at Lick Observatory covering a range from 4300 to 7100 Å with a resolution of 2.35 Å per pixel. The spectroscopic monitoring campaign is discussed at length in Bentz et al. (2009). The continuum-subtracted line-profile variations used in Bentz et al. (2010b) to reconstruct VDMs using MEMECHO was graciously provided by Misty Bentz Ph.D. This allows the direct comparison between the MEMECHO reconstructed VDMs and the TLDR reconstructed VDMs in the following sections without the risk of the many pitfalls associated with preparing the spectra. Additionally this dataset has been studied using other RM methods allowing for additional comparison.

5.2 Continuum Modelling

In section 4.2, the $H\beta$ feature for the Arp 151 was reconstructed using the linearly interpolated continuum data. As noted in section 3.3.6, TLDR simply applies a linear interpolation to the input continuum light curve so that the convolution operator can properly be constructed. It does not consider the uncertainties of the continuum light curve, or the problem

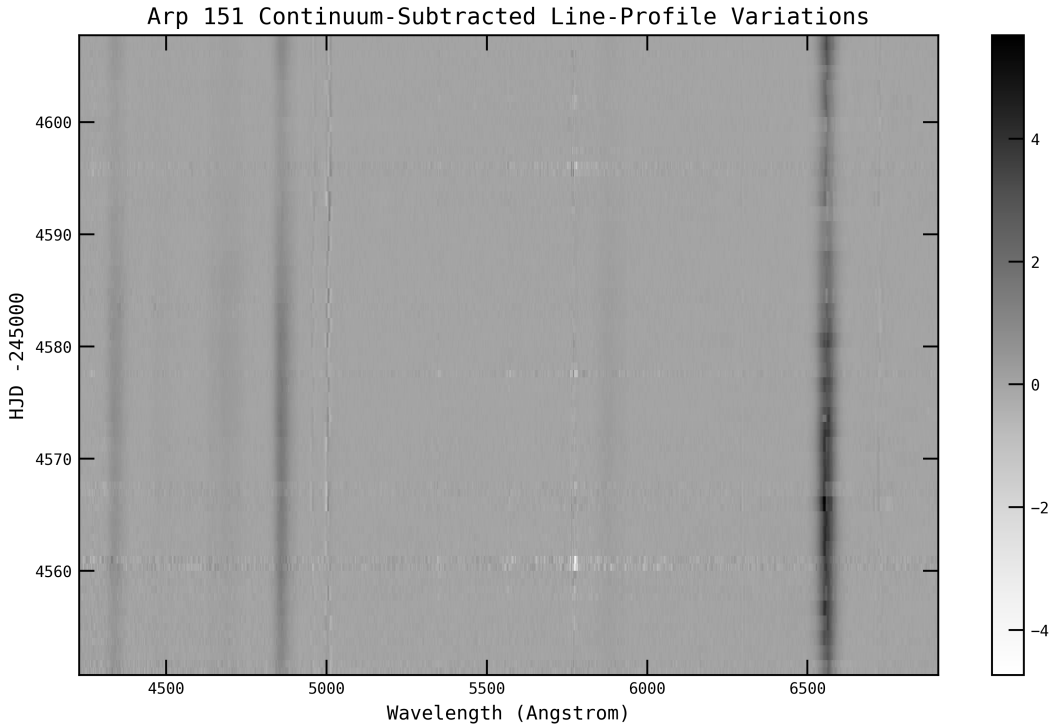

Figure 5.1 Image view of the continuum-subtracted line-profile variation data of Arp 151 as prepared in Bentz et al. (2010b).

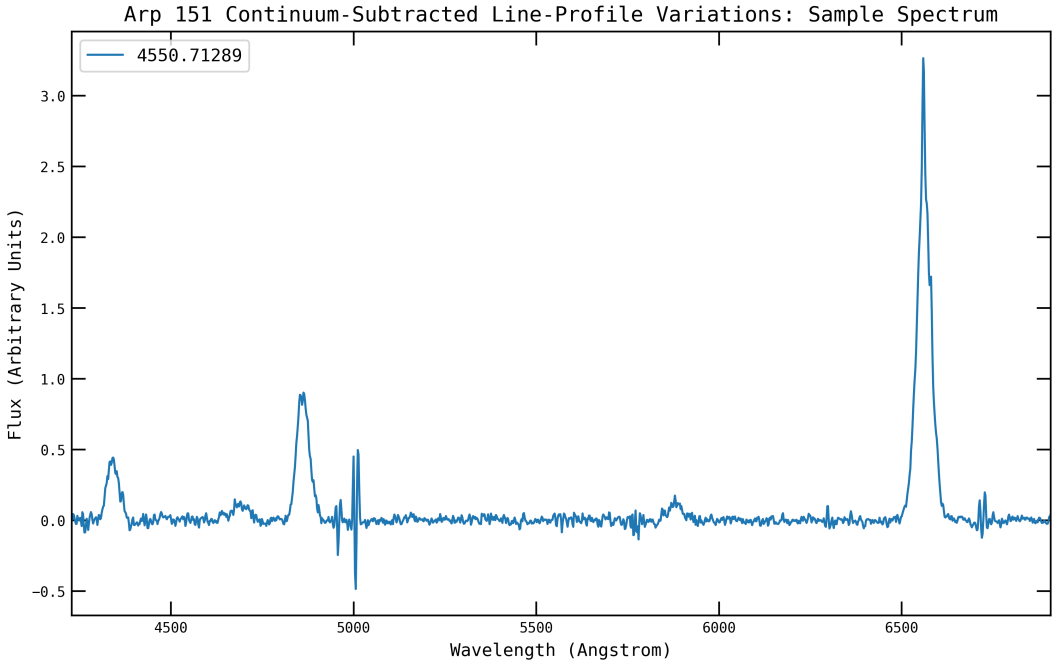

Figure 5.2 A sample spectrum of the Arp 151 continuum-subtracted line-profile variations as prepared in Bentz et al. (2010b).

posed by large gaps in the data. In order to make a more careful reconstruction a VDM from the Arp 151 data, the continuum light curve is first modelled.

The use of Gaussian Processes to model variability in many types of astronomical data has lately been gaining popularity and it can be adapted to the continuum light curves for RM quite easily. Using the Celerite2 software package (Foreman-Mackey et al. 2017) a generic GP model consisting of two stochastically-driven damped harmonic oscillator (SHOT) terms is fit to the continuum data using the SciPy (Virtanen et al. 2020) minimization engine. Where each of the two SHOT terms has a power spectra density of

$$S(\omega) = \sqrt{\frac{2}{\pi}} \frac{S_0 \omega_0^4}{\left(\omega^2 - \omega_0^2\right)^2 + \omega_0^2 \omega^2 / Q^2}, \tag{5.1}$$

in which ω_0 is the undamped angular frequency, S_0 is the power at $\omega = 0$, and Q is the quality factor. These parameters are handled through the Celerite2 interface and minimization engine by the following arguments.

1. The standard deviation of the process.

$$\sigma = \sqrt{S_0 \omega_0 Q} \tag{5.2}$$

2. The undamped period of the oscillator.

$$\rho = 2\pi / \omega_0 \tag{5.3}$$

3. The damping timescale of the process.

$$\tau = 2Q / \omega_0 \tag{5.4}$$

The first term in the GP model is a quasi-periodic term and the second is a nonperiodic term with a quality factor of 0.25. In addition to the parameter values in each term, a mean value

Table 5.1. GP Fit Initial Guesses.

Object	Mean	$\sigma_{T1}^{\dagger}$	$\rho_{T1}^{\dagger}$	$\tau_{T1}^{\dagger}$	$\sigma_{T2}^{\dagger}$	$\rho_{T2}^{\dagger}$	$\theta^{\dagger}$
Arp 151	100.0	3.0	3.0	log(10.0)	0.0	log(5)	log(0.01)

Note. — Initial parameter guesses for the 2-term GP models for continuum data.† Value given is log(value).

Table 5.2. GP Fit Parameters.

Object	N_{its}	Status	Mean	$\sigma_{T1}^{\dagger}$	$\rho_{T1}^{\dagger}$	$\tau_{T1}^{\dagger}$	$\sigma_{T2}^{\dagger}$	$\rho_{T2}^{\dagger}$	$\theta^{\dagger}$
Arp 151	15	True	99.873	4.457	10.033	1.751	-2.779	3.774	-10.048

Note. — L-BFGS-B parameter fits for the 2-term GP model for the continuum data. † Value given is log(value). N_{its} is the number of iterations for L-BFGS-G minimization to converge. Status is the final convergence status for the minimization.

and a jitter θ are also fit. The minimization is then started from a set of guess parameters for each target value in the fit. The initial guesses for Arp 151 are shown in table 5.1. where the guesses were selected so that the minimization converged to a reasonable fit for the GP model. The final values for each parameter in the GP model for the Arp 151 continuum light curve are listed in table 5.2 along with the number of iterations required for the convergence of the bounded memory limited Broyden–Fletcher–Goldfarb–Shanno (L-BFGS-B) minimization algorithm in the N_{its} column and the final convergence status of the minimization.

The resulting GP model fit for Arp 151 shown in figure 5.3. The original data points and their uncertainties are shown by black circles with error bars. The smooth GP model is shown as a solid blue line surrounded by the pale blue ribbon showing the $2-\sigma$ confidence region of the model.

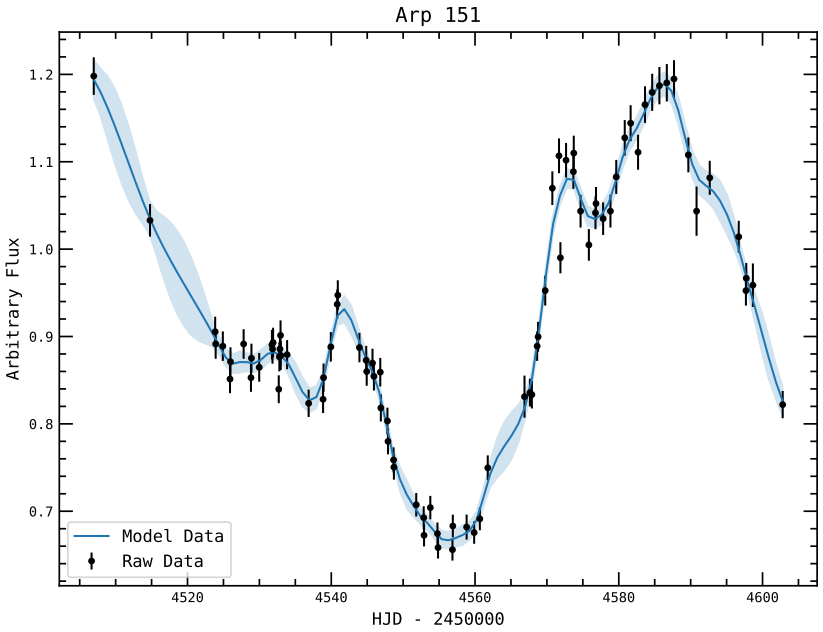

Figure 5.3 GP fit, using the Celerite2 fitting package, to the continuum light curve for Arp 151 from the LAMP2008 data set. The black circles with error bars show the original measurements and uncertainties and the solid blue line represents the GP model fit and the pale blue ribbon the uncertainty on the GP model fit.

5.3 Preliminaries for TLDR Velocity Delay Maps

For each of the TLDR reconstructions of the broad emission features of the Arp 151 data from LAMP2008, the same strategy for hyper-parameter selection was used. Each regularization term's hyper-parameter was started at zero and gradually increased. The final values of each parameter were selected by balancing the value of the reduced χ^2, the fit of the reconstructed spectral lines to the model subtracted input data, and the appearance of the response in the VDM. For the sparsity hyper-parameter, this usually means that the value was increased until the noise dropped to almost nothing outside of the central response feature, or any negative response was eliminated. For the smoothing regularizers, a judgement call for the final values was made so that the VDM was smooth enough to make sense, but not so smooth that the reconstructed spectral lines failed to follow the general trends of the input data. For every reconstruction in this chapter, neither Tikonov initialization or positivity enforcement was used, unless specifically noted. Additionally, automatic penalty parameter tuning was used, making the process quite straightforward. TLDR was set to a maximum number of iterations of 1000, although all finalized TLDR reconstructions converged in less than half the maximum allowed number of iterations.

In the presentation of each VDM in the following chapters, the wavelength of each spectral channel is converted into line-of-sight velocity. The velocity is calculated from the Doppler shift of the spectral channel's rest-frame wavelength away from the center line of the spectral feature. Mathematically, the velocity is

$$V = c\frac{\lambda - \lambda_C}{\lambda_c}, \tag{5.5}$$

where c is the speed of light, λ is the wavelength of the spectral channel, and λ_c is the center wavelength of the spectral feature being reconstructed.

While the main goal of this work is to reconstruct VDMs which can be interpreted to find the geometry of the reverberating gas, the evaluation of an image is quite subjective in

most cases. As the determination of the mass of the SMBH at the heart of AGNs has been a primary goal for RM campaigns, the mass estimate, or it's reverberating dependent measure lag can be used as another point of comparison for the performance of TLDR. The measure originating in RM which helps provide the mass measurement is the lag of the response of different broad lines. This lag coupled with the width of the spectral line response gives the Virial Mass of the SMBH. Mathematically, the mass is

$$M_{BH} = \langle f \rangle \frac{RV^2}{G}, \tag{5.6}$$

where R is the radius of the orbiting gas measured by the response lag, V is the orbital velocity of the gas measured from the width of the variable spectral features, G is the gravitational constant, and $\langle f \rangle$ is a scaling factor. The scaling factor $\langle f \rangle$ is a multiplicative factor that brings the $M - \sigma$ relationship for AGN into agreement with inactive galaxies. There are several different estimates for the scaling factor ranging in value from 2.8 (Graham et al. 2011) to 5.8 (Onken et al. 2004). Where SMBH masses are listed, a scaling factor $\langle f \rangle$ of 4.3 (Grier et al. 2013b) is used, despite more recent work indicating a slightly higher value of 4.8 (Batiste et al. 2017).

As the lag is important for making a mass estimate, it has been measured for most of the objects in the LAMP2008 data set including Arp 151. Most often the lag is measured using the cross-correlation function (CCF), where the peak of the correlation function between the spectral light curve and the continuum light curve is the lag. In some cases, the lag has also been extracted from VDMs reconstructed using other methods. As an additional point of comparison between the VDMs reconstructed using TLDR and other results, the response-weighted mean lag is calculated for each VDM reconstructed. The response-weighted mean lag is calculated as

$$\bar{\tau} = \frac{\sum_{i=1}^{n} w_i \tau_i}{\sum_{i=1}^{n} w_i}, \tag{5.7}$$

where w_i is the value of the i^{th} pixel in the VDM and τ_i is the delay time corresponding to that pixel. The listed uncertainty is the standard deviation of the weighted mean,

$$\sigma = \sqrt{\frac{1}{\sum_{i=1}^{n} w_i} \sum_{i=1}^{n} w_i \left(\tau_i - \bar{\tau}\right)^2}, \tag{5.8}$$

in which all variables are the same as in equation 5.7. In nearly every case, the uncertainty for the response-weighted mean lag is quite high. This is due to the noisy nature of the VDMs reconstructed with a focus on sparsity. Nevertheless, the lag values provide a valuable way to compare the TLDR results with other results for these objects.

5.4 TLDR Reconstructions of Arp 151

TLDR was run on the Hydrogen features $H\alpha$, $H\beta$, and $H\gamma$ features of the Arp 151 data individually and the final parameters used for the reconstruction of each VDM are shown in table 5.3. For each feature, the VDM was reconstructed from 0 to 40 days with $\delta\tau$ of 0.125 days. All reconstructions used an initial penalty parameter of 5×10^7 and a penalty parameter update interval of 20 iterations.

5.4.1 $H\alpha$ Reconstruction

The $H\alpha$ feature reconstruction achieved a χ^2 of 2.293 and the reconstructed VDM is shown in figure 5.7a. In the VDM, strong positive response is visible at delays less than 15 days. Some negative response is also present at very long delays with some noise both positive and negative appearing outside the virial mass envelope shown as a dotted line. The virial mass envelope uses a SMBH mass of $4.7 \times 10^6 M_\odot$ for Arp 151 using all hydrogen features from the Georgia State Univerisy AGN Black Hole Mass Database (Bentz & Katz 2015b). The shape of the positive response does not clearly indicate any geometry. The generally straight line near a delay of 10 days could arise from a circular orbit viewed at a high angle of inclination or could indicate a problem with the calibration or modelling of the spectra. The negative

response does not appear as an echo of the positive response and is not likely an attempt by the algorithm to better fit a nonlinear response with a linear model. A selection of spectra light curves and velocity delay curves are shown in figure 5.4 where the velocity delay curve is shown on the left and the reconstructed spectral light curve on the right as the solid black lines and the open circles with error bars show the continuum-subtracted light curve. The reconstructed spectral light curve follows the general trends of the data, but in some spectral channels there is unfit and or under-fit variation.

5.4.2 $H\beta$ *Reconstruction*

The $H\beta$ feature reconstruction converged in 141 iterations with a χ^2 of 1.066. The reconstructed VDM is shown in figure 5.7b. As with the VDM for the $H\alpha$ feature, the $H\beta$ feature has strong positive response at shorter delay times and negative response at longer delays with noise outside of the virial envelope shown as the dotted black line. The shape of the $H\beta$ positive response can be interpreted as indicating a disk geometry. The negative response does not appear as an echo of the positive response. As before, a selection of spectra light curves are shown for the $H\beta$ feature are shown in figure 5.7b. In comparison to the reconstructed spectral lines of the $H\alpha$ feature, there is much less unfit or under-fit variation as indicated by the χ^2 value being closer to 1.0. There are still some outlying data points which are not tightly fit with the reconstructed light curve, but overall the reconstructed light curves fit the measured light curves very well.

5.4.3 $H\gamma$ *Reconstruction*

The $H\gamma$ feature reconstruction converged to a χ^2 of 1.15 in 146 iterations. The reconstructed VDM for the $H\gamma$ feature is shown in figure 5.7c. As with the other two hydrogen features, the $H\gamma$ VDM shows strong positive response at short delays and some negative response at longer delays with some noise ouside of the virial envelope shown by the dotted black line. Similar to the $H\beta$ feature, the $H\gamma$ feature can be interpreted as indicating a disk structure.

Table 5.3. TLDR Parameters Arp 151.

Parameter	$H\alpha$	$H\beta$	$H\gamma$
μ_X	1.0e5	1.0e6	1.0e6
μ_N	5.0e3	4.0e3	5.0e3
μ_T	1.0e-2	1.0e-1	0.0
μ_V	1.0e-2	1.0e-1	0.0
ρ_{final}	97656.25	390625.0	390625.0
λ_C	$H\alpha$	$H\beta$	$H\gamma$
λ_{min}	6484.5	4782.4	4261.1
λ_{max}	6643.1	4941.0	4420.0
$\#\lambda$	83	82	82
$\#L_{samples}$	86	86	86
$\#\tau$	321	321	321
χ^2/dof	2.293	1.066	1.15
Converged	True	True	True
Iterations	194	141	146

Note. — Each object run with a maximum delay of 40 days and a delay step of 0.125 days. Additionally, Tikonov initialization and positivity enforcement were not used. ϵ_{ABS} and ϵ_{REL} were set to 1.0e-5. $\rho_{initial}$ was 5.0e7 and the update frequency was 20 iterations for all reconstructions.

As in the previous two VDMs, the negative response does not appear as an echo of the positive response. A number of selected spectra light curves for the $H\gamma$ feature are shown in figure 5.6 with the response curve for the corresponding spectral channel shown on the left and the reconstructed light curve on the right. The reconstructed light curves track the variation of the measured spectra well, but the uncertainties on the spectra for this feature are large, especially at later dates.

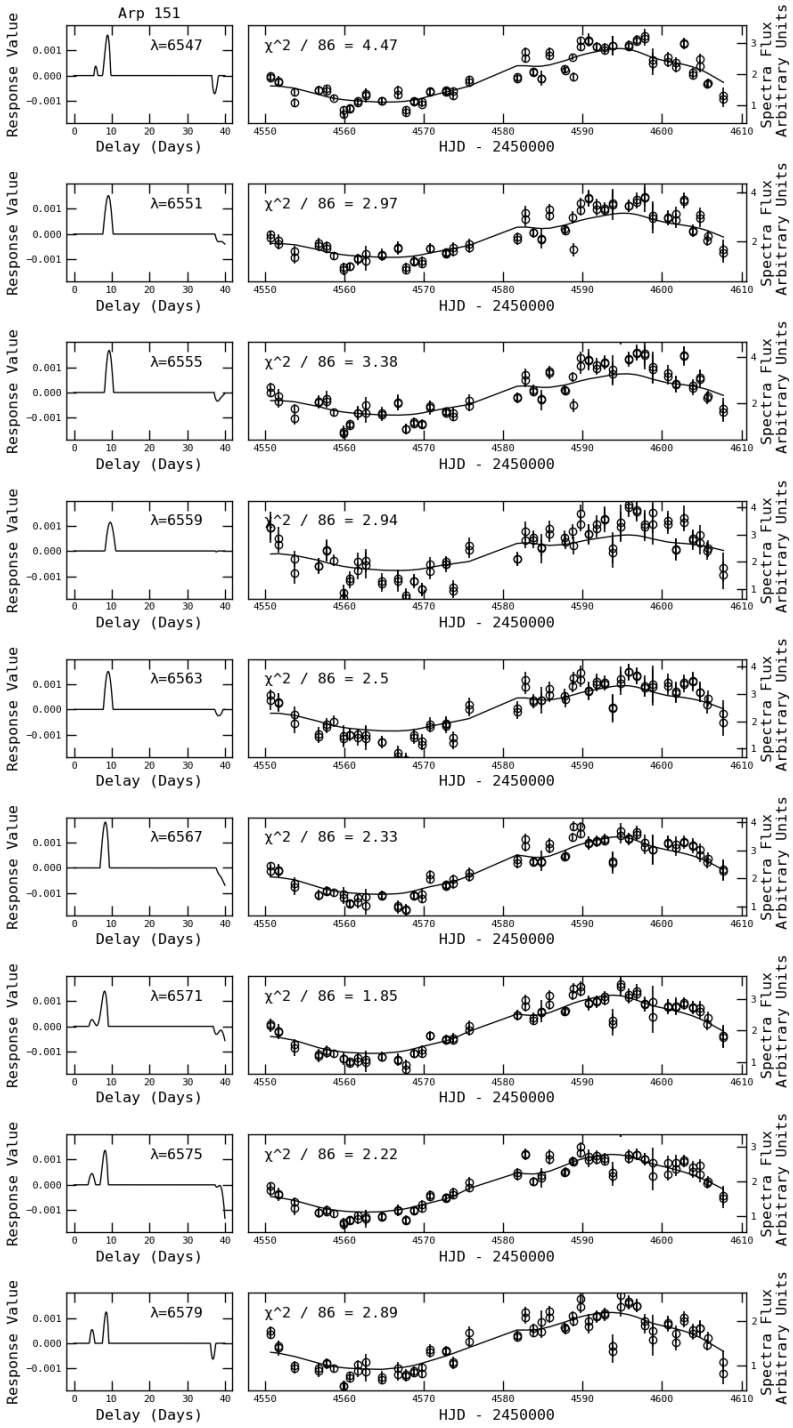

Figure 5.4 The $H\alpha$ response function, and spectral line for selected wavelengths from the TLDR VDM reconstruction of Arp 151 from the LAMP2008 data set.

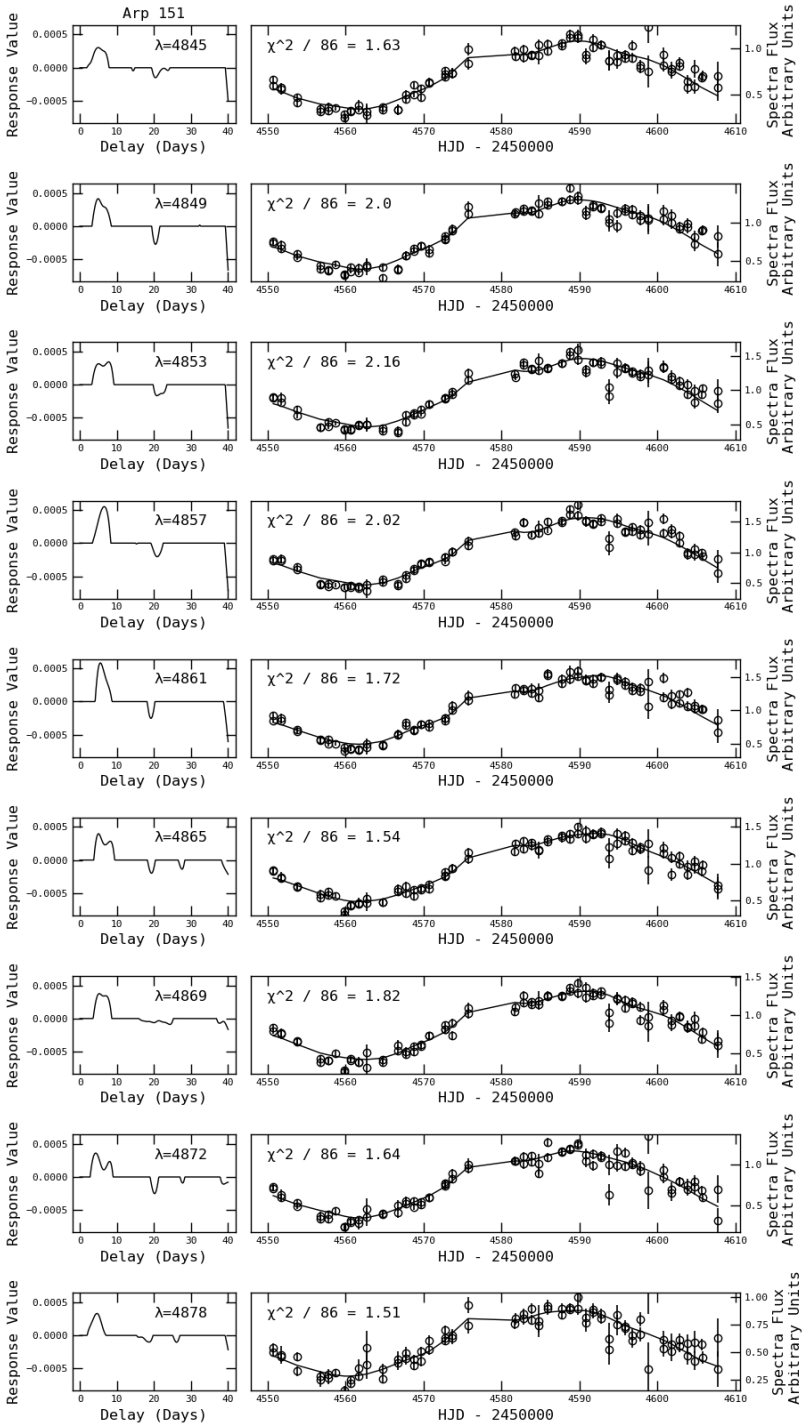

Figure 5.5 The $H\beta$ response function, and spectral line for selected wavelengths from the TLDR VDM reconstruction of Arp 151 from the LAMP2008 data set.

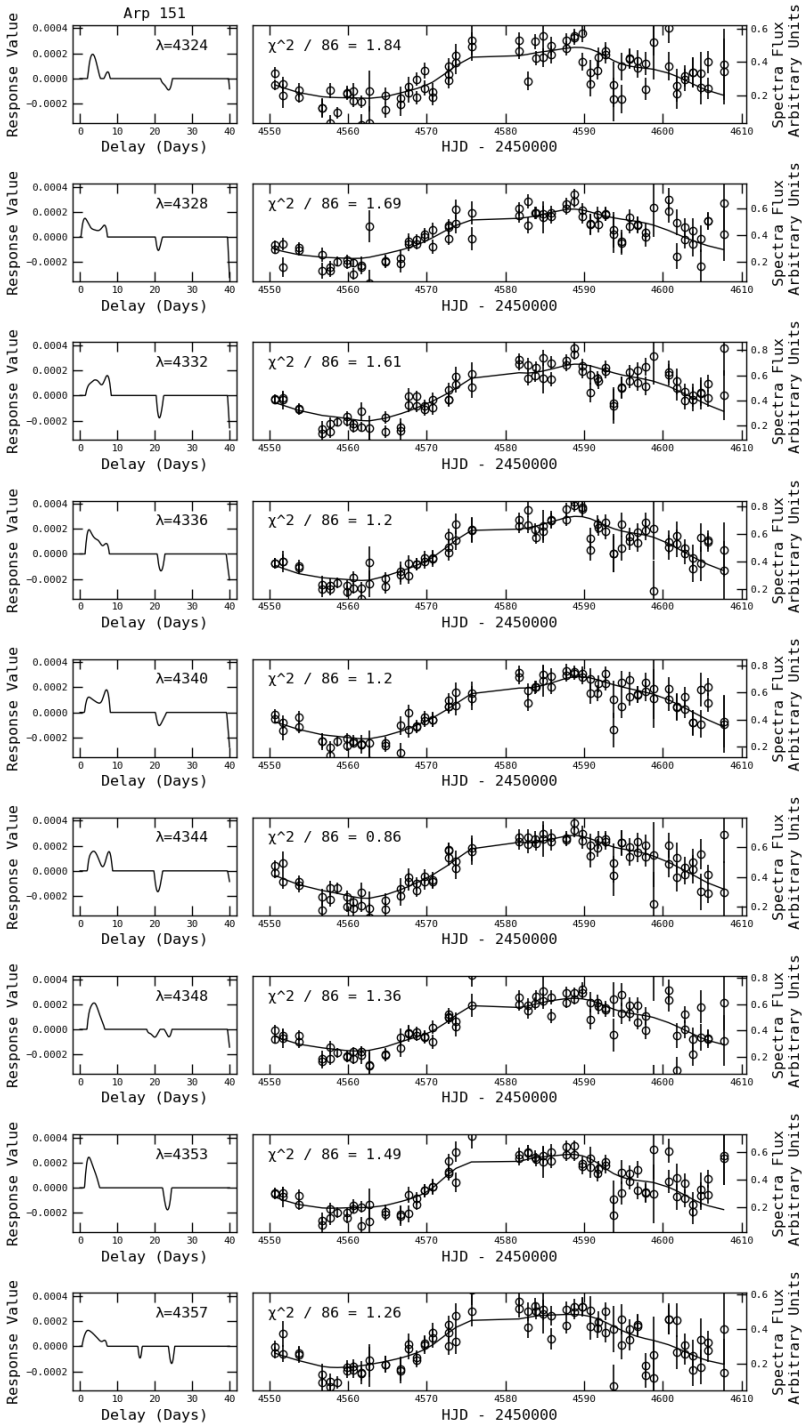

Figure 5.6 The $H\gamma$ response function, and spectral lines for selected wavelengths from the TLDR VDM reconstruction of Arp 151 from the LAMP2008 data set.

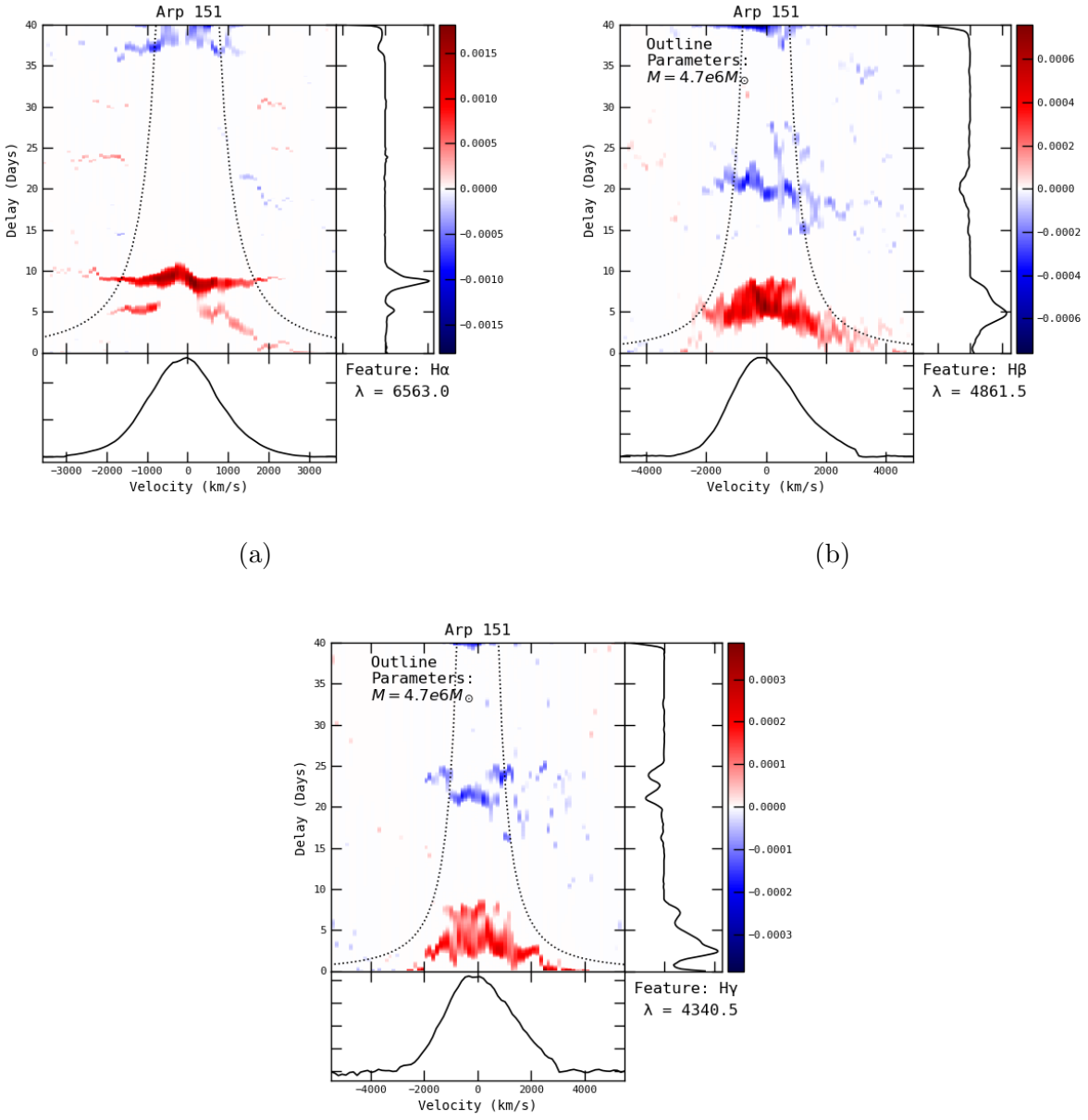

Figure 5.7 Final TLDR reconstructed VDMs for Arp 151 where (a) is $H\alpha$, (b) is $H\beta$, and (c) is $H\gamma$.

5.5 VDM Comparisons

The Arp 151 data from the LAMP2008 data set has been studied extensively with other VDM reconstruction methods. The quality of the data and significant response in the $H\alpha$, $H\beta$, and $H\gamma$ broad line emission features has allowed the reconstruction of the VDMs for each line with multiple methods. This allows the TLDR reconstructed VDMs for each feature to be compared with others from the literature.

5.5.1 $H\alpha$ Comparisons

The $H\alpha$ feature has VDMs reconstructed by both RLI (Skielboe et al. 2015), and MEM (Bentz et al. 2010b). The VDMs from RLI and MEM are shown alongside the VDM reconstructed with TLDR in figure 5.8. The RLI reconstructed VDM, figure 5.8c appears similar to the TLDR VDM, although the smoothing and lower temporal resolution make direct comparison difficult. The response rising from zero delay at 2000km/s, with a gap before picking back up at -1000km/s is clearly identifiable. Similarly, the broad response near 10 days in the TLDR VDM with most of its response inside $\pm$1000km/s is also seen in the RLI VDM. The smoothing present in the RLI VDM connects some of the features that are not connected in the TLDR VDM.

Many of the points made in comparing the RLI VDM to the TLDR VDM also apply to the MEM VDM, figure 5.8b. As the MEM VDM is displayed with delay time out to 20 days, it is better to compare it to the full TLDR VDM for $H\alpha$ shown in figure 5.7a. The broad flat response across a delay of approximately 10 days seen in the TLDR VDM can be seen in the MEM VDM quite easily as it extends outside the virial envelope for both. The smooth long blue sweeping response between 15 and 20 days in the MEM VDM is also seen in the TLDR VDM, although in the TLDR VDM, it appears as clumps of response with slightly longer delays. Overall, the MEM VDM appears as a very smoothed out version of the TLDR VDM, with the most significant difference being the low delay response seen on

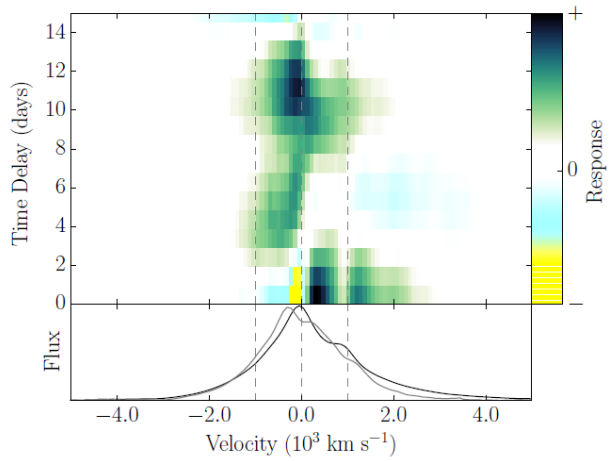

(a) The RLI reconstruction from Skielboe et al. (2015).

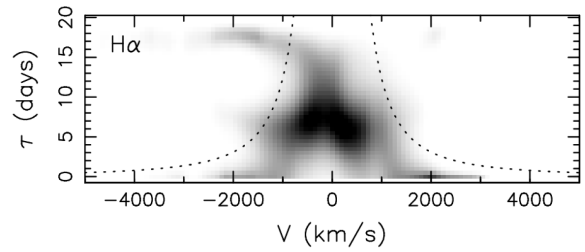

(b) The MEM reconstruction from Bentz et al. (2010b).

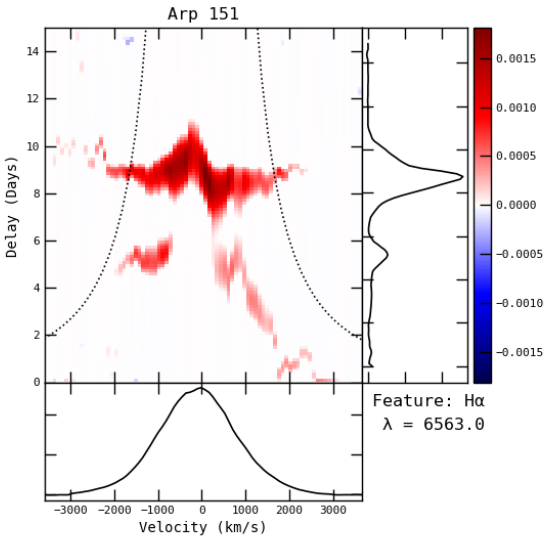

(c) The TLDR reconstruction.

Figure 5.8 Arp151 $H\alpha$ VDMs reconstructed via various methods including TLDR for comparison.

the blue wing of the MEM VDM all the way down to a delay of zero days. This discrepancy might also simply be a result of the large smoothing used in the MEM reconstruction.

5.5.2 $H\beta$ Comparisons

As with the $H\alpha$ broad line feature, there exist VDMs from RLI and MEM for the $H\beta$ broad line feature as well, but there is also a VDM reconstructed using dynamical modelling to compare to. The other existing VDMs for the Arp 151 $H\beta$ feature are shown in figure 5.9a from Skielboe et al. (2015), with the RLI recovered VDM on the right, in the middle, the VDM recovered with MEM originally presented in Bentz et al. (2010b), and on the left, the VDM recovered via dynamical modelling was originally presented in Pancoast et al. (2014b).

Below these, the TLDR reconstructed VDMs are shown with a maximum delay of 15 days. On the left (figure 5.9b), the initial reconstructed VDM favoring smoothness with a delay resolution of 1.0 days. On the right (figure 5.9c), the final reconstructed VDM favoring sparsity with a delay resolution of 0.125 days.

Generally speaking, the TLDR, RLI, and MEM show the same structure, indicating a disk-like structure with more response on the red win than the blue. The RLI VDM and the heavily-smoothed initial TLDR VDM are nearly indistinguishable and the final TLDR VDM favoring sparsity does not tell a vastly different story, although it indicates that the red-wing is more diffuse in response than the others do. While the MEM VDM is not vastly different than the RLI and TLDR VDMs , the main difference is that the MEM VDM indicates an unresolved response on the red wing rather than the resolved response shown in the other VDMs.

On the other hand the Dynamical Modelling reconstructed VDM bears almost no resemblance to the other VDMs. It matches the MEM VDM in the enhanced red-wing response at low delay, but fails to show the disk-like response signature seen in the other VDMs. Anecdotally, it is usually the case that the Dynamical Modelling reconstructed VDMs in the literature do not match the VDMs recovered by deconvolution methods. The discrepancy between Dynamical Modelling VDMs and those reconstructed by convolution methods is a major issue for RM VDM reconstructions at present and warrants serious consideration in the future.

5.5.3 $H\gamma$ Comparisons

Lastly, for the $H\gamma$ feature there exist VDMs reconstructed with RLI and MEM that the TLDR VDM can be compared with. The RLI reconstructed VDM appears in figure 5.10c from Skielboe et al. (2015) and the MEM reconstructed VDM is shown in figure 5.10b from Bentz et al. (2010a). In general, both the RLI VDM and the MEM VDM look a lot like the TLDR VDM shown in figure 5.10a, shown here with a maximum delay of 15 days. All three

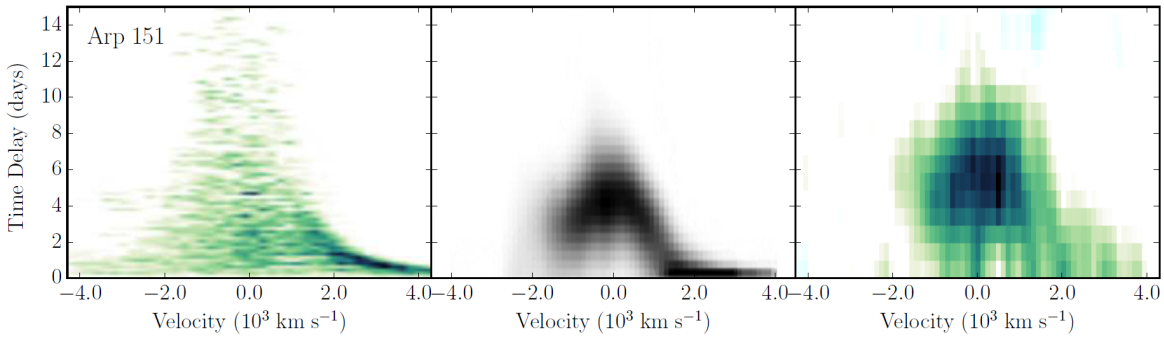

(a) From Skielboe et al. (2015). Left: Dynamical Modelling VDM. Middle: MEM VDM. Left: RLI VDM.

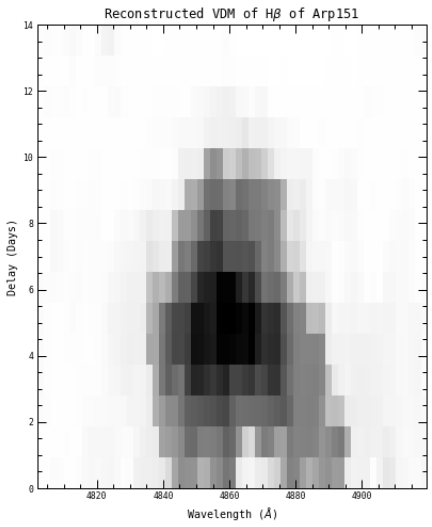

(b) Initial TLDR VDM emphasizing smoothness described in section 4.2.

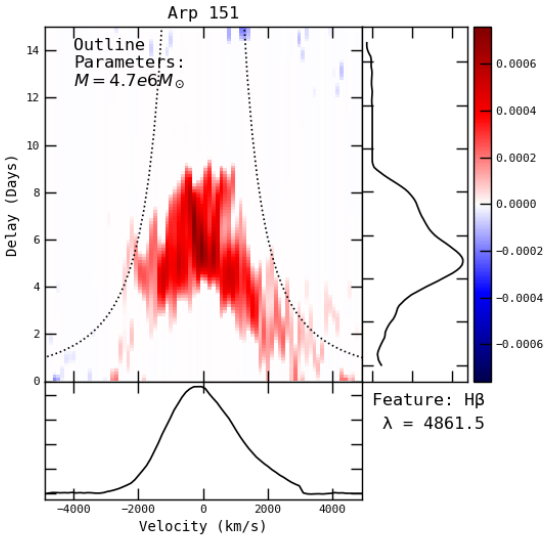

(c) The TLDR VDM emphasizing CS regularization.

Figure 5.9 Arp151 $H\beta$ VDMs reconstructed via various methods including TLDR for comparison.

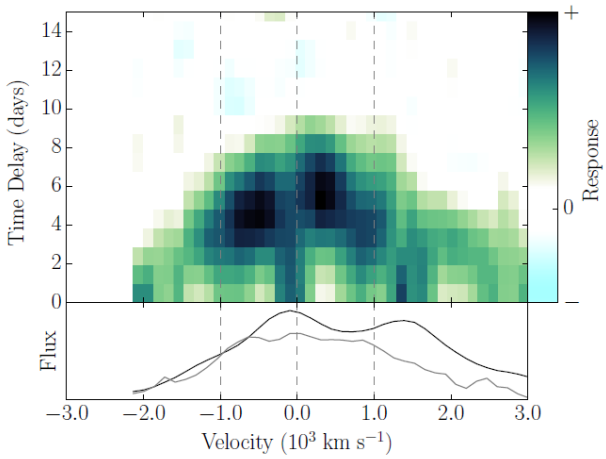

(a) RLI VDM from Skielboe et al. (2015).

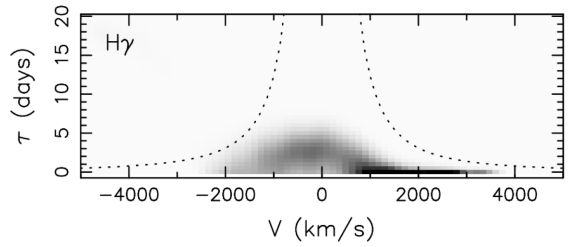

(b) MEM VDM from Bentz et al. (2010a).

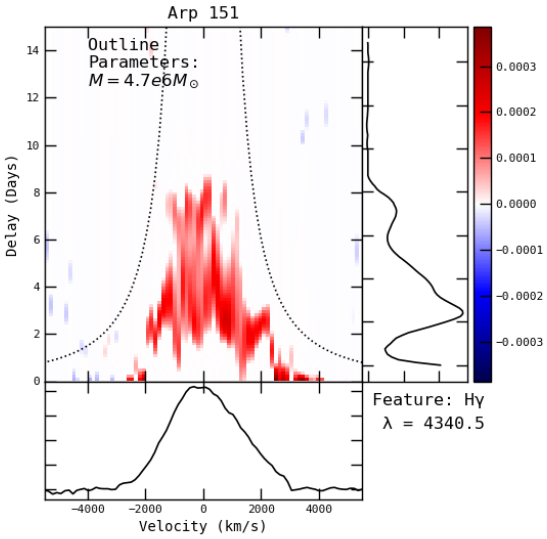

(c) TLDR VDM.

Figure 5.10 Arp151 $H\gamma$ VDMs reconstructed via various methods including TLDR for comparison.

VDMs strongly suggest a disk structure with the strongest response in the central part of the VDM around 4 days. All three also show an enhanced response on the red wing extending out to or past 3000km/s. While the MEM VDM looks very much like the TLDR VDM with a bit more smoothing across the disk, the RLI VDM appears to have much more smoothing. In either case, the TLDR VDM provides a much more defined response. Importantly, the enhanced red wing that appears to have a hook extending to longer delays with a maximum near 2000km/s in the TLDR VDM, may be evident although smoothed out in the RLI VDM which shows a resolved response in this area. On the other hand, the MEM VDM indicates a totally unresolved response across the enhanced red wing.

5.5.4 Lag Times

The lag times used for estimating the mass of the SMBH in Arp 151 provide another point of comparison as listed in table 5.4. The response weighted mean lag calculated from the TLDR VDMs yield a $H\alpha$ lag of 7.9 ± 2.0 days, a $H\beta$ lag of 5.1 ± 1.8 days, and a $H\gamma$ lag of 3.5 ± 2.1 days. The $H\alpha$ lag measured from the TLDR VDM is consistent with both the CCF measured lag of $7.84^{1.03}_{-0.98}$ (Bentz et al. 2010a) and the RLI measured lag of $6.8^{+0.9}_{-1.4}$ (Skielboe et al. 2015). Similarly, the $H\beta$ lag measured from the TLDR VDM is also consistent with the lags obtained with other methods, where a lag of $3.99^{+0.49}_{-0.68}$ days is reported from CCF (Bentz et al. 2009), a lag of $3.6^{+0.70}_{-0.20}$ days was obtained by JAVELIN (Grier et al. 2013b), and a lag of $4.0^{+0.7}_{-0.8}$ days was measured by RLI (Skielboe et al. 2015). Finally, the lags calculated for the $H\gamma$ feature are also consistent between the TLDR calculated value and those measured with other methods. The $H\gamma$ lag calculated from RLI is $3.0^{+0.8}_{-0.8}$ (Skielboe et al. 2015), and the lag calculated from the CCF is $1.36^{+0.79}_{-0.73}$ (Bentz et al. 2010a). In each case, the uncertainty on the values obtained from the TLDR is high, this is due to the relatively noisy VDMs, and the method used to calculate the lag discussed in section 5.3. Despite the large uncertainty on the TLDR measured lag values, the fact that these values are consistent with other methods across each of the three hydrogen broad line features indicates that the reconstructions provided by TLDR are not indicating a vastly different mass for the SMBH in the system.

Further concluding comments on the development, application, and future of the TLDR algorithm can be found in chapter 11.1.

Table 5.4. Lags for Arp 151.

Method	$H\alpha$	$H\beta$	$H\gamma$	Source
TLDR	7.9 ± 2.0	5.1 ± 1.8	3.5 ± 2.1	This work.
CCF	$7.84^{+1.03}_{-0.98}$	$3.99^{+0.49}_{-0.68}$	$1.36^{+0.79}_{-0.73}$	Bentz et al. (2009, 2010a)
JAVELIN	-	$3.6^{+0.70}_{-0.20}$	-	Grier et al. (2013b)
RLI	$6.8^{+0.9}_{-1.4}$	$4.0^{+0.7}_{-0.8}$	$3.0^{+0.8}_{-0.8}$	Skielboe et al. (2015)

Note. — Comparison of the TLDR based lag measurements with other measurements for the $H\alpha$, $H\beta$, and $H\gamma$ feature of Arp 151.

CHAPTER 6
OPTICAL INTERFEROMETRY

6.1 An Introduction to Optical Interferometry

An interferometer is, in its most basic of form, an application of Young's Double Slit where the two apertures form the slits and the projection screen where the interference pattern appears is the detector at the back end of the system. Interferometry was first proposed as a method for measuring stellar diameters by Hippolyte Fizeau in 1868 (Danjon 1922) and the theory of interferometry for astronomy was formalized by Albert Michelson in 1891 (Michelson 1891). The theory was further formalized and utilized by Michelson using the 40 inch refractor at Yerkes Observatory, as well as the 60-inch and 100-inch reflectors at Mount Wilson Observatory to measure the diameters of the satellites of Jupiter and the angular separation of the spectroscopic binary Capella by masking the objectives of the telescopes (Michelson 1920). In 1921, Michelson and Pease measured the first diameter of a star, Betelgeuse, using the 100-inch reflecting telescope at Mount Wilson Observatory with a 20-foot long beam increasing the effective diameter of the telescope using mirrors in a double periscope configuration (Michelson & Pease 1921).

It would take many decades for technology to make interferometry a productive method for astronomy. Photoelectric detectors, lasers, computers, and piezoelectric devices are just some of the multitudinous advancements in technology that have allowed interferometry to begin to attain its potential. Despite a growing community and positive mention in the resulting publication from the Decadal Survey on Astronomy and Astrophysics 2020 (National Academies of Sciences, Engineering, and Medicine 2021) Optical interferometry remains a niche method relative to single aperture based studies in astronomy.

A simple schematic for a two-telescope interferometer is shown in figure 6.1. The telescopes are separated by a baseline distance shown by the red line, resulting in a projected baseline shown by a dark blue line. The light from the two telescopes is routed to an instrument that combines the light resulting in an interference pattern called an interference

fringe. Note that the light travelling to the telescope on the left has to travel farther than the light travelling to the telescope on the right, noted by the green line. In order for the interference fringe to be seen, the optical path length must be equal between the two paths the light takes, so some extra path is added to the path on the right, also shown in green, so that the two beams arrive at the combiner having travelled the same distance. Of course, this depends on the coherence length of the light being combined. For a very narrow optical bandwidth, the coherence length is long and the path-length correction need not be very precise. However if the optical bandwidth is broad then the path-length correction must be more precise. The required precision of the path-length correction must be balanced with the amount of signal expected in the optical bandwidth for any viable optical interferometer design.

The type of interferometer described here uses a homodyne detection scheme, where the light from the two telescopes creates an interference pattern seen and recorded by the detector in the combiner. This is in comparison to a heterodyne detection scheme used in radio interferometry in which a locally oscillating signal with a frequency near that of the frequency of interest is interfered with the science signal and recorded (Townes et al. 1994). The introduction of a local oscillator allows the science signal of each telescope to be recorded independently. Then the interference fringe between the two telescopes can be extracted later. While there are great advantages to heterodyne detection, recording the interaction between the local oscillator and the science signal at optical frequencies is not yet practical. As such, interferometry, discussed here as Optical Interferometry (OI), refers to systems that combine light from telescopes using beam transport consisting of mirrors or optical fibers and homodyne detection.

Between the optical path length control and the complexity of operating multiple telescopes simultaneously, not to mention the myriad complications in beam combination, one might question why attempt interferometry at all. It all comes down to angular resolution. A single aperture has an angular resolution defined by the diffraction limit of the aperture.

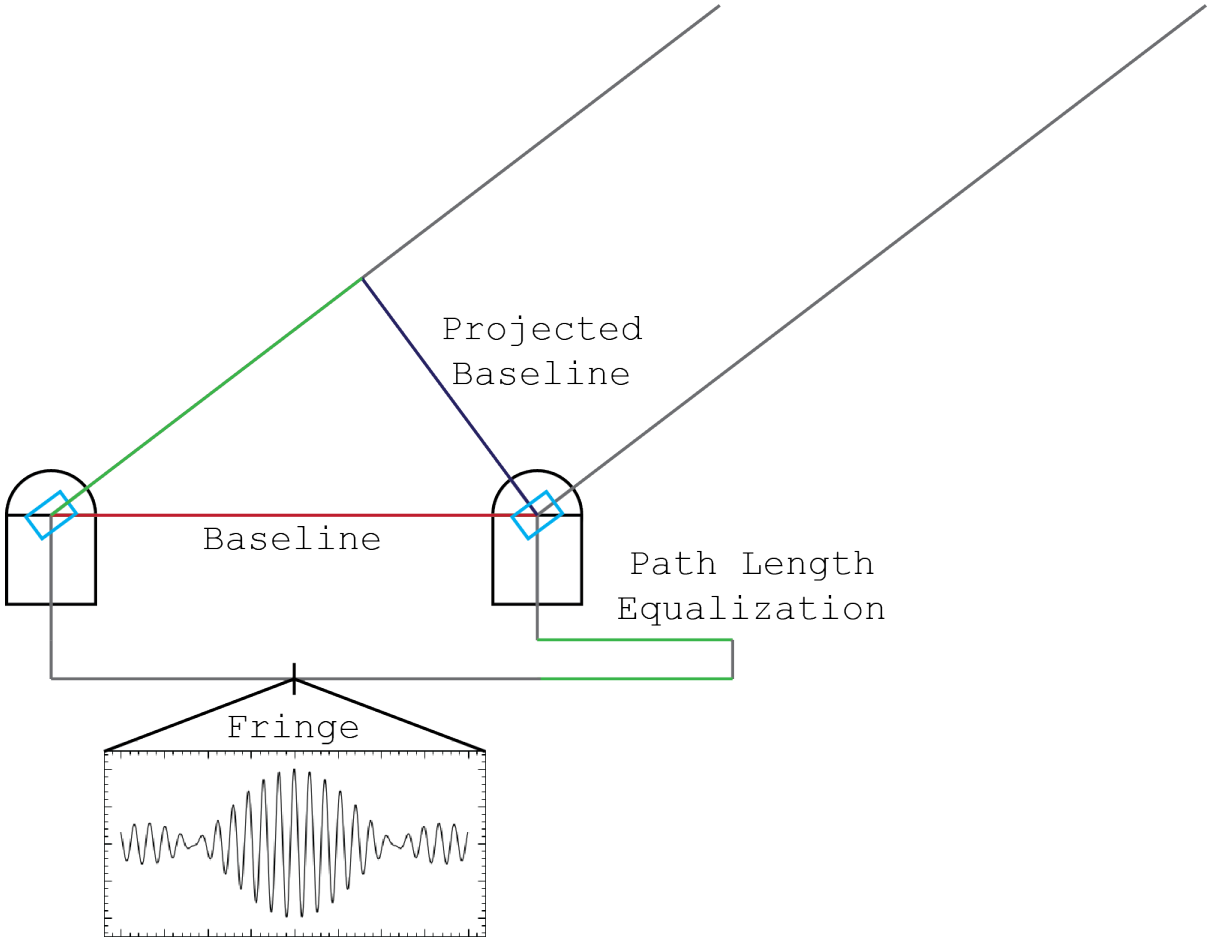

Figure 6.1 Simple schematic for a two-collector interferometer. The extra path-length added by the geometry of the telescopes and position of the target on sky must be compensated for by extra delay in the beam train of the shorter path-length.

Where the resolution of a telescope is the smallest resolvable detail subtending an angle R. The Rayleigh Criterion for circular apertures says that the smallest angle R at which two point sources can be determined is proportional to the wavelength λ divided by the diameter of the aperture,

$$R_{Circular\ Aperture} = 1.22\frac{\lambda}{D}. \tag{6.1}$$

To resolve smaller, more distant objects, a larger and larger telescope is needed. For apertures on the scale of tens of meters, this becomes difficult and expensive. For apertures on the scale of hundreds of meters, this becomes practically impossible with current technology. For an interferometer, the angular resolution is determined by the separation between telescopes, called the baseline, rather than each aperture's size. The resolution, or smallest resolvable angle, R is proportional to the wavelength λ divided by the baseline B. Using interferometry allows us to have much greater resolution at a much lower cost using smaller apertures spread over longer baselines than any single aperture. One complication is that the use of smaller apertures reduces the light-gathering power and therefore the sensitivity of an interferometer in comparison to a single large aperture telescope.

6.1.1 Interferometric Math

The principle value measured by OI is the visibility, defined by Michelson (1891, 1920) as:

$$V = \frac{I_{max} - I_{min}}{I_{max} + I_{min}} = \frac{\text{Fringe Amplitude}}{\text{Average Intensity}}, \tag{6.2}$$

in which I_{max} is the maximum fringe intensity measured and I_{min} is the minimum fringe intensity measured. When properly normalized, the visibility is the amplitude of the fringes. The second value measured by OI is the phase of the fringes. The linchpin for all of interferometry is the van Cittert-Zernike theorem which relates these observables to the Fourier component of the brightness distribution observed (van Cittert 1934; Zernike 1938). In more obvious terms, the van Cittert-Zernike theorem states that the values measured by an

interferometer result from the Fourier transform of the brightness distribution sampled at the spatial frequency corresponding to the projected baseline between the telescopes. The observables measured by an interferometer directly reflect the mutual coherence function of the electric field of the source sampled by the two telescopes. Since astronomical objects are so far away, the incoherent light emanating from all across the surface of the object appears as nearly coherent light due to spreading of the wavefront over distance. Assuming that the brightness distribution comes from a small enough portion of the sky that the region can be treated as flat, the van Cittert-Zernike theorem can be shown mathematically using Cartesian coordinates (dx_Ω, dy_Ω) centered on the middle of the brightness distribution as in Monnier (2003), which appears as

$$\left|\mathcal{V}_\nu\left(\frac{\vec{D}}{\lambda}\right)\right| e^{-i\phi_{v_\nu}} = \frac{\int_{d\Omega} dx_\Omega dy_\Omega I_\nu\left(\vec{r_\Omega}\right) e^{-2\pi i\left(\frac{\vec{D}}{\lambda}\cdot\vec{r_\Omega}\right)}}{\int_{d\Omega} dx_\Omega dy_\Omega I_\nu\left(\vec{r_\Omega}\right)}. \tag{6.3}$$

The vector $\vec{D}$ describes the baseline between telescopes projected in the plane of the sky. The vector is commonly broken into components **u** pointing east and **v** pointing north in the plane of the sky. The plane described by $(\mathbf{u}, \mathbf{v})$ is commonly used in describing interferometric measurements and is simply referred to as "The uv Plane". Getting back on track, $\vec{r_\Omega} = (dx_\Omega, dy_\Omega)$, and I_ν is the brightness distribution. Lastly, the complex visibility is always normalized to 1 at $\vec{D}/\lambda = 0$.

Due to the atmospheric turbulence above each telescope in an interferometer, the phase of the incident light at each telescope will be delayed by different amounts. For a two-element optical interferometer, there are not any simple options for recovering accurate absolute phase measurements. Fortunately, two-element interferometric measurements generally focus on measuring the size of objects where simple visibility function modelling suffices.

The phase delay issue becomes a more important problem to solve when more complicated information is required, such as imaging. For imaging, three or more interferometric elements are used to measure more points in the uv plane simultaneously. The case of an interferometer

using three or more telescopes offers a solution to the phase delay problem. For any three interferometric elements, the atmospheric phase delay introduced at each element is cancelled out by the sum of the phases of all three elements. The sum of phases for the triangle defined by the three elements is called the closure phase.

The closure phase can be used to recover nearly all phase information for an observation, provided enough telescopes are used. For an interferometer consisting of N elements, each pair of elements measures a single phase giving $\frac{1}{2N}(N-1)$ phases. Each triangle formed by a trio of telescopes yields a closure phase giving $\frac{1}{2}(N-1)(N-2)$ independent closure phases. While there will always be more unknown phases than known closure phases, the more interferometric elements that are used the more phase information can be recovered. Figure 6.2 shows the number of phases, closure phases as they increase in number with the number of interferometric elements along with the percentage of closure phases to Fourier phases. Clearly, more interferometric elements are better in terms of phase recovery, but there are serious complications to building interferometers with large numbers of elements. Any interferometer must be designed carefully to balance the number of elements with the overall sensitivity of the array as the beam combination process requires splitting the light from each element once for each phase.

6.2 Visibility Modelling

In the most basic case of measuring the size of objects with a two-element interferometer, the visibility measured at various positions in the uv plane is the end result. By comparing the visibility at different baseline lengths and position angles on sky with the visibilities of a brightness distribution model, the size of the observed object is measured. This assumes that the brightness distribution model correctly describes the object. In general, it is not safe to assume that simple geometric models will adequately describe astronomical objects in detail, but for general parameters such as the radius of a star or the separation of two stars in a binary system, simple models do suffice.

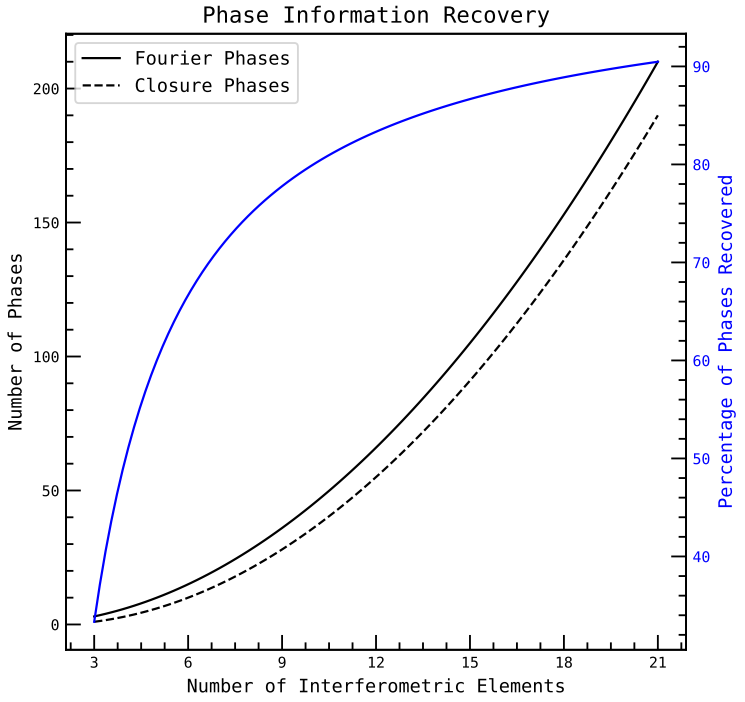

Figure 6.2 The amount of phase recovery from interferometers of increasing number of elements. The percentage of phases recovered is shown in blue matching the right y-axis. The number of Fourier phases, and independent closure phases, shown in black match the left y-axis.

For the case of objects with circular symmetry, modelling the visibility function is relatively straightforward. With an intensity distribution in hand, it need only be run through equation 6.3 to obtain the visibility function. While daunting at first, when considering the circularly symmetric case, things get easier. For the simple models considered here, the equations for different intensity distributions and their resulting visibility functions can be found in numerous places in the literature, so the functions need only be looked up. The functions for the examples of a circular disk of uniform brightness, a disk whose brightness as a function of radius is described by a Gaussian, and an infinitesimally thin ring of constant intensity at a fixed radius discussed next are listed in Berger & Segransan (2007).

The simplest model for a resolved object is that of a circular disk of uniform brightness. Such an object has a fixed intensity inside its radius and zero intensity outside of it. In this case, the visibility function is that of an Airy disk which as a function of $r = \sqrt{u^2 + v^2}$ is

$$V(r) = 2\frac{J_1(\pi\Theta r)}{\pi\Theta r}, \tag{6.4}$$

where Θ is the diameter of the disk and the function $J_1()$ is the first-order Bessel function of the first kind.

Adding some complexity, a disk whose intensity drops off as a function of radius according to a Gaussian is a common model for determining the size of stars. The visibility function for such a Gaussian disk with a full width at half maximum (FWHM) of Θ is

$$V(r) = \exp\left(-\frac{(\pi\Theta r)^2}{4\ln 2}\right). \tag{6.5}$$

A slightly more complicated geometry is that of the thin ring model. The thin ring model is described by an intensity distribution where all model intensity appears at the specified radius from the center, described by a δ-function, and is accompanied by a well-known visibility function. The visibility function is described by a zeroth-order Bessel function of the first kind and appears as

$$V(r) = J_0(2\pi\rho_0 r), \tag{6.6}$$

The intensity distributions and visibility functions for each of these models are shown in figure 6.3 with the intensity distribution shown on the left, and the corresponding visibility function on the right. The uniform disk model, shown by the solid red line, had a radius of 5 mas, the Gaussian disk model, shown as the dashed blue line, had a FWHM of 2.5 mas, and the thin ring, shown by the dotted green line, had a radius of 2.5 mas. While the three models are very hard to distinguish with short baseline measurements, the objects become more resolved with longer baseline measurements and the models become readily distinguishable from one another. Although the example of the uniform disk was chosen as a simple example for examples' sake, the Gaussian disk model and thin ring model are valid examples to be used when measuring the size of an AGN and will be utilized in chapter 10.

6.3 Optical Interferometers

There are several optical interferometers currently in regular science operation in the world today, as well several which have recently been decommissioned. With several of the currently active facilities pursuing expansion and upgrades and the ongoing development of another, the future of optical interferometry is bright. Some of these facilities are applicable to the interferometry of AGN and some are not due to sensitivity or resolution constraints, yet each warrants mention.

The Large Binocular Telescope Interferometer (LBTI) combines the light from the two 8.4 meter apertures of the Large Binocular Telescope with the center-to-center separation of the telescopes providing a baseline of 14.4 meters (Hill et al. 2006; Defrère et al. 2015). The Navy Precision (formerly prototype) Optical Interferometer (NPOI) combines the light of up to four or six 0.5 meter siderostats depending on mode with baselines from 2 to a planned 437 meters (Johnston 1998; Armstrong et al. 1998). The Very Large Telescope Interferometer

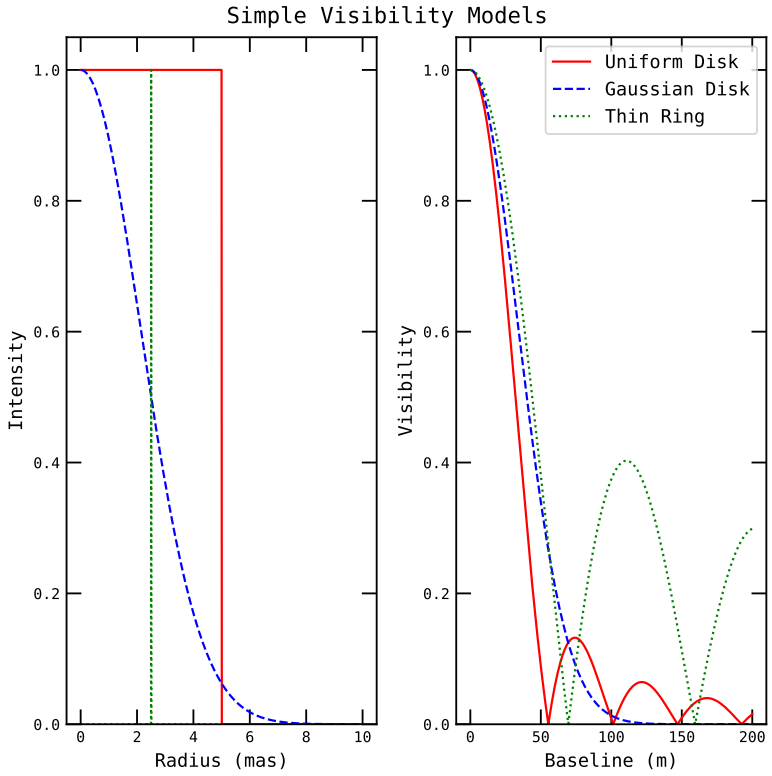

Figure 6.3 Intensity distributions and corresponding visibility functions at K-band for a uniform disk of radius 5 mas, a Gaussian disk with FWHM of 2.5 mas, and a thin ring at radius 2.5 mas.

(VLTI) operated by the European Southern Observatory combines the light from the four 8.2 meter unit telescopes or four 1.8 meter auxillary telescopes with baselines up to 140 meters (Haguenauer et al. 2008). The CHARA Array utilizes six one-meter telescopes with baselines up to 322 meters with development underway to add a seventh telescope at larger baselines (ten Brummelaar et al. 2005). The CHARA Array will be discussed in detail in chapter 7.

Currently under development, the Magdalena Ridge Observatory Interferometer (MROI) is designed to combine the light from ten 1.4 meter telescopes with reconfigurable baselines of up to 340 meters (Buscher et al. 2013).

There are several legacy optical interferometers whose technological development or scientific results have contributed directly to the regular operation of optical interferometers today. A few, but not all of these are mentioned here. The Sydney University Stellar Interferometer combined light from 12 centimeter telescopes using a single baseline at a time Davis et al. (1999). The Infrared Optical Telescope Array(IOTA) combined the light from up to three 0.45m telescopes at a vaiety of wavelengths (Traub 1998). The Palomar Testbed Interferometer consisted of three 0.45 meter siderostats with baselines up to 38 meters (Reasenberg 1990; Jankov 2010). The Keck Interferometer (KI) combined the light from the two 10 meter Keck Telescopes separated by an 85 meter baseline (Colavita et al. 1998).

6.4 Optical Interferometry of AGN

As the majority of optical interferometers utilize apertures of 1 meter diameter or less and the beam transport optics of these instruments add numerous imperfect reflections before and inside of their detection systems, the sensitivity is generally quite limited. The existing interferometers, except for the VLTI and the decommissioned KI, are limited to objects brighter than 8th magnitude in the near infrared (NIR) under average seeing conditions. At the general limit, there are only two AGNs bright enough to consider attempting with most active optical interferometers with apertures at the 1 meter scale and smaller. Despite

this, AGN science with optical interferometers has been of long been of interest. During the development of the CHARA Array, AGN science was considered as a challenging goal (Mason & ten Brummelaar 1995) and regular attempts have been made to observe AGNs at CHARA since 2010 (Kishimoto et al. 2010). Despite attempts, seeing conditions and sensitivity limits have made AGN observations elusive at this scale. Implementation of adaptive optics (AO) has begun to change the experience and the deployment of new detectors with lower noise characteristics promise to open up more AGN science at the smaller aperture scale.

The optical interferometers with larger apertures have conducted observations of numerous AGNs in the past. Primarily utilizing the KI and the VLTI with the eight meter unit telescopes upwards of 40 AGNs have been observed (Swain et al. 2003a; Burtscher et al. 2016; Hönig 2019). Overwhelmingly, these objects have been observed at the $10\mu m$ N-band in the mid infrared (MIR) with the MIDI instrument at the VLTI (Leinert et al. 2003; Burtscher et al. 2013; López-Gonzaga & Jaffe 2016). Relatively few of of the total number of AGNs observed have been observed in the near infrared with KI observing in the neighborhood 10 objects (Kishimoto et al. 2009, 2013b) and perhaps a dozen observed by VLTI (Wittkowski et al. 2004; Weigelt et al. 2012; Gravity Collaboration et al. 2020b). However, with the recent deployment of the K-band ($2.2\mu m$) GRAVITY combiner (Gravity Collaboration et al. 2017) this number should rapidly increase.

Despite the technical challenges, AGN science through OI remains a popular topic garnering attention in reviews and discussions of OI (Berger et al. 2012; Hönig et al. 2018; Kishimoto et al. 2019).

6.5 Science Cases for the Interferometry of AGN

Combining the large apertures of the Unit Telescopes at the VLTI with numerous instruments and the relative brightness of AGNs in the MIR has allowed substantial study of these objects at the L, M, and N bands. In the MIR, an interferometer primarily observes emission from warm dust. Warm dust is pervasive near AGN cores and extends to multi-parsec

scales (Tristram et al. 2008). In nearly every case, the distribution of warm dust consists of two components, a disk-like small scale structure perpendicular to the system's axis, and a large-scale cone oriented along the system axis (Burtscher et al. 2016; Leftley et al. 2018). Although the extended component largely consists of cooler dust, it is responsible for a significant portion of the MIR emission (Asmus 2019). In the case of the well studied Circinus galaxy, the extended component is responsible for $\sim 80\%$ of the N-band emission (Tristram et al. 2007, 2014).

The pervasive appearance of two or more components in the MIR OI results for so many AGNs directly contradicts the standard model for AGN unification (Tristram et al. 2009; López-Gonzaga & Jaffe 2016). As discussed in section 1.3.1, the standard model for AGN unification assumes a single toroidal structure. The complications for the standard model increase when imaging results in the MIR are considered. MIR interferometry finds that the models required to fit OI data must differ significantly in covering factor of MIR dust, not just in line of sight angle (López-Gonzaga & Jaffe 2016). The uniqueness of extended components has also been seen in the MIR for other AGNs as well, where the shapes and sizes of of the AGNs are different even if the resolution of the observations are very similar (Burtscher et al. 2013). Said in Burtscher et al. (2016),

> "It seems not exaggerated to blame mid-IR interferometry for 'killing' the postulated AGN torus by dissecting it into a thin disk and a polar-elongated outflow, none of which are represented in the classical AGN torus cartoon."

In comparison to the numerous AGNs studied with OI in the MIR, very few objects have been observed in the NIR due to these objects being fainter and smaller in the NIR. Using their larger apertures, the KI and the VLTI have observed a few AGNs. Recently, the type-2 Seyfert NGC 1068 was imaged in the NIR with the GRAVITY instrument at VLTI (Gravity Collaboration et al. 2020a), although no other images in the NIR exist, yet. While observations in the MIR probed cool dust, in the NIR hot dust is the primary emitter. This hot dust $\sim$ 1200 to $1500K$ lies very near to the dust sublimation radius (Kishimoto et al. 2011).

Numerous observations have been conducted of NGC 4151 in the NIR with both the KI and the VLTI. The relatively short 85m baseline of the KI results in visibilities above 0.9 (Swain et al. 2003b; Kishimoto et al. 2009; Pott et al. 2010; Kishimoto et al. 2011; Burtscher et al. 2009). The VLTI observations with baselines up to 140m measures lower visibilities, yet still above 0.8 (Kishimoto et al. 2013b; Burtscher et al. 2009). These visibility measurements can generously be considered to indicate partial resolution of of the NIR emitting region. While these measurements can give an estimate for the overall size of the NIR emitting region, longer baselines are required to learn any more. Combining the interferometric measured size of NGC 4151 with infrared reverberation mapping has allowed for a very precise measurement of the distance to the AGN (Hönig et al. 2014).

While the quotation above suggests that OI is responsible for killing the idea of grand unification of AGN, it would be more appropriate to say that OI is responsible for changing the grand unification to a more accurate form. It seems naive to think that the original proponents of unification imagined that all AGNs have strictly identical geometries. Rather, that grand unification sets up a paradigm in which elements are refined as we learn the specifics of the environments around AGNs.

The overall picture developing from OI of AGNs suggests some refinements to the normal picture of AGN unification. In the original cartoon for AGN unification shown in figure 1.4 a large single torus is shown as the obscurer providing the absorbing medium which differentiates type-1 from type-2 AGN depending on the viewing angle. OI in the NIR and MIR indicates no such single structure, but a compact dusty disk in the plane of the UV emitting accretion disk at the AGN's core and a large diffuse cone formed by out-flowing dusty wind (Hönig 2019). This two component model without a single large obscuring torus is not a new idea and evidence for an optically thin outflow in the polar region has been seen in the extended narrow line region of both Seyfert type II NGC 1068 (Crenshaw & Kraemer 2000) and Seyfert type I NGC 4151 (Crenshaw et al. 2000) A new cartoon shown

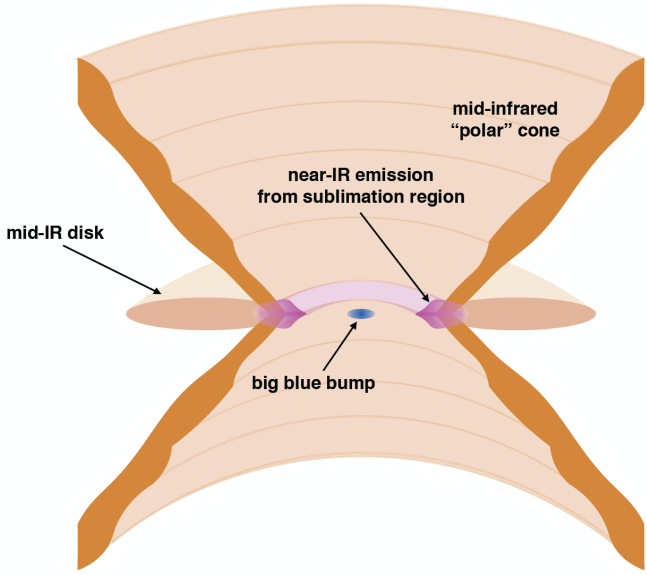

Figure 6.4 From Hönig (2019). New torus model assembled from interferometric studies of AGNs in the MIR and NIR

in figure 6.4 from Hönig (2019) provides a more accurate description of the torus than the original shown in figure 1.4.

The high visibilities measured for most AGNs, including for NGC 4151, with the KI and the VLTI in the NIR make it clear that longer baselines are required to more accurately constrain our understanding of the innermost regions of AGNs. Though challenging, the need for longer baselines drove the pursuit of such measurements with the longer baselines and smaller apertures which will be described in the coming chapters.

CHAPTER 7
THE CHARA ARRAY

7.1 An Overview of the CHARA Array

Located at the historic Mount Wilson Observatory just outside of Los Angeles, California, the Center for High Angular Resolution Astronomy (CHARA) Array is the highest angular resolution optical interferometer in the world (ten Brummelaar et al. 2005). Consisting of six 1-meter diameter telescopes, arranged in a Y-shape configuration with baselines ranging from 33 to 320 meters, and a number of beam combining instruments operating from the visible to the near-infrared, CHARA offers numerous options for the study of celestial objects. An overview of the CHARA Array can be seen in figure 7.1 with the array nestled amongst the historic telescopes on Mount Wilson.

In order for the light from each telescope to be combined at the science instrument, the light from each telescope is directed to the beam combination laboratory (BCL) as a 125mm diameter beam by a series of mirrors, shown in schematic form in figure 7.2. Once it reaches the lab, the light from each telescope goes through the optical path length equalization (OPLE) system. The OPLE system for each telescope consists of a series of fixed optical delay mirrors known as the Pipes of Pan (POPs), followed by a mobile delay system with 44 meters of travel.

After exiting the OPLE system, the beam is reduced from 125mm to 25mm by a beam reducing telescope (BRT) seen as M17 and M18 in figure 7.2. The secondary mirror of the BRT feeds the beam to a small deformable mirror (DM) by way of a beam splitter which sends some visible light to a Shack-Hartmann wave-front sensor. This DM/WFS combination which composes the laboratory-based AO (LABAO) system is followed by an optical switchyard which splits the visible and infrared light into two paths and allows the beam from any telescope to be fed to any beam combiner in the BCL.

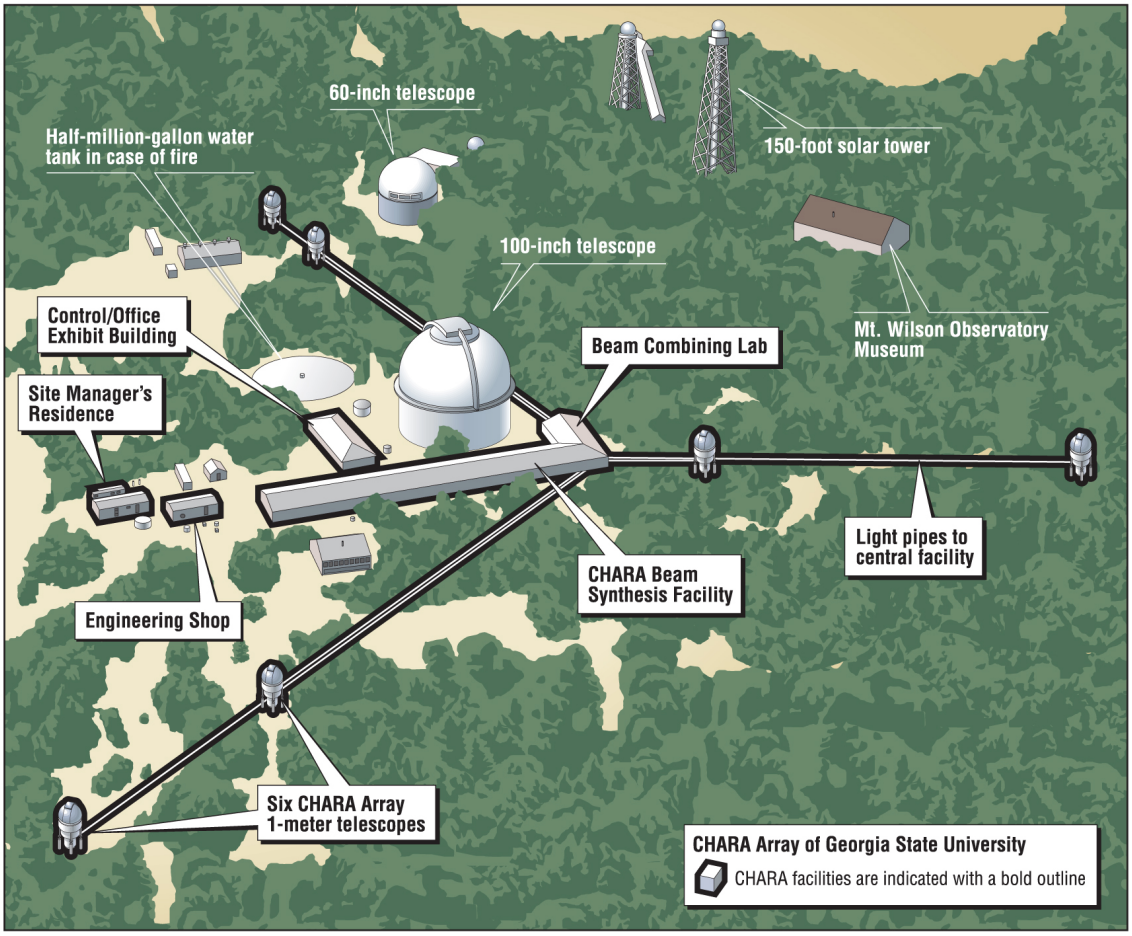

Figure 7.1 Schematic overview of the CHARA Array.

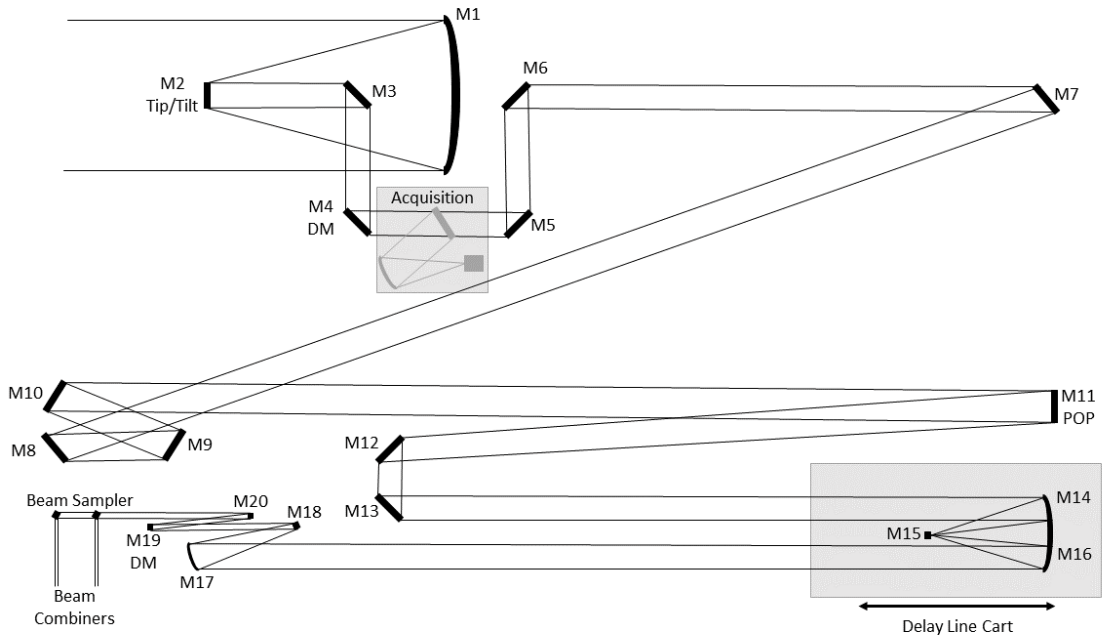

Figure 7.2 Schematic overview of the CHARA Array optical beam train for a single telescope.

7.2 The CLASSIC Beam Combiner

While there are numerous beam combiners available at CHARA, only one is suitable for AGNs due to the faintness of these objects. The CLASSIC Beam Combiner at CHARA combines the light from two telescopes in a very simple, yet efficient scheme (Ten Brummelaar et al. 2013). With only two telescope beams and its simple combination scheme, the CLASSIC beam combiner offers the greatest sensitivity available at CHARA.

The CLASSIC beam combiner is an open air pupil plane combiner. Combining the light from two telescopes, only fringe visibility is measured. Temporal modulation of the fringe occurs by dithering a mirror on one of the two beams with the dither synchronized with the camera readout rate. The basic optical layout of the optical combination used in the CLASSIC beam combiner is shown in figure 7.3.

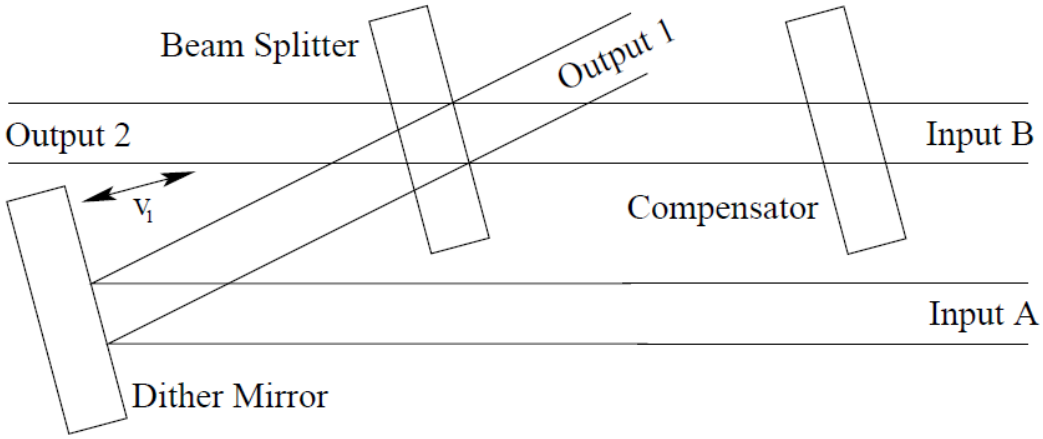

Figure 7.3 Schematic representation of the beam combination optics for the CLASSIC beam combiner. Figure from ten Brummelaar (2014).

7.3 The Adaptive Optics Program at CHARA

Strictly speaking, the technical aspects of the AO program at CHARA lie outside the purview of this thesis. However, the AO program as it has evolved has played a pivotal role in the successful observations to be presented in chapter 8, as such different parts of the program will be discussed and mentioned. To provide clarity, it is necessary to include an overview of the AO program at CHARA and outline those parts which have had an impact on the success of the observations discussed in this thesis.

AO is the process by which aberrations in the wavefront of a beam of light are corrected. It is important to note that the benefits of AO correction to the light gathered by the telescopes of an interferometer differ from those of a single large aperture imaging telescope (ten Brummelaar et al. 2012, 2018). The main benefit experienced by an interferometer using an AO system at each of its telescopes is the preservation of flux from the star or other object through the optical beam train. In plain words, the purpose of an AO system for an interferometer such as CHARA is to improve sensitivity.

At CHARA, there are two AO systems. The first system deployed was the previously mentioned LABAO system. The LABAO system unsurprisingly resides inside the beam

combination laboratory, its main job is to correct for noncommon path aberrations that arise in the hundreds of meters of optical train that exist between telescopes and the beam combiners. The LABAO has the additional job of maintaining the alignment of the optical beam train for each telescope with high precision. Consider the schematic of a CHARA telescope's beam train shown in figure 7.2. The LABAO system looks at a light, called the beacon, injected into the path of the science beam from the telescope at the Acquisition System between M4 and M5. Using the beacon light, the LABAO DM, which is M19 in figure 7.2, corrects for the wavefront errors the beam train develops between M5 and M19. While some of the path length between the beacon injection and the LABAO DM is under vacuum, up to 100 meters of the path length is through open air.

The second AO system at CHARA is the telescope AO (TAO) system. The TAO system acts as a traditional AO correcting the aberrations of the starlight caused by the atmosphere as well as any static aberration in the telescope optics. The TAO system consists of a large deformable mirror at the M4 position in figure 7.2 and the Telescope Wave-front Sensor (TWFS), a part of the Acquisition System shown in between M4 and M5. The TWFS consists primarily of a Shack-Hartmann lenslet array and an Andor EMCCD camera. While the wave-front correction provided by the TAO system represents the main drive behind the TAO part of the CHARA AO program, the TWFS system at each telescope itself is a valuable system upgrade even without a DM to complete the system.

Historically at CHARA, the tip-tilt control of the telescope secondary mirror (M2) was controlled by a CCD located in the BCL after an additional 4 reflections from the 21st reflection shown as the Beam Sampler in figure 7.2. Neglecting a couple of dichroics with two surfaces each, the original tip-tilt detector was after 25 reflections. This system performed very well for many years, but with a limiting magnitude of 10.0 in R-band always struggled with faint red objects. The TWFS system, which now controls the tip-tilt correction of the telescope secondary mirror, comes behind only 6 reflections. Coupled with the increased sensitivity provided by the Andor EMCCD camera used over the older HAWAII technology,

the limiting magnitude of the tip-tilt system has been improved to beyond 15th magnitude in R-band (Che et al. 2014).

Throughout the course of the research discussed in this thesis, various parts of the CHARA AO program have been completed. The current status of the LABAO, TWFS, and TAO subsystems of the CHARA AO program are listed in table 7.3. To date, all telescope LABAO systems are installed and seeing active use. Likewise, all telescope TWFS systems have been installed and are used for all NIR observation programs. Three telescopes, S1, S2, and W1, have or did have full TAO installed and actively in use at the time of the successful observations discussed in chapter 8. Three other TAO systems have been online at one point or another. Unfortunately, the DMs installed at E1, E2, and S1 developed instabilities that put the observations at risk and were removed. CHARA staff and the manufacturer of the DMs are currently working on servicing the troublesome DMs. The final DM was damaged during the installation process, it has subsequently been repaired twice, and damaged during the return shipment to CHARA twice, to the great consternation of all involved.

Table 7.1. CHARA AO Program Status at time of Observations.

Telescope	LABAO	TWFS	TAO
E1	Active	Active	Unavailable*
E2	Active	Active	Unavailable*
S1	Active	Active	Unavailable*
S2	Active	Active	Active
W1	Active	Active	Active
W2	Active	Active	Unavailable

Note. — * Represents a telescope where the TAO was available at one time. Ongoing issues with the reliability of these DMs resulted in this DM being removed to safeguard observing time. At the time of the finalization of this dissertation, all telescopes have fully functioning AO systems, except for W2.

CHAPTER 8
AGN OBSERVATIONS AT CHARA

NGC 4151 is the brightest Seyfert type 1 AGN seen from Earth. As an extended object the listed K-band magnitude of 7.4 (Skrutskie et al. 2006) is somewhat misleading as the AGN core has a K-band magnitude of 8.5 according to the 2MASS Point Source Catalog (Cutri et al. 2003) which at the very least must be taken with a grain of salt as AGNs are variable.

The most sensitive instrument at the CHARA array is the CLASSIC beam combiner described in section 7.2. The combiner has a listed best performance K-band magnitude limit of 8.5. Making observing even the brightest AGNs a challenge, at best. In order to make observing of NGC 4151 or fainter AGNs practical, full adaptive optics is all but required, as such all observation attempts have been paired with AO engineering on which I have been working.

8.1 Observing Strategies

Because of the difficulty posed by observing so near the faint limit of CHARA, a number of observing strategies were developed and tested during my observations of NGC 4151. These strategies would evolve as the implementation of Adaptive Optics at each of the CHARA telescopes progressed. In this section, the three main observing strategies used will be described.

8.1.1 General Observing

In order to eliminate systematic problems with visibility measurement at CHARA, be they due to alignment, instrumental, or atmospheric issues, targets are usually observed in sequence with stars of known sizes, called calibrators. These sequences are known as observing brackets. An observing bracket usually consists of a data recording done on a calibrator star, followed by the data recording on the object of interest, followed by a data recording done on another calibrator star. Some observers use multiple calibrators both before and after

the object of interest. These brackets are recorded at the same camera settings as the object of interest and without any instrumental alignments conducted. With data of objects with known sizes and therefore visibilities, the visibility data recorded on the object of interest can be calibrated. Throughout the observations described here, brackets of calibrator 1 - object of interest - calibrator 2 (Cal-Obj-Cal) were used.

8.1.2 CLASSIC Observing in Four Pixel Mode

Under normal observing with the CLASSIC Beam Combiner, the light from each telescope is aligned so that Airy disk lies centered on a single pixel on the detector. The data collected would include the measurement of flux on this single pixel only. For faint objects, a mode was added to the CLASSIC software in which the system would measure the flux on a two-by-two pixel area. In this mode, the airy disk of an object would lie centered on the center of the two by two pixel readout area.

8.1.3 Blind Recording with CLASSIC

For the NGC 4151 program, the calibrator stars and the target AGN lie so close together in the sky, that the fringe is expected to lie within the same scan window of the CLASSIC beam combiner. Therefore, by recording data on the target in the same place as the fringe was seen with the calibrator, the observer can be relatively sure that the fringe would be present if enough flux is incident at the beam combiner's detector. This strategy requires measuring the speed of the delay offset and manually compensating for it by manually moving the delay line an appropriate distance every few minutes.

8.1.4 Fringe Spoofing with CLASSIC

A major difficulty with using the CLASSIC beam combiner is the relatively old computer system used to run the detector. Due to sequencing and depending on the camera settings, it can take anywhere from twenty seconds to a minute for the software and camera to be

ready to record. During this delay and another delay due to the shutter sequence, the fringe of a faint object can easily wander out of the scan window. To mitigate this, the following procedure is followed.

1. With the system pointed at the target object, but not locked onto the AO/tip-tilt system, start a CLASSIC data recording sequence. This locks the file name for the data file.

2. Slew the telescopes to a calibrator of similar, yet brighter, brightness to the target object and lock it on the AO/tip-tilt system.

3. Locate the fringe position on the calibrator, this should be much easier than finding it on the target object.

4. With the known fringe position in hand, slew the telescopes back to the target object and lock it on the AO/tip-tilt system as fast as possible.

5. If the slew is fast enough, and the objects are close enough in the sky, the fringe will appear in the scan window just below the fringe seen on the calibrator.

6. Begin saving data.

To date, this has been the only consistently successful strategy for recording fringe data on NGC 4151. Strictly speaking, this is not a novel observing strategy.

8.2 Overview of Observations

Along with the science object are a fairly bright star for alignment of the near infrared camera system at the end of the CLASSIC beam combiner, which also happens to be a good star for locating the fringe offset for the OPLE system. Additionally, there are a number of calibrator stars. These stars are meant to provide a calibration of the beam combiner and are chosen to be unresolved and of similar brightness to the science object. Table 8.2

shows information about the target NGC 4151, along with the calibrators SAO 62878, HD 105881, and TYC 3017-1666-1, and the alignment star HD 105663, including each object's brightness in V, R, and K magnitudes..

Table 8.1. Object List for Observations at CHARA.

Common ID	Purpose	CHARA No.	2MASS ID	RA	Dec.	V_{mag}	R_{mag}	K_{mag}
NGC 4151	Target	CN 320097	2MASS J12103258+3924210	12 10 32.0577	+39 24 21.0578	11.5	11.6	7.38
HD 105663	Alignment	CN 147983	2MASS J12095369+3926004	12 09 53.7087	+39 26 00.6349	8.2	7.5	4.1
SAO 62878	Calibrator	CN 148118	2MASS J12104360+3919251	12 10 43.5867	+39 19 25.0187	***	10.4	8.31
TYC 3017-1666-1	Calibrator	CN 320264	2MASS J12111971+3914148	12 11 19.7097	+39 14 14.9018	11.57	11.0	8.71
HD 105881	Calibrator	CN 148184	2MASS J12110971+3907488	12 09.7168	+39 07 48.7151	8.0	7.8	6.98

Note. — Right ascension (RA) and declination are given in IRCS J2000 coordinates from Gaia Collaboration (2018). Unless otherwise noted, all object information was accessed through the SIMBAD database, operated at CDS, Strasbourg, France (Wenger et al. 2000). The CHARA No. is an object identification number that exists inside the CHARA computer network.

As a part of the general observing strategy used at CHARA, the alignment star and calibrators are chosen to be as close to the science object as possible. For NGC 4151 the alignment star HD 105663 and both calibrators SAO 62878 and TYC 3017-1666-1 can all be found in the same field on each telescopes' finder telescope as the AGN itself as shown in Figure 8.1 and the other calibrator, HD 105881, lies just off the bottom of the image.

Since the inception of the CHARA Array, AGN science has been considered a goal. Because of the growing importance of optical interferometry in extragalactic astronomy, I have been quite successful in being awarded observing time to attempt observations of NGC 4151 at CHARA. Table 8.2 lists all observational time awarded for attempting observations of NGC 4151 since 2016. This list includes time awarded to me personally, as well as a number of awards to Makoto Kishimoto of Kyoto Sangyo University. These awards include time given in trade for funding provided for upgrades to the CHARA telescope acquisition and finder telescope systems, as well as time awarded through the NOIR Labs Open access program. The time awarded to Makoto Kishimoto serves as an indicator of the importance of AGN observations as viewed by NOIR Labs and CHARA, as well as demonstrating the difficulty in AGN programs at CHARA. Additionally, as the local faint object expert, and steward of the telescope AO system at CHARA, I personally conducted these observations.

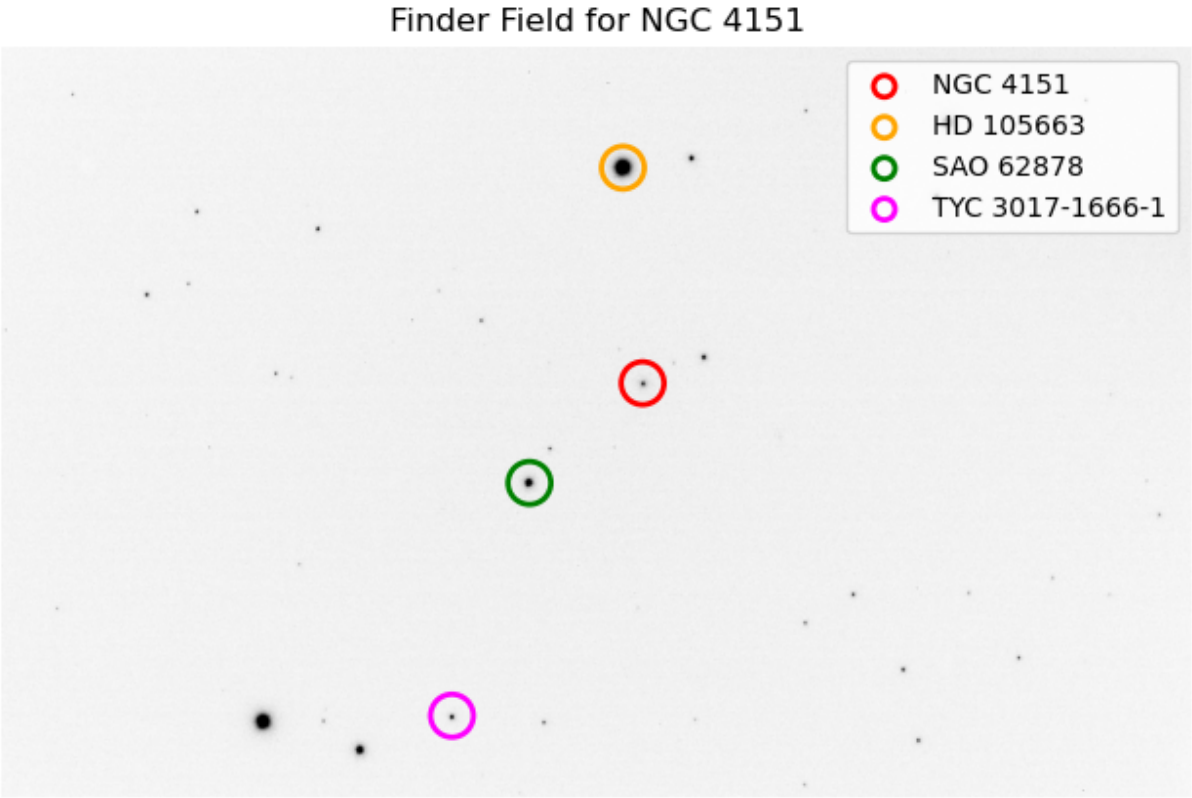

Figure 8.1 Finder telescope view of NGC 4151, the alignment star, and calibrators. All of these objects falling within the same finder field shows just how close together these objects are in the sky. The finder field is 27 by 43 arc-minutes.

Table 8.2. Overview of AGN Observations at CHARA.

Observing Semester	Dates	Program Title	# Nights
2016	May 29 - 31	On-Sky Adaptive Optics Test Observing of NGC 4151	3
2017A	Mar 28 - 3	On-Sky Adaptive Optics Test Observing of NGC 4151	7
2017A*	May 9 - 10	Scrutinizing AGN thermal Emission at the Highest Spatial Resolution	2
2017B*	Sep 2 - 4	Resolving the nature of the AGN Torus	1.5
2018A	Mar 28 - 31	On-Sky Adaptive Optics Test Observing of NGC 4151	3
2018A*	Apr 16 - 19	AGN Accretion Structure beyond Milli-arcsecond resolution	4
2018B*	Sep 1 - 4	NGC 4154 and NGC 1068 with CHARA	2
2019A*	Feb 27 - Mar 3	AGN Torus: Dissecting the Dusty Wind Launching Region	2.5
2019A	Mar 15 - 21	On-sky Adaptive Optics Testing on NGC 4151	7
2019B†	Oct 28 - Nov 2	Full Adaptive Optics Testing: Observing NGC 1068 AGN Torus	5
2020	Feb 15 - 16	Shutdown Observing of NGC 4151	2

Table 8.2 (cont'd)

Observing Semester	Dates	Program Title	# Nights
2020A	Mar 25 - 31	On-sky Adaptive Optics Testing on NGC4151	6
2021A	Mar 16 - 22	On-sky Adaptive Optics Testing on NGC4151	7
2021A	Apr 24 - 28	AGN Torus: Dissecting the Dusty Wind Launching Region	2
2021A	Apr 29	Supplementary Time	1
		Number of Observing Nights[A] :	55
		Number of Calendar Nights[B]:	66

Note. — * denotes program where Makoto Kishimoto was P.I. for which I handled the observing and data taking attempts. † denotes a combined/joint program.[A] Observing nights are defined by total amount of night-time awarded. [B] Calendar nights are defined as the individual date on which any observing time was awarded. For example, a night on which half the night was awarded contributes 0.5 nights to the number of observing nights, but 1.0 nights to the number of calendar nights.

In the following sections, each program awarded observing time for which NGC 4151 was noted as a probable target is summarized. Important events, observing strategies, AO system status updates, and notes are given with each program synopsized in table form. Each of the 66 calendar dates of awarded observing time is given a classification based on the observing activities or lack there of.

- Attempt: An attempt to observe NGC 4151 occurred. The array was pointed at the AGN and fringe searching occurred. Data may or may not have been recorded.
- Conditions: Seeing conditions prohibited faint object observing. Usually wind or jet-stream related.
- Engineering: The majority of the night was spent on AO related engineering tasks. This may have been due to technical issues that interfered with an observation attempt, weather conditions were un-conducive to observing faint objects, or engineering tasks required completion before observing could occur.
- Other: In all cases, the program description lists NGC 4151 as a potential target, but was not observed that night.
- Weather: The weather conditions did not allow observing. Humidity, clouds, precipitation, and smoke/ash are all examples of weather conditions requiring closure.

8.2.1 2016 Observing: May 29 - 31

During the first half of 2016, 3 nights were awarded. This program coupled AO testing with observations of the AGN 4151. Although each night during this run has been classified as lost to weather conditions, some observations were attempted. Largely, each night was effectively lost due to high wind conditions.

At this time, the CLASSIC data recording process relied on dark frames taken with the shutters closed in the BCL. With warm shutters and such a faint target, the camera sees more

Table 8.3. 2016 CHARA Observing Nightly Synopsis.

Date	Notes	
2016/05/29	Attempts made on NGC 4151. High wind ended night early.	Weather
2016/05/30	Poor seeing with high wind.	Weather
2016/05/31	High wind prevented observing.	Weather

counts in K-band from the shutters than from the object, making fringe tracking during a data recording sequence nearly impossible. These observations were attempted using 4-pixel mode on the NIRO camera using the nondestructive readout mode with a speed of 500 Hz and a medium length dither.

This observing program occurred before the installation of the TWFS systems, as such, tip-tilt control of the telescopes was accomplished via the old tip-tilt system in the BCL. In visible wavelengths the target is right at the limit for the old system. To keep the target locked, the tip-tilt camera had to be run very slowly on the order of 5-10 Hz.

8.2.2 2017A Observing: Mar 28 - Apr 03

In the first half of the 2017 observing year, 7 days were awarded for joint AO testing and observations of NGC 4151. At the beginning of this observing run, the TWFS systems were installed at the S1 and S2 telescopes. Using the TWFS camera for tip-tilt has the benefit of far fewer reflections when compared to the lab-based tip-tilt system. Much of this run was dedicated to learning how to align and optimize the TWFS tip-tilt procedure for general use, as well as for faint objects.

During this run, TWFS camera settings for NGC 4151 were found that gave satisfactory performance of the tip-tilt system using the TWFS for control. This is fortunate as the tip-tilt system in the BCL failed and was unusable. It was also during this run that a decoupling

Table 8.4. 2017A CHARA Observing Nightly Synopsis.

Date	Notes	Classification
2017/03/28	Night spent on AO system alignments and TWFS parameter tuning. Lab tip-tilt system offline. No data recorded.	Engineering
2017/03/29	TWFS tuning, tip-tilt tests and software trouble. Poor seeing. Fringes not located.	Engineering
2017/03/30	High winds prevented observing.	Weather
2017/03/31	Observing attempted with lab tip-tilt. Balance of the night spent on software troubleshooting. Seeing too poor for AGN.	Engineering
2017/04/01	Software/hardware issues with AOB dominate. Not enough counts on NIRO with AGN.	Engineering
2017/04/02	AOB troubleshooting. TWFS tip-tilt testing. Not enough counts on NIRO with AGN.	Engineering
2017/04/03	TWFS tip-tilt testing and camera settings tuning. Poor seeing conditions.	Engineering

of the starlight from the beacon light sent to the lab was first observed. This would lead to the development of many automatic alignment routines and schemes.

8.2.3 2017A Observing: May 09 - 10*

Also in the first half of the 2017 observing year, two nights were awarded to Makoto Kishimoto attempting AGN, including NGC 4151. Unfortunately, poor weather and technical problems resulted in no data being recorded.

Table 8.5. 2017A^* CHARA Observing Nightly Synopsis.

Date	Notes	Classification
2017/05/09	High humidity and fog. No observing.	Weather
2017/05/10	High humidity for the first part of the night. Second part of the night lost to tip-tilt trouble.	Weather

Table 8.6. 2017B^* CHARA Observing Nightly Synopsis.

Date	Notes	Classification
2017/09/02	Closed due to smoke and ash.	Weather
2017/09/03	Fog and rain gave way to high humidity.	Weather
2017/09/04	High humidity for most of the night. A brief observing attempt made, but TWFS tip-tilt did not lock object.	Weather

8.2.4 2017B^* Observing: Sep 02 - 04

Another AGN program for Makoto Kishimoto, this one during the second half of the observing year. This program was awarded three half-nights during which this program was the second half of the night, allowing for the possibility of observing NGC 4151 near dawn. Poor weather conditions and a nearby wildfire kept the telescopes closed. The final night allowed for an observing attempt on NGC 1068, but the TWFS tip-tilt system refused to consistently hold the object. NGC 4151 was not observed.

8.2.5 2018A Observing: Mar 29 - 31

Three nights awarded for joint AO testing and observations of NGC 4151. The first night of this run was dedicated to continued troubleshooting of the TWFS tip-tilt system. with a

Table 8.7. 2018A CHARA Observing Nightly Synopsis.

Date	Notes	Classification
2018/03/29	First half: TWFS tip-tilt tests. Second half: Observing with lab tip-tilt. Lab tip-tilt could not lock faint objects consistently.	Engineering
2018/03/30	Continuous high thin clouds prevent observing AGN. Data recorded on the bright calibrator. Offsets tracked.	Weather
2018/03/31	A solid cloud layer kept the telescopes closed.	Weather

brief attempt at the AGN with the lab tip-tilt system near dawn. During the second night, the TWFS tip-tilt systems behaved well, but a bright moon and a layer of high, thin clouds made observing NGC 4151 impossible. The final night brought high humidity and cloud cover, no observing occurred.

8.2.6 2018A Observing: Apr 16 - 19*

During the first half of the 2018 observing year, four half-nights were awarded to Makoto Kishimoto to observe AGNs. Weather consumed much of the four calendar nights. The second night was moderately successful despite technical issues, but NGC 4151 was not observed. The third night ended early due to high humidity, but an attempt was made at NGC 4151.

8.2.7 2018B Observing: Sep 01 - 04*

Four half-nights were awarded to Makoto Kishimoto for observing AGN, including the option to look at NGC 4151. Trouble with getting the TWFS tip-tilt system to lock and hold faint objects under a thin sheet of clouds pushed much of the night to engineering tests. The rest of the run went smoothly with multiple attempts being made on NGC 1068, but NGC 4151 was not observed.

Table 8.8. 2018A^* CHARA Observing Nightly Synopsis.

Date	Notes	Classification
2018/04/16	Clouds, high humidity, and high winds. No observing.	Weather
2018/04/17	Second half-program. Decent observing. Did not observe NGC 4151.	Other
2018/04/18	Humidity and fog shut observing down early. First data recorded with telescope tip-tilt.	Weather
2018/04/19	High winds and humidity. No observing.	Weather

Table 8.9. 2018B^* CHARA Observing Nightly Synopsis.

Date	Notes	Classification
2018/09/01	TWFS tip-tilt troubleshooting dominated.	Engineering
2018/09/02	Night dedicated to attempts on NGC 1068.	Other
2018/09/03	Night dedicated to NGC 1068. TWFS tip-tilt troubleshooting.	Other
2018/09/04	Night dedicated to NGC 1068. TWFS tip-tilt troubleshooting.	Other

8.2.8 2019A Observing: Mar 15 - 21

During the first half of the 2019 observing year, seven nights were awarded for AO testing and AGN observations during the annual CHARA meeting where I was responsible for running the array so that the observing staff had the option to attend the annual meeting which was held at Lowell Observatory this year. The final three nights of the observing run were lost to wet conditions including snow.

The first four nights of the run were dedicated to engineering time. The telescope DMs had arrived just two months ahead of this run. Eager for fringes with full AO, the first two nights of the run were dedicated to getting the DMs installed at the S1 and S2 telescopes. Installation and flattening of the DMs was successful.

Unfortunately, the dome drive for S1 burned out thwarting the hopes of the first fringes with AO. Despite having the full AO ready on S1 and S2, the loss of S1's dome meant shifting gears. The third and fourth nights of the run saw observing attempts with the S2 and E2 telescopes, but increasingly poor weather and a technical problem with the OPLE system meant fringes were never found.

8.2.9 2019A* Observing: Feb 27 - Mar 03

Five second-half-nights were awarded to Makoto Kishimoto during the first half of the 2019 observing year for AGN observations. High humidity kept the telescopes closed for nearly all of the 5 calendar nights. A brief opening on the second night saw an attempt at NGC 4151, but never progressed past getting the target locked with the TWFS tip-tilt system.

8.2.10 2019B† Observing: Oct 28 - Nov 02

During the second half of the 2019 observing year, my personal proposal and Makoto Kishimoto's proposal were jointly awarded 5 full nights of telescope time over 2 second half-nights and four full nights. Although there were some weather-related slowdowns and technical hiccups, this run was the first time where the full AO systems at the S1, S2, E1, and E2

Table 8.10. 2019A CHARA Observing Nightly Synopsis.

Date	Notes	Classification
2019/03/15	High winds. Night spent working on S2 DM installation and associated alignments.	Engineering
2019/03/16	Night spent getting S1 and S2 TAO systems online and on sky.	Engineering
2019/03/17	S1 dome is offline. Attempt made with S2-E1. Fringes never found, poor seeing.	Engineering
2019/03/18	S1 dome still offline. Attempt made with S2-E1. Fringes never found, poor seeing.	Engineering
2019/03/19	High humidity, fog, and rain. No observing.	Weather
2019/03/20	High humidity, fog, and snow! No observing.	Weather
2019/03/21	Fog cleared after sunset. Humidity persisted all night. No observing.	Weather

Table 8.11. 2019A^* CHARA Observing Nightly Synopsis.

Date	Notes	Classification
2019/02/27	Clouds, fog, high humidity, and eventually rain. No observing.	Weather
2019/02/28	AGN was locked with TWFS tip-tilt. Clouds prevented anything further.	Weather
2019/03/01	Clouds and high humidity gave way to heavy rain by 2 a.m. No observing.	Weather
2019/03/02	High humidity and heavy fog kept the telescopes closed all night. No observing.	Weather
2019/03/03	Fog cleared out around 1 a.m. but the high humidity remained. No observing.	Weather

Table 8.12. 2019$B^{\dagger}$ CHARA Observing Nightly Synopsis.

Date	Notes	
2019/10/28	Poor seeing for faint objects.	Conditions
2019/10/29	High wind delay, followed by poor seeing. No AGN observations.	Conditions
2019/10/30	Time lost to TWFS tip-tilt troubles. Blind record complete on NGC 1068. No fringe seen on AGN. High winds closed us early.	Conditions
2019/10/31	Smooth night technically. Blind data recorded on NGC 1068 and NGC 4151 No evidence of fringes seen.	Attempt
2019/11/01	Fringes found and recorded on calibrators down to $K_{mag} = 8.5$ with full AO. Blind data recorded on NGC 1068 and NGC 4151. No evidence of fringes was seen.	Attempt
2019/11/02	Calibrator data recorded down to $K_{mag} = 9.4$! Blind data recorded on NGC 4151. No evidence of fringes seen.	Attempt

telescopes ran smoothly. This run saw attempts made on NGC 1068, Mrk 509, Mrk 6, and NGC 4151. While no evidence of fringes was seen, several blind data sets were recorded.

One event worth a special note occurred on the sixth night of the run (2019/11/02) fringes were recorded on a calibrator of Kmag = 9.4 with full AO. The previous best performance of the CLASSIC beam combiner was at Kmag=8.5, showing that the AO system offered a best case improvement of nearly one full magnitude, in line with theory.

No evidence of fringes on NGC 4151 were seen during this run. Despite this, six brackets of data were recorded on the object under the blind recording procedure discussed in section 8.1.3.

Table 8.13. 2020 Supplementary CHARA Observing Nightly Synopsis.

Date	Notes	Classification
2020/02/15	AO testing. NGC 4151 and calibrators recorded. Possible fringe detection of poor quality.	Attempt
2020/02/16	More AO testing in more difficult conditions. Data recorded on a calibrator and NGC 4151.	Attempt

8.2.11 2020 Supplementary Observing: Feb 15 -16

As a staff member on site at the CHARA Array, I was able to sneak in two nights of preseason observing during the 2020 winter shutdown. Data was recorded during both nights on NGC 4151 where fringes were visible using the S1 and S2 telescopes with full AO. Fringe quality was noted as being questionable. So close to the detection limit, the fringes on the target cannot be servo-ed and must be tracked by eye. The second of the two nights was ended quite early by high winds. This observing run resulted in two brackets of data.

8.2.12 2020A Observing: Mar 25 - 31

Six nights were awarded for attempts on NGC 4151 and AO testing during the first half of 2020. Unfortunately, March is typically wet at Mount Wilson and high humidity, fog, rain, and snow kept the telescopes closed for the duration of this run. No observing occurred.

8.2.13 2021A Observing: Mar 16 - 22

During the first half of 2021, seven full nights were awarded for continued AO testing and observing of NGC 4151. During the 2020 calendar year, in the midst of the COVID 19 pandemic, actuator issues arose with the DMs at the S1, E1, and E2 telescopes. With limited staff on-site and a desire to preserve observing time, the troublesome DMs were removed. With the full AO available only at the S2 and W2 telescopes, they were used

Table 8.14. 2020A CHARA Observing Nightly Synopsis.

Date	Notes	Classification
2020/03/25	High humidity, fog, and a dusting of snow. No observing.	Weather
2020/03/26	High humidity, fog, and snow flurries. No observing.	Weather
2020/03/27	High humidity and fog. No observing.	Weather
2020/03/28	High humidity and fog. No observing.	Weather
2020/03/29	High humidity and light rain. No observing.	Weather
2020/03/30	High humidity and fog. No observing.	Weather
2020/03/31	High humidity and fog. No observing.	Weather

Table 8.15. 2021A CHARA Observing Nightly Synopsis.

Date	Notes	Classification
2021/03/16	High humidity most of the night. TWFS settings confirmed on target.	Weather
2021/03/17	High humidity and cloud cover. No observing.	Weather
2021/03/18	A few technical issues ate a lot of time. A single bracket recorded on NGC 4151, with possible fringe detection.	Attempt
2021/03/19	High humidity to start, then heavy fog. No observing.	Weather
2021/03/20	High humidity until the end of the night. Opened briefly near dawn.	Weather
2021/03/21	Gusty winds and jet stream made fringe detection on bright objects very difficult. Fringes not found on faint calibrators. No data taken.	Weather
2021/03/22	High humidity all night. No observing.	Weather

exclusively for this run. While poor weather conditions made observing impossible for most of this run, one night was suitable for observing. During the third night, a single dataset was recorded on NGC 4151 with a possible fringe detection. Unfortunately, a power glitch took the OPLE system and some network components offline shutting down observing for the night. During this observing run, a single bracket of data was recorded on NGC 4151 was recorded.

8.2.14 2021A Observing: Apr 24 - 28*

Five first half-nights awarded to Makoto Kishimoto for AGN observations in the first half of 2021. The first night saw poor seeing, but a single bracket of data on NGC 4151 was recorded

Table 8.16. 2021A^* CHARA Observing Nightly Synopsis.

Date	Notes	Classification
2021/04/24	Rising humidity. Observing Attempted. Blind data taken on NGC4151 and calibrators. No evidence of fringe.	Attempt
2021/04/25	Fog, drizzle, and snow. No observing.	Weather
2021/04/26	High humidity and clouds. No observing.	Weather
2021/04/27	High humidity turned to high winds. Looked at the alignment star during a short opening.	Weather
2021/04/28	Poor seeing conditions made fringes unstable. Some blind data taken on NGC 4151 and calibrators. No evidence of fringe.	Attempt

blindly. The subsequent three nights saw high humidity, rain, and snow. The final night of the observing run was suitable for observing, but poor seeing made the fringes unstable for bright objects. Despite poor seeing, two brackets were recorded on NGC 4151 using the fringe spoofing strategy of section 8.1.4, though the object's fringe was never seen. During this run, three brackets of data were recorded on NGC 4151.

8.2.15 2021A Supplementary Observing: Apr 29

An unused night scheduled for OPLE engineering allowed me to observe NGC 4151 for an additional night. This proved to be quite fruitful as this additional night had some of the best seeing I have observed under at CHARA. With great seeing and fully functioning telescope AO, the fringes of the faint calibrators were quite easy to record. The fringe on NGC 4151 was even quite obvious and could easily be tracked by eye in the waterfall plot (See section 9.3.6 for details and figures). Four brackets were recorded using the fringe spoofing

Table 8.17. 2021A Supplementary CHARA Observing Nightly Synopsis.

Date	Notes	Classification
2021/04/29	Exceptional seeing conditions allow for several brackets on NGC4151 to be recorded. Very strong fringe evidence!!!!	Attempt

Table 8.18. Observation Classification Summary.

Classification	#	% of Calendar Nights
Attempt	9	13.6
Conditions	3	4.5
Engineering	12	18.2
Other	4	6.1
Weather	38	57.6

technique of section 8.1.4 with varying degrees of fringe obvious in the data. During this single night, four brackets of data on NGC 4151 were recorded.

8.3 Success of Observations

To summarize the preceding sections. Since 2016, the CHARA Array has dedicated part of 66 calendar nights, or 55 total observing nights, to attempting observations of NGC 4151. The breakdown for each calendar night's classification is shown in Table 8.18, where it is clear that the weather has been the biggest obstacle to successful observations. Anyone who has observed at the CHARA Array in the early spring time will not be surprised by the fact that over 57% of awarded observing time was lost to the weather.

Despite battling the weather at the height of the southern California rainy season and the many technical hurdles involved in getting the AO systems online, a number of bracket's worth of data has been recorded on NGC 4151 at CHARA. In all, 55 nights of telescope

observing time allocated have resulted in 16 data sets on this AGN. Unfortunately, simply recording data does not guarantee a fringe will appear in the data. On top of that, even a data set in which a fringe appears does not guarantee a usable data point. So near the faint limit of the CLASSIC beam combiner's detector, even the best data sets on NGC 4151 offer serious challenges regarding the data reduction and visibility calibration.

CHAPTER 9
CHARA DATA REDUCTION

9.1 Introduction

Out of the 66 calendar nights of observing awarded to observing NGC 4151 only nine nights ended up with observations of the target object. These nine nights result in a total of 16 Cal-Obj-(Cal) brackets of data being recorded. To see if any of the data contains valuable information, the visibility measurements for the AGN must be extracted from these data. This chapter contains the data reduction done for each of the data files taken during the observations at CHARA.

There are two primary steps for extracting visibilities from data recorded at CHARA with the CLASSIC beam combiner. First, the visibilities must be calculated from each recording. Then, the visibilities measured on the science target must be calibrated against the visibilities measured on so-called calibrator objects.

9.2 CLASSIC Data Reduction Procedure

Data recorded with the CLASSIC beam combiner at CHARA is most often reduced using the pipeline written by Theo ten Brummelaar (ten Brummelaar 2014) with a number of updates provided by Gail Schaefer (Schaefer 2019) named REDFLUOR. The pipeline is equipped with many options to provide the best reduction of CLASSIC data depending on the circumstances of the objects being observed. Due to the faintness of NGC 4151, a relatively specific set of options are chosen for reducing the data recorded on it. In this section, the general reduction procedure will be described with emphasis on the options most appropriate to reducing the faint AGN data.

The complete list of options for the REDFLUOR data reduction pipeline are:

```
    Flags:
-a        Toggle apodize for FFT (ON)
-A        Use shutter sequence A for noise (TRUE)
-b        Bootstrap to estimate the Median Error (OFF)
-c        Force this to be treated as CLASSIC data (OFF)
-d[0,1,2,3,4]    Set display level(1)
-D[Dir]        Directory for results (Basename)
-e        Toggle edit scans (ON)
-E[min_weight]    Edit scans by fringe weight (OFF)
-f        Force this to be treated as JOUFLU data (OFF)
-F[env_mult]    Change # of envelopes to include (3)
-g              Use mean photometry to normalize signal (OFF)
-h        Print this message
-H[n]        Set percentage definition of high frequency (20)
        Use 0.0 to force using upper integration limit.
-i        Toggle manual integration range (OFF)
-I[start-stop]    Set integration range of data (AUTO)
-j        Toggle adjusting filter width using Vg (ON)
-J        Toggle ignoring photometric data (OFF)
-k[0,1]    Set method of calculating Kappa (KAPPA_BY_SCAN)
            0 - Calculate for each scan.
            1 - Calculate for total mean.
-l[freq-fwhm] Use low pass instead of Wiener filter (0).
-L        Toggle use photometry for noise estimate (OFF)correct
-m        Toggle compute V2 from weighted mean power spectrum (ON)
-M        Use weighted mean (ON)
-n        Use new data sequence for Fluor (OFF)
-N        Toggle correct PS for linear slope after noise subtraction (ON)
-O        Toggle Photometry Only (OFF)
-o[n_sigma]    Number (float) of standard deviations for outlier removal (OFF, <=0 to turn off)
-p        Toggle use postscript (OFF)
-P[smooth_noise_size]    Change noise PS +-smooth size (5)
-q        Toggle ignore off star data (OFF)
-Q        K band shutter background percentage (3.63%)
-R        Toggle remote mode (OFF)
-s[spec-chan]    Change spectral channel (0=ALL)
-S[smooth_signal_size]    Change +-smooth size (1)
-t[start,stop]    Truncate scans (OFF)
-u        Toggle noise PS multiplier (OFF)
-U[freq]    Set DC suppression frequency (20.0 Hz)
-v        Toggle PLPLOT verbose mode (OFF)
-V        Toggle REDFLUOR verbose mode (OFF)
-x        Toggle use dither freq for fringes (OFF)
-X[stddevmult]    Set stddev multiplier (0)
-y        Toggle use fringe signal for waterfall (OFF)
-Y        Toggle use filter for waterfall (ON)
-z[pixmult]    Set pixel multiplier (2)
-Z        Toggle mean PS for noise estimate (ON)
```

Most of the available options remain at their default settings with relatively few being used during any single data reduction. A few of these options are essential to reducing data taken on faint objects. These important options will often be used in the reduction of the data taken on NGC 4151 in the coming sections.

REDFLUOR options which are often changed from their defaults:

- -e Skip fringe editing. Often the raw waterfall plot used for fringe editing shows no evidence of the fringe on the faint object. This is considered observing blind and no scan edits will be done, except in a few cases.
- -d1 Set display level 1. This shows relatively few plots. Again, due to the faint object, many plots that REDFLUOR displays are of little help so the minimum number of plots are displayed.
- -g Use mean photometry to normalize signal.
- -I Manually set the integration range where the fringe is expected. The integration range is found using the calibrator and then maintained at the fixed range for the whole observing bracket. By default, the integration range is set by fitting a Gaussian to the fringe envelope which does not reliably work for faint objects.
- -U Set the DC suppression frequency. This option alters where the system cuts off the data for noise estimation. This value is sometimes moved from its default to have more noise available for the noise calculation where it is appropriate.
- -S Signal smoothing.
- -P Noise smoothing in the power spectra.

REDFLUOR options which are intentionally left in their default state:

- -Z Use the mean Power Spectra for noise estimate is left on.
- -m Calculated V2 from the weighted mean power spectrum is left on. This option is critical as often the fringe of the faint science object is only seen in the mean power spectrum.
- -q Ignore star data is left off. This means that REDFLUOR will use the off-star data for noise subtraction. This is critical as the warm shutters inside the BCL emit more photons in the K-band than will be received by the camera from the AGN.

9.2.1 The General Reduction for CLASSIC Data

As an example of the general data reduction process for CLASSIC data, the data reduction process for the calibrator SAO 62878 observed on March 30, 2021 will be shown and explained here.

The REDFLUOR program is invoked from a command line environment with relevant flags as:

```
redfluor -dev xwin -D... -d1 -e -g -I38.0-59.0 -o3.0 -U15.0 -S10.0 -P10.0 2021_04_30_SAO_62878_ird_002.fit
```

In which the -D... sets the output directory where the reduced data is stored, the -d1 sets the minimum number of plots to be displayed, the -e skips the scan editing phase, the -I38.0-59.0 sets the fringe integration range to 38.0 to 59.0 Hertz, the -o3.0 sets the outlier rejection at 3.0σ, the -U15.0 sets the DC noise suppression to 15.0 Hertz, the -S10.0 sets the signal smoothing weight to 10.0, the -P10.0 sets the power spectrum noise smoothing weight to 10.0. The last part of the invocation is simply the input file name.

In this case, the program begins by displaying plots of the photometry of the data. First as raw data showing in figure 9.2 and then with the background subtracted as in figure 9.3. In both of these plots, the flux measured by the camera is displayed on the Y-axis and the scan number through the data set on the X-axis. The vertical red lines in the plot area denote different parts of the data sequence. The first three lines denote the ends of the initial shutter sequence taken to provide a background estimate which is used to provide real-time feedback of the amount of signal during the fringe scans. The fourth vertical line denotes the end of the fringe scans during which the fringe should be present. The fifth vertical line indicates the end of the off-fringe scans during which the OPLE delay line is moved far away from the place where the fringe is present. The last two vertical lines and the end of the plot denote the final background sequence which is a sky background. Because the warm shutters in the BCL yield more K-band counts on the detector than the AGN, this off-star background sequence is critical for observing the AGN.

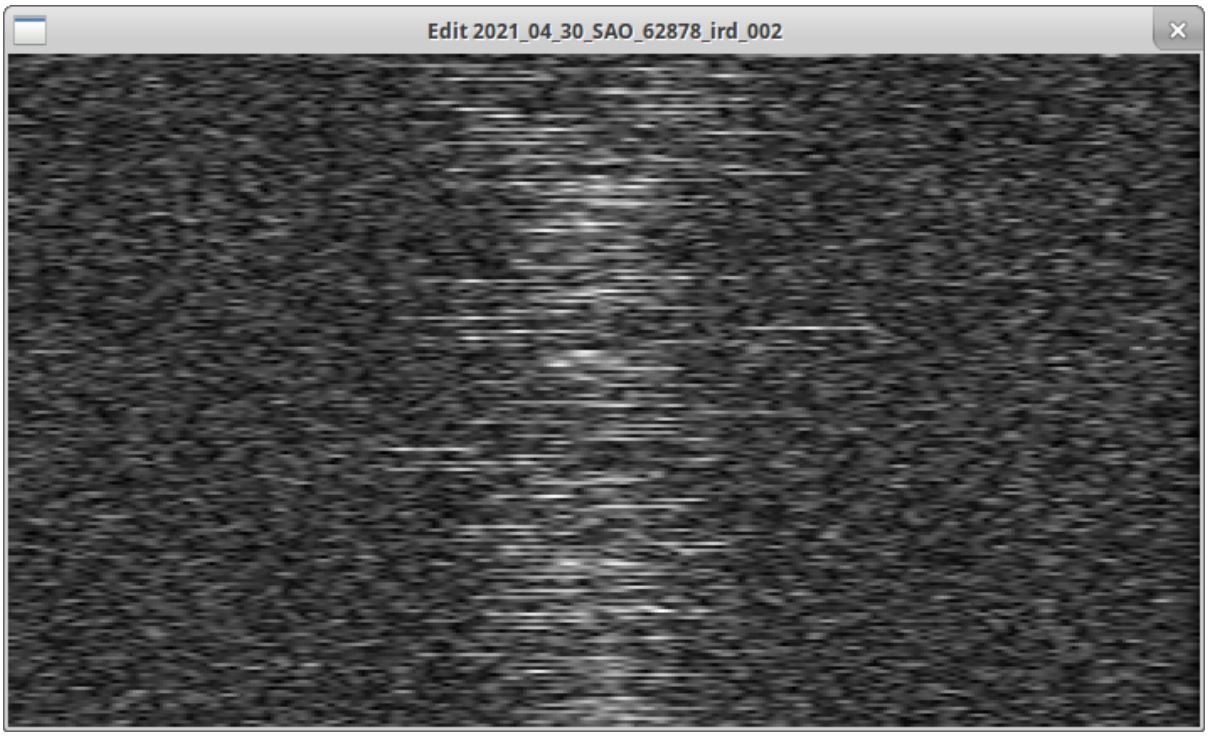

Figure 9.1 The scan waterfall plot for scan editing where the fringe can be seen as the white colored strip running down the center of the plot on most objects.

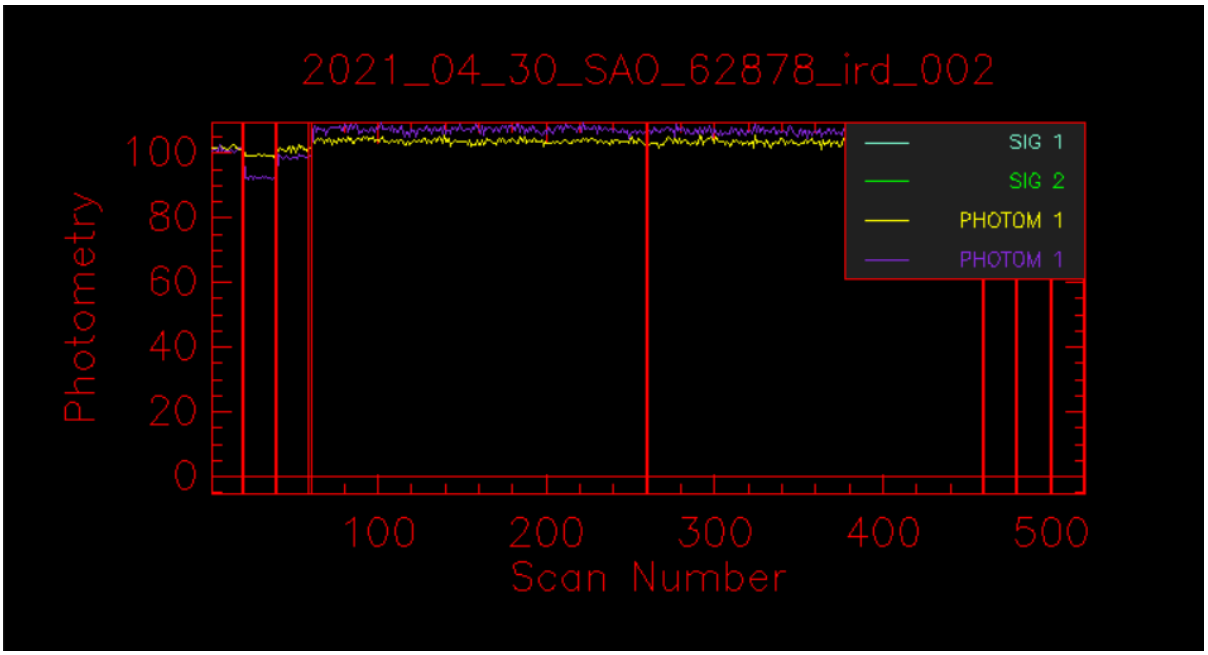

Figure 9.2 The raw photometry for the data.

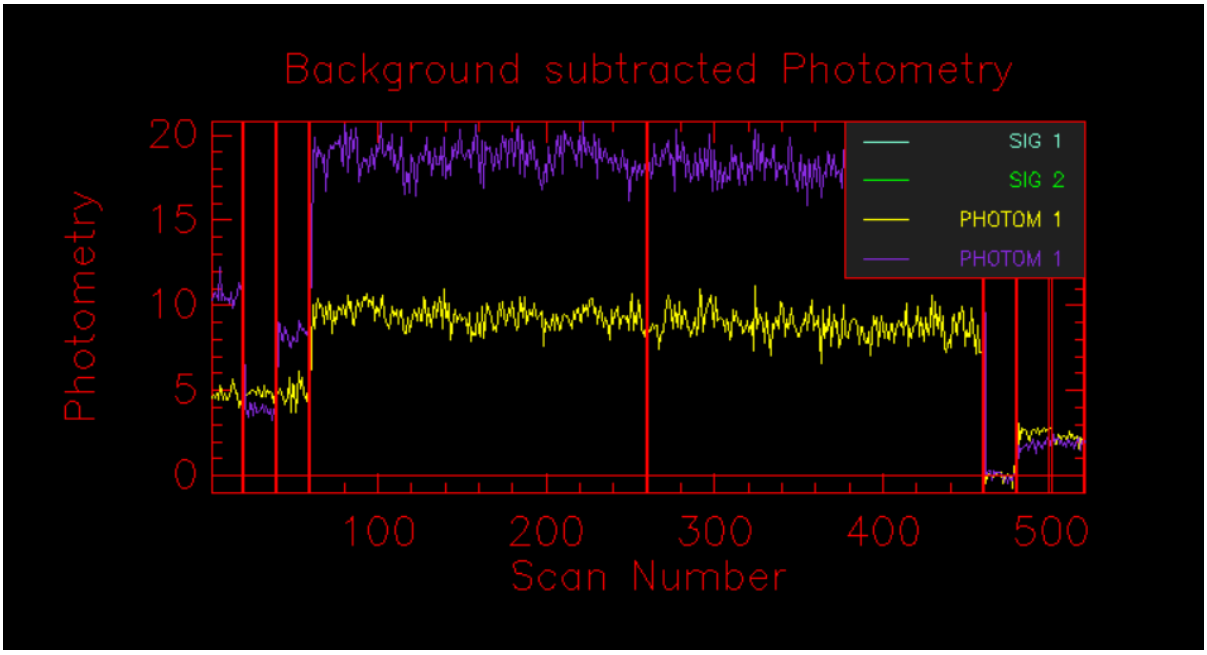

Figure 9.3 The background subtracted photometry for the data.

The background subtracted photomotery should show relatively constant flux levels between the two channels. Problems with telescope and beam train alignments can appear as rapid changes in the flux above the noise level. The photometry will also show if the target being observed is dropped by the TWFS system, in which case these plots can provide a scan number estimate for fringe editing even when the fringes are not obvious in the waterfall plot shown for fringe editing.

The program then displays a plot of the signal to estimated noise power for the power spectrum of the data as shown in figure 9.4. In this plot, the power of the fringe signal should be much higher than the power of the noise. Along with the signal to estimated noise power, the program plots the noise subtracted power spectra of the data set shown in figure 9.5. In this plot, the power spectra are shown and should have a floor near zero due to the noise subtraction. Shown with the data are the integration limits showing the fringe signal comfortably between the 38.0 and 59.0 hertz limits without too much extra space on the wings of the fringe envelope. This plot also shows the Gaussian fit to the two channels. Next, the program displays the low pass filters applied to each channel.

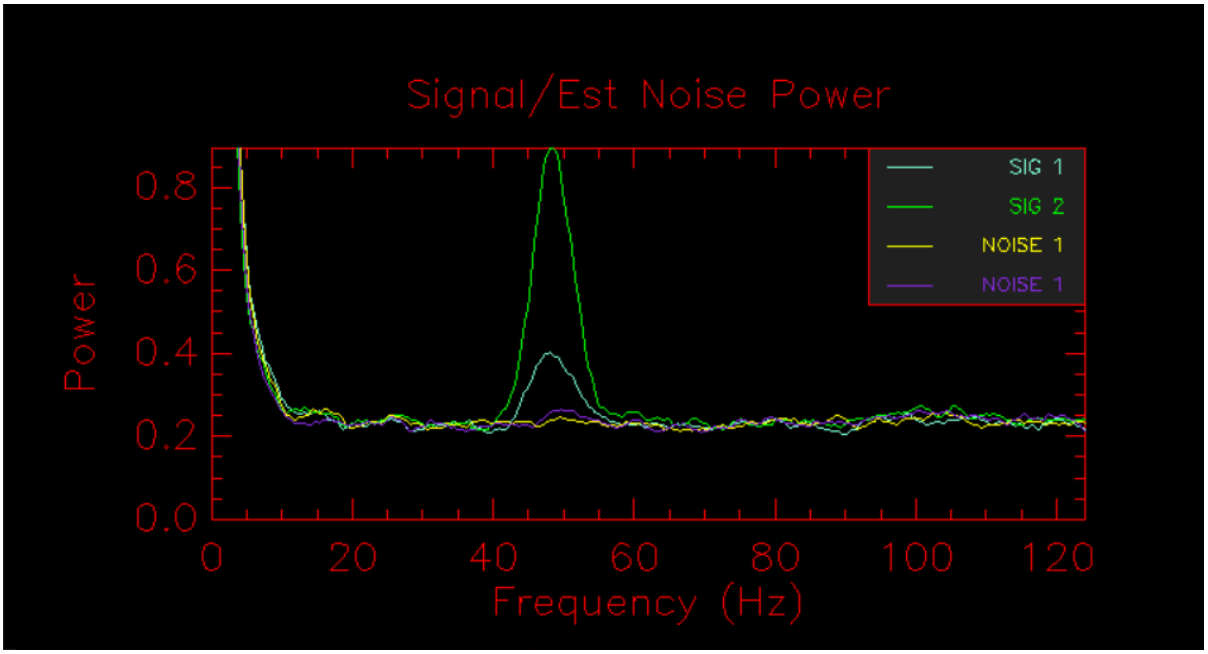

Figure 9.4 The estimated Signal to Noise Power Spectrum.

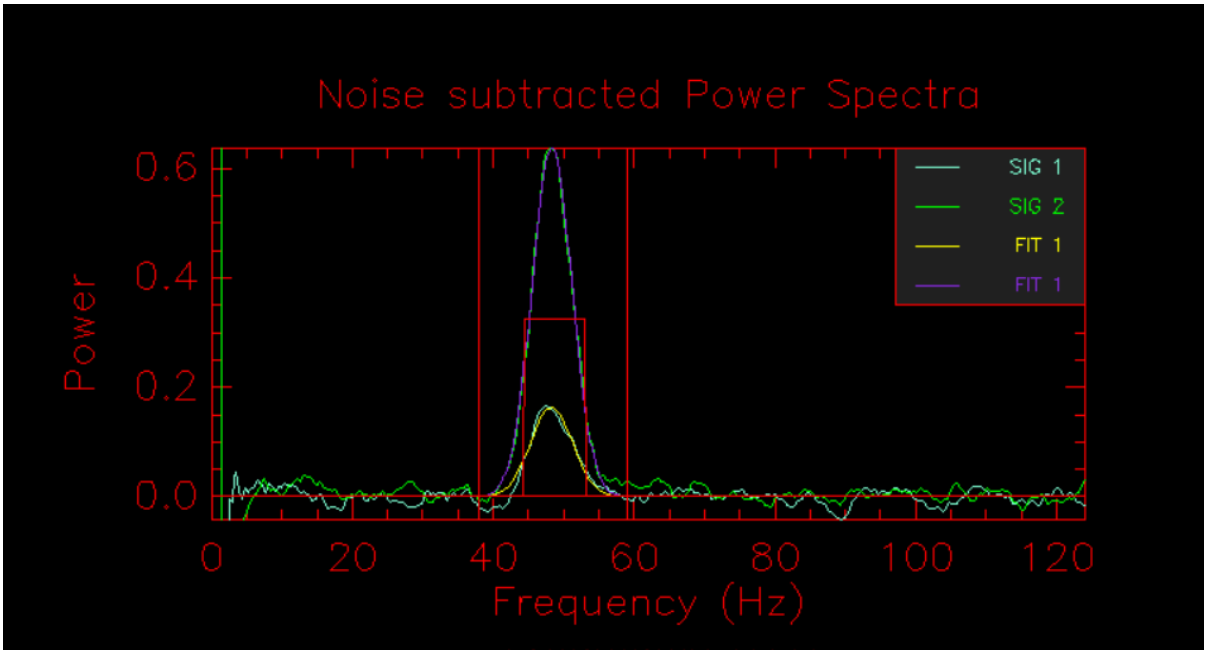

Figure 9.5 The noise subtracted power spectrum.

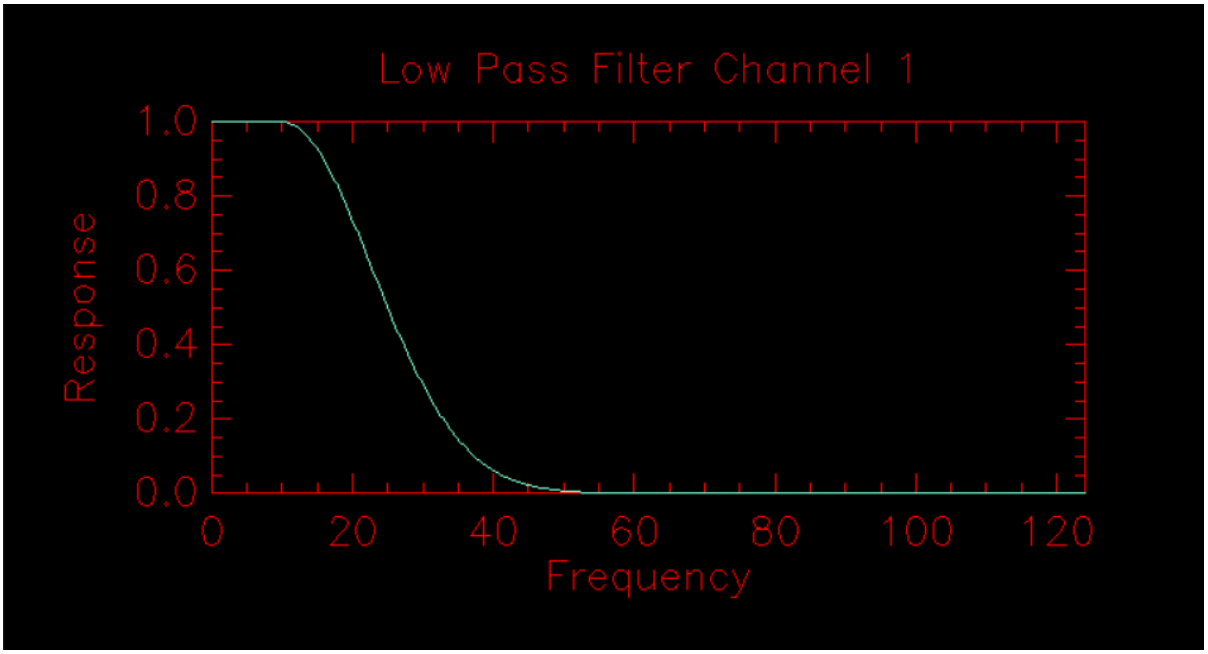

Figure 9.6 The low pass filter used for channel 1.

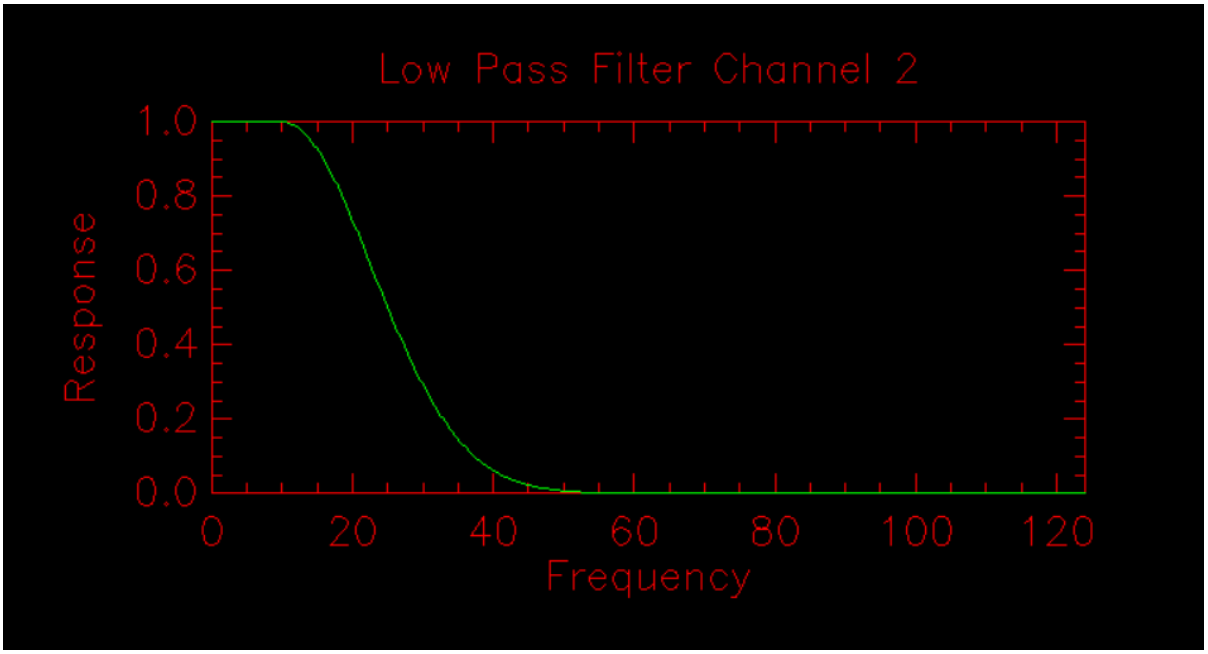

Figure 9.7 The low pass filter used for channel 2.

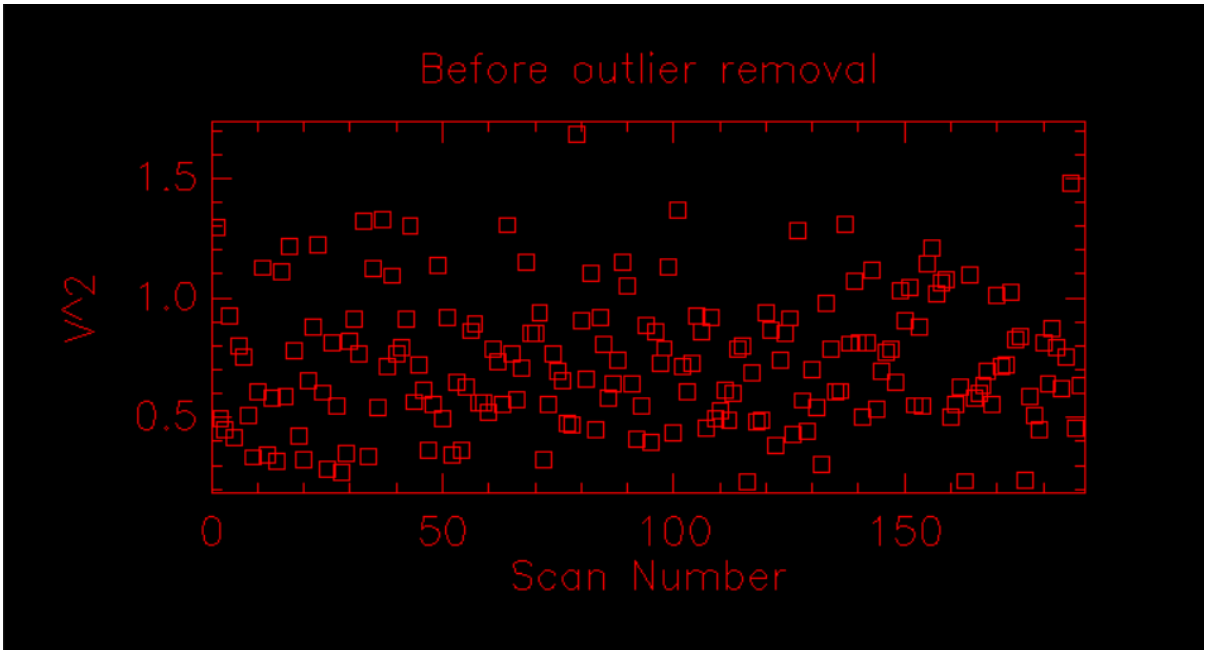

Figure 9.8 The V^2 values of each individual scan.

If activated, the program next plots the outlier rejection set by the number of σ specified by the -o flag. First, it shows a plot containing the squared visibility of each scan in the data shown in figure 9.8. The program shows the remaining squared visibilities after the outlier removal as shown in figure 9.9. In the displayed example for SAO 62878, the 3.0σ outlier rejection trims only a few high squared visibilities out of the data set. Generally, for the faint AGN no outlier rejection will be used, although in some cases it is necessary as some extremely high values appear.

Next, the program displays a correlation histogram for all data scans, shown in figure 9.10, along with a histogram of the fringe weight of each scan in the data sequence shown as figure 9.11.

Nearing the end, the program displays a repeat of the scan Waterfall plot 9.12 with some nicer formatting along with a plot of the power spectra of each scan in a waterfall plot as seen in figure 9.13. The power spectra waterfall plot is often where evidence for fringes for very faint objects, such as the AGN, are seen.

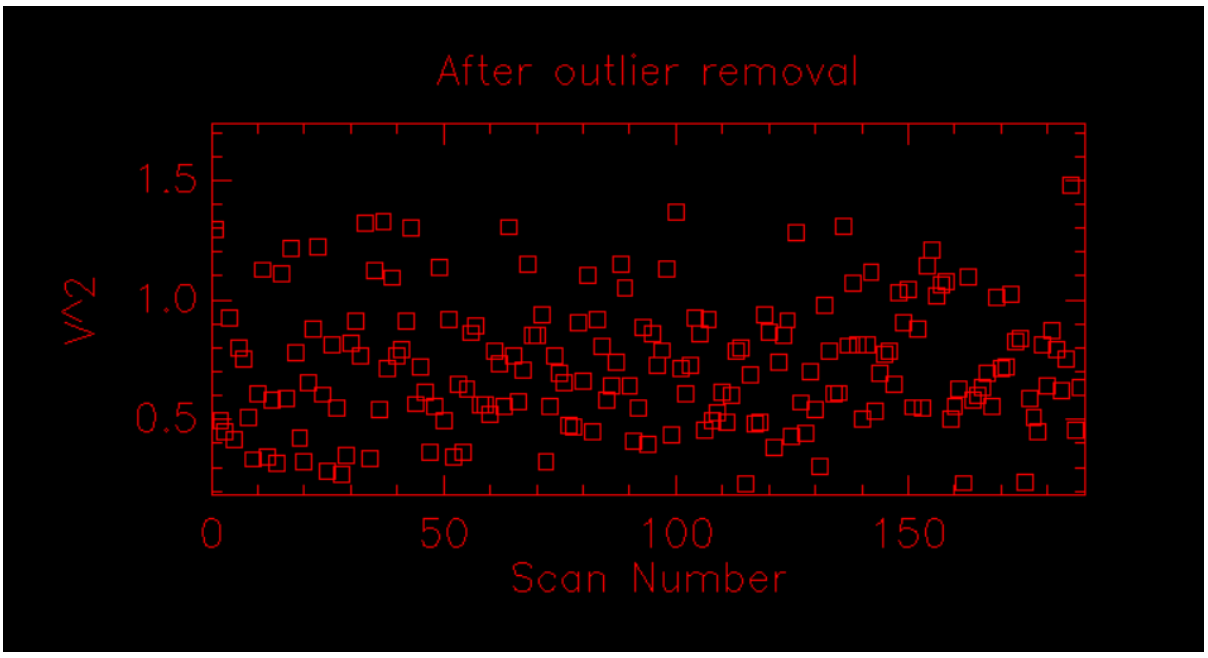

Figure 9.9 The V^2 values of each individual scan after the removal of outliers.

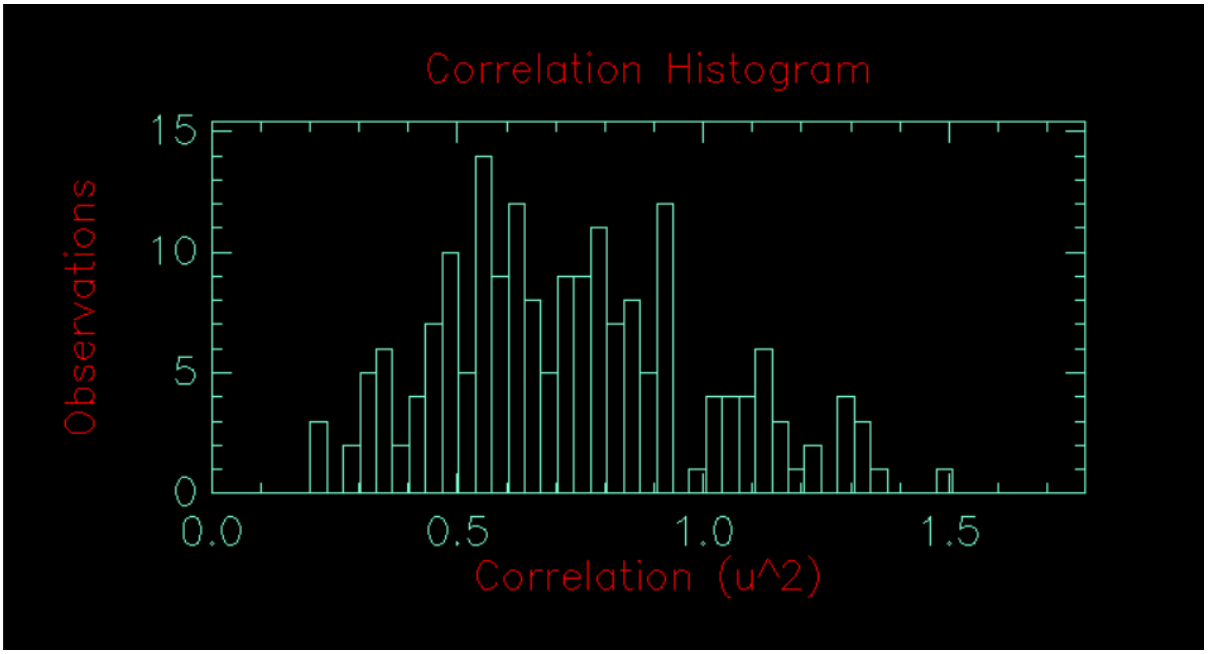

Figure 9.10 The correlation histogram

Figure 9.11 The fringe weight histogram.

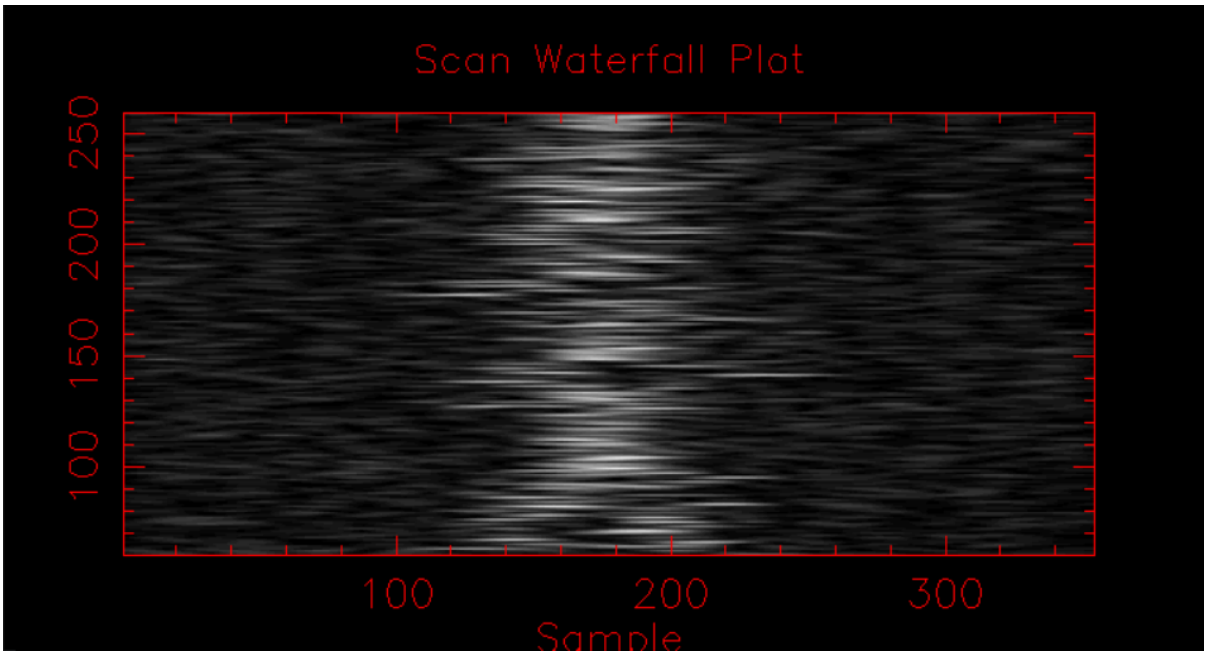

Figure 9.12 The scan waterfall plot where the fringe can be seen as the white colored strip running down the center of the plot..

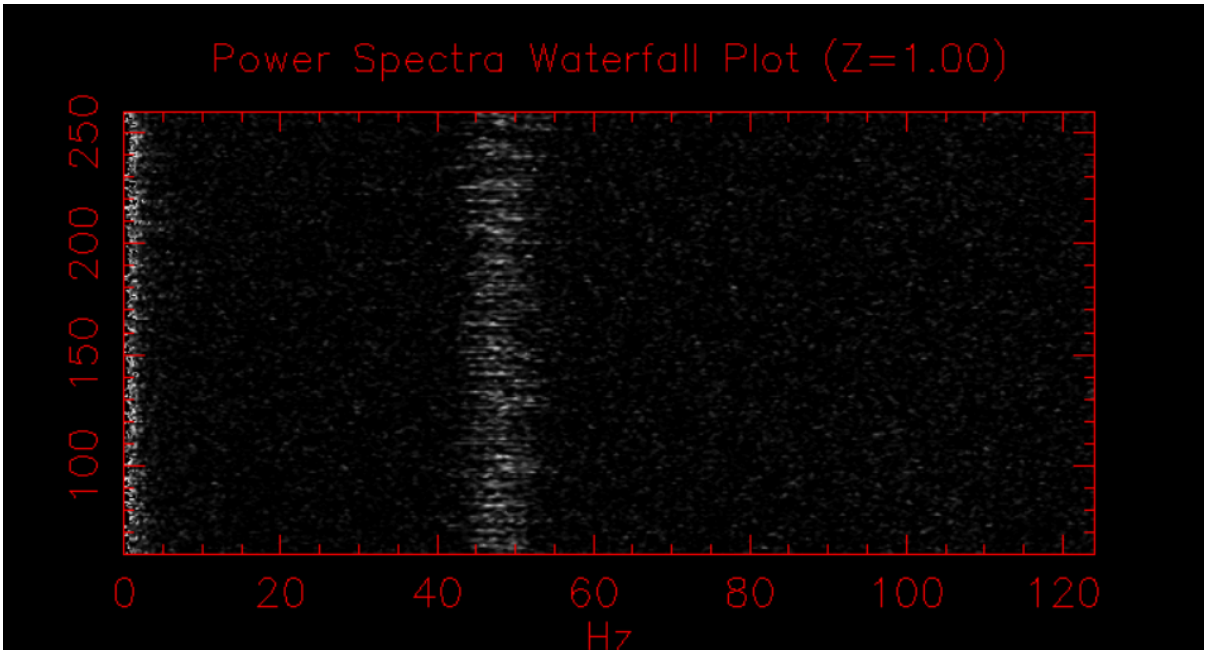

Figure 9.13 The power spectra waterfall plot.

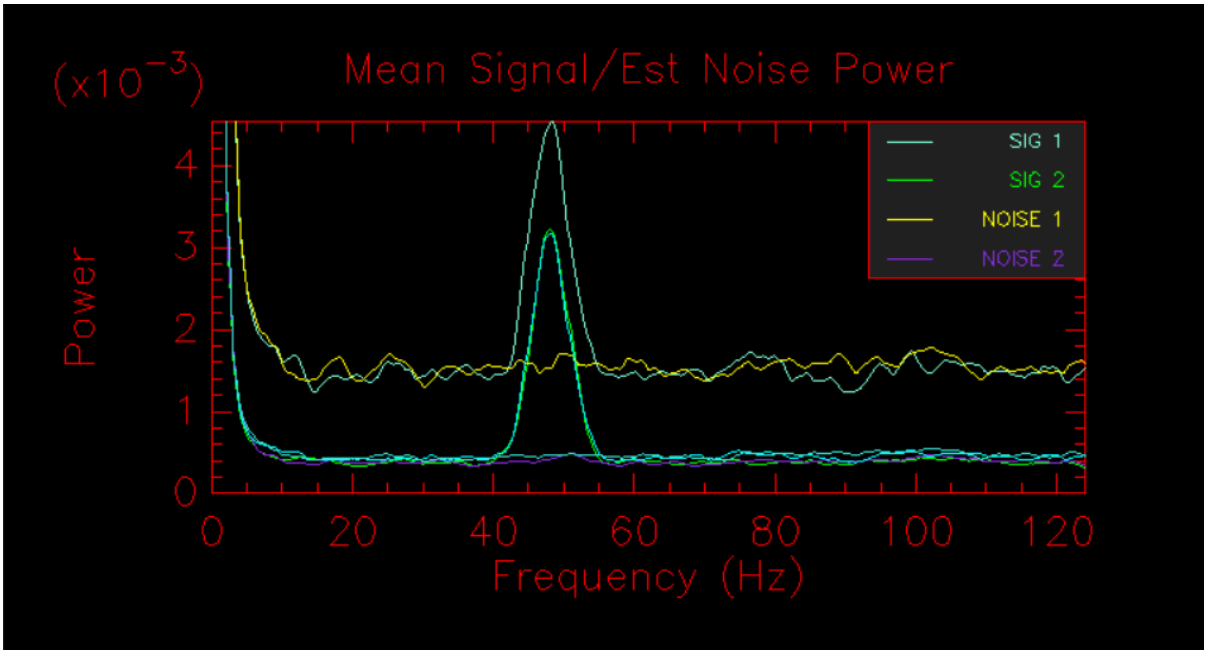

Figure 9.14 The mean signal to noise power spectra plot.

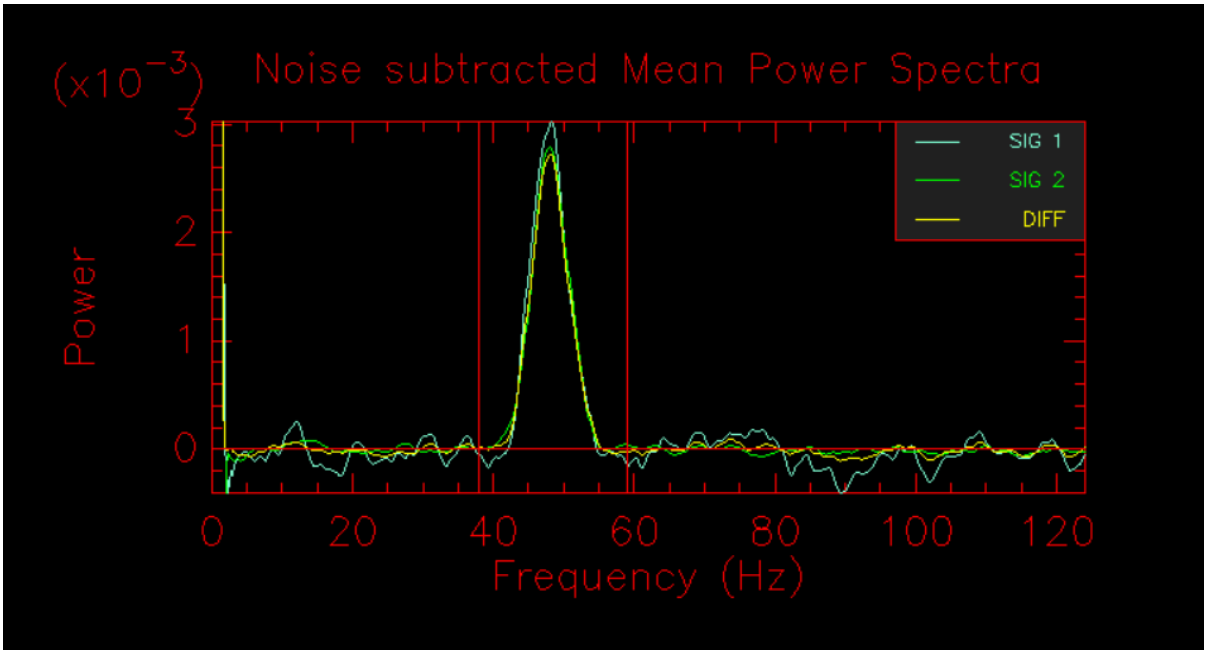

Figure 9.15 The noise subtracted mean power spectrum.

The program then displays the mean signal to estimated noise power spectra as figure 9.14. This plot is effectively the same as the scan signal to estimated noise plot shown in figure 9.4, except that it is calculated on the mean signal. Accompanying this is the final plot, the noise subtracted mean power spectra seen in figure 9.15. For all data taken, this plot is critical, as the visibility estimates calculated from the mean power spectrum are the ones that will be used. This is due to the faintness and the resulting low signal-to-noise ratio of NGC 4151.

The program will then display all calculated visibilities using each of the available visibility estimators, shown below. In all cases, the $V2\_MEAN\_PS$ visibility estimator will be used. The error bars on the mean visibility are calculated using a bootstrapping method.

Table 9.1. Observation Programs, dates, and number of brackets aquired.

Program	Date	# of Brackets
2020 S	2020 Feb 15	1
2020 S	2020 Feb 16	1
2021A	2021 Mar 19	1
2021A*	2021 Apr 25	1
2021A*	2021 Apr 29	2
2021A S	2021 Apr 30	4

```
    # Results from FLUOR PS calculation method:
N_SCANS 187
#                Mean    Stddev
FRINGE_WEIGHT 2.0667 1.575042
#                   Detector 1     Detector 2      Combined
#                Mean    StdDev  Mean    StdDev  Mean    StdDev
Vg 102.586 2.535 102.929 2.461 102.917 2.534
T0_SCANS 133.9 137.9 134.0
T0_500NM 23.5 24.2 23.5
V2_SCANS 1.56191 0.51310 0.80868 0.23974 0.82361 0.24162
V2_CORR -0.89515
V2_CHI2 1.04876 3.00661
V2_SQRT 1.24976 0.41056 0.89927 0.26659 0.90753 0.26624
V_SCANS 1.23354 0.20123 0.88926 0.13416 0.89826 0.13610
V_NORM 1.23265 0.34792 0.88928 0.22668 0.89766 0.22646
V_LOGNORM 1.23394 0.19827 0.88990 0.12948 0.89826 0.12938
V2_MEDIAN 1.42748 0.41253 0.69265 0.27406 0.71088 0.25204
V_MEDIAN 1.19477 0.17294 0.83225 0.16454 0.84314 0.15316
Move on, toggle Log, zoom in, zoom out or zoom = 1 (m/l/z/Z/1)?

Finished computing visibility from mean power spectrum.
Hit enter to continue.


# Calculating bootstrap uncertainties for mean PS...
V2_MEAN_PS 0.56411 0.03505 0.55676 0.02456 0.53383 0.01938
```

9.3 The Data Reductions

This section will detail the reduction of each of the data sets taken with the CHARA Array. Programs for which promising data were recorded are listed in table 9.1. Rather than include every single plot from each data reduction, only the plots relevant to the individual file under consideration will be included.

Table 9.2. Feb 15 2020 Data Filenames.

Bracket #	Target	Filename
1	NGC 4151	2020_02_15_2MASS_J12103258+3924210_ird_001.fit
1	SAO 62878	2020_02_15_SAO_62878_ird_002.fit

Note. — Data bracket and files for the 2020 supplementary observing time.

9.3.1 Feb 15 2020

The night of February 15, 2020 during the 2020 Supplementary Observing time yielded a single imperfect bracket of data on NGC 4151 using the S1 and S2 telescopes (33 meter baseline). Specifically, a data file on the AGN is accompanied by a single calibrator rather than two. The file names for this bracket are listed in table 9.2.

The first step in the reduction is to examine the science target file for any evidence of fringes. Looking at the waterfall plot of all data scans from the 2020_02_15_2MASS_J12103258+3924210_ird_001.fit file, shown in figure 9.16, there is evidence of a fringe visible as brighter regions in the scans especially during the early scans near the bottom of the waterfall plot. Moving on to the scan power spectra waterfall (figure 9.17), the fringe in this file is still more evident with many scans showing a peak in the 40 to 60 Hertz range. Lastly, looking at the noise subtracted mean power spectra for this data file (figure 9.18) there is a clear fringe envelope present. Both channels from the camera have good signals and the applied smoothing appears appropriate. The integration range was set where the difference signal crossed zero on either side of the fringe envelope shown in the noise subtracted mean power spectra.

The science data for NGC 4151, contained in 2020_02_15_2MASS_J12103258+3924210_ird_001.fit, shown in the plots above was processed by REDFLUOR using the following invocation:

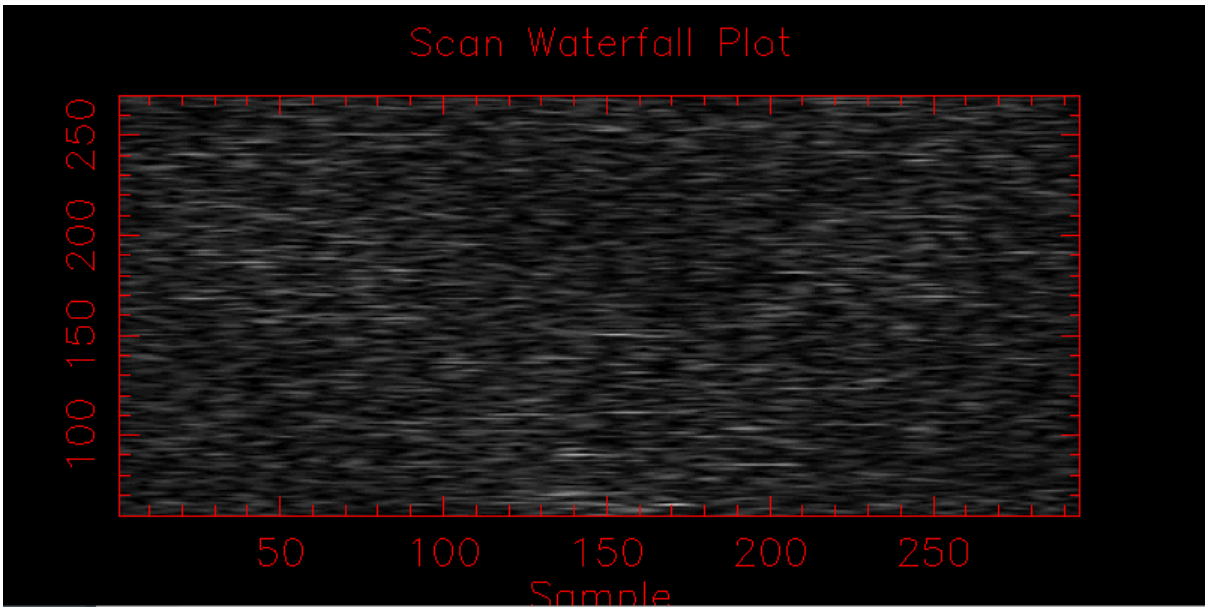

Figure 9.16 The scan waterfall plot for the data file on NGC 4151 taken on Feb 02, 2020.

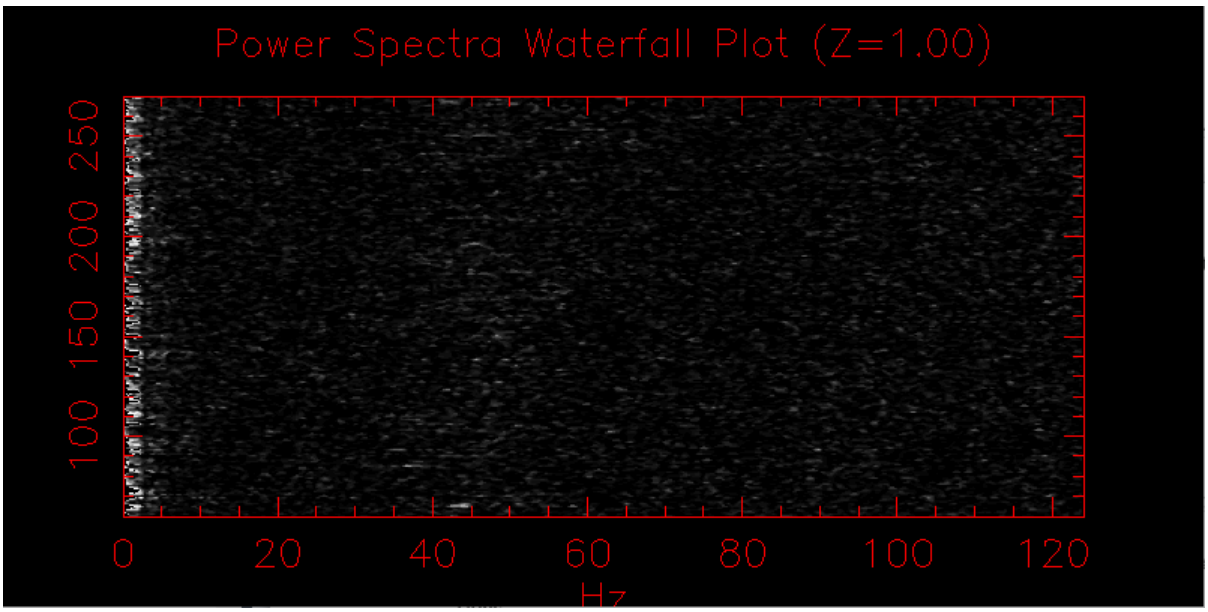

Figure 9.17 The scan power spectra waterfall plot for the data file on NGC 4151 taken on Feb 02, 2020.

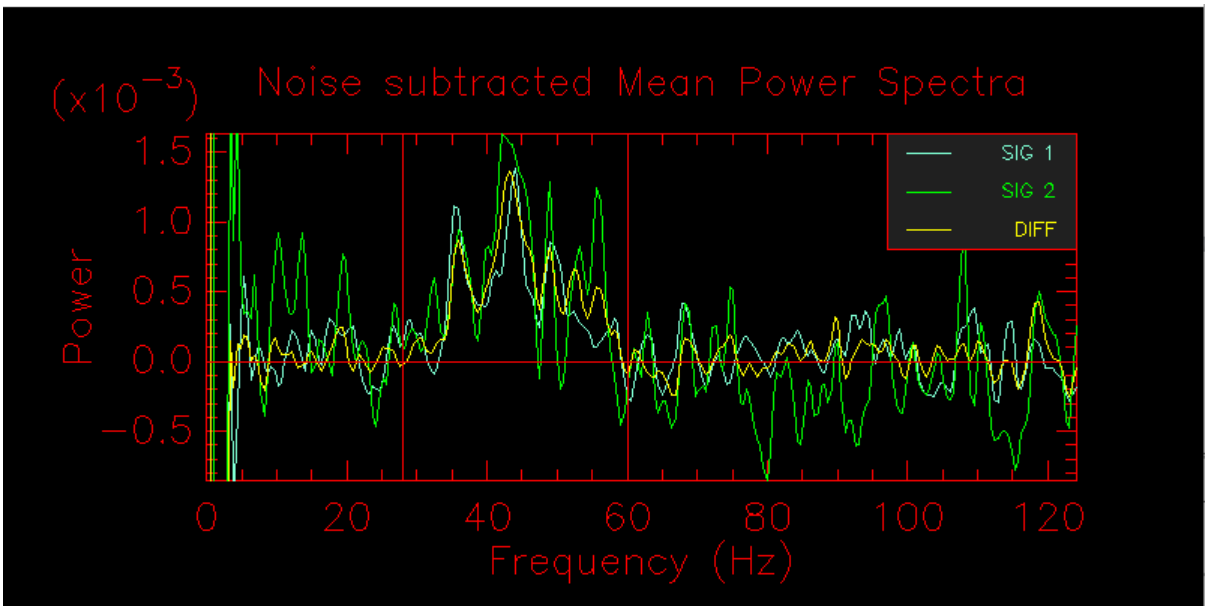

Figure 9.18 The noise subtracted mean power spectra waterfall plot for the data file on NGC 4151 taken on Feb 02, 2020.

```
redfluor -dev xwin -D... -d1 -e -g -I38.0-58.0 -o3.0 -S2.0  2021_04_30_2MASS_J12103258+3924210_ird_001.fit.
```

The data reduces to the following visibilities from the settings above. Since there is plenty of signal in both channels, the combined visibility estimate is used.

	Detector 1		Detector 2		Combined	
	Mean	StdDev	Mean	StdDev	Mean	StdDev
V2_MEAN_PS	0.38897	0.08159	0.51634	0.14312	0.46137	0.07211

The calibrator data for SAO 62878, contained in 2020_02_15_SAO_62878_ird_002.fit, is run through the REDFLUOR program by

```
redfluor -dev xwin -D... -d1 -e -g -I32.0-63.0 -o3.0 -S1.0  2020_02_15_SAO_62878_ird_002.fit.
```

Where the integration range was set manually and only default signal smoothing is applied. The scan waterfall plot can be seen in figure B.1, along with the scan power spectra waterfall plot in figure B.2 and the noise subtracted mean power spectra plot in figure B.3. In the first two of these figures, it is evident by the scatter of peaks in the scan waterfall and the broad range over which the peaks appear in the power spectra waterfall plot that seeing was not particularly good on this night. Yet, the file processes well, yielding the following visibility estimate from REDFLUOR:

Table 9.3. Feb 16 2020 Data Filenames.

Bracket #	Target	Filename
1	NGC 4151	2020_02_16_2MASS_J12103258+3924210_ird_001.fit
1	SAO 62878	2020_02_16_SAO_62878_ird_002.fit

Note. — Data bracket and files for the 2020 supplementary observing time.

```
                          Detector 1     Detector 2      Combined
                        Mean    StdDev  Mean    StdDev  Mean    StdDev
V2_MEAN_PS             0.46575 0.10017 0.55771 0.09048 0.45700 0.07070
```

This bracket is calibrated with the following command:

```
calibir -c -BV2_MEAN_PS -s0.0922-0.0021 320097 148118
```

9.3.2 Feb 16 2020

The second night of the 2020 Supplementary observing time also resulted in a single data set recorded on NGC 4151 using the S1 and S2 telescopes (33 meter baseline) with a single set of calibrator data recorded on SAO 62878, the file names for these files are listed in table 9.3. While a set of calibrator data was recorded prior to the AGN, it is clear from the observing notes that this file is not suitable for accompanying the science data due to a full alignment of the combiner being done in between. Therefore, only a calibrator data set following the object's recording is used for calibration.

In the scan waterfall plot, shown in figure 9.19, for this file, there is no evidence of the fringe being present. In the power spectra waterfall plot (figure 9.20) there is some evidence for a fringe seen as a higher density of white peaks inside the range where the fringe is expected to appear (40-60 Hz). It is not until the noise subtracted mean power spectra plot shown in figure 9.21 that clear evidence for the fringe is seen. Even in the noise subtracted mean power spectra, the fringe envelope is very weak and is barely stronger than the noise.

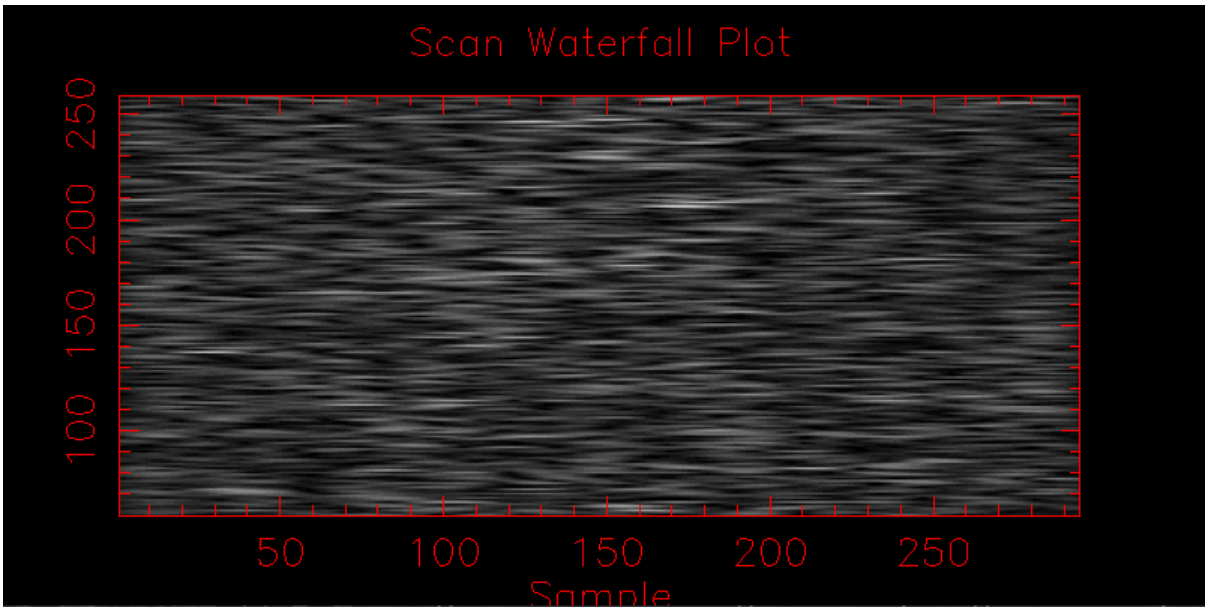

Figure 9.19 The scan waterfall plot for the data file on NGC 4151 taken on Feb 16, 2020.

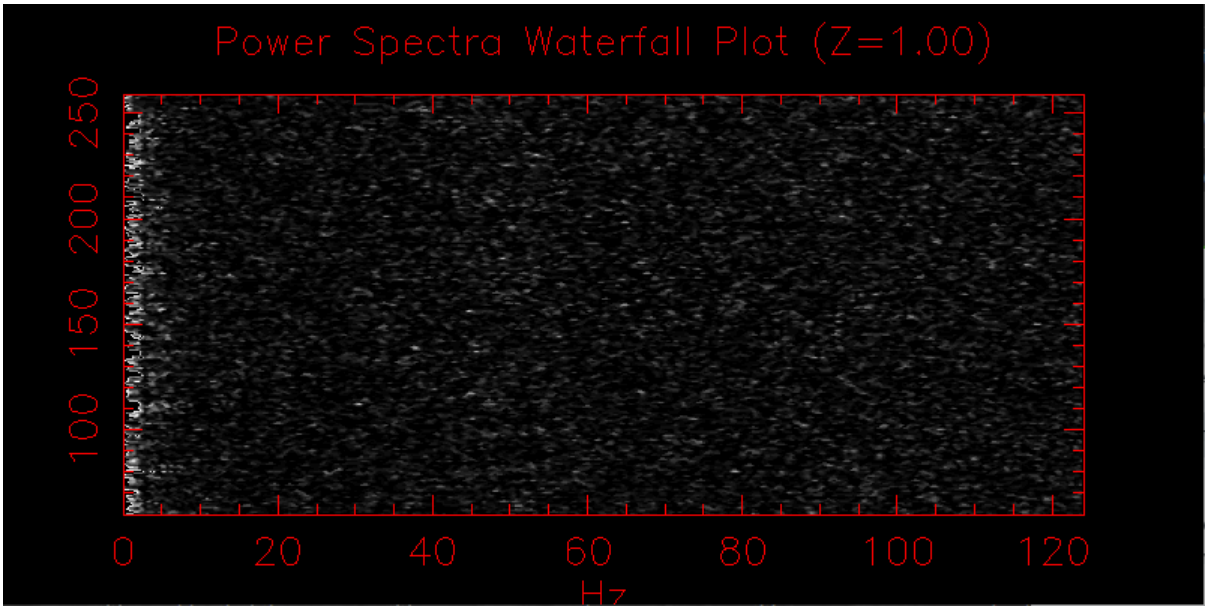

Figure 9.20 The scan power spectra waterfall plot for the data file on NGC 4151 taken on Feb 16, 2020.

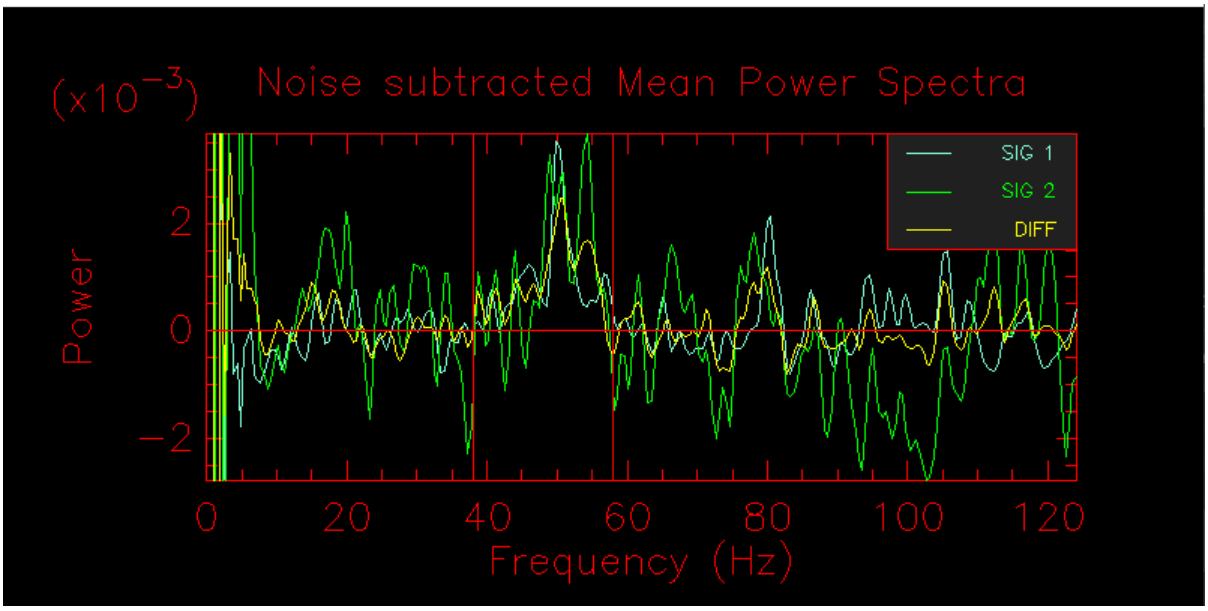

Figure 9.21 The noise subtracted mean power spectra waterfall plot for the data file on NGC 4151 taken on Feb 16, 2020.

The data for the AGN is reduced with REDFLUOR with the following command:

```
redfluor -dev xwin -D... -d1 -e -g -I38.0-58.0 -o3.0 -S2.0  2020_02_16_2MASS_J12103258+3924210_ird_001.fit.
```

where the integration range was set in the usual way and the signal smoothing was increased from the default only slightly. The resulting visibility estimate for the data enclosed in the file 2020_02_16_2MASS_J12103258+3924210_ird_001.fit is:

	Detector 1		Detector 2		Combined	
	Mean	StdDev	Mean	StdDev	Mean	StdDev
V2_MEAN_PS	0.58320	0.10865	0.72070	0.24216	0.58467	0.08882

The calibrator for this data file was reduced similarly, with the following command,

```
redfluor -dev xwin -D... -d1 -e -g -I33.0-61.5 -o3.0 -S1.0  2020_02_16_SAO_62878_ird_002.fit.
```

While, the calibrator data required no extra signal smoothing, it is apparent in the scan waterfall plot (figure B.1), scan power spectra waterfall plot (figure B.2), and noise subtracted mean power spectra (figure B.3) that the seeing conditions were poor on this night. This is evident in the scatter of the fringe in both waterfall plots and in the broadness

Table 9.4. Mar 19 2021 Data Filenames.

Bracket #	Target	Filename
1	SAO 62878	2021_03_19_SAO_62878_ird_001.fit
1	NGC 4151	2021_03_19_2MASS_J12103258+3924210_ird_001.fit
1	SAO 62878	2021_03_19_SAO_62878_ird_002.fit

Note. — Data bracket and files for the 2021A* observing time.

of the fringe in the noise subtracted power spectra. The calibrator data contained in 2020_02_16_SAO_62878_ird_002.fit results in the following visibility estimate:

```
                    Detector 1      Detector 2       Combined
                  Mean     StdDev  Mean     StdDev  Mean     StdDev
V2_MEAN_PS       0.46261 0.07118 0.63069 0.07899 0.49712 0.05770
```

The two results can then be used to get the calibrated visibility with the following command.

```
calibir -c -BV2_MEAN_PS -s0.0922-0.0021 320097 148118
```

9.3.3 Mar 19 2021

During the 2021A observing time, the S2 and W1 telescopes were used with a baseline of 250 meters resulting in one full bracket consisting of a recording of a calibrator, a recording of the AGN, and a second recording of the calibrator was taken with the file names listed in table 9.4. Once again, this file was recorded blind with no clear evidence of the fringe being seen until the very end of the recording with the mean power spectrum being displayed. This is clear in figure 9.22 where there is no obvious fringe seen. Although there are a few brighter patches in the waterfall that may indicate the presence of the fringe.

In both the power spectra waterfall plot shown in figure 9.23 and in the noise subtracted mean power spectra shown in figure 9.18, the fringe is clearly visible. It is worth noting that

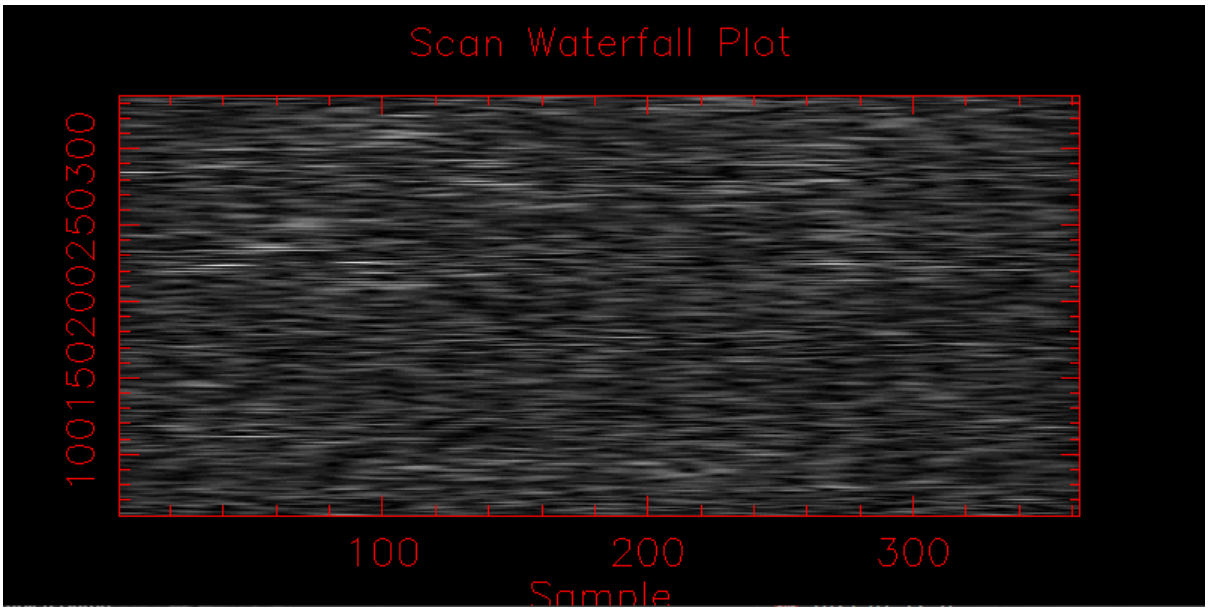

Figure 9.22 The scan waterfall plot for the data file on NGC 4151 taken on Mar 19, 2021.

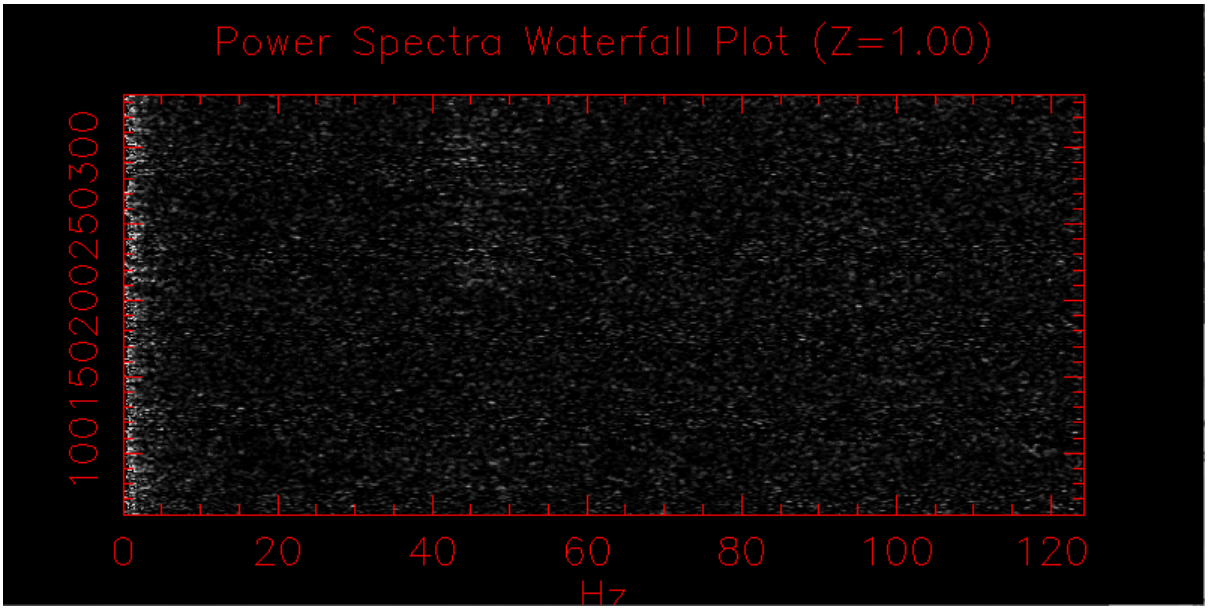

Figure 9.23 The scan power spectra waterfall plot for the data file on NGC 4151 taken on Mar 19, 2021.

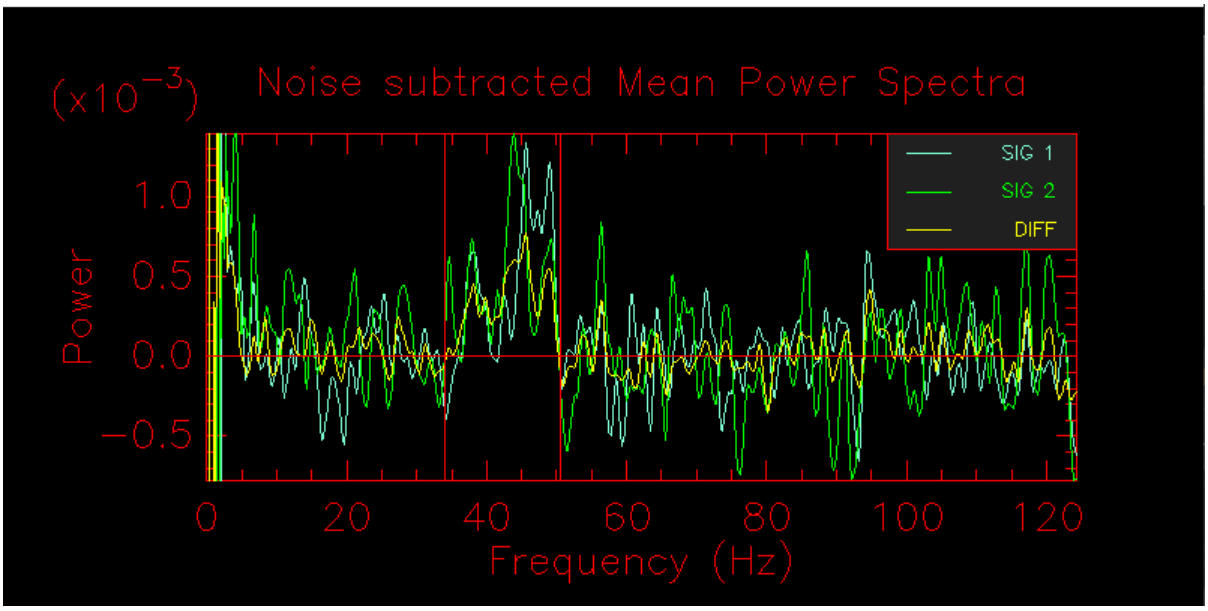

Figure 9.24 The noise subtracted mean power spectra waterfall plot for the data file on NGC 4151 taken on Mar 19, 2021.

the apparent drop out of the fringe seen in the scan power spectra waterfall plot corresponds to a brief dropping of the object by the tip-tilt/AO system seen in the background subtracted photometry of this file. It is brief enough that no scan editing was done.

The data recorded on the AGN contained in the file 2021_03_19_2MASS_J12103258+3924210_ird_001.fit, is reduced using the following command,

```
redfluor -dev xwin -D... -d1 -e -g -I34.0-50.5 -o3.0 -S2.0  2021_03_19_2MASS_J12103258+3924210_ird_001.fit.
```

Resulting in the following visibility estimate:

	Detector 1		Detector 2		Combined	
	Mean	StdDev	Mean	StdDev	Mean	StdDev
V2_MEAN_PS	0.21970	0.03975	0.22465	0.03005	0.16063	0.01820

The first calibrator data recording is contained in the file 2021_03_19_SAO_62878_ird_001.fit , the scan waterfall plot, scan power spectra waterfall plot, and noise subtracted mean power spectra can be seen in figures B.7, B.8, and B.9. This file is reduced using the following command,

```
redfluor -dev xwin -D... -d1 -e -g -I32.0-62.0 -o3.0 -S1.0  2021_02_19_SAO_62878_ird_001.fit.
```

which results in the following visibility estimate,

	Detector 1		Detector 2		Combined	
	Mean	StdDev	Mean	StdDev	Mean	StdDev
V2_MEAN_PS	0.66662	0.03097	0.65063	0.02420	0.60147	0.02211

The second calibrator data recording contained in the file 2021_03_19_SAO_62878_ird_002.fit with the the scan waterfall plot, scan power spectra waterfall plot, and noise subtracted mean power spectra visible in figures B.10, B.11, and B.12. It is reduced using

```
redfluor -dev xwin -D... -d1 -e -g -I34.0-60.0 -o3.0 -S1.0  2021_02_19_SAO_62878_ird_002.fit.
```

Resulting in this visibility estimate

	Detector 1		Detector 2		Combined	
	Mean	StdDev	Mean	StdDev	Mean	StdDev
V2_MEAN_PS	0.48781	0.03028	0.60161	0.04455	0.48593	0.03072

This data file may be calibrated using the following:

```
calibir -c -BV2_MEAN_PS -s0.0922-0.0021 320097 148118
```

9.3.4 Apr 25 2021

During the 2021A* observing time, a single incomplete bracket consisting of a recording on NGC 4151 and a recording on the bright calibrator HD 105881 was taken with the S2 and W1 telescopes with a 250 meter baseline. The names of the resulting files listed in table 9.5. The recording on the AGN was made totally blind with no indication of fringe presence until the data was reduced.

As normal, there is no evidence of a fringe in the scan waterfall plot (figure 9.25). There are a few bright spots in the power spectra waterfall plot (figure 9.26 in the expected frequency range. In the final noise subtracted mean power spectra, there is a nicely shaped fringe envelope shown in figure 9.27.

Table 9.5. Apr 25 2021 Data Filenames.

Bracket #	Target	Filename
1	HD 105881	2021_04_25_HD_105881_ird_001.fit
1	NGC 4151	2021_04_25_2MASS_J12103258+3924210_ird_001.fit

Note. — Data bracket and files for the 2021A* observing time.

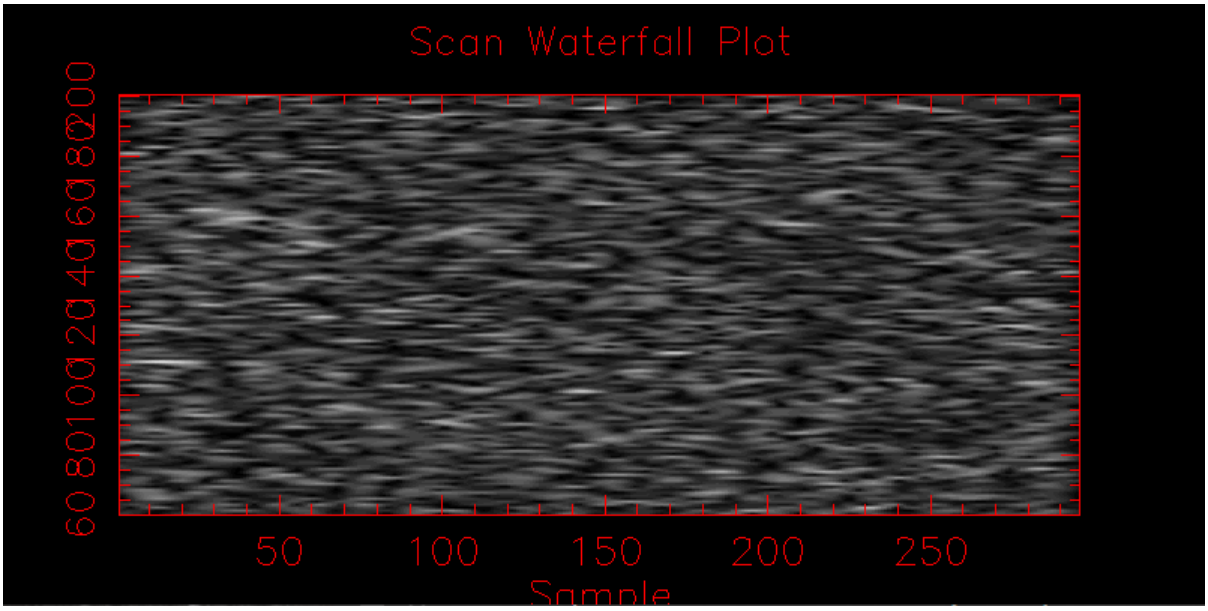

Figure 9.25 The scan waterfall plot for the data file on NGC 4151 taken on Apr 25, 2021.

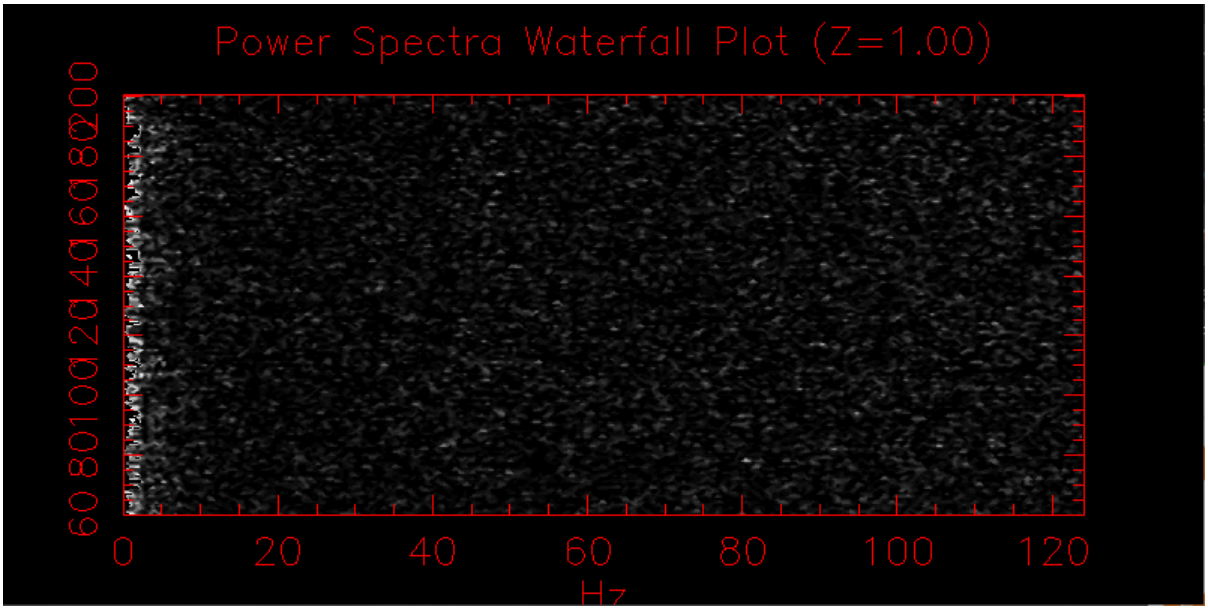

Figure 9.26 The scan power spectra waterfall plot for the data file on NGC 4151 taken on Apr 25, 2021.

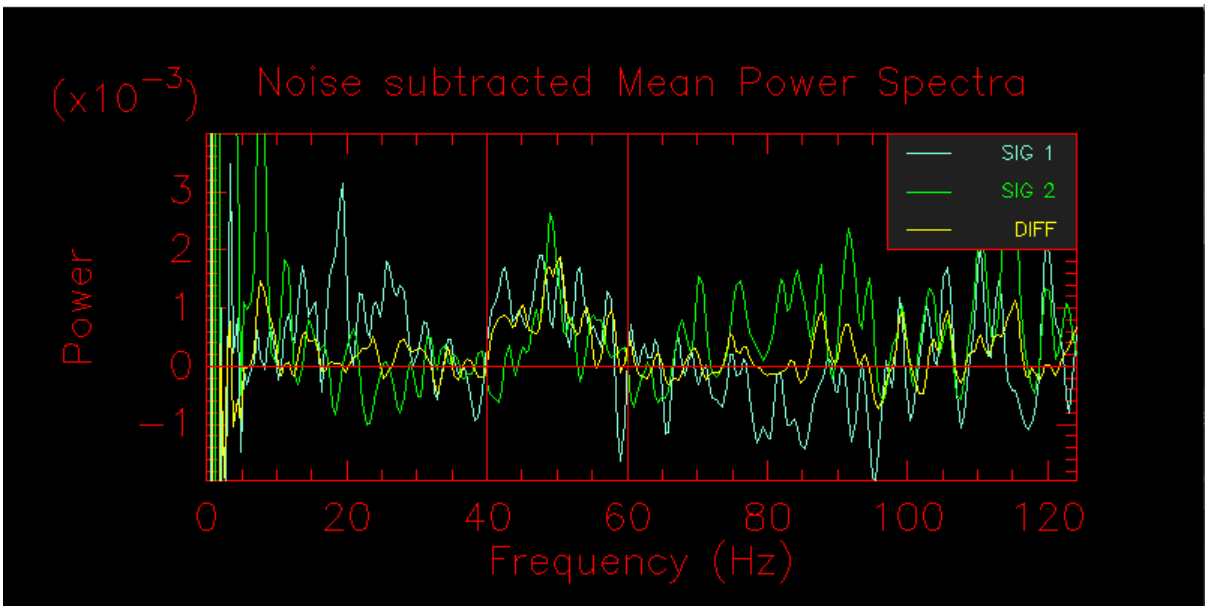

Figure 9.27 The noise subtracted mean power spectra waterfall plot for the data file on NGC 4151 taken on Apr 25, 2021.

The data recorded on the AGN contained in the file 2021_04_25_2MASS_J12103258+3924210_ird_001.fit, is reduced using the following command,

```
redfluor -dev xwin -D... -d1 -e -g -I40.0-60.0 -o3.0 -S2.0  2021_04_25_2MASS_J12103258+3924210_ird_001.fit.
```

Resulting in the following visibility estimate:

	Detector 1		Detector 2		Combined	
	Mean	StdDev	Mean	StdDev	Mean	StdDev
V2_MEAN_PS	0.52478	0.24828	0.35591	0.18833	0.49377	0.11711

Unfortunately, the calibrator recording is severely compromised and cannot be used. The scan waterfall plot shown in figure B.13, shows severe bouncing of the fringe back and forth across each scan and is not often in the middle. Similarly, the scan power spectra waterfall plot shown in figure B.14 shows significant smearing of the fringe across and outside of the expected 40 to 60 Hz range, and plenty of scans where the fringe is simply missing. Figure B.15 shows the noise subtracted mean power spectra in which no recognizable fringe envelope is seen. Without a valid calibration point, the data on NGC 4151 is not usable from this date.

9.3.5 Apr 29 2021

On another night during the 2021A* observing time, two brackets were recorded totally blind on NGC 4151 along with recordings on the bright calibrator HD 105881 before, between, and after the AGN with the filenames listed in table 9.6. Once again, the S2 and W1 telescopes were used with a baseline of 250 meters.

Unfortunately, there is no evidence of a fringe in either data recording, in either the power spectra waterfall plot shown in figures 9.28 and 9.30 or in the noise subtracted mean power spectra shown in figures 9.29 and 9.31.

Furthermore, the calibrator files taken on HD 105881 are very messy. For each of the three files, the scan waterfall plots shown in figures B.16, B.19, and B.22 exhibit some very

Table 9.6. Apr 29 2021 Data Filenames.

Bracket #	Target	Filename
1	HD 105881	2021_04_29_HD_105881_ird_001.fit
1	NGC 4151	2021_04_29_2MASS_J12103258+3924210_ird_001.fit
1	HD 105881	2021_04_29_HD_105881_ird_002.fit
1	NGC 4151	2021_04_29_2MASS_J12103258+3924210_ird_002.fit
1	HD 105881	2021_04_29_HD_105881_ird_003.fit

Note. — Data bracket and files for the 2021A* observing time.

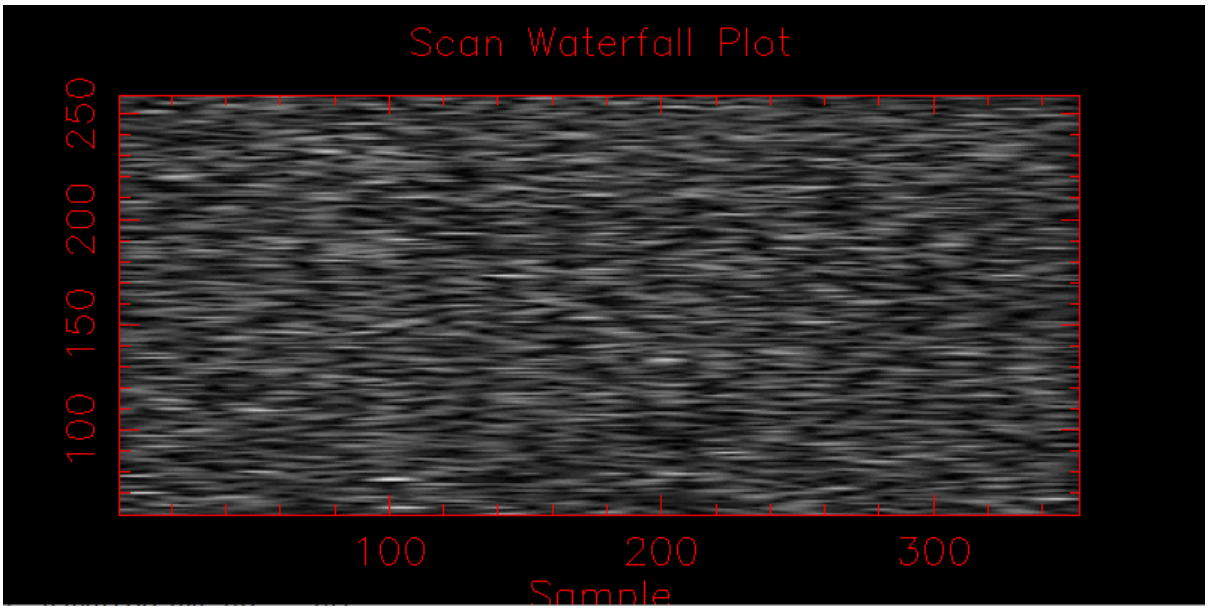

Figure 9.28 The scan waterfall plot for the first data file on NGC 4151 taken on Apr 29, 2021.

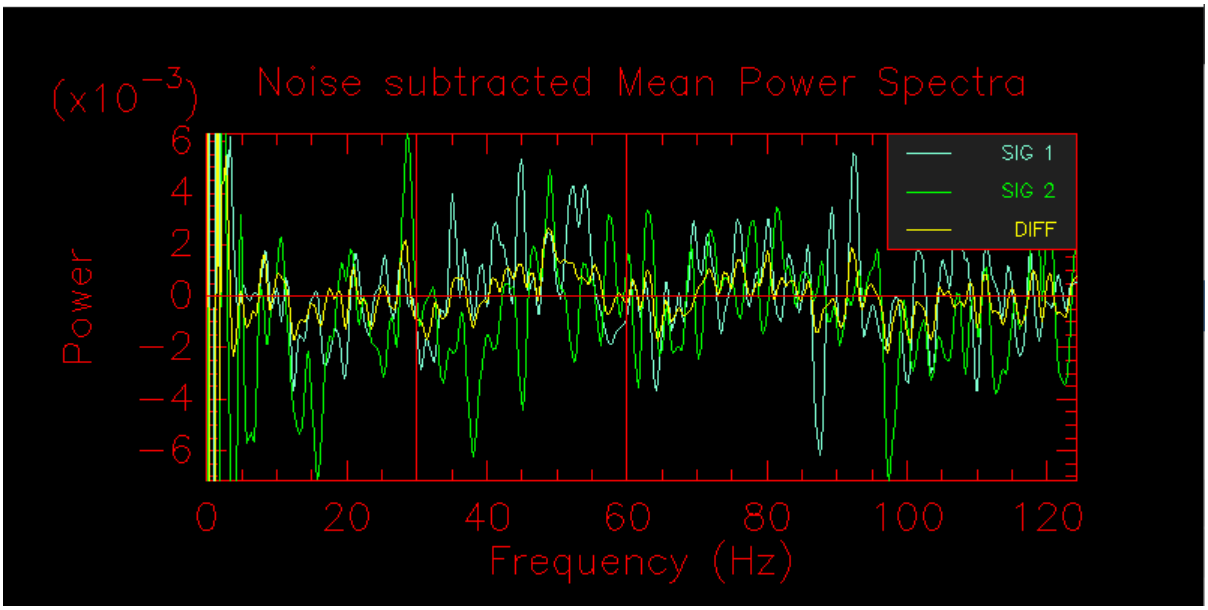

Figure 9.29 The noise subtracted mean power spectra waterfall plot for the first data file on NGC 4151 taken on Apr 29, 2021.

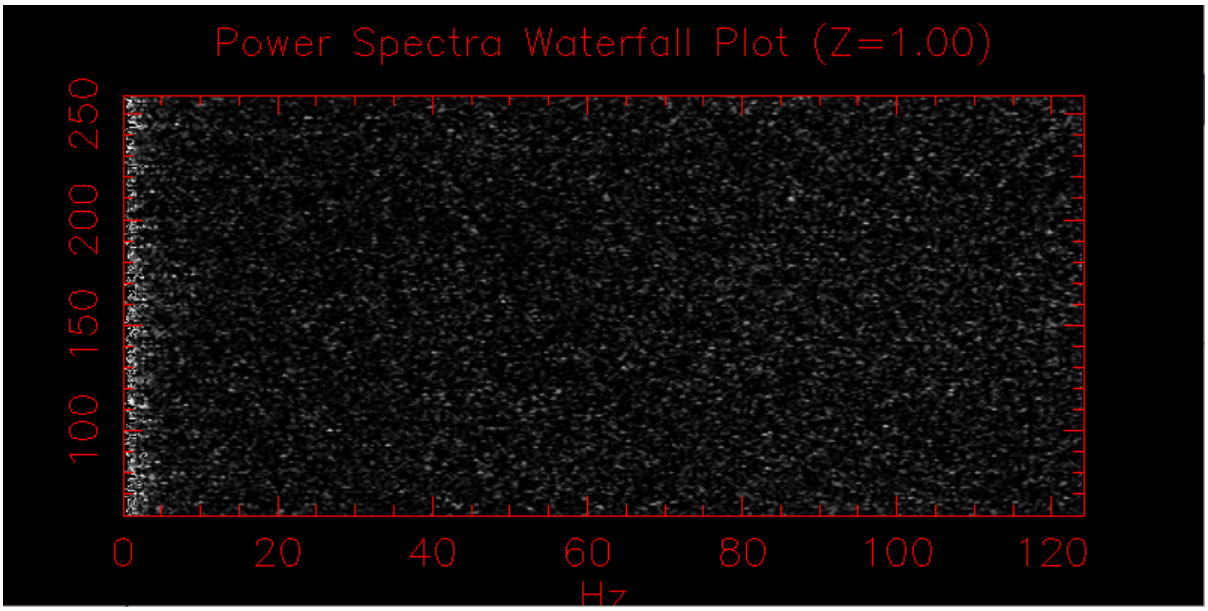

Figure 9.30 The scan power spectra waterfall plot for the second data file on NGC 4151 taken on Apr 29, 2021.

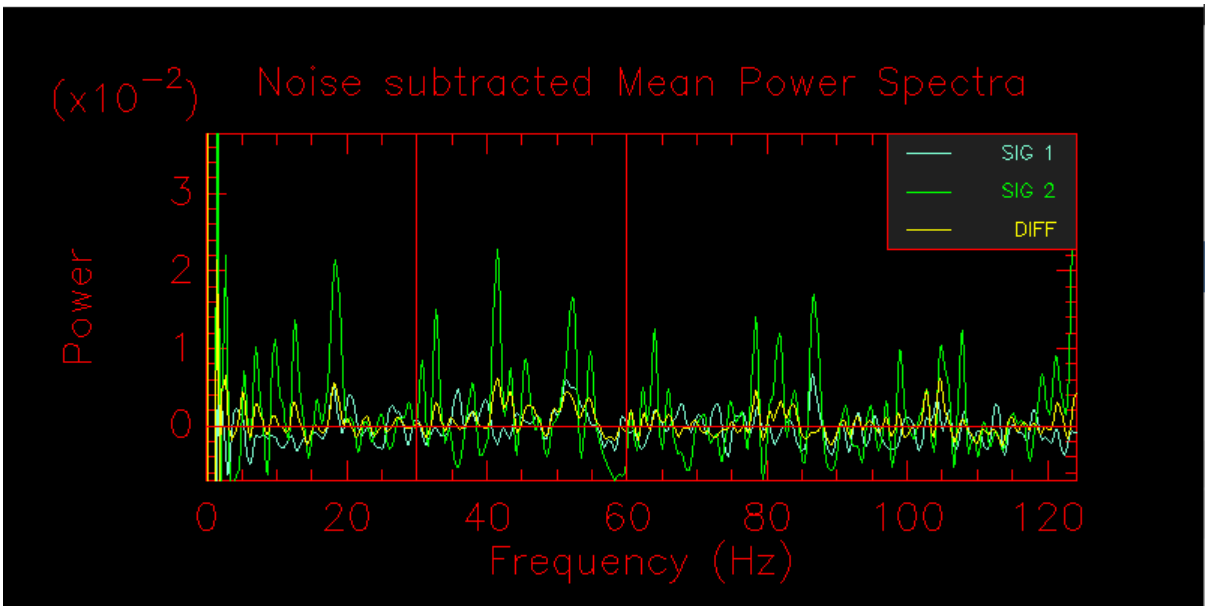

Figure 9.31 The noise subtracted mean power spectra waterfall plot for the second data file on NGC 4151 taken on Apr 29, 2021.

bad seeing conditions where the fringe signal bounces wildly back and forth across the scan window. This is visible again in each of the three files' power spectra waterfall plots shown in figures B.17, B.20, and B.23 where the fringe signal often appears outside the normal 40 to 60 Hz region and changes significantly in strength between each scan. Things are a bit stranger in the noise subtracted mean power spectra plots, where the first file shown in figure B.18 contains no recognizable fringe. The second and third files on the calibrator seen in figures B.21 and B.24 do show a fringe signal, but the noise subtraction is corrupted so that the signal floor away from the fringe signal is below zero.

With the obvious poor seeing conditions, it is reasonable to conclude that all data from this night is a loss. If the conditions were good, as exhibited by clean calibrator data with narrow consistent fringe signals in the scan waterfalls, it would be worth attempting a cautious reduction of the data files. In such a case, the lack of fringe evidence in the AGN data files could indicate low visibility intrinsic to the AGN. Unfortunately, this was not the case on April 29, 2021.

Table 9.7. Apr 30 2021 Data Filenames.

Bracket #	Target	Filename
1	TYC 3017-1666-1	2021_04_30_2MASS_J12111971+3914148_ird_001.fit
1	NGC 4151	2021_04_30_2MASS_J12103258+3924210_ird_001.fit
2	SAO 62878	2021_04_30_SAO_62878_ird_001.fit
2	NGC 4151	2021_04_30_2MASS_J12103258+3924210_ird_002.fit
2	HD 105881	2021_04_30_HD_105881_ird_001.fit
3	SAO 62878	2021_04_30_SAO_62878_ird_002.fit
3	NGC 4151	2021_04_30_2MASS_J12103258+3924210_ird_003.fit
3	HD 105881	2021_04_30_HD_105881_ird_002.fit
4	SAO 62878	2021_04_30_SAO_62878_ird_003.fit
4	NGC 4151	2021_04_30_2MASS_J12103258+3924210_ird_004.fit
4	HD 105881	2021_04_30_HD_105881_ird_003.fit

Note. — Data brackets and files for the 2021A Supplementary observing time.

9.3.6 Apr 30 2021

During the night of April 30, 2021, a bonus night for observing NGC 4151, observing conditions were very good. Using the S2 and W1 telescopes with a baseline of 250 meters, one partial bracket and three full brackets were recorded on the AGN. The files for the target recording as well as the calibrators are listed in table 9.7. The data reduction for each bracket will be treated individually here. For brighter objects, the reduction might be handled in bulk, but the challenge posed by observing so near the limit for CLASSIC warrants a more careful reduction.

9.3.6.1 Bracket #1

The first bracket on NGC 4151 is an unmatched bracket with only one calibrator file. In this case, the calibrator is TYC 3017-1666-1. There is no strong evidence for the fringe in any of the data reduction plots for this file. The scan water fall plot shown in figure 9.32, appears

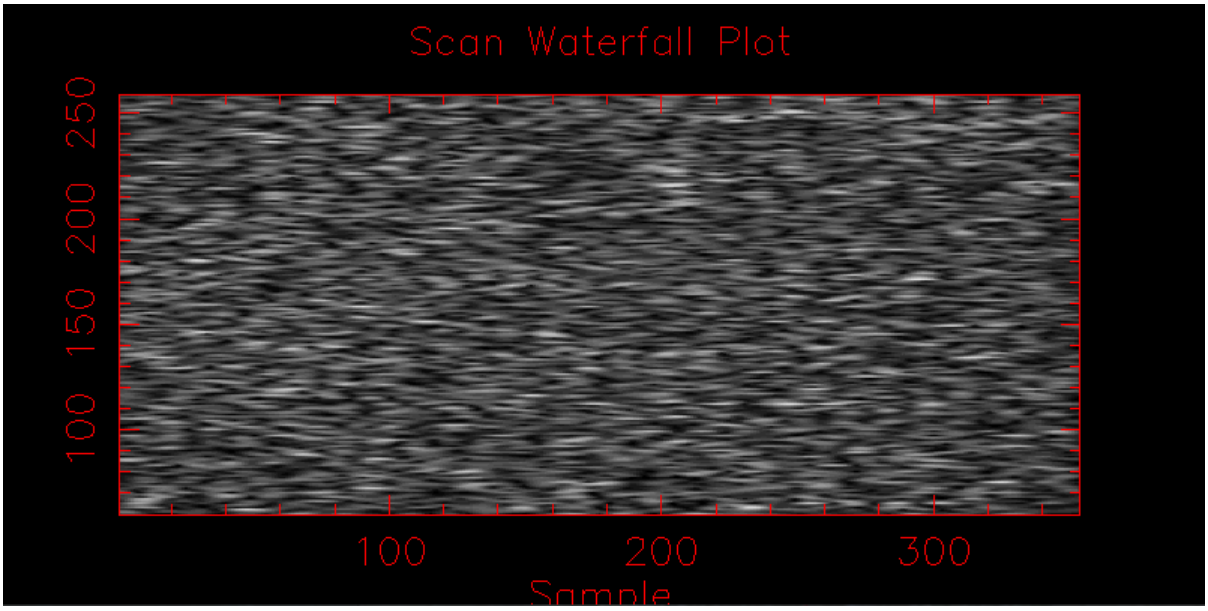

Figure 9.32 The scan waterfall plot for the data file on NGC 4151 taken on Apr 30, 2021.

to contain only noise. Similarly, the power spectra waterfall plot shown in figure 9.33, shows no convincing pattern for a fringe in the expected range between 40 and 60 Hz. Lastly, the noise subtracted mean power spectra (figure 9.34) shows no strong fringe envelope. It could be argued that there is an extremely weak fringe signal present in the noise subtracted mean power spectra due to the fact that the difference signal is consistently higher than zero in the expected frequency range.

Taking a look at the calibrator data, it is immediately clear that TYC 3017-1666-1 is significantly fainter than the other calibrators used. At a K-band magnitude of 8.7, this calibrator is much more like what is seen on NGC 4151 than the other calibrators. In both the scan waterfall plot (figure B.25 and the power spectra waterfall plot (figure B.26) the presence of the fringe is evident, though scattered due to the faintness of the object. Despite the faintness, the fringe is nicely visible in the noise subtracted power spectra (figure B.27).

With a faint calibrator, on par with the AGN, observing notes that specifically note exceptional observing conditions, and a possible fringe present in the noise subtracted mean power spectrum shown in figure 9.34, an attempt to reduce the data recorded on NGC 4151 is

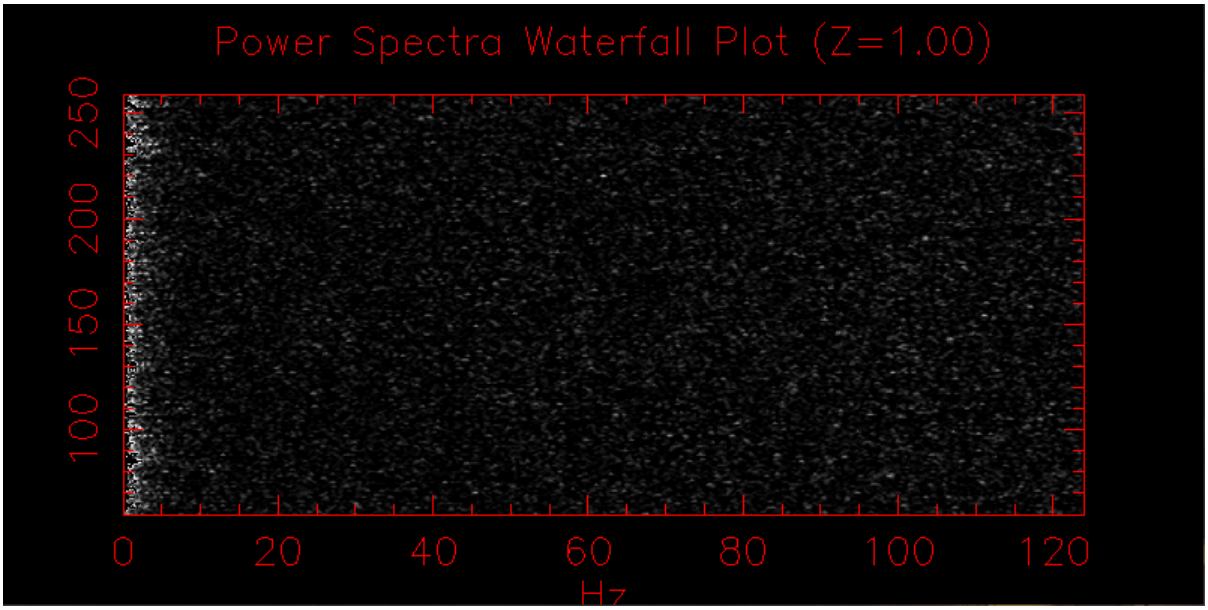

Figure 9.33 The scan power spectra waterfall plot for the first data file on NGC 4151 taken on Apr 30, 2021.

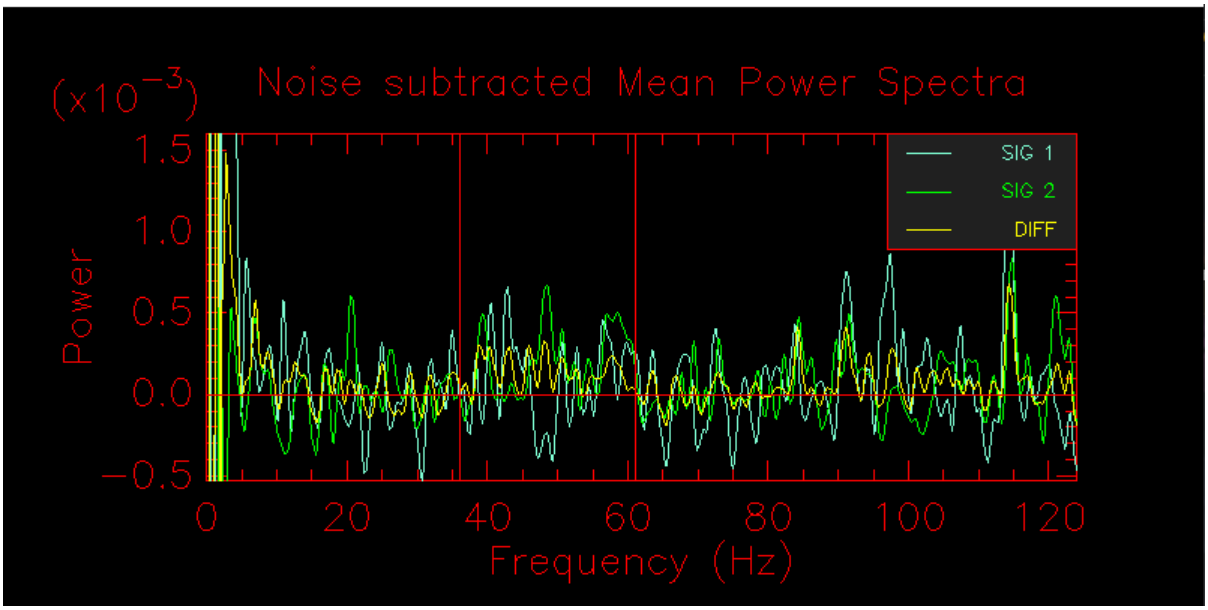

Figure 9.34 The noise subtracted mean power spectra waterfall plot for the first data file on NGC 4151 taken on Apr 30, 2021.

made. The file on the AGN, 2021_04_30_2MASS_J12103258+3924210_ird_001.fit, is reduced using the following command,

```
redfluor -dev xwin -D... -d1 -e -g -I36.0-61.0 -o3.0 -S2.0  2021_04_30_2MASS_J12103258+3924210_ird_001.fit.
```

Which reduces to

	Detector 1		Detector 2		Combined	
	Mean	StdDev	Mean	StdDev	Mean	StdDev
V2_MEAN_PS	0.07312	0.03960	0.17530	0.06328	0.10201	0.02032

The data on the calibrator TYC 3017-1666-1 contained in 2021_04_30_2MASS_J12111971+3914148_ird_001.fit is similarly reduced with the command

```
redfluor -dev xwin -D... -d1 -e -g -I36.0-61.0 -o3.0 -S2.0  2021_04_30_2MASS_J12103258+3924210_ird_001.fit.
```

Resulting in the following raw visibility:

	Detector 1		Detector 2		Combined	
	Mean	StdDev	Mean	StdDev	Mean	StdDev
V2_MEAN_PS	0.63235	0.13847	0.93320	0.15540	0.68396	0.08626

The AGN visibility is calibrated against the calibrator visibility using the command:

```
calibir -c -BV2_MEAN_PS -s0.0913-0.0023 320097 320264
```

This bracket calibrates with a reasonably low visibility as expected from such a weak fringe signal, As such, this data point will be kept.

9.3.6.2 Bracket #2

The second bracket recorded on April 30, 2021, was a complete bracket with calibrator files recorded on either side of the object recording. Once again, there is no obvious fringe present in the scan waterfall plot shown in figure 9.35. However, there is a consistent higher

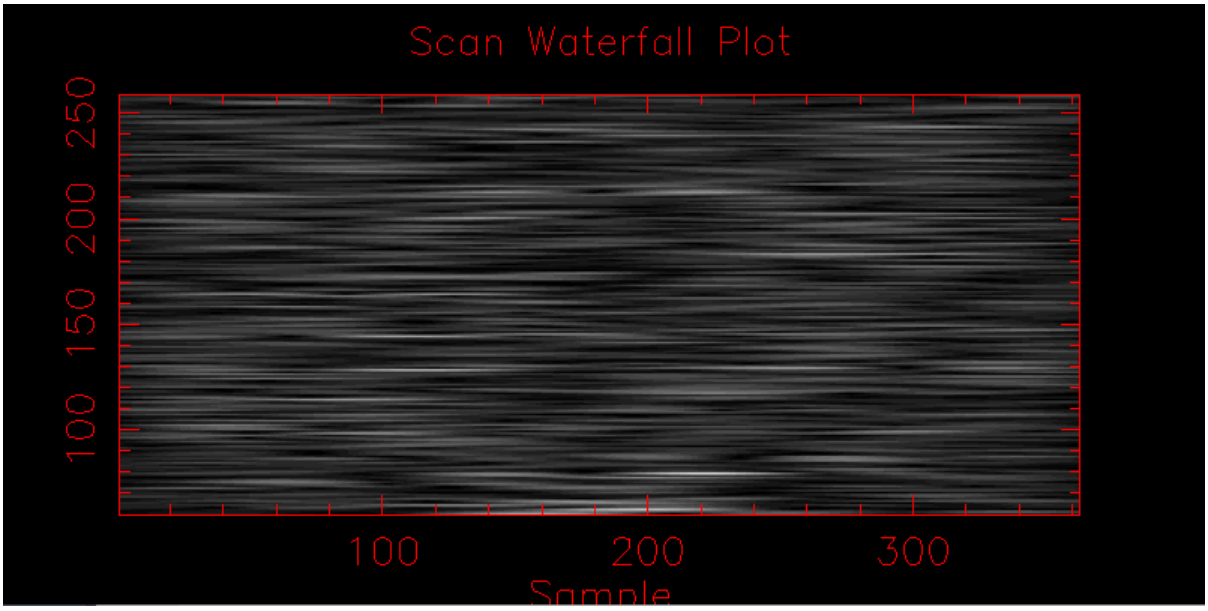

Figure 9.35 The scan waterfall plot for the second data file on NGC 4151 taken on Apr 30, 2021.

density of peaks in the fringe region of the power spectra waterfall plot shown in figure 9.36. Looking at the noise subtracted mean power spectra shown in figure 9.37, there is a very clear fringe present. The file on the AGN, 2021_04_30_2MASS_J12103258+3924210_ird_002.fit, is reduced using the following command,

```
redfluor -dev xwin -D... -d1 -e -g -I43.0-50.0 -o3.0 -S2.0  2021_04_30_2MASS_J12103258+3924210_ird_002.fit.
```

The first calibrator in this bracket SAO 62878 for which the scan waterfall, scan power spectra waterfall, and noise subtracted mean power spectra can be seen in figures B.28, B.29, and B.30 respectively, is reduced by,

```
redfluor -dev xwin -D... -d1 -e -g -I28.0-64.0 -o3.0 -S1.0  2021_04_30_SAO_62878_ird_001.fit.
```

And the second calibrator in this bracket HD 105881 is similarly reduced

```
redfluor -dev xwin -D... -d1 -e -g -I32.0-60.0 -o3.0 -S1.0  2021_04_30_HD_105881_ird_001.fit.
```

Where the normal scan waterfall can be seen in figure B.31, the scan power spectra waterfall can be seen in figure B.32, and the noise subtracted mean power spectra can be seen in figure B.33.

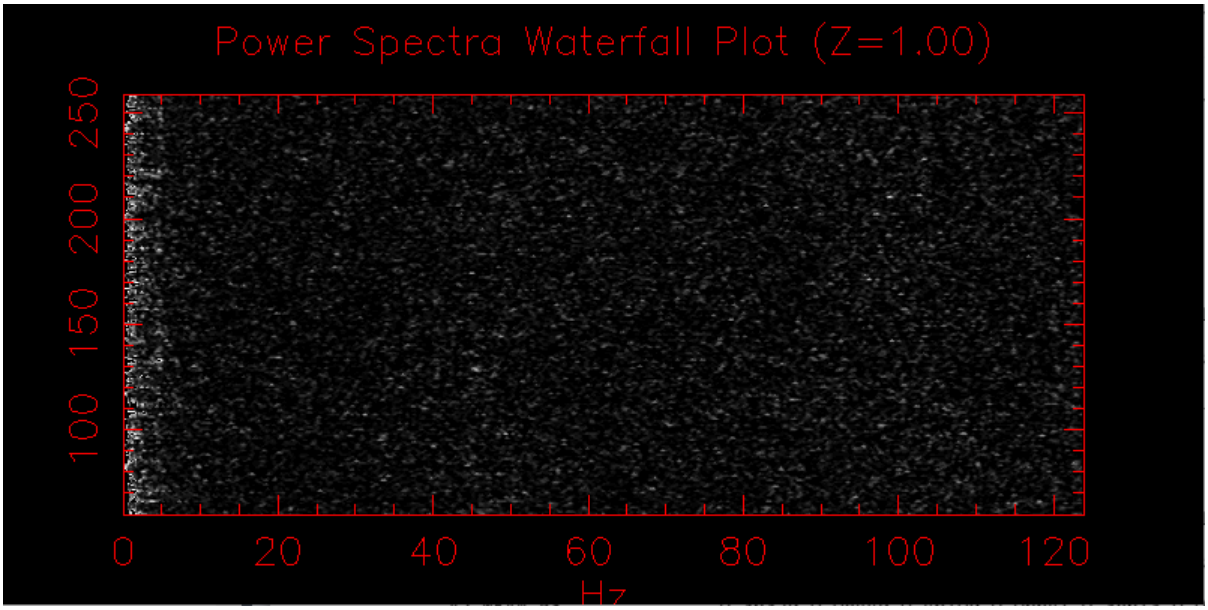

Figure 9.36 The scan power spectra waterfall plot for the second data file on NGC 4151 taken on Apr 30, 2021.

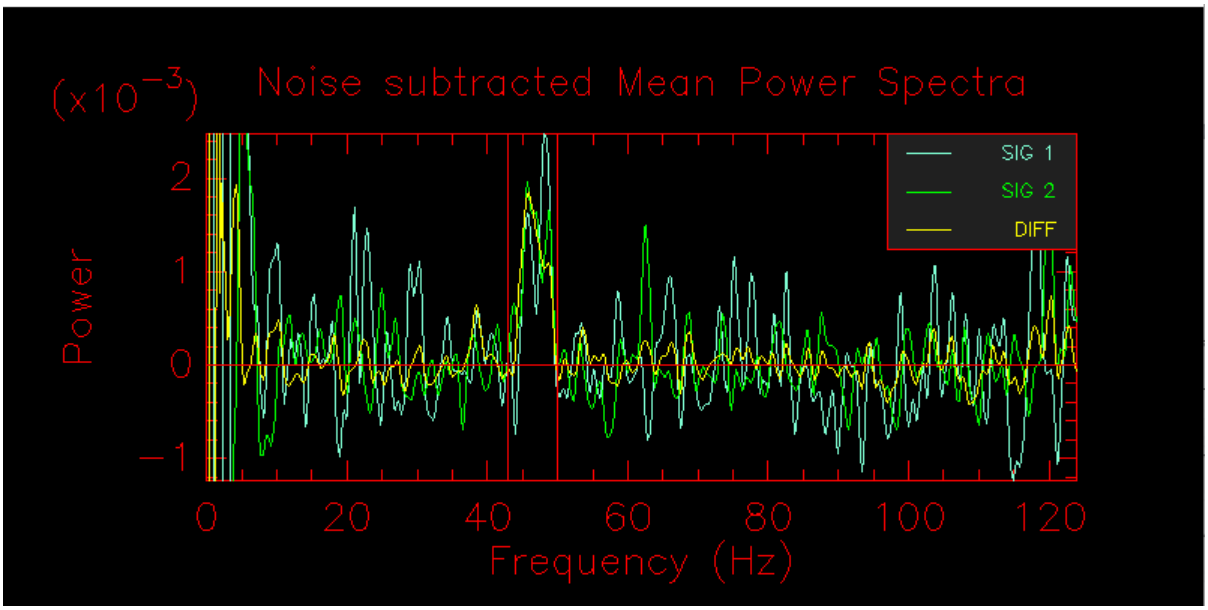

Figure 9.37 The noise subtracted mean power spectra waterfall plot for the second data file on NGC 4151 taken on Apr 30, 2021.

The CLASSIC data reduction pipeline results in the following raw visibilities for each of the files in this bracket. The AGN data contained in 2021_04_29_2MASS_J12103258+3924210_ird_002.fit results in:

	Detector 1		Detector 2		Combined	
	Mean	StdDev	Mean	StdDev	Mean	StdDev
V2_MEAN_PS	0.19817	0.11315	0.22964	0.08525	0.20057	0.05521

The first calibrator, SAO 62878, data contained in 2021_04_30_SAO_62878_ird_001.fit yeilds:

	Detector 1		Detector 2		Combined	
	Mean	StdDev	Mean	StdDev	Mean	StdDev
V2_MEAN_PS	0.62280	0.03624	0.59836	0.04643	0.53834	0.03369

Lastly, the second calibrator data recorded on HD 105881 and contained in 2021_04_30_HD_105881_ird_001.fit gives:

	Detector 1		Detector 2		Combined	
	Mean	StdDev	Mean	StdDev	Mean	StdDev
V2_MEAN_PS	0.35485	0.05285	0.46329	0.07013	0.35177	0.05447

These calibrator data are used to calibrate the NGC 4151 data using the command,

```
calibir -c -P -BV2_MEAN_PS -s0.0922-0.0021,0.1612-0.0038 320097 148118 148184
```

9.3.6.3 Bracket #3

The third bracket recorded on NGC 4151 on the night of April 30, 2021, which was by far the easiest observation made of the AGN. In some combination of good observing conditions, good optical alignment, and fortuitous position angle of the object, the fringe was obvious and easily tracked through the whole recording. In both the scan waterfall plot (figure 9.32) and the scan power spectra waterfall plot (figure 9.33), the fringe track is bright and obvious throughout the recording. The noise subtracted mean power spectra also contain a very

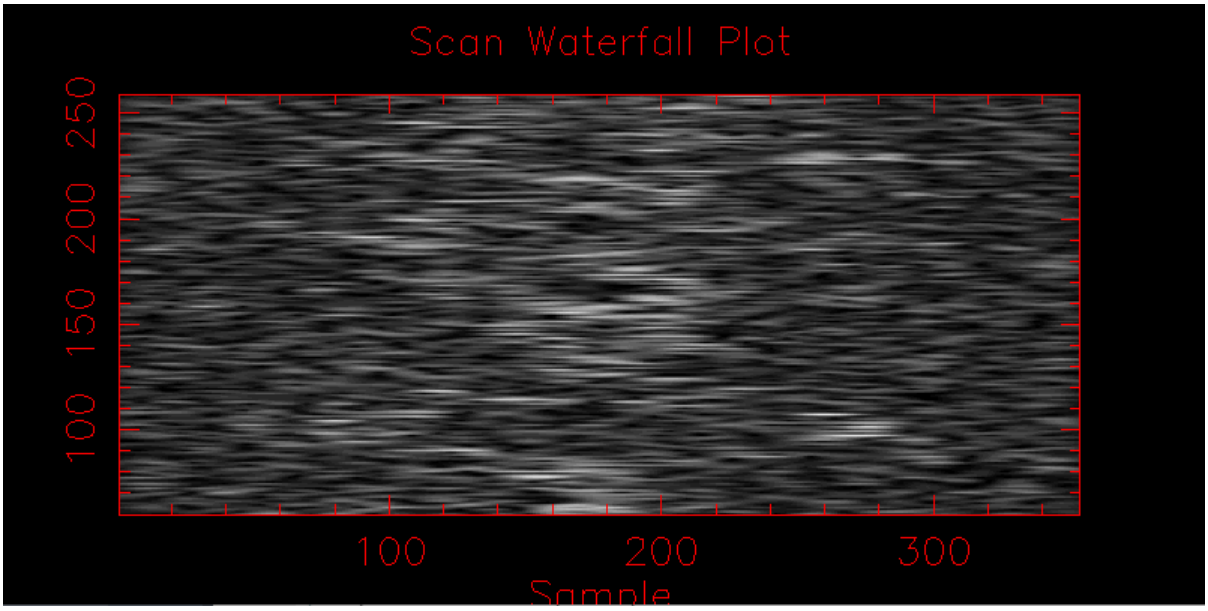

Figure 9.38 The scan waterfall plot for the third data file on NGC 4151 taken on Apr 30, 2021.

nice strong fringe as seen in figure 9.34. With such a strong fringe, no signal smoothing is required beyond the default in the CLASSIC reduction pipeline and the file for this recording named 2021_04_29_2MASS_J12103258+3924210_ird_003.fit is reduced by

```
redfluor -dev xwin -D... -d1 -e -g -I40.0-55.0 -o3.0 -S1.0  2021_04_30_2MASS_J12103258+3924210_ird_003.fit.
```

Which results in the following uncalibrated visibility:

	Detector 1		Detector 2		Combined	
	Mean	StdDev	Mean	StdDev	Mean	StdDev
V2_MEAN_PS	0.46576	0.09042	0.40611	0.03663	0.39334	0.03332

For both calibrator data sets, the fringes in both the scan waterfall plots and the scan power spectra waterfall plots show strong, consistent fringe signals. The first calibrator was, once again, SAO 62878 who's waterfall plots and noise subtracted mean power spectra can be seen in figures B.34, B.35, and B.36. The second calibrator remained HD 105881. The waterfall plots and noise subtracted mean power spectra can similarly be seen in figures B.37, B.38, and B.39. The data for the first calibrator contained in the file 2021_04_30_SAO_62878_ird_002.fit, is reduced as follows,

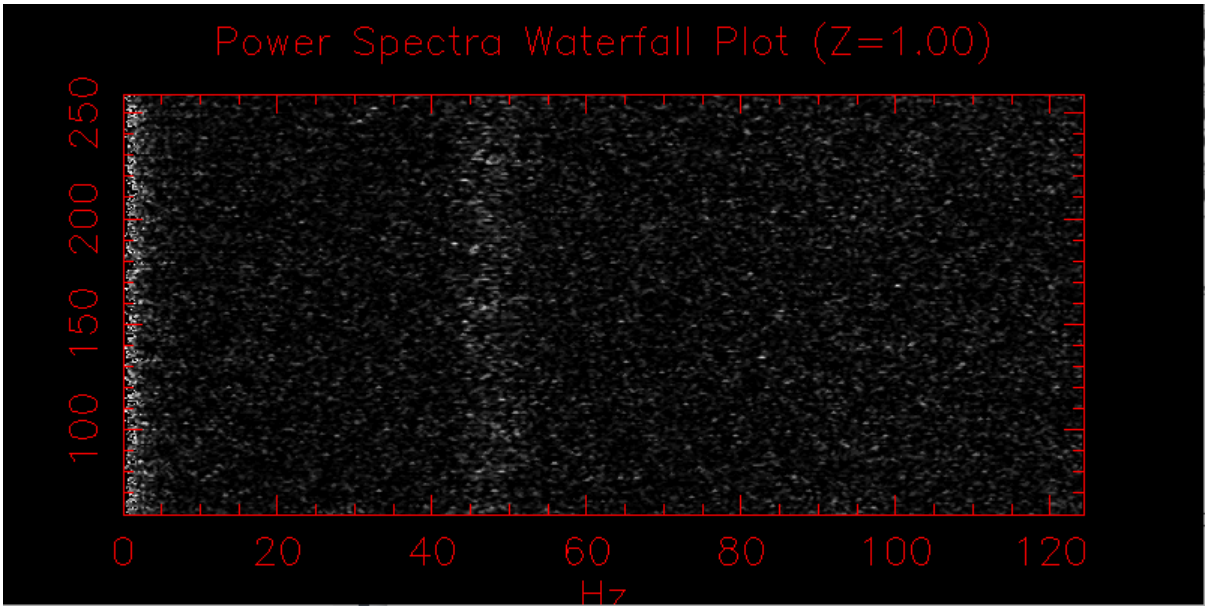

Figure 9.39 The scan power spectra waterfall plot for the third data file on NGC 4151 taken on Apr 30, 2021.

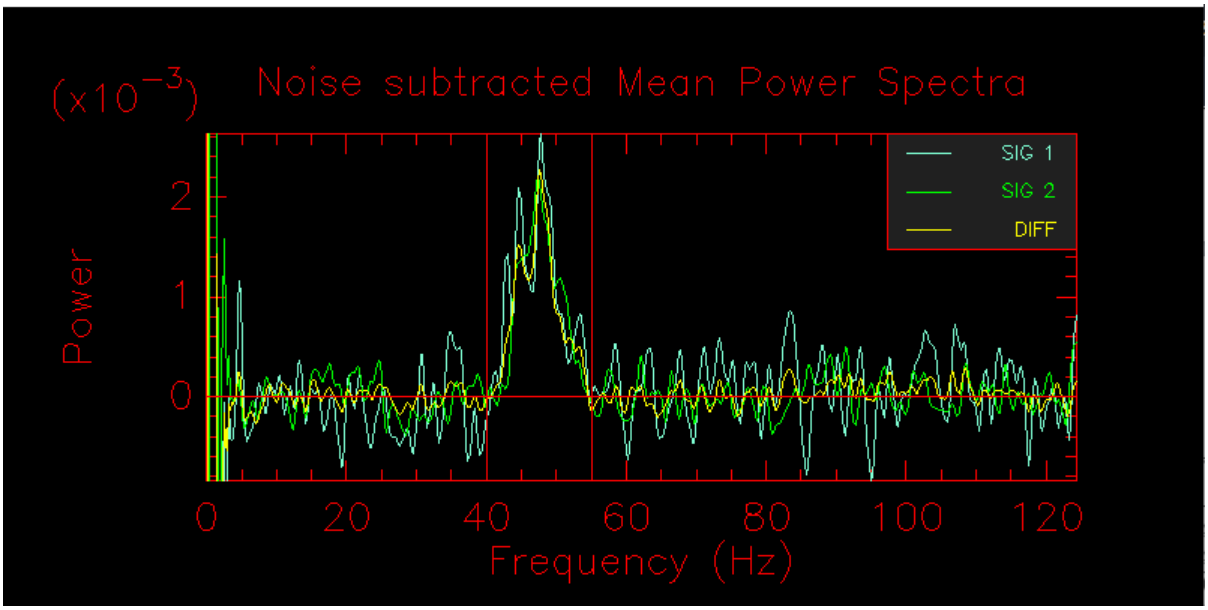

Figure 9.40 The noise subtracted mean power spectra waterfall plot for the third data file on NGC 4151 taken on Apr 30, 2021.

```
redfluor -dev xwin -D... -d1 -e -g -I41.0-55.0 -o3.0 -S1.0  2021_04_30_SAO_62878_ird_002.fit.
```

Resulting in these raw visibilities,

	Detector 1		Detector 2		Combined	
	Mean	StdDev	Mean	StdDev	Mean	StdDev
V2_MEAN_PS	0.60708	0.03840	0.54739	0.02493	0.53840	0.02092.

The second calibrator data contained in 2021_04_30_HD_105881_ird_002.fit is reduced the same way with a slightly different integration window,

```
redfluor -dev xwin -D... -d1 -e -g -I36.5-57.0 -o3.0 -S1.0  2021_04_30_HD_105881_ird_002.fit,
```

resulting in these raw visibilities,

	Detector 1		Detector 2		Combined	
	Mean	StdDev	Mean	StdDev	Mean	StdDev
V2_MEAN_PS	0.54515	0.02360	0.57544	0.01805	0.49773	0.01725.

Much as with the preceding brackets, this data file is used to calibrate the raw visibility for NGC 4151 using

```
calibir -c -BV2_MEAN_PS -s0.1612-0.0038,0.0922-0.0021 320097 148184 148118
```

9.3.6.4 Bracket #4

In several ways, the fourth bracket of data recorded on NGC 4151 is quite similar to the third bracket. Mainly, the notable presence of an obvious fringe in both the scan waterfall plot shown in figure 9.41 and the scan power spectra plot shown in figure 9.42. There is, however, a bit of a problem. In the background subtracted photometry plot shown in figure 9.43, there is a steady drop-off in the flux measured by the camera from scan 160 to scan 220 where the object drifted away from the tip-tilt system. To salvage the data contained in this file, the scans where the object was drifting away are edited out.

To edit the scans where the AGN was drifting away, the user has to click on the beginning and ending scans to be removed on a waterfall plot of the raw scan data. Shown in figure 9.44,

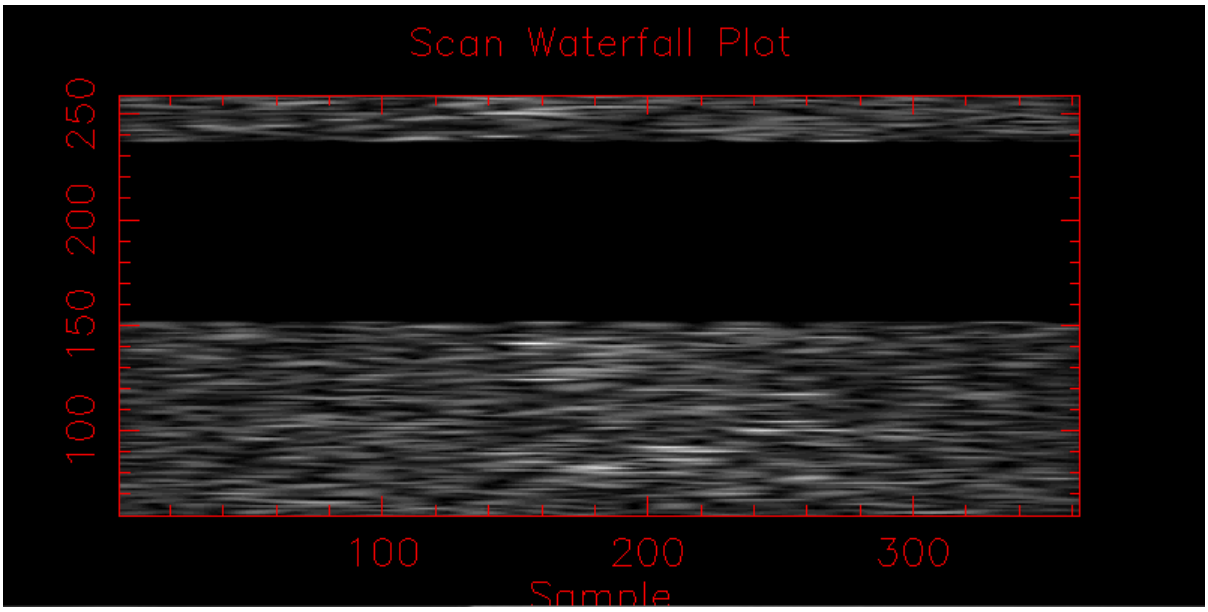

Figure 9.41 The scan waterfall plot for the fourth data file on NGC 4151 taken on Apr 30, 2021.

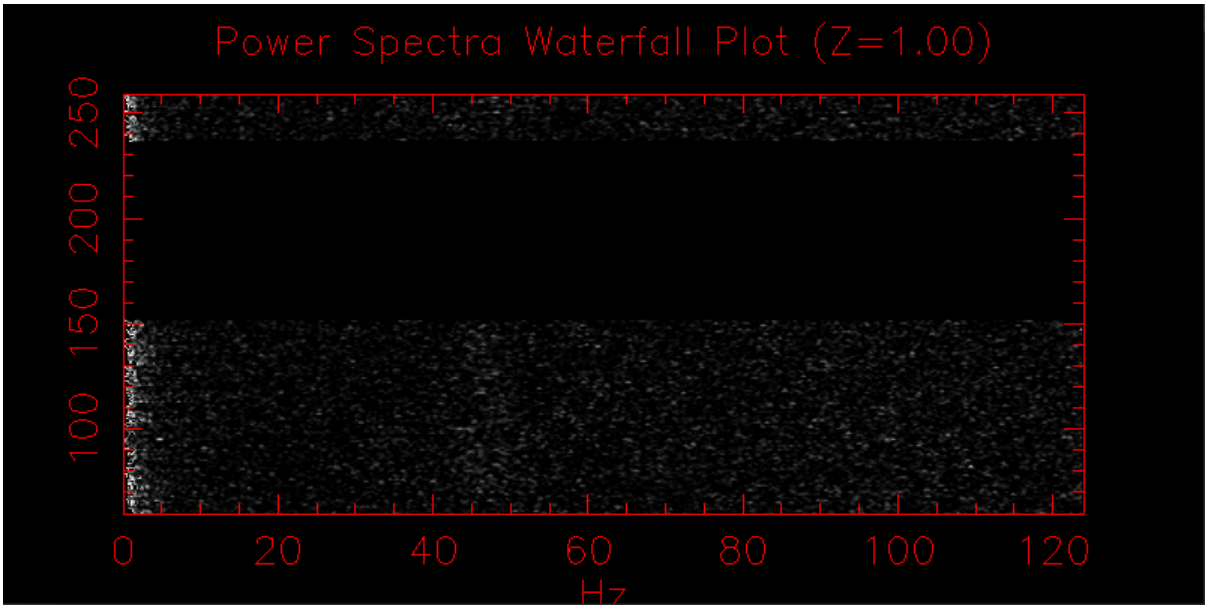

Figure 9.42 The scan power spectra waterfall plot for the fourth data file on NGC 4151 taken on Apr 30, 2021.

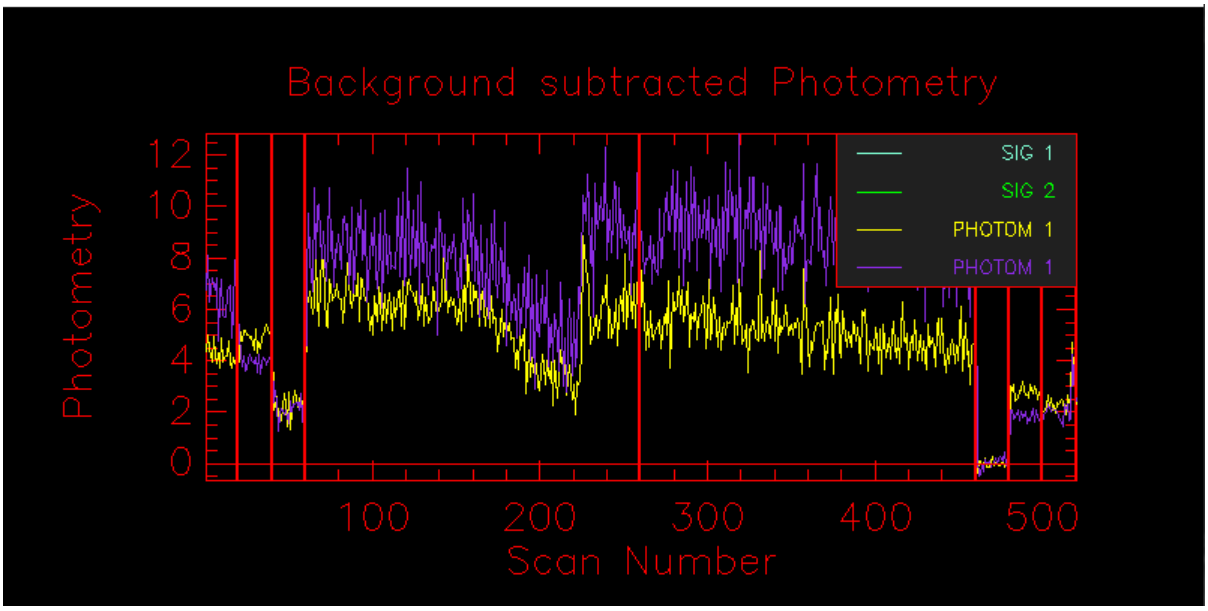

Figure 9.43 Background subtracted photometry plot for the fourth data file on NGC 4151 taken on Apr 30, 2021.

there is no obvious fringe visible. Without visible fringes in the scans, editing the data is by trial and error. An edit was selected and the reduction software allowed to continue until the power spectra waterfall plot was displayed. Based on the power spectra waterfall, the software would be restarted and a change to the edit region made. This process was repeated until the final edit was arrived upon. As shown in figure 9.42, there is a fringe signal both before and after the scan region that was removed.

With the data satisfactorily edited, the data reduction continues. The noise subtracted mean power spectra of the data after editing is shown in figure 9.45 with a clear fringe seen in the expected 40 to 60 Hz region. However, there is a strange negative signal on either wing of the fringe.

The data on NGC 4151 contained in the file

2021_04_29_2MASS_J12103258+3924210_ird_004.fit, is reduced by

```
redfluor -dev xwin -D... -d1 -g -I39.0-56.0 -o3.0 -S2.0  2021_04_30_2MASS_J12103258+3924210_ird_004.fit.
```

Which results in the raw visibility

```
                                Detector 1      Detector 2      Combined
```

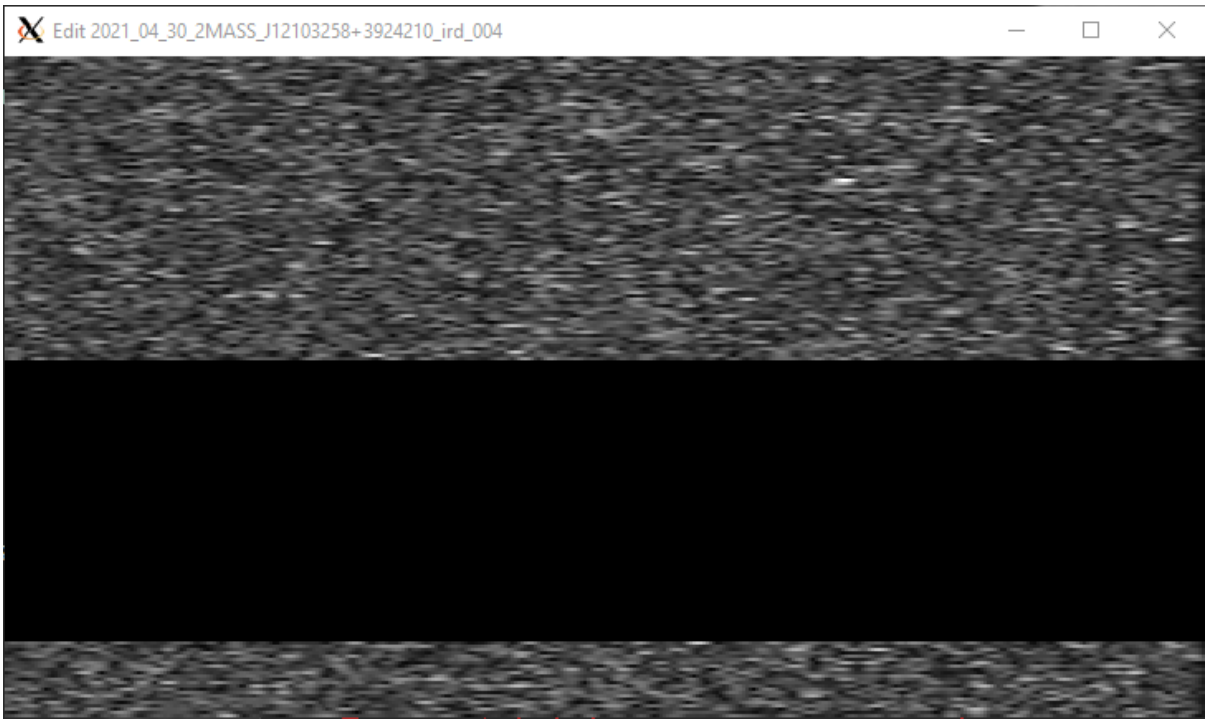

Figure 9.44 The scan editing window for the fourth data file on NGC 4151 taken on Apr 30, 2021.

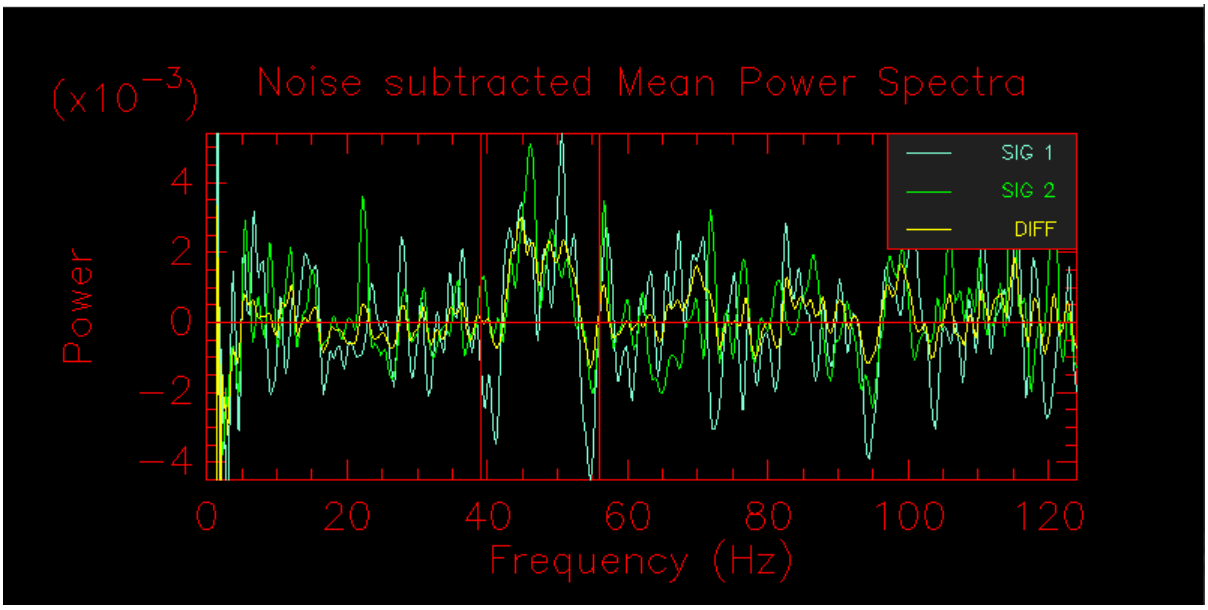

Figure 9.45 The noise subtracted mean power spectra waterfall plot for the fourth data file on NGC 4151 taken on Apr 30, 2021.

	Mean	StdDev	Mean	StdDev	Mean	StdDev
V2_MEAN_PS	0.24750	0.22721	0.50572	0.29048	0.53307	0.09562

The calibrator data of SAO 62878 in the file named 2021_04_30_SAO_62878_ird_003.fit is reduced by

```
redfluor -dev xwin -D... -d1 -e -g -I37.0.0-56.0 -o3.0 -S1.0  2021_04_30_SAO_62878_ird_003.fit,
```

results in the following raw visibilities:

	Detector 1		Detector 2		Combined	
	Mean	StdDev	Mean	StdDev	Mean	StdDev
V2_MEAN_PS	0.63186	0.07361	0.61131	0.03525	0.55241	0.04094.

This last set of data is calibrated by:

```
calibir -c -P -BV2_MEAN_PS -s0.0922-0.0021 320097 148118
```

9.4 Calibration Results

At the end of the discussion of each bracket of viable recorded data, a command for the calibration software "calibir" is shown. The resulting calibration of each of those commands is listed and tabulated in this section.

2020 Feb 15 Bracket 1:

#	Name	HD	Num	CHARA#	Type	MJD	WL	T1	T2	U(m)	V(m)	BL(m)	S1bal	S2bal	Vis	Stddev	Scans	Syst/Stat	Chi2	Vcal	Err	dT	HA
O	2MASS_J12103258+3924210		-1	320097	OBJ	58894.390	2.133	S1	S2	-0.57	33.94	33.94	0.92	1.21	0.4614	0.0721	71	1.0000	0.0819	1.0094	0.1578	0.00	-0.97
C		SAO_62878	-1	148118	CAL1	58894.399	2.133	S1	S2	-1.68	33.90	33.94	0.83	0.98	0.4570	0.0707	129						

2020 Feb 16 Bracket 1:

#	Name	HD	Num	CHARA#	Type	MJD	WL	T1	T2	U(m)	V(m)	BL(m)	S1bal	S2bal	Vis	Stddev	Scans	Syst/Stat	Chi2	Vcal	Err	dT	HA
O	2MASS_J12103258+3924210		-1	320097	OBJ	58895.347	2.133	S1	S2	4.30	33.63	33.91	1.05	1.65	0.5847	0.0888	101	1.0000	0.0717	1.1760	0.1786	0.00	-1.98
C		SAO_62878	-1	148118	CAL1	58895.357	2.133	S1	S2	3.12	33.79	33.93	1.06	1.39	0.4971	0.0577	118						

2021 Mar 19 Bracket 1:

#	Name	HD	Num	CHARA#	Type	MJD	WL	T1	T2	U(m)	V(m)	BL(m)	S1bal	S2bal	Vis	Stddev	Scans	Syst/Stat	Chi2	Vcal	Err	dT	HA
C		SAO_62878	-1	148118	CAL1	59292.288	2.133	S2	W1	-120.41	215.60	246.94	0.52	0.93	0.6015	0.0221	227						
O	2MASS_J12103258+3924210		-1	320097	OBJ	59292.323	2.133	S2	W1	-152.67	196.86	249.12	0.46	0.79	0.1606	0.0182	132	1.3654	0.3569	0.2965	0.0337	75.13	0.51
C		SAO_62878	-1	148118	CAL1	59292.341	2.133	S2	W1	-166.78	185.41	249.39	0.76	0.91	0.4859	0.0307	133						

2021 Apr 30 Bracket 2:

#	Name	HD	Num	CHARA#	Type	MJD	WL	T1	T2	U(m)	V(m)	BL(m)	S1bal	S2bal	Vis	Stddev	Scans	Syst/Stat	Chi2	Vcal	Err	dT	HA
C		SAO_62878	-1	148118	CAL2	59334.208	2.133	S2	W1	-152.30	197.11	249.09	0.64	1.01	0.5383	0.0337	184						
O	2MASS_J12103258+3924210		-1	320097	OBJ	59334.221	2.133	S2	W1	-163.44	188.37	249.39	0.75	0.96	0.2006	0.0552	94	1.2193	0.0123	0.4143	0.1142	42.43	0.19
C		HD_105881	105881	148184	CAL1	59334.237	2.133	S2	W1	-174.30	178.08	249.18	0.59	0.55	0.3518	0.0545	187						

2021 Apr 30 Bracket 3:

#	Name	HD	Num	CHARA#	Type	MJD	WL	T1	T2	U(m)	V(m)	BL(m)	S1bal	S2bal	Vis	Stddev	Scans	Syst/Stat	Chi2	Vcal	Err	dT	HA
C		SAO_62878	-1	148118	CAL2	59334.340	2.133	S2	W1	-201.91	97.71	224.31	0.96	1.27	0.5384	0.0209	186						
O	2MASS_J12103258+3924210		-1	320097	OBJ	59334.355	2.133	S2	W1	-198.96	85.71	216.63	1.00	2.58	0.3933	0.0333	140	1.0710	0.3857	0.7589	0.0645	39.05	3.00
C		HD_105881	105881	148184	CAL1	59334.367	2.133	S2	W1	-195.27	76.85	209.85	0.96	1.16	0.4977	0.0173	195						

2021 Mar 30 Bracket 4:

#	Name	HD	Num	CHARA#	Type	MJD	WL	T1	T2	U(m)	V(m)	BL(m)	S1bal	S2bal	Vis	Stddev	Scans	Syst/Stat	Chi2	Vcal	Err	dT	HA
C		SAO_62878	-1	148118	CAL1	59334.378	2.133	S2	W1	-190.74	67.61	202.37	1.02	1.32	0.5524	0.0409	181						
O	2MASS_J12103258+3924210		-1	320097	OBJ	59334.391	2.133	S2	W1	-184.40	57.66	193.20	1.91	3.10	0.5331	0.0956	69	1.0000	0.4042	0.9607	0.1723	0.00	3.90

Table 9.8. Calibrated CHARA Data Points of NGC 4151.

Date	Telescopes	Projected Baseline (m)	U (m)	V (m)	Visibility^2	Visibility^2 Error
2020 02 15	S1-S2	33.94	-0.57	33.94	1.0094	0.1578
2020 02 16	S1-S2	33.91	4.3	33.63	1.1760	0.1786
2021 03 19	S2-W1	249.12	-152.67	196.86	0.2965	0.0337
2021 04 30 B2	S2-W1	249.39	-163.44	188.37	0.4143	0.1142
2021 04 30 B3	S2-W1	216.63	-198.96	85.71	0.7589	0.0645
2021 04 30 B4	S2-W1	193.20	-184.40	57.66	0.9607	0.1723

Note. — The calibrated squared-visibility for each viable bracket of data.

The resulting data is tabulated in a more digestible format in table 9.8 and is displayed in figure 9.46. In which the visibility plot appears on the left with observations from each night color coded. Data measured within a single night are distinguishable by marker shape. The two thin ring visibility curves are added to give a perspective on what might be expected in the visibility function of the AGN. On the right, the UV point for each observation are displayed, showing across what region of sky the AGN was sampled during observations.

Although there are only a few data points, a couple of things are easily observed with regards to this data. Most importantly, observations at similar UV sampling are consistent with each other. Each of the six data points lies near to another and in each case, the measured visibility value is within the error bars of its nearest neighbor. Second, each of the neighboring sets of measurements measured on the W1-S2 baseline are reasonably fit by simple thin rings applied by eye. This indicates that the data is acceptable and worthy of analyzing.

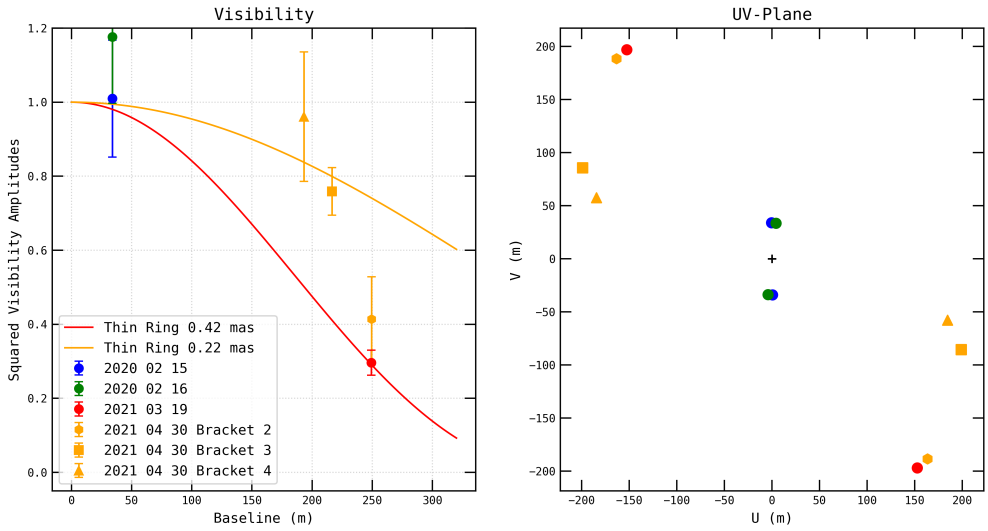

Figure 9.46 The standard visibility and uv-plane plots for the data on NGC 4151 from the CHARA Array.

CHAPTER 10
CHARA DATA ANALYSIS

As the data presented in chapter 9 appears to be good and self-consistent, it provides an opportunity for analysis of the shape and position of the NIR emitting region in the core of NGC 4151.

10.1 Supplementary Data: Keck Interferometer

To provide a bit more data for the analysis, the observations of NGC 4151 completed with the Keck Interferometer (Colavita & Wizinowich 2003) will be included. The Keck Interferometer combined the light from the two ten-meter telescopes at the W. M. Keck Observatory in the near-infrared and mid-infrared. With a baseline of 85 meters, the Keck Interferometer provides projected baselines in between the short 33 meter S1-S2 baseline and the long 250 meter W1-S2 baseline of the CHARA Array. The additional points from Swain et al. (2003a), Kishimoto, M. et al. (2011), and Kishimoto et al. (2013a) are listed in table 10.1, where the data listed includes the date of observation, the projected baseline, position angle, visibility, and uncertainty on the visibility. The UV-points in table 10.1 were derived from the projected baseline and the position angles listed.

The combined CHARA observations and Keck Interferometer observations of NGC 4151 can be seen in figure 10.1. The added Keck Interferometer data, shown in cyan clearly provides supplementary sampling of the UV-plane both in the position angle offset to the S1-S2 data as well as sampling the projected baseline space between the two CHARA baselines used.

10.2 The Gaussian Model

The simplest geometric model for the dust sublimation region around the super massive black hole at the heart of an AGN that still provides some information about the dust distribution in the region is a Gaussian disk. While previously described in section 6.2 in a simplified

Table 10.1. Keck Interferometer Data Points.

Date	Projected Baseline (m)	Position Angle	u (m)	v (m)	V^2	V^2 Error	Source
2003 05 21	82.7	37.0	66.05	49.77	0.84	0.06	§
2010 05 01	72.4	51.0	45.56	56.27	0.920	0.017	†
2010 05 01	81.3	40.7	61.64	53.02	0.878	0.049	†
2010 05 02	84.9	21.7	78.90	31.39	0.883	0.048	†
2011 06 14	84.9	5.6	66.05	49.77	0.961	0.104	‡
2012 05 03	84.9	22.9	84.49	8.28	0.714	0.079	‡
2012 05 04	81.3	40.6	78.21	33.04	0.791	0.105	‡

Note. — Supplementary data on NGC 4151 measured by the Keck Interferometer. Sources: § Swain et al. (2003a) † Kishimoto, M. et al. (2011) ‡ Kishimoto et al. (2013a)

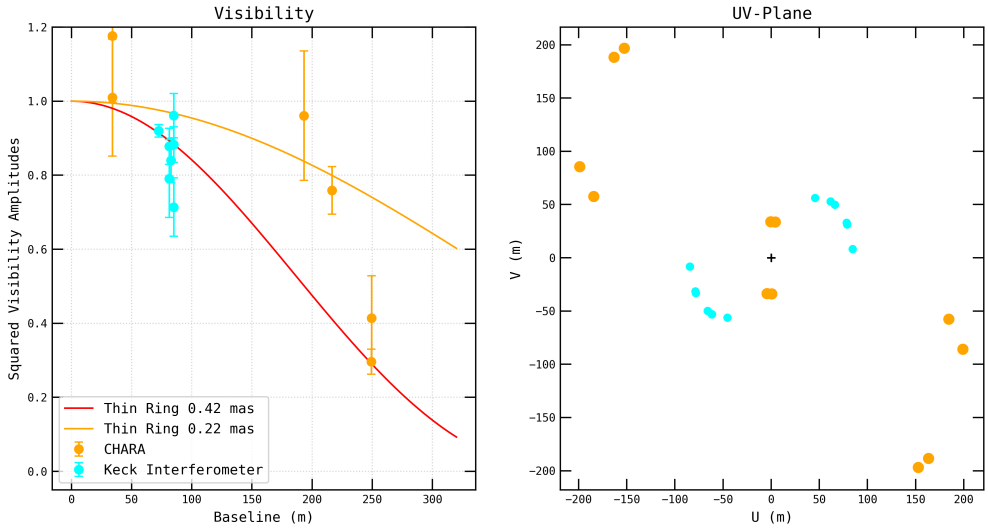

Figure 10.1 The standard visibility and uv-plane plots for the data on NGC 4151 from the CHARA Array and the Keck Interferometer.

form, for this practical application, the intensity distribution is now better described with the mathematical function of Berger & Segransan (2007),

$$I(\alpha,\beta) = \frac{1}{\sqrt{\pi/4\ln 2\phi}} \exp - \left(\frac{4\ln 2\rho^2}{\Theta^2}\right) \text{ where } \rho = \sqrt{\alpha^2+\beta^2}. \tag{10.1}$$

In which Θ is the full width at half maximum (FWHM) of the Gaussian, α and β are the physical coordinates of the sampling point. The visibility function then is

$$V(u,v) = \exp\left(-\frac{(\pi\Theta r)^2}{4\ln 2}\right), \tag{10.2}$$

where r is the coordinate in the plane given by

$$r = \sqrt{u^2+u^2} \tag{10.3}$$

Given that the AGNs are not expected to be viewed face-on, or at any particular position angle, provisions must be added to equation 10.3 to allow for different views of the object. Introducing the position angle ϕ and inclination angle i allows the view to be rotated as a general coordinate transform in three dimensions.

$$r = \sqrt{(u\cos\phi + v\sin\phi)^2 + ((-u\sin\phi + v\cos\phi)\cos i)^2} \tag{10.4}$$

It is the position angle and the FWHM considered in concert with the inclination angle which will reveal some aspects of the shape of the dust forming region around the AGN.

10.3 The Thin Ring Model

A slightly more complicated geometry that may nicely describe the dust emitting region around an AGN is the thin ring model previously described in section 6.2. The thin ring model is described by an intensity distribution where all model flux appears at the specified

radius from the center and is accompanied by a known visibility function. This intensity distribution is described mathematically as,

$$I(\rho) = \frac{1}{2\pi\rho_0}\delta(\rho - \rho_0). \tag{10.5}$$

Where ρ_0 is the radius at which the ring appears. The visibility function is described by a zeroth-order Bessel function of the first kind and appears as

$$V(u,v) = J_0(2\pi\rho_0 r), \tag{10.6}$$

in which,

$$r = \sqrt{u^2 + v^2}. \tag{10.7}$$

For fitting a thin ring model to interferometric data, the fact that the result is not expected to be face-on must be taken into account. As with the Gaussian disk in section 10.2, equation 10.7 needs to be modified. The same transform in equation 10.4 is applied.

10.4 Model Fitting of the NGC 4151 Observations

With a model function relating the model visibility to the sampled point on the uv plane, the data observed with the CHARA Array and the additional data from the Keck Interferometer shown in figure 10.1 can be fitted by a model Gaussian disk and a thin ring to reveal the measured radius, position angle and inclination angle of the dust sublimating region around NGC 4151.

All model fitting of the NGC 4151 observations will be done using Optical Interferometry Tools (OITOOLS), a software package written by Dr. Fabien Baron in the Julia programming language specifically for dealing with OI data. The package contains many functions relating to OI, including observation preparation, creation of simulated data sets for various optical interferometers, model fitting, and image reconstruction. Within its model fitting functions, OITOOLS contains a number of options for fitting observed data with simple visibility

functions including both the Gaussian disk and the thin ring. Using this framework, both models will be fit to the data independently. The position angle, inclination angle, and the FWHM or radius from the resulting fits will place constraints on the orientation of NIR emitting material near the AGN.

Using a built-in function of OITOOLS, both the Gaussian disk and thin ring models' three parameters are fit to the observed interferometric data. As input, the function takes the observed data, a predefined model for the thin ring which includes acceptable ranges for the three parameters as well as a few additional options. The function then calculates the log-likelihood and prior information for the model and provides them to Ultranest, a nested sampling Bayesian inference model fitting engine (Buchner 2021). The Ultranest fitting algorithm returns the maximum likelihood estimate (MLE) for the thin ring model parameters which fit the observed data.

To fit the Gaussian disk model to the observed data, model parameter ranges must be defined. The FWHM of the Gaussian was set to a range of 0 to 3 mas. The inclination angle was allowed to range from 0 to 90 degrees. Lastly, the position angle was given a range from 0 to 180 degrees. The fitting routine returns the MLE for the model parameters given the observed data, listed in table 10.2. These parameter values given by the MLE are accompanied by a reduced χ^2 value of 1.29.

Similarly, the model parameter ranges must be fixed for the thin ring model. For the radius of the ring, the range is set at 0 to 1 mas. The position angle is allowed to vary from 0 to 180 degrees. Lastly, the inclination angle is allowed to vary from 0 to 90 degrees. The fitting routine returns the MLE for the model parameters given the observed data, which is listed in table 10.2. These parameter values given by the MLE are accompanied by a reduced χ^2 value of 1.19.

Along with the MLE for the model parameters, Ultranest also gives a traditional Corner plot (Foreman-Mackey 2016). The Corner plot for the Gaussian disk Ultranest Monte Carlo ensemble (MCE) fit is shown in figure 10.2a and the Corner plot for the thin ring fit is

Table 10.2. Ultranest model fits for NGC 4151.

Model	Fit Type	Radius (mas)	Position Angle (deg)	Inclination Angle (deg)
Gaussian	MLE	0.454	85.316	68.146
Gaussian	MCE	$0.37^{+0.08}_{-0.06}$	$90.28^{+47.66}_{-41.88}$	$39.11^{+30.07}_{-26.14}$
Thin Ring	MLE	0.518	82.317	64.679
Thin Ring	MCE	$0.42^{+0.09}_{-0.06}$	$87.90^{+48.48}_{-38.03}$	$39.76^{+29.00}_{-26.67}$

Note. — Fit parameters for the visibility models applied to the combined CHARA and Keck Interferometer data.

displayed in figure 10.2b. The one-dimensional histograms on the diagonal show the fit for each parameter in a MCE and the two-dimensional histograms with contours show the correlation between the ensemble of each parameter with the other. Note that the order of terms for the Gaussian disk model and the thin ring model shown in the Corner plots is not the same. The histograms for both model fits show that the two models are doing very nearly the same thing where the FWHM and ring radius are performing the same job. The final terms for each model, both the MLE and MCE results, agree very well. Furthermore, the histograms for FWHM/ring radius and position angle along the diagonal indicate the strong dependence of the model on that parameter regarding fitting the observed data. The relatively flat histogram for the inclination angle for both models suggests that the fit for the inclination angle is not well established. This is very likely due to a degeneracy where the data can be fit with different ring radii and position angles and a wide variety of inclination angles to achieve a similar quality of fit. Overall, the uncertainties for both position angle and inclination angle fits show that the fit is not particularly well constrained. The only true way to solve this is to acquire more data to fill in the UV-plane in that direction.

The MLE model visibility for a Gaussian disk fitted to the CHARA and KI data is shown in figure 10.3. On the top, the measured squared visibilities with error bars are shown in

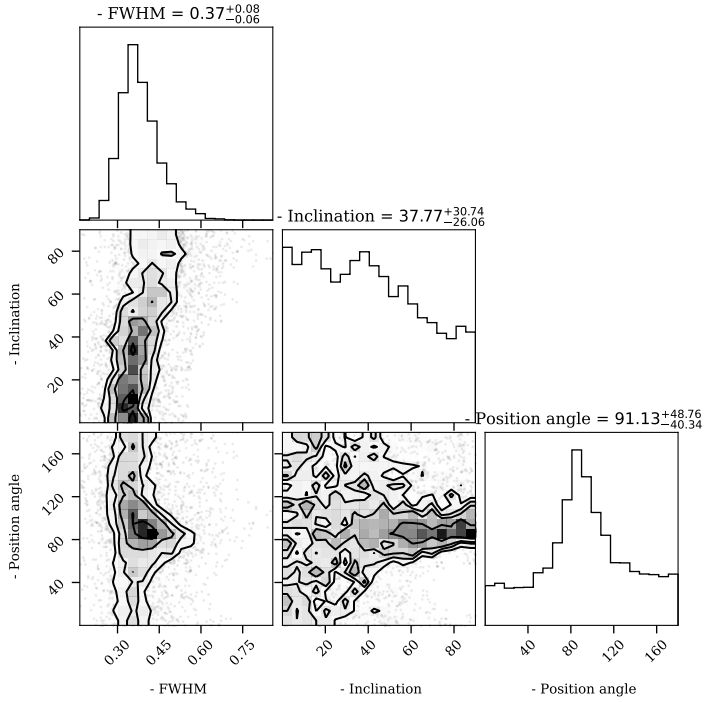

(a) Gaussian disk model fit.

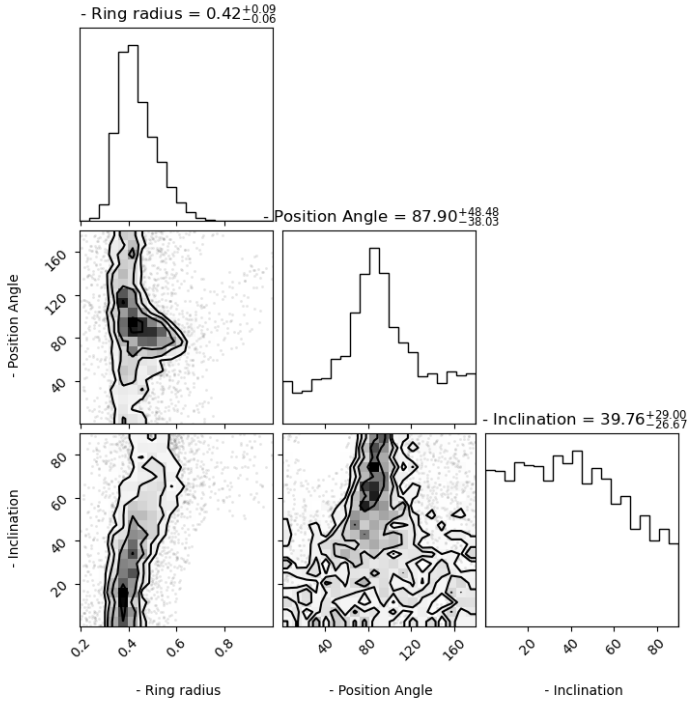

(b) Thin ring model fit.

Figure 10.2 Ultranest corner plots for model fits to combined CHARA and Keck Interferometer data.

black with the model sampled visibilities shown in red. On the bottom, the residuals on the model fit are shown in number of sigmas.

10.5 Results of the NGC 4151 CHARA Observations

The combined CHARA and KI data with a position angle between 82 and 90 degrees depending on the model is in agreement with the position angle measured at radio wavelengths. The average P.A. over the whole jet seen in the radio is 77 degrees with the P.A. of 83 degrees near the nucleus (Ulvestad et al. 1998). Where the nucleus lies in the component labeled D in the VLBA+VLA composite radio image shown in figure 10.4a (Ulvestad et al. 2005). Remarkably, both the P.A. measured here and the radio measurement appear to be in agreement with a 100pc bicone outflow approximately aligned with the measured P.A. of the jet shown in figure 10.4b from Kishimoto et al. (In Prep). To further show the agreement, the radio image and the 100pc flux distribution are shown with a model image of the Gaussian disk fit to the CHARA and KI data with the position angle of the disk shown as a red line in figure 10.4. The geometries indicated by each of the images and the model line up.

The distance to NGC 4151 was measured using the dust parallax method combining the interferometric data of the KI and K-band reverberation lag measurements yielding a precise measurement of $19.0^{+2.4}_{-2.6} Mpc$ (Hönig et al. 2014). Though variable, Koshida et al. (2009) found an average K-band lag time corresponding to a dust sublimation radius of 0.4 pc (Koshida et al. 2009). Assuming the dust parallax distance measurement, the average radius combining both the Gaussian and Thin ring model fits listed in table 10.2, a dust sublimation radius of 0.4pc is confirmed. This indicates that the longer baseline sampling provided by the CHARA Array measurement does not significantly alter the conclusion made on the KI data alone.

Although the inclination angles from the two model fits to the CHARA and KI data are very uncertain, the consensus between the two models suggests an inclination of about 38

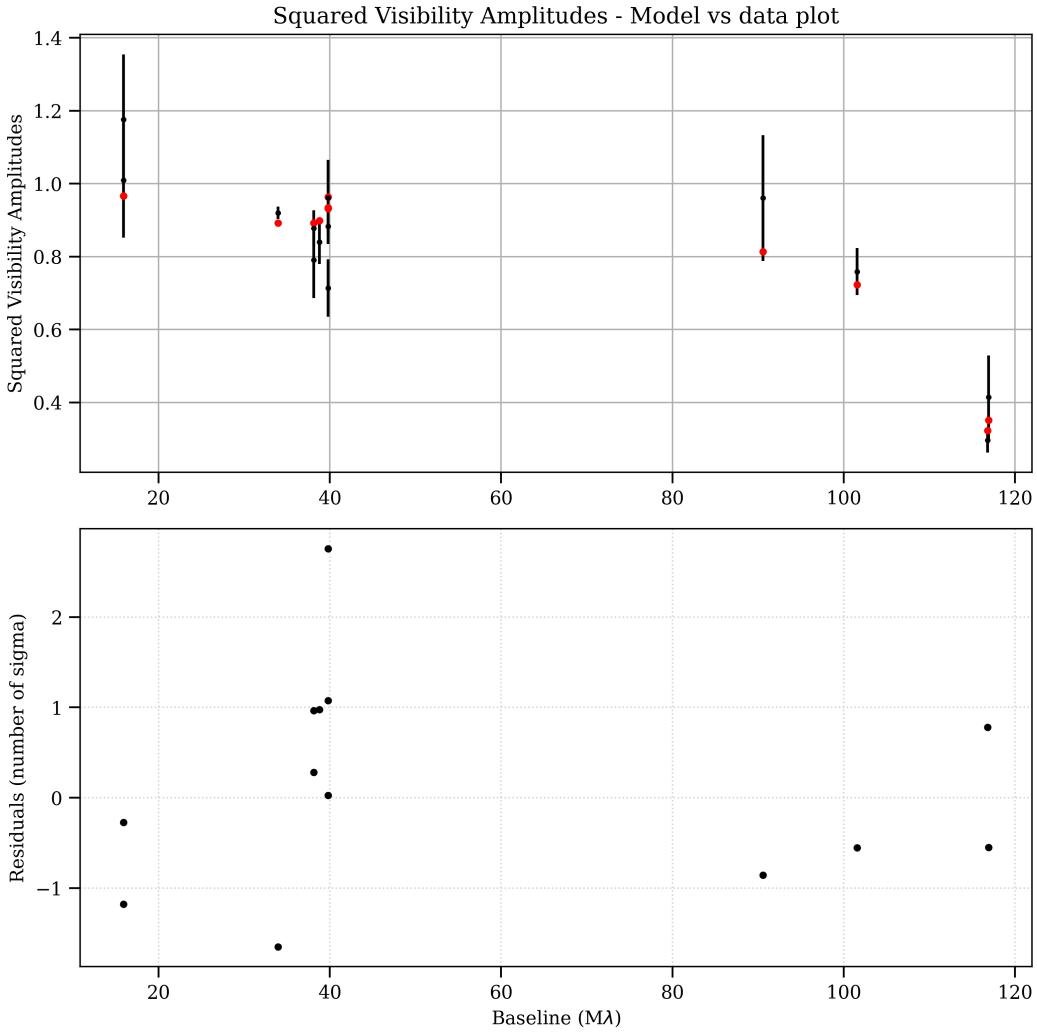

Figure 10.3 Gaussian disk model fit to the CHARA data of NGC 4151 with supplementary data from KI. (top) Showing measured squared visibilities with uncertainties in black and the resulting model sampled visibilities in red. (bottom) Showing the residuals on the fit in number of sigma.

degrees. Once again turning to the radio, Pedlar et al. (1993) measured the inclination of the inclination of the radio jet at 40 degrees. Again a consistent measurement!

The NIR emission is extended in a direction perpendicular to the axis of the jet. Outflows and disk winds seen in the MIR might lead one to expect that the NIR emission would be extended in the direction of the jet as well. However, this orientation of the compact NIR emission source in the core of NGC 4151 fits well with the conclusions found with the VLTI in the MIR and NIR, backing the conclusions of Hönig (2019) for the new torus model illustrated in figure 6.4.

10.6 Prospects for future AGN Observations at CHARA

While interferometry of AGN is likely to remain challenging, a number of ongoing developments in the field should make it easier and more rewarding in the coming years. The recent deployment of the GRAVITY beam combiner at the VLTI should produce interesting data and images in the near future. A new generation of detectors being deployed at the CHARA Array in the form of a replacement for the CLASSIC beam combiner named SILMARIL that will increase the sensitivity limit of CHARA by 2 magnitudes with the new camera and the potential for an additional 1 magnitude with the addition of cold optics dewar. This would bring the limiting magnitude for CHARA to approximately 12th magnitude in K-band allowing for the study of a number of AGNs with long baselines. The eventual completion of the MROI combining long baselines and larger apertures is sure to lead to delightful images of AGNs in the future. Further concluding remarks can be found in section 11.2.

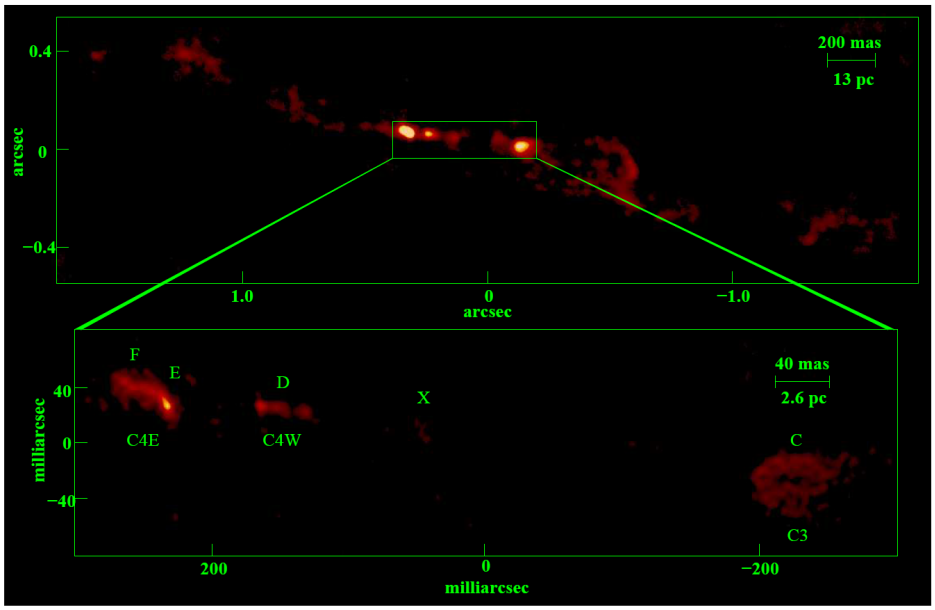

(a) VLBA+VLA composite radio image of NGC 4151 from Mundell et al. (2003).

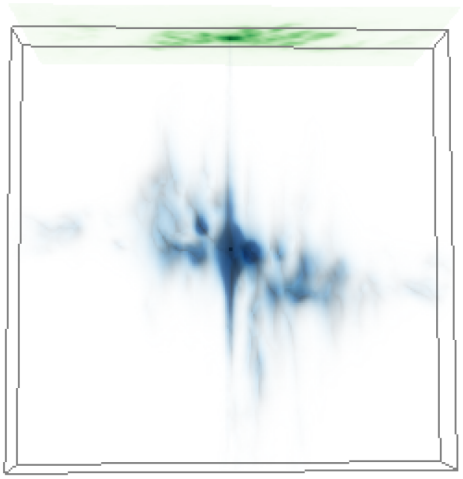

(b) Reconstructed Three Dimensional flux distribution at 100pc scale from HST data. From Kishimoto et al. (In Prep)

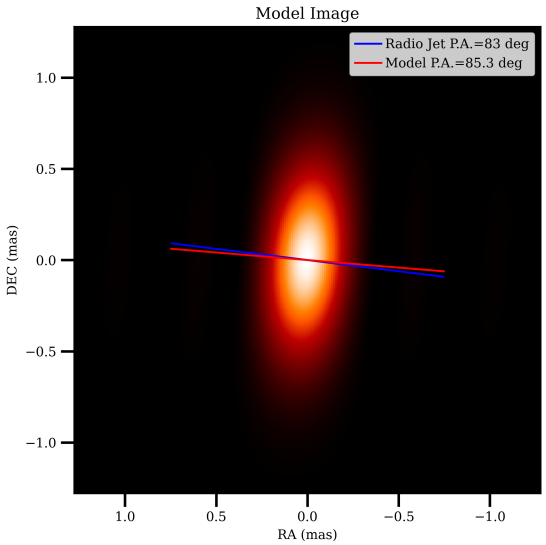

(c) Image of Gaussian Disk fit to CHARA + KI data. This Work.

Figure 10.4 Views of NGC 4151 at various scales.

CHAPTER 11
CONCLUSIONS

11.1 Reverberation Mapping and the TLDR Algorithm

The development of a VDM reconstructing algorithm began as a bit of side project, but quickly evolved into a significant undertaking. Despite some complications, the development of the TLDR algorithm has been successful. The original aim was to bring compressed sensing regularization to RM where MEM has dominated since the very beginning of VDM reconstructions. In this, the TLDR algorithm is successful and does it's job well. The flexibility and simplicity of the algorithm's implementation makes prospects for future improvements straightforward from the programmer's perspective.

The VDMs reconstructed with TLDR of the Arp 151 data from the LAMP2008 project show that more sparse VDMs can be recovered. However, these VDMs appear very similar to VDMs reconstructed with other inverse methods. On one hand, this means that no new information has been revealed about the BLR. On the other hand, this suggests that the inverse methods used are all working. The glaring remaining problem is that the VDMs constructed using the forward method of dynamical modelling bear little to no resemblance to any of the VDMs reconstructed with inverse methods. The forward method relies on a library of phenomenological models, so we are left to conclude that something is quite wrong with either the deconvolution used in the inverse methods, or there are no phenomenological models in the library used for the forward method which reflect the actual geometry of the BLR, or some combination of both.

A logical next step to address the apparent incompatibility between the VDMs reconstructed via forward and inverse methods is to combine the two. A library of VDMs could be built based on phenomenological models which could then be used to train a machine learning regularizer to apply to an inverse method. The ADMM loop at the core of TLDR is well suited to adding such a regularizer and poses a good next step in the evolution of the TLDR algorithm.

With ongoing RM observational campaigns, data is becoming available with higher observational cadence posing opportunities for more VDMs to be reconstructed. As more VDMs are available, the community will learn more about the physical geometry of the BLR and the heart of AGNs in general. Despite the quality and amount of data increasing, working on VDM reconstruction remains difficult due to the arduous process of preparing spectra for the TLDR or any other VDM reconstructing algorithm. Despite the challenges, work should continue on studying the geometry of the BLR via RM as at present it remains the only way to probe these regions with high resolution.

11.2 Interferometry of AGN at CHARA

After many nights of struggling to get fringes on NGC 4151, data was finally acquired. Even with AO, AGN observations at CHARA are still a difficult prospect due to sensitivity constraints. However, the strategies developed here can be used in order to increase the chance of successful observations in the future.

The data obtained on NGC 4151 pose a significant step forward for the CHARA Array as the first extra galactic result for the array. The finding that the NIR emission is extended perpendicular to the radio jet offers confirmation of the current evolution of the unified model for AGNs. The NIR result obtained with the CHARA Array is precisely that which would be expected from the two component model developed in through MIR interferometry. As shown in figure 6.4 the two component model, with the diffuse cone along the polar axis and the dense torus-like structure on along the equatorial axis, expects the NIR emission stemming from the dust sublimation radius to occur perpendicular to the polar axis at the base of the polar-extended structure and coincident with the inner edge of the torus-like structure. Further study of type 1 AGNs at CHARA in the NIR have the potential to further confirm the evolving Unified Model of AGN, or to provide contradictory evidence.

The relatively high visibilities measured with the long 250m baseline between the S2 and W1 telescopes at CHARA show that even longer baselines are necessary to study type 1

AGNs. At present no other optical interferometer has baselines long enough to truly constrain the sizes of these distant objects. Observations will continue of NGC 4151 at CHARA with a focus on obtaining complementary uv sampling using other long baselines. The prospects for using 3 telescopes to obtain a closure phase with the forthcoming SILMARIL instrument offers an exciting future option. In addition, the increased sensitivity promised for SILMARIL opens a significant number of other type 1 AGNs for study at CHARA.

Ultimately, the CHARA array should continue to dedicate observing time to AGN observing campaigns. The potential scientific impact of high resolution study type 1 AGNs in particular is great in terms of refining the Unified Model for AGN. The long baselines available and sensitivity improvements under development for the CHARA Array means that the facility is uniquely poised to make significant contribution to the field in the next few years.

Bibliography

Anderson M. D., Baron F., Bentz M. C., 2021, MNRAS, 505, 2903

Antonucci R., 1993, ARA&A, 31, 473

Armstrong J. T., et al., 1998, ApJ, 496, 550

Asmus D., 2019, MNRAS, 489, 2177

Baron F., et al., 2012, in Delplancke F., Rajagopal J. K., Malbet F., eds, Society of Photo-Optical Instrumentation Engineers (SPIE) Conference Series Vol. 8445, Optical and Infrared Interferometry III. p. 84451E (arXiv:1207.7141), doi:10.1117/12.924907

Batiste M., Bentz M. C., Raimundo S. I., Vestergaard M., Onken C. A., 2017, ApJ, 838, L10

Bennett A. S., 1962, Memoirs of the RAS, 68, 163

Bentz M., 2009, Improving the Radius-Luminosity Relationship for Broad-Lined AGNs with a New Reverberation Sample, HST Proposal

Bentz M. C., Katz S., 2015a, Publications of the Astronomical Society of the Pacific, 127, 67

Bentz M. C., Katz S., 2015b, PASP, 127, 67

Bentz M. C., et al., 2009, ApJ, 705, 199

Bentz M. C., et al., 2010a, ApJ, 716, 993

Bentz M. C., et al., 2010b, ApJ, 720, L46

Bentz M. C., et al., 2013, ApJ, 767, 149

Berger J. P., Segransan D., 2007, New Astronomy Review, 51, 576

Berger J. P., et al., 2012, A&A Reviews, 20, 53

Besard T., Foket C., De Sutter B., 2019, IEEE Transactions on Parallel and Distributed Systems, 30, 827

Bezanson J., Edelman A., Karpinski S., Shah V. B., 2017, SIAM Review, 59, 65

Blandford R. D., McKee C. F., 1982, ApJ, 255, 419

Boley D., 2013, SIAM Journal on Optimization, 23, 2183

Booth C. M., Schaye J., 2009, MNRAS, 398, 53

Boyd S., Parikh N., Chu E., Peleato B., Eckstein J., 2011, Found. Trends Mach. Learn., 3, 1

Bryan K., Leise T., 2013, SIAM Review, 55, 547

Buchner J., 2021, The Journal of Open Source Software, 6, 3001

Burtscher L., Jaffe W., Raban D., Meisenheimer K., Tristram K. R. W., Röttgering H., 2009, ApJ, 705, L53

Burtscher L., et al., 2013, A&A, 558, A149

Burtscher L., Hönig S., Jaffe W., Kishimoto M., Lopez-Gonzaga N., Meisenheimer K., Tristam K. R. W., 2016, in Malbet F., Creech-Eakman M. J., Tuthill P. G., eds, Society of Photo-Optical Instrumentation Engineers (SPIE) Conference Series Vol. 9907, Optical and Infrared Interferometry and Imaging V. p. 99070R (`arXiv:1607.04533`), doi:10.1117/12.2231077

Buscher D. F., Creech-Eakman M., Farris A., Haniff C. A., Young J. S., 2013, Journal of Astronomical Instrumentation, 2, 1340001

Candes E. J., Wakin M. B., 2008, IEEE Signal Processing Magazine, 25, 21

Cao N., Nehorai A., Jacob M., 2007, Opt. Express, 15, 13695

Che X., et al., 2014, in Marchetti E., Close L. M., Vran J.-P., eds, Society of Photo-Optical Instrumentation Engineers (SPIE) Conference Series Vol. 9148, Adaptive Optics Systems IV. p. 914830, doi:10.1117/12.2055693

Chiang J., Murray N., 1996, ApJ, 466, 704

Colavita M. M., Wizinowich P. L., 2003, in Traub W. A., ed., Vol. 4838, Interferometry for Optical Astronomy II. SPIE, pp 79 – 88, https://doi.org/10.1117/12.456768

Colavita M. M., et al., 1998, in Reasenberg R. D., ed., Vol. 3350, Astronomical Interferometry. SPIE, pp 776 – 784, doi:10.1117/12.317145, https://doi.org/10.1117/12.317145

Cotton W., et al., 2008, in Schöller M., Danchi W. C., Delplancke F., eds, Society of Photo-Optical Instrumentation Engineers (SPIE) Conference Series Vol. 7013, Optical and Infrared Interferometry. p. 70131N, doi:10.1117/12.788903

Crenshaw D. M., Kraemer S. B., 2000, ApJ, 532, L101

Crenshaw D. M., et al., 2000, AJ, 120, 1731

Cromwell R., Weymann R., 1970, ApJ, 159

Cutri R. M., et al., 2003, VizieR Online Data Catalog, p. II/246

Czerny B., 2006, in Gaskell C. M., McHardy I. M., Peterson B. M., Sergeev S. G., eds, Astronomical Society of the Pacific Conference Series Vol. 360, AGN Variability from X-Rays to Radio Waves. p. 265

Danjon A., 1922, The Diameters of the Stars. The Smithsonian Institution, p. 165–179

Davenport M. A., Duarte M. F., Eldar Y., Kutyniok G., 2011, in , Compressed Sensing: Theory and Applications. Cambridge University Press

Davis J., Tango W. J., Booth A. J., Brummelaar T. A. t., Minard R. A., Owens S. M., 1999, Monthly Notices of the Royal Astronomical Society, 303, 773

De Rosa G., et al., 2015, ApJ, 806, 128

Defrère D., et al., 2015, ApJ, 799, 42

Donoho D. L., 1995, IEEE transactions on information theory, 41, 613

Eckstein J., Yao W., 2012, RUTCOR Research Reports, 32

Eddington A. S., 1921, Zeitschrift fur Physik, 7, 351

Edge D. O., Shakeshaft J. R., McAdam W. B., Baldwin J. E., Archer S., 1959, Memoirs of the RAS, 68, 37

Ferrari A., Deguignet J., Ferrari C., Mary D., Schutz A., Smirnov O., 2015, in SKA Pathfindes Radio Continuum Surveys (SPARCS).

Ford K. E. S., McKernan B., 2021, Binary Black Hole Merger Rates in AGN Disks versus Nuclear Star Clusters: Loud beats Quiet (`arXiv:2109.03212`)

Foreman-Mackey D., 2016, The Journal of Open Source Software, 1, 24

Foreman-Mackey D., Agol E., Ambikasaran S., Angus R., 2017, The Astronomical Journal, 154, 220

Gaia Collaboration 2018, VizieR Online Data Catalog, p. I/345

Graham A. W., Onken C. A., Athanassoula E., Combes F., 2011, MNRAS, 412, 2211

Gravity Collaboration et al., 2017, A&A, 602, A94

Gravity Collaboration et al., 2020a, A&A, 634, A1

Gravity Collaboration et al., 2020b, A&A, 635, A92

Grier C. J., Peterson B. M., Horne K., Bentz M. C., Pogge R. W., Denney K. D. e. a., 2013a, ApJ, 764, 47

Grier C. J., et al., 2013b, ApJ, 773, 90

Haguenauer P., et al., 2008, Proc SPIE, 7013, 11

Han D., Yuan X., 2013, SIAM Journal on Numerical Analysis, 51, 3446

Heckman T. M., 1980, A&A, 500, 187

Hill J. M., Green R. F., Slagle J. H., 2006, in Stepp L. M., ed., Vol. 6267, Ground-based and Airborne Telescopes. SPIE, pp 318 – 332, doi:10.1117/12.669832, https://doi.org/10.1117/12.669832

Ho L. C., Filippenko A. V., Sargent W. L., 1995, ApJS, 98, 477

Hoerl A. E., Kennard R. W., 1970, Technometrics, 12, 55

Hönig S. F., 2019, ApJ, 884, 171

Hönig S. F., Watson D., Kishimoto M., Hjorth J., 2014, Nature, 515, 528

Hönig S. F., Alonso Herrero A., Gandhi P., Kishimoto M., Pott J.-U., Ramos Almeida C., Surdej J., Tristram K. R. W., 2018, Experimental Astronomy, 46, 413

Horne K., 1994, in Gondhalekar P. M., Horne K., Peterson B. M., eds, Astronomical Society of the Pacific Conference Series Vol. 69, Reverberation Mapping of the Broad-Line Region in Active Galactic Nuclei. pp 23–25

Horne K., Peterson B. M., Collier S. J., Netzer H., 2004, PASP, 116, 465

Horne K., et al., 2020, arXiv e-prints, p. arXiv:2003.01448

Horne K., et al., 2021, ApJ, 907, 76

Jankov S., 2010, Serbian Astronomical Journal, 181

Jansky K. G., 1933, Nature, 132, 66

Johnston K. J., 1998, in Reasenberg R. D., ed., Society of Photo-Optical Instrumentation Engineers (SPIE) Conference Series Vol. 3350, Astronomical Interferometry. pp 941–946, doi:10.1117/12.317161

Joss P. C., Salpeter E. E., Ostriker J. P., 1973, ApJ, 181, 429

Kelly B. C., Bechtold J., Siemiginowska A., 2009, ApJ, 698, 895

Khachikian E. Y., Weedman D. W., 1974, ApJ, 192, 581

Kishimoto, M. Hönig, S. F. Antonucci, R. Barvainis, R. Kotani, T. Tristram, K. R. W. Weigelt, G. Levin, K. 2011, A&A, 527, A121

Kishimoto M., Hönig S. F., Antonucci R., Kotani T., Barvainis R., Tristram K. R. W., Weigelt G., 2009, A&A, 507, L57

Kishimoto M., Antonucci R., Barvainis R., Hoenig S., Millour F., Tristram K., Weigelt G., 2010, Probing the innermost infrared emission in the brightest Type 1 AGN with the CHARA array, NOAO Proposal

Kishimoto M., Hönig S. F., Antonucci R., Barvainis R., Kotani T., Tristram K. R. W., Weigelt G., Levin K., 2011, A&A, 527, A121

Kishimoto M., et al., 2013a, The Astrophysical Journal Letters, 775

Kishimoto M., et al., 2013b, ApJ, 775, L36

Kishimoto M., et al., 2019, Bulletin of the AAS, 51

Koshida S., et al., 2009, ApJ, 700, L109

Kovačević A. B., Wang J.-M., Popović L. Č., 2020, A&A, 635, A1

Krolik J. H., 1994, in Gondhalekar P. M., Horne K., Peterson B. M., eds, Astronomical Society of the Pacific Conference Series Vol. 69, Reverberation Mapping of the Broad-Line Region in Active Galactic Nuclei. p. 53

Krolik J. H., Done C., 1995, ApJ, 440, 166

LAMP2016 Collaboration 2017, in American Astronomical Society Meeting Abstracts. p. 414.04

Lawson P. R., et al., 2004, in Traub W. A., ed., Society of Photo-Optical Instrumentation Engineers (SPIE) Conference Series Vol. 5491, New Frontiers in Stellar Interferometry. p. 886, doi:10.1117/12.550710

Leftley J. H., Tristram K. R. W., Hönig S. F., Kishimoto M., Asmus D., Gandhi P., 2018, ApJ, 862, 17

Leinert C., et al., 2003, AP&SS, 286, 73

Li Y.-R., et al., 2016a, ApJ, 822, 4

Li M., Zhang C., Peng C., Guan Y., Xu P., Sun M., Zheng J., 2016b, BioMed Research International, 2016, 12

Li Y.-R., Xiao M., Wang J.-M., 2021a, arXiv e-prints, p. arXiv:2109.12387

Li Y.-P., Dempsey A. M., Li S., Li H., Li J., 2021b, ApJ, 911, 124

López-Gonzaga N., Jaffe W., 2016, A&A, 591, A128

Mangham S. W., Knigge C., Matthews J. H., Long K. S., Sim S. A., Higginbottom N., 2017, MNRAS, 471, 4788

Mangham S. W., et al., 2019, MNRAS, 488, 2780

Mason B., ten Brummelaar 1995, CHARA Technical Reports, TR-25

Matthews T. A., Sandage A., 1962, PASP, 74, 406

Matthews T. A., Sandage A. R., 1963, ApJ, 138, 30

McKernan B., Ford K. E. S., Lyra W., Perets H. B., 2012, MNRAS, 425, 460

Mérand A., et al., 2018, in Creech-Eakman M. J., Tuthill P. G., Mérand A., eds, Society of Photo-Optical Instrumentation Engineers (SPIE) Conference Series Vol. 10701, Optical and Infrared Interferometry and Imaging VI. p. 107011U, doi:10.1117/12.2500674

Michelson A. A., 1891, PASP, 3, 217

Michelson A. A., 1920, ApJ, 51, 257

Michelson A. A., Pease F. G., 1921, ApJ, 53, 249

Miller J. S., Goodrich R. W., Mathews W. G., 1991, ApJ, 378, 47

Monnier J. D., 2003, Reports on Progress in Physics, 66, 789

Monnier J. D., et al., 2014, in Rajagopal J. K., Creech-Eakman M. J., Malbet F., eds, Society of Photo-Optical Instrumentation Engineers (SPIE) Conference Series Vol. 9146, Optical and Infrared Interferometry IV. p. 91461Q, doi:10.1117/12.2057312

Mundell C. G., Wrobel J. M., Pedlar A., Gallimore J. F., 2003, ApJ, 583, 192

Murray N., Chiang J., Grossman S. A., Voit G. M., 1995, ApJ, 451, 498

National Academies of Sciences, Engineering, and Medicine 2021, Pathways to Discovery in Astronomy and Astrophysics for the 2020s. The National Academies Press, doi:10.17226/26141, https://www.nap.edu/catalog/26141/pathways-to-discovery-in-astronomy-and-astrophysics-for-the-2020s

Netzer H., 2015, ARA&A, 53, 365

Nishihara R., Lessard L., Recht B., Packard A., Jordan M. I., 2015, in Proceedings of the 32Nd International Conference on International Conference on Machine Learning - Volume 37. ICML'15. JMLR.org, pp 343–352, http://dl.acm.org/citation.cfm?id=3045118.3045156

Onken C. A., Ferrarese L., Merritt D., Peterson B. M., Pogge R. W., Vestergaard M., Wandel A., 2004, ApJ, 615, 645

Osterbrock D. E., 1977, ApJ, 215, 733

Osterbrock D. E., 1981, ApJ, 249, 462

Osterbrock D. E., Koski A. T., 1976, MNRAS, 176, 61P

Pancoast A., Brewer B. J., Treu T., 2011, ApJ, 730, 139

Pancoast A., Brewer B. J., Treu T., 2014a, MNRAS, 445, 3055

Pancoast A., Brewer B. J., Treu T., Park D., Barth A. J., Bentz M. C., Woo J.-H., 2014b, MNRAS, 445, 3073

Pedlar A., Kukula M. J., Longley D. P. T., Muxlow T. W. B., Axon D. J., Baum S., O'Dea C., Unger S. W., 1993, MNRAS, 263, 471

Penston M. V., Penston M. J., Selmes R. A., Becklin E. E., Neugebauer G., 1974, MNRAS, 169, 357

Peterson B. M., 1988, PASP, 100, 18

Peterson B. M., 1993, PASP, 105, 247

Peterson B. M., 1994, in Gondhalekar P. M., Horne K., Peterson B. M., eds, Astronomical Society of the Pacific Conference Series Vol. 69, Reverberation Mapping of the Broad-Line Region in Active Galactic Nuclei. p. 1

Peterson B. M., 1997, An Introduction to Active Galactic Nuclei. Cambridge University Press, doi:10.1017/CBO9781139170901

Peterson B. M., Wandel A., 2000, ApJ, 540, L13

Pina R. K., Puetter R. C., 1993, PASP, 105, 630

Pott J.-U., Malkan M. A., Elitzur M., Ghez A. M., Herbst T. M., Schödel R., Woillez J., 2010, ApJ, 715, 736

Reasenberg R. D., 1990, in Breckinridge J. B., ed., Vol. 1237, Amplitude and Intensity Spatial Interferometry. SPIE, pp 128 – 137, doi:10.1117/12.19287, https://doi.org/10.1117/12.19287

Rudin L. I., Osher S., Fatemi E., 1992, Physica D Nonlinear Phenomena, 60, 259

Sanchez-Bermudez J., et al., 2016, in Malbet F., Creech-Eakman M. J., Tuthill P. G., eds, Society of Photo-Optical Instrumentation Engineers (SPIE) Conference Series Vol. 9907, Optical and Infrared Interferometry and Imaging V. p. 99071D, doi:10.1117/12.2231982

Sandage A., 1967, ApJ, 150, L177

Schaefer G. H., 2019, CHARA Technical Reports, TR-98

Schmidt M., 1963, Nature, 197, 1040

Schutz A., Ferrari A., Mary D., Soulez F., Thiébaut É., Vannier M., 2014, Journal of the Optical Society of America A, 31, 2334

Schutz A., Ferrari A., Mary D., Thiébaut É., Soulez F., 2015, in EUSIPCO. NICE, France, https://hal.archives-ouvertes.fr/hal-01123500

Seyfert C. K., 1943, ApJ, 97, 28

Shen Y., et al., 2015, ApJS, 216, 4

Shen Y., et al., 2016, ApJ, 818, 30

Skielboe A., Pancoast A., Treu T., Park D., Barth A. J., Bentz M. C., 2015, MNRAS, 454, 144

Skrutskie M. F., et al., 2006, AJ, 131, 1163

Songsheng Y.-Y., Xiao M., Wang J.-M., Ho L. C., 2020, ApJS, 247, 3

Sparke L. S., Gallagher III J. S., 2007, Galaxies in the Universe: An Introduction, 2 edn. Cambridge University Press, doi:10.1017/CBO9780511807237

Spinoglio L., Fernández-Ontiveros J. A., 2021, in Pović M., Marziani P., Masegosa J., Netzer H., Negu S. H., Tessema S. B., eds, Vol. 356, Nuclear Activity in Galaxies Across Cosmic Time. pp 29–43 (arXiv:1911.12176), doi:10.1017/S1743921320002549

Storchi-Bergmann T., Schnorr-Müller A., 2019, Nature Astronomy, 3, 48–61

Swain M., et al., 2003a, The Astrophysical Journal, 596, L163

Swain M., et al., 2003b, ApJ, 596, L163

Ten Brummelaar T. A., et al., 2013, Journal of Astronomical Instrumentation, 2, 1340004

Thiébaut E., 2005, in Foy R., Foy F. C., eds, NATO ASIB Proc. 198: Optics in astrophysics. p. 397

Thiebaut E., Giovannelli J.-F., 2010, IEEE Signal Processing Magazine, 27, 97

Thiébaut É., Soulez F., 2012, in Optical and Infrared Interferometry III. p. 84451C, doi:10.1117/12.926862

Tikhonov A. N., 1963, Soviet Math. Dokl., 4, 1035

Torrealba J., Chavushyan V., Cruz-González I., Arshakian T. G., Bertone E., Rosa-González D., 2012, Revista Mexicana de Astronomia y Astrofisica, 48, 9

Townes C. H., Bester M., Danchi W. C., Degiacomi C. G., Greenhill L. J., 1994, Infrared Physics and Technology, 35, 503

Traub W. A., 1998, in Reasenberg R. D., ed., Vol. 3350, Astronomical Interferometry. SPIE, pp 848 – 855, doi:10.1117/12.317152, https://doi.org/10.1117/12.317152

Tristram K. R. W., et al., 2007, A&A, 474, 837

Tristram K. R. W., Raban D., Burtscher L., Meisenheimer K., Jaffe W. J., 2008, MEMSAI, 79, 1144

Tristram K. R. W., et al., 2009, A&A, 502, 67

Tristram K. R. W., Burtscher L., Jaffe W., Meisenheimer K., Hönig S. F., Kishimoto M., Schartmann M., Weigelt G., 2014, A&A, 563, A82

Ulrich M.-H., Maraschi L., Urry C. M., 1997, ARAA, 35, 445

Ulvestad J. S., Roy A. L., Colbert E. J. M., Wilson A. S., 1998, ApJ, 496, 196

Ulvestad J. S., Wong D. S., Taylor G. B., Gallimore J. F., Mundell C. G., 2005, AJ, 130, 936

Urry C. M., Padovani P., 1995, PASP, 107, 803

Virtanen P., et al., 2020, Nature Methods, 17, 261

Walker M. F., 1968, ApJ, 151, 71

Walsh J. L., et al., 2009, ApJS, 185, 156

Wang Y., Yin W., Zeng J., 2018a, Journal of Scientific Computing

Wang J.-M., Songsheng Y.-Y., Li Y.-R., Yu Z., 2018b, ApJ, 862, 171

Waters T., Kashi A., Proga D., Eracleous M., Barth A. J., Greene J., 2016, ApJ, 827, 53

Weigelt G., et al., 2012, A&A, 541, L9

Welsh W. F., Horne K., 1991, ApJ, 379, 586

Wenger M., et al., 2000, A&AS, 143, 9

Wittkowski M., Kervella P., Arsenault R., Paresce F., Beckert T., Weigelt G., 2004, A&A, 418, L39

Wohlberg B., 2017, ADMM Penalty Parameter Selection by Residual Balancing (arXiv:1704.06209)

Xiao M., et al., 2018a, The Astrophysical Journal, 864, 109

Xiao M., et al., 2018b, ApJ, 865, L8

Xu Z., Taylor G., Li H., Figueiredo M. A. T., Yuan X., Goldstein T., 2017, CoRR, abs/1706.02869

Yao J., Tian F., Rakvongthai Y., Oraintara S., Liu H., 2015, Biomed. Opt. Express, 6, 2961

Zernike F., 1938, Physica, 5, 785

Zu Y., Kochanek C. S., Peterson B. M., 2011, ApJ, 735, 80

ten Brummelaar T., 2014, CHARA Technical Reports, TR-96

ten Brummelaar T. A., et al., 2005, ApJ, 628, 453

ten Brummelaar T. A., et al., 2012, in Ellerbroek B. L., Marchetti E., Véran J.-P., eds, Vol. 8447, Adaptive Optics Systems III. SPIE, pp 1207 – 1216, https://doi.org/10.1117/12.927031

ten Brummelaar T. A., et al., 2018, in Close L. M., Schreiber L., Schmidt D., eds, Vol. 10703, Adaptive Optics Systems VI. SPIE, pp 24 – 34, https://doi.org/10.1117/12.2312311

van Cittert P. H., 1934, Physica, 1, 201

APPENDIX A
MATRIX DERIVATIVE IDENTITIES

These matrix identities are used in the derivation of analytic solutions for the ADMM block of TLDR.

$$\boxed{\frac{\partial\left(x^{\top}a\right)}{\partial x}=\frac{\partial\left(a^{\top}x\right)}{\partial x}=a} \tag{A.1}$$

$$\boxed{\frac{\partial\left(\mathbf{a}^{\top}\mathbf{X}\mathbf{b}\right)}{\partial\mathbf{X}}=\mathbf{a}\mathbf{b}^{\top}} \tag{A.2}$$

$$\boxed{\frac{\partial}{\partial x}\left(x-s\right)^{\top}W\left(x-s\right)=2W\left(x-s\right)} \tag{A.3}$$

$$\boxed{\frac{\partial}{\partial\mathbf{A}}\left[\left(\mathbf{x}-\mathbf{A}\mathbf{s}\right)^{\top}\mathbf{W}\left(\mathbf{x}-\mathbf{A}\mathbf{s}\right)\right]=-2\mathbf{W}\left(\mathbf{x}-\mathbf{A}\mathbf{s}\right)\mathbf{s}^{\top}} \tag{A.4}$$

$$\boxed{\frac{\partial}{\partial\mathbf{x}}\left[\left\|x\right\|_{2}^{2}\right]=\frac{\partial}{\partial\mathbf{x}}\left[\left\|x^{\top}x\right\|_{2}\right]=2x} \tag{A.5}$$

APPENDIX B
CHARA DATA REDUCTIONS OF CALIBRATORS

This appendix contains the figures for each calibrator used in the data reduction of the CHARA observations of NGC 4151.

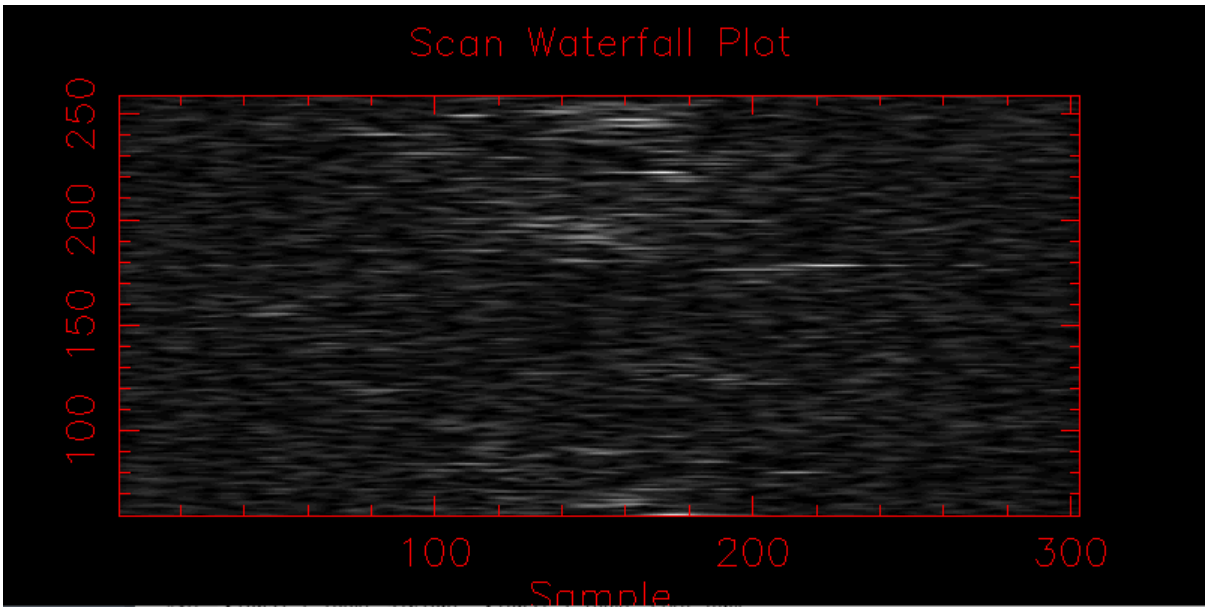

Figure B.1 The scan waterfall plot for the data file on SAO 62878 taken on Feb 15, 2020, contained in the file 2020_02_15_SAO_62878_ird_002.fit.

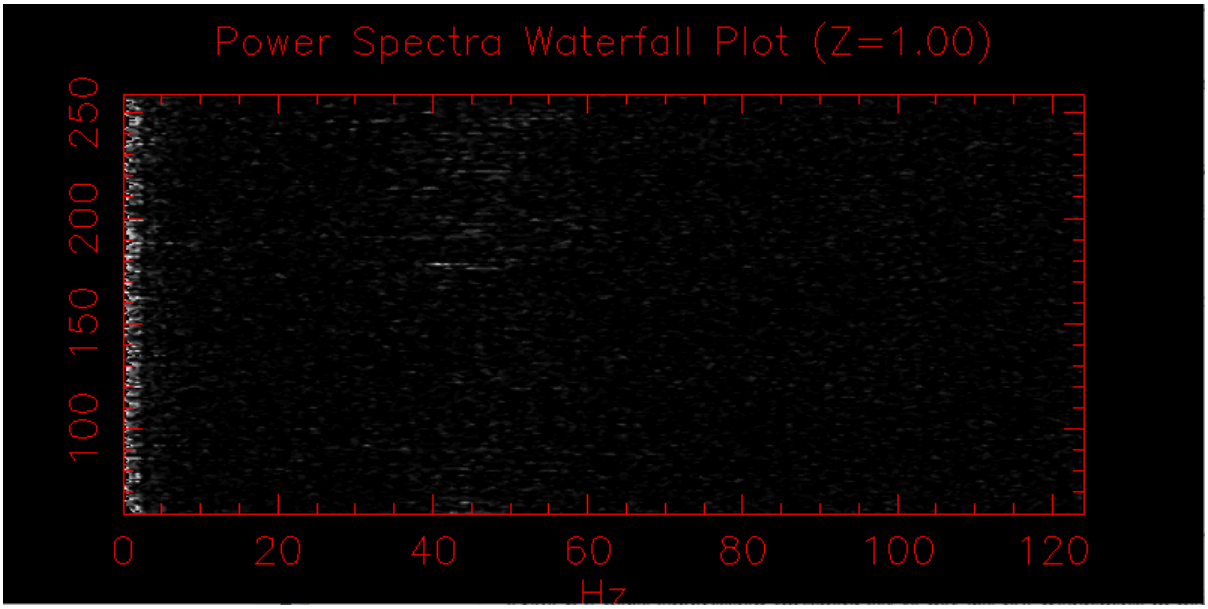

Figure B.2 The scan power spectra waterfall plot for the data file on SAO 62878 taken on Feb 15, 2020, contained in the file 2020_02_15_SAO_62878_ird_002.fit.

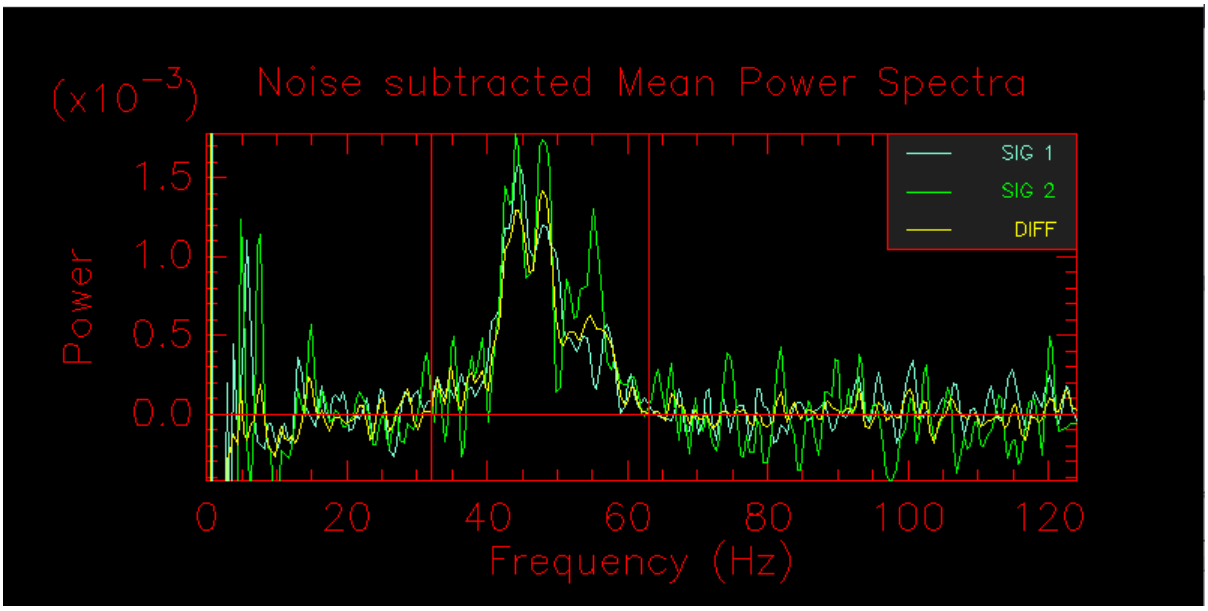

Figure B.3 The noise subtracted mean power spectra waterfall plot for the data file on SAO 62878 taken on Feb 15, 2020, contained in the file 2020_02_15_SAO_62878_ird_002.fit.

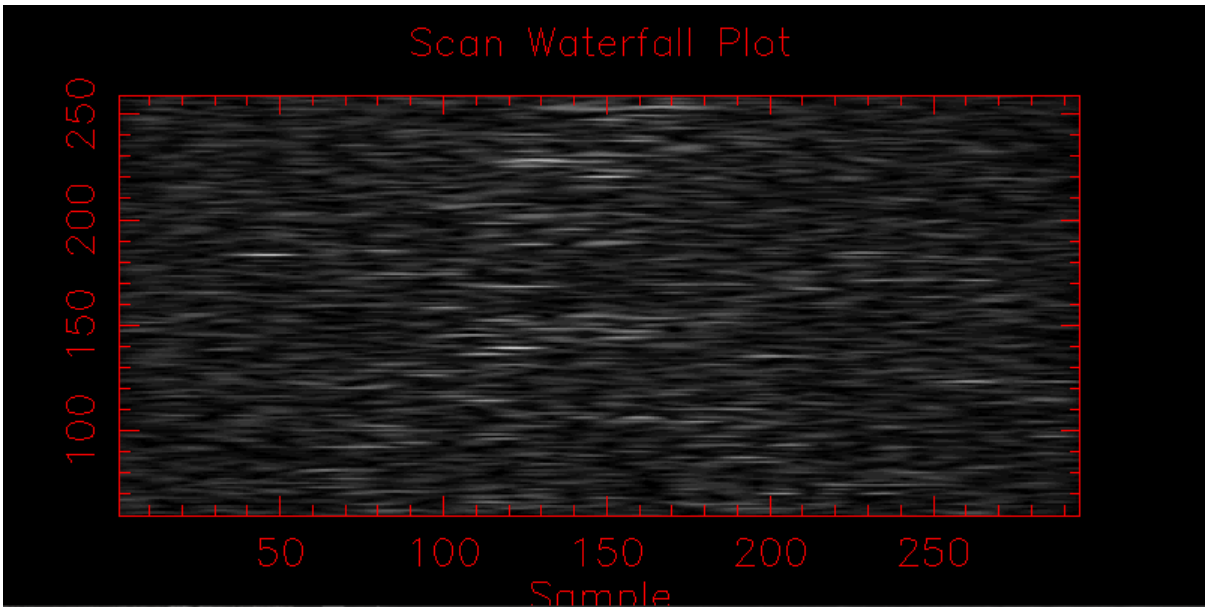

Figure B.4 The scan waterfall plot for the data file on SAO 62878 taken on Feb 16, 2020, contained in the file 2020_02_16_SAO_62878_ird_002.fit.

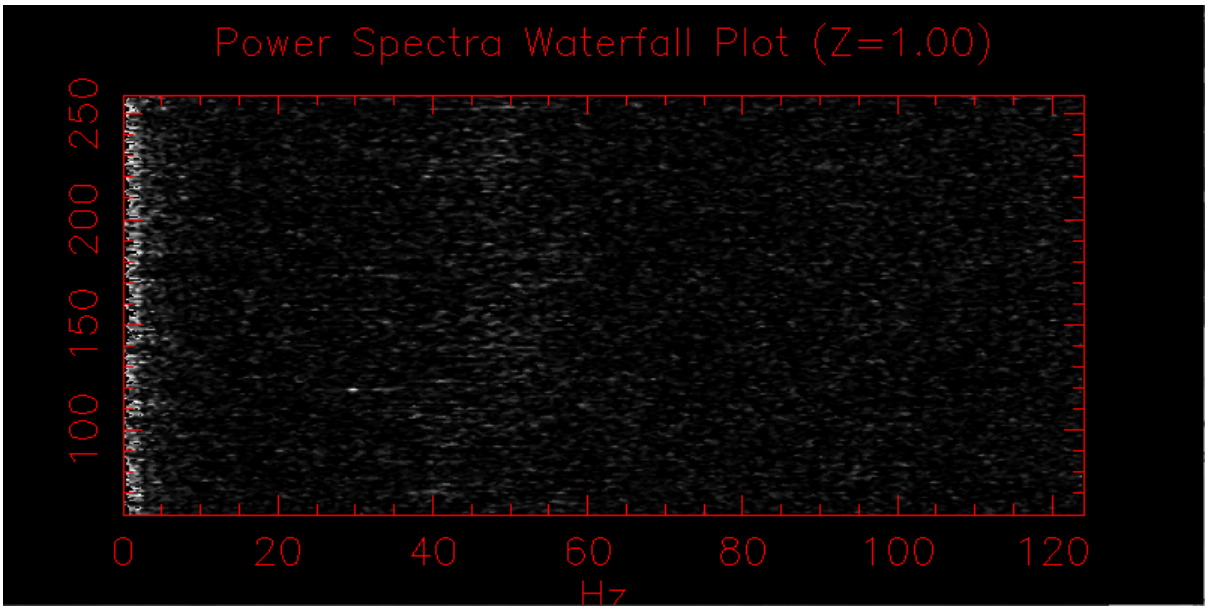

Figure B.5 The scan power spectra waterfall plot for the data file on SAO 62878 taken on Feb 16, 2020, contained in the file 2020_02_16_SAO_62878_ird_002.fit.

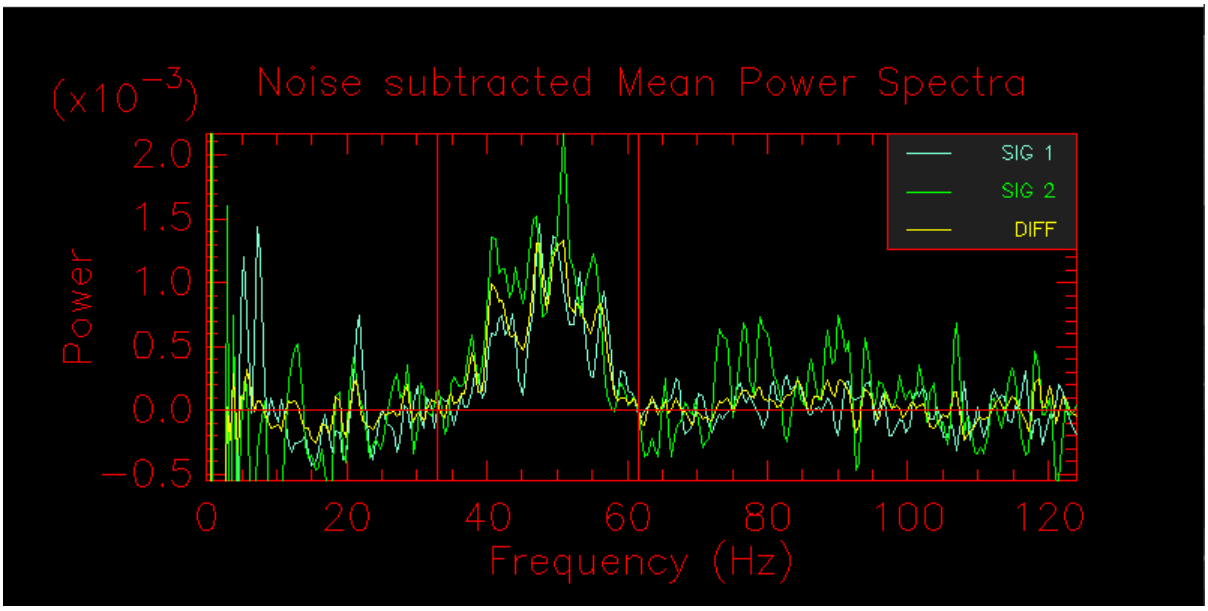

Figure B.6 The noise subtracted mean power spectra waterfall plot for the data file on SAO 62878 taken on Feb 16, 2020, contained in the file 2020_02_16_SAO_62878_ird_002.fit.

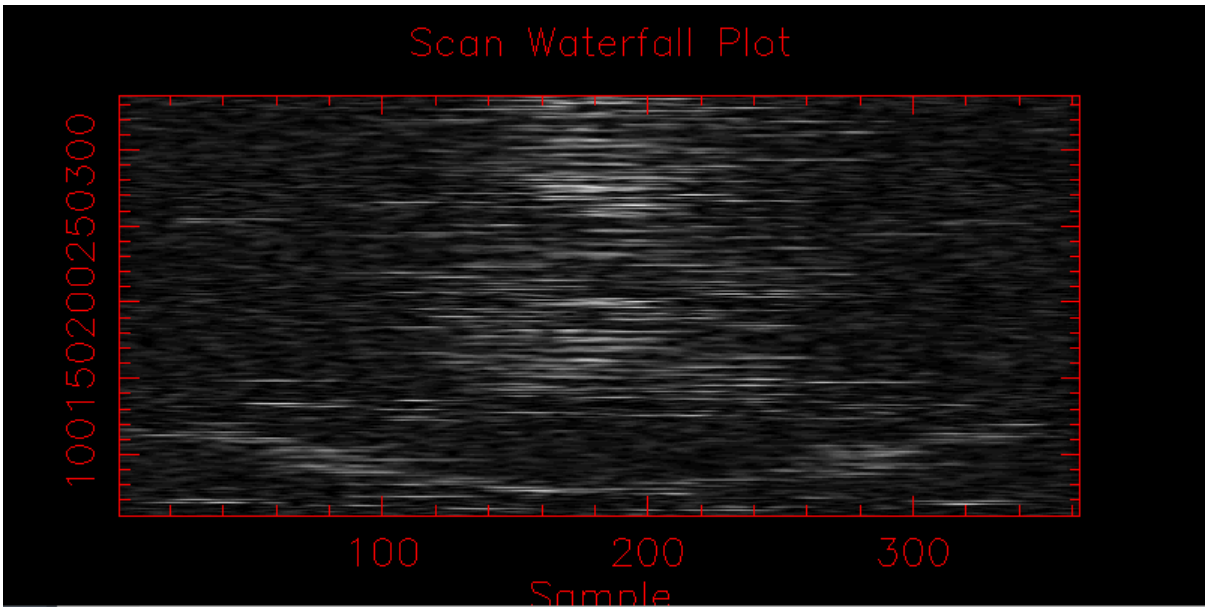

Figure B.7 The scan waterfall plot for the data file on SAO 62878 taken on Mar 19, 2021, contained in the file 2021_03_19_SAO_62878_ird_001.fit.

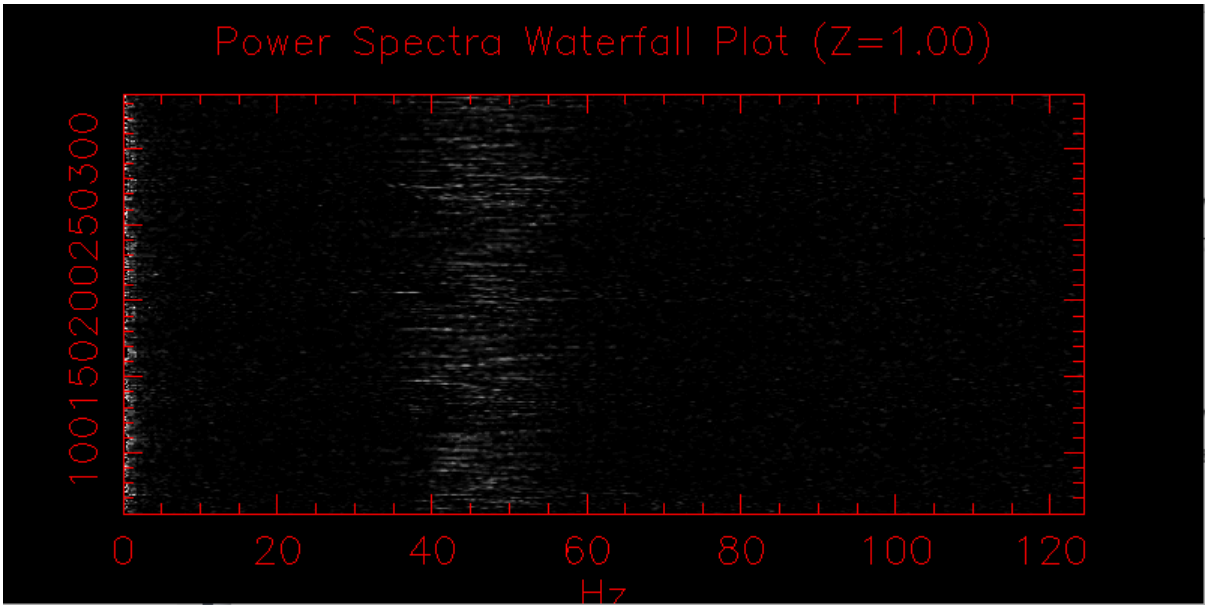

Figure B.8 The scan power spectra waterfall plot for the data file on SAO 62878 taken on Mar 19, 2021, contained in the file 2021_03_19_SAO_62878_ird_001.fit.

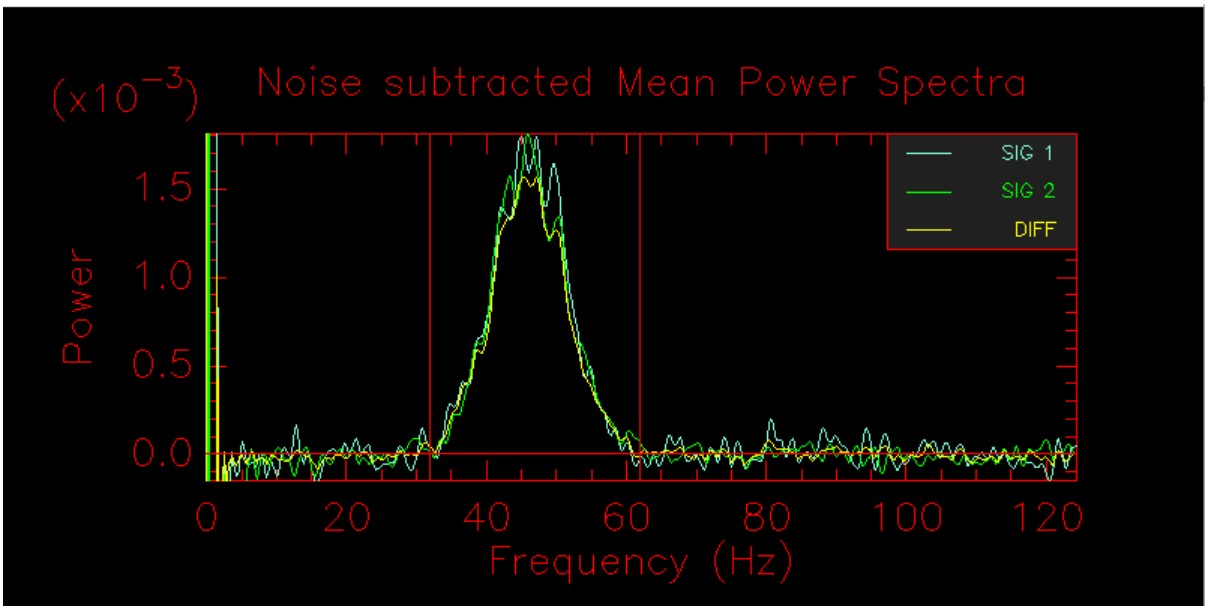

Figure B.9 The noise subtracted mean power spectra waterfall plot for the data file on SAO 62878 taken on Mar 19, 2021, contained in the file 2021_03_19_SAO_62878_ird_001.fit.

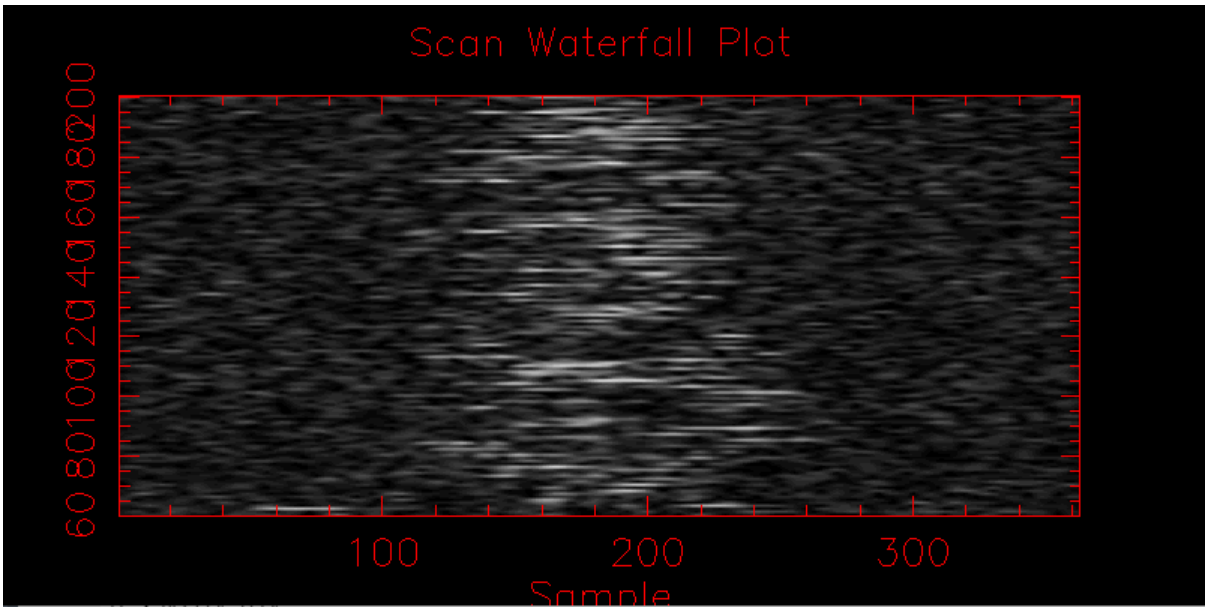

Figure B.10 The scan waterfall plot for the data file on SAO 62878 taken on Mar 19, 2021, contained in the file 2021_03_19_SAO_62878_ird_002.fit.

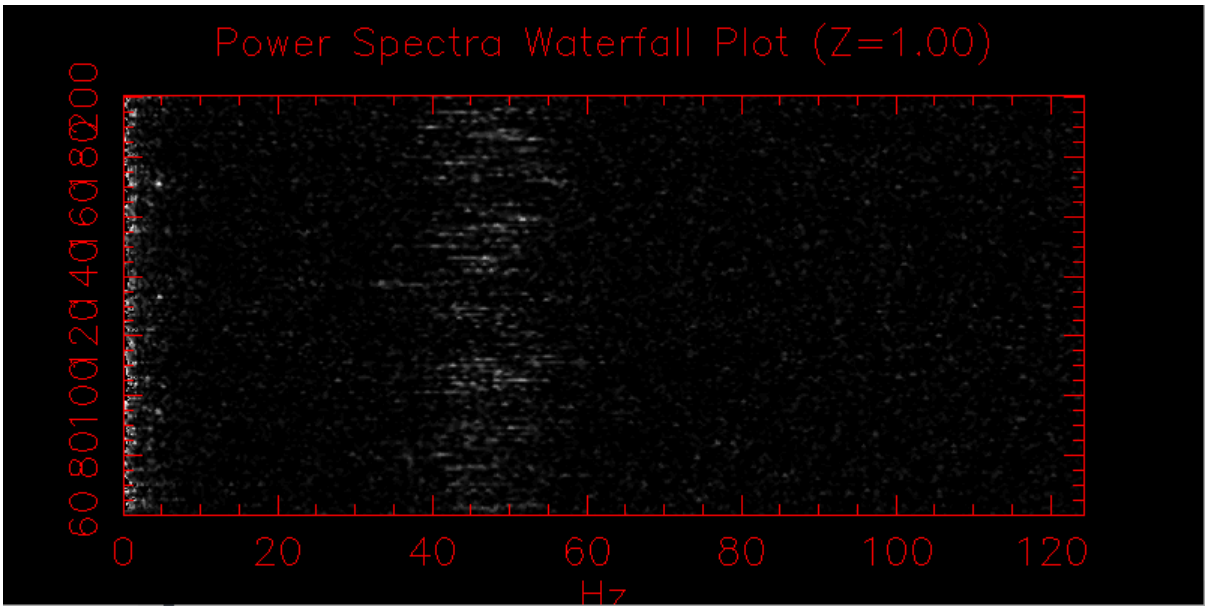

Figure B.11 The scan power spectra waterfall plot for the data file on SAO 62878 taken on Mar 19, 2021, contained in the file 2021_03_19_SAO_62878_ird_002.fit.

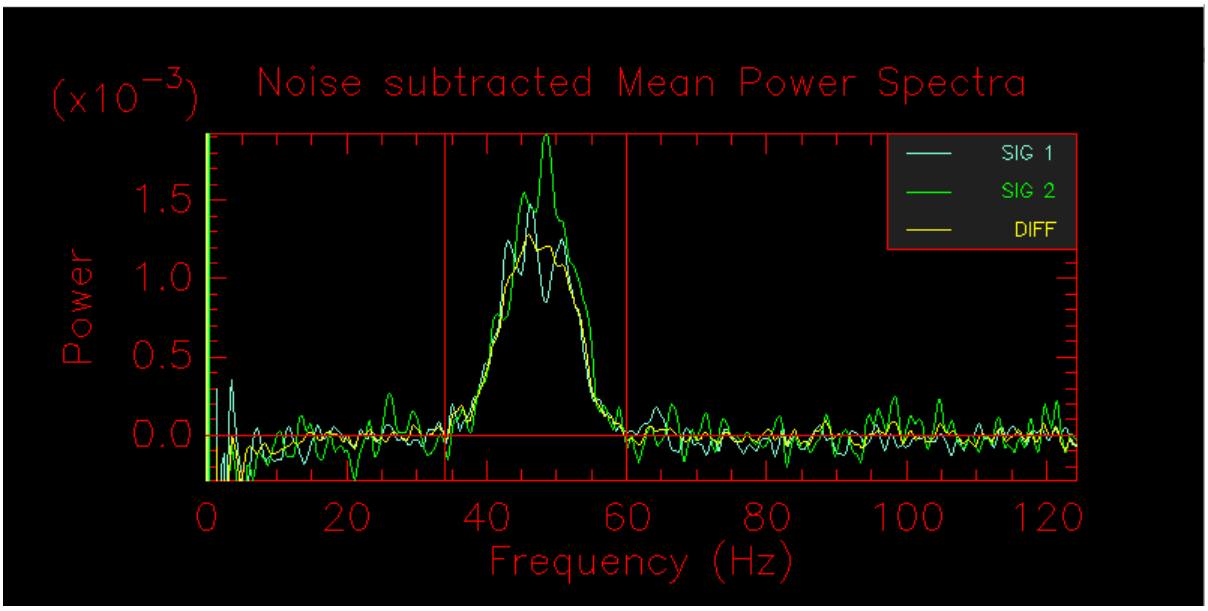

Figure B.12 The noise subtracted mean power spectra waterfall plot for the data file on SAO 62878 taken on Mar 19, 2021, contained in the file 2021_03_19_SAO_62878_ird_002.fit.

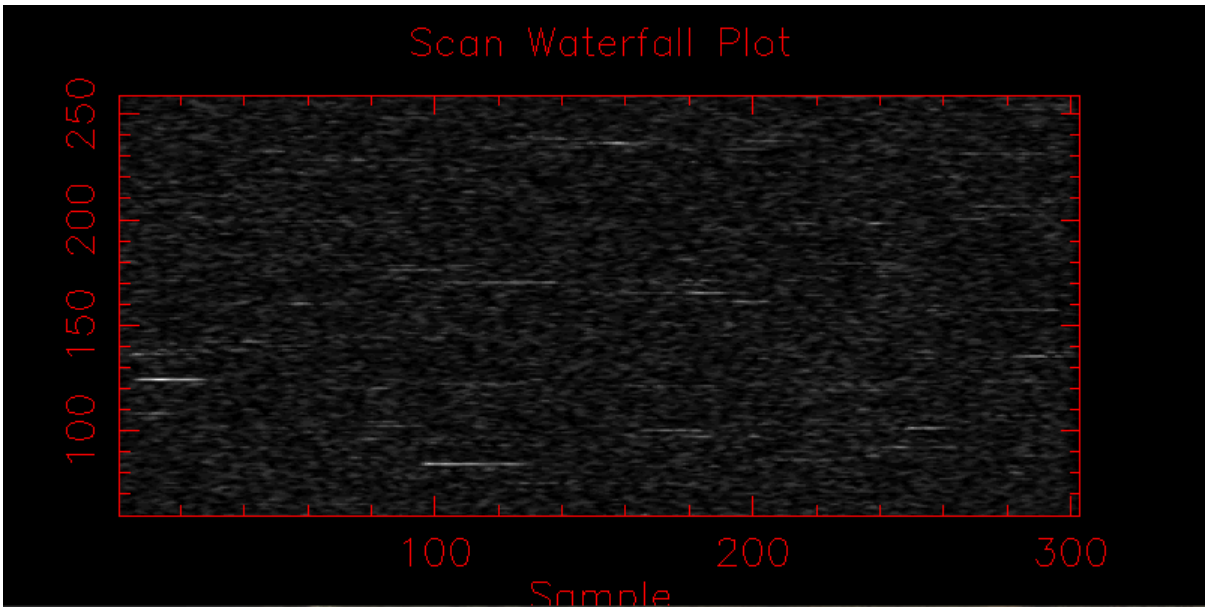

Figure B.13 The scan waterfall plot for the data file on HD 105881 taken on Apr 25, 2021, contained in the file 2021_04_25_HD_105881_ird_001.fit.

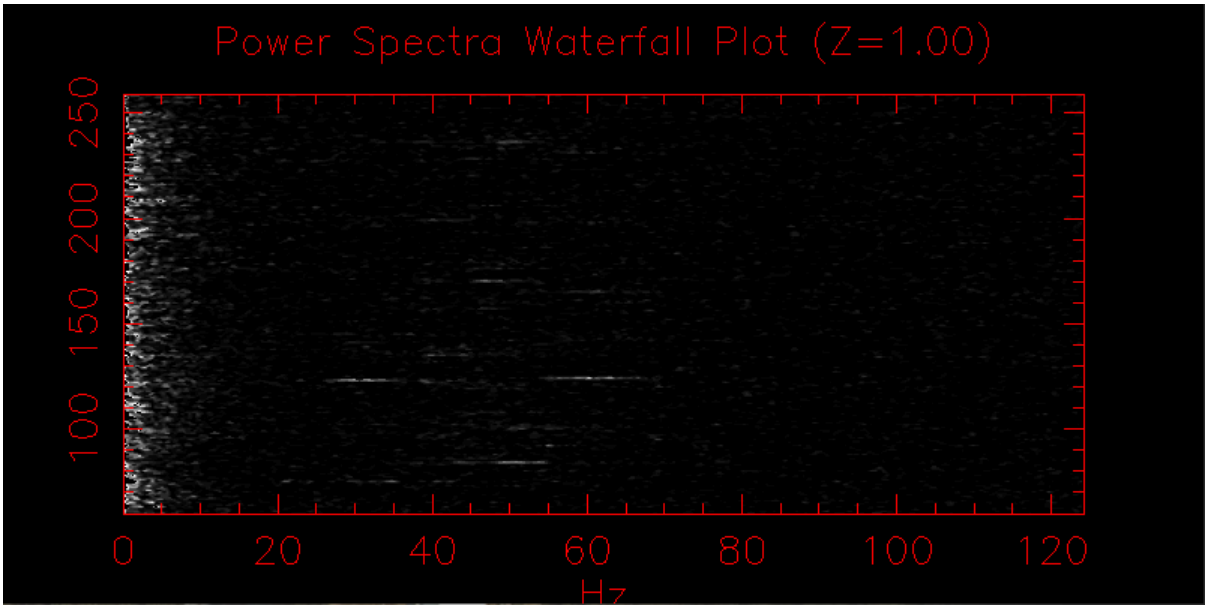

Figure B.14 The scan power spectra waterfall plot for the data file on HD 105881 taken on Apr 25, 2021, contained in the file 2021_04_25_HD_105881_ird_001.fit.

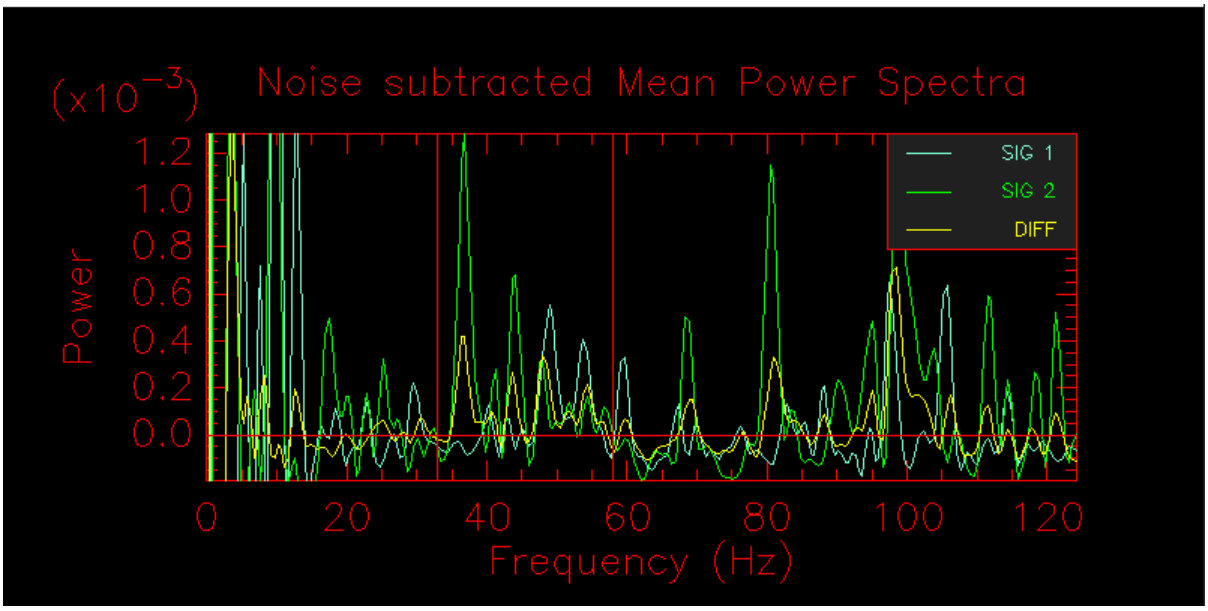

Figure B.15 The noise subtracted mean power spectra waterfall plot for the data file on HD 105881 taken on Apr 25, 2021, contained in the file 2021_04_25_HD_105881_ird_001.fit.

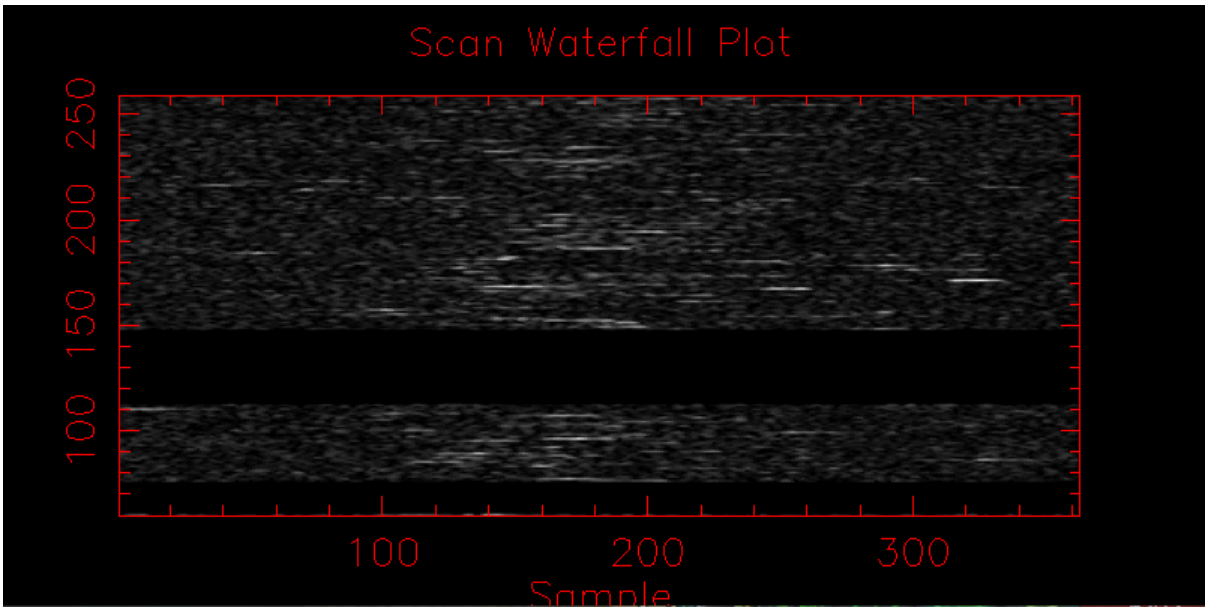

Figure B.16 The scan waterfall plot for the data file on HD 105881 taken on Mar 29, 2021, contained in the file 2021_04_29_HD_105881_ird_001.fit.

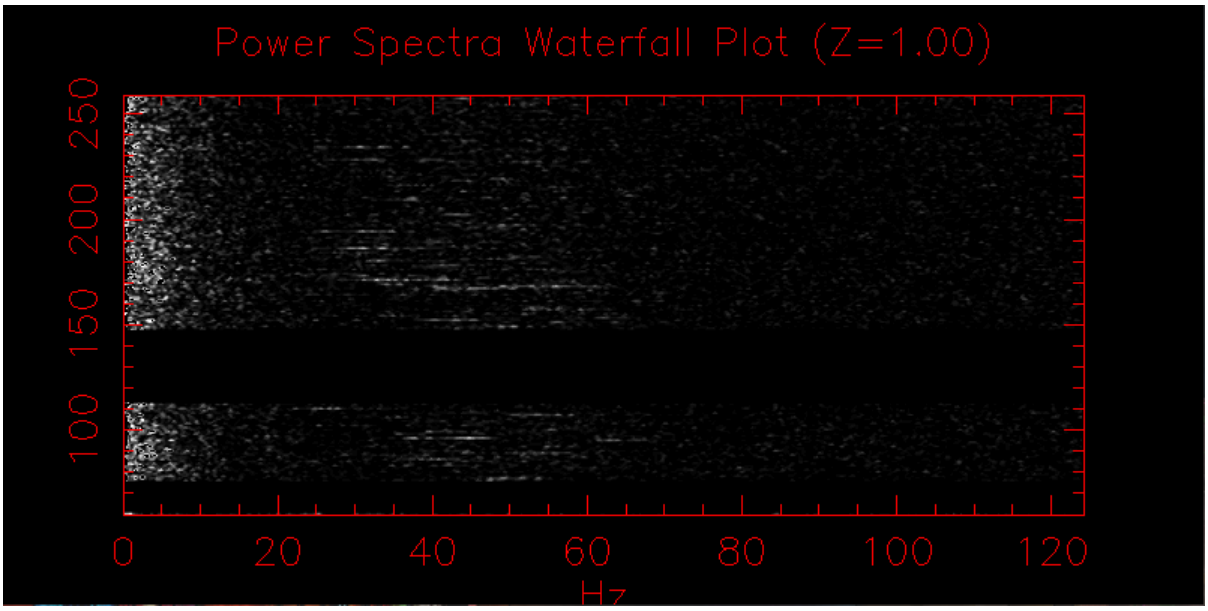

Figure B.17 The scan power spectra waterfall plot for the data file on HD 105881 taken on Mar 29, 2021, contained in the file 2021_04_29_HD_105881_ird_001.fit.

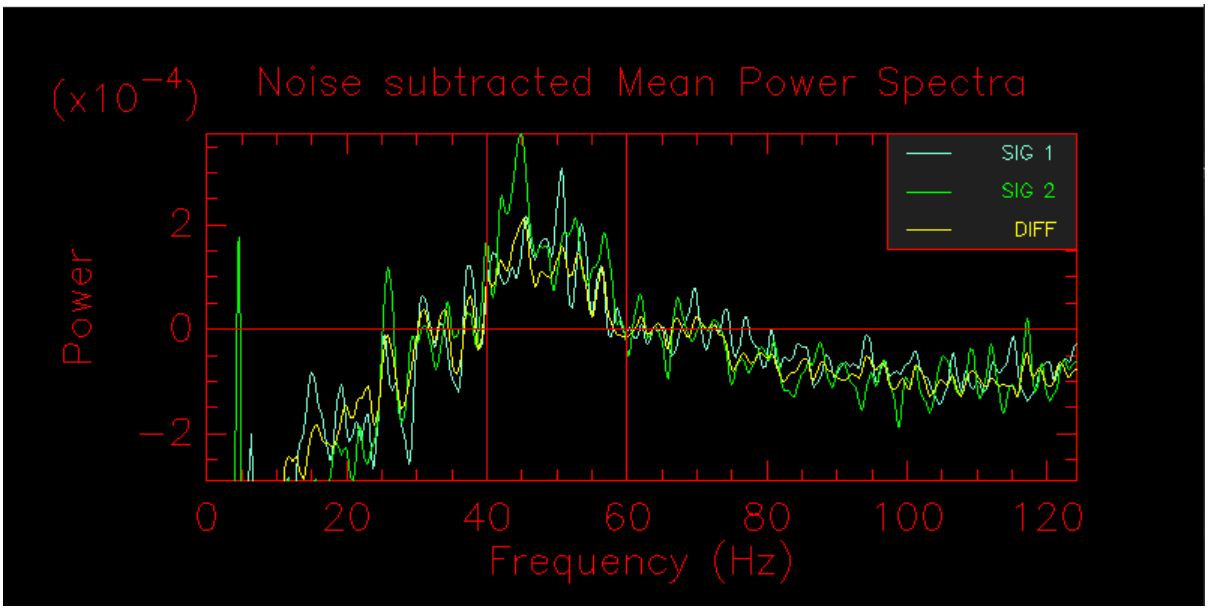

Figure B.18 The noise subtracted mean power spectra waterfall plot for the data file on HD 105881 taken on Mar 29, 2021, contained in the file 2021_04_29_SAO_HD105881_ird_001.fit.

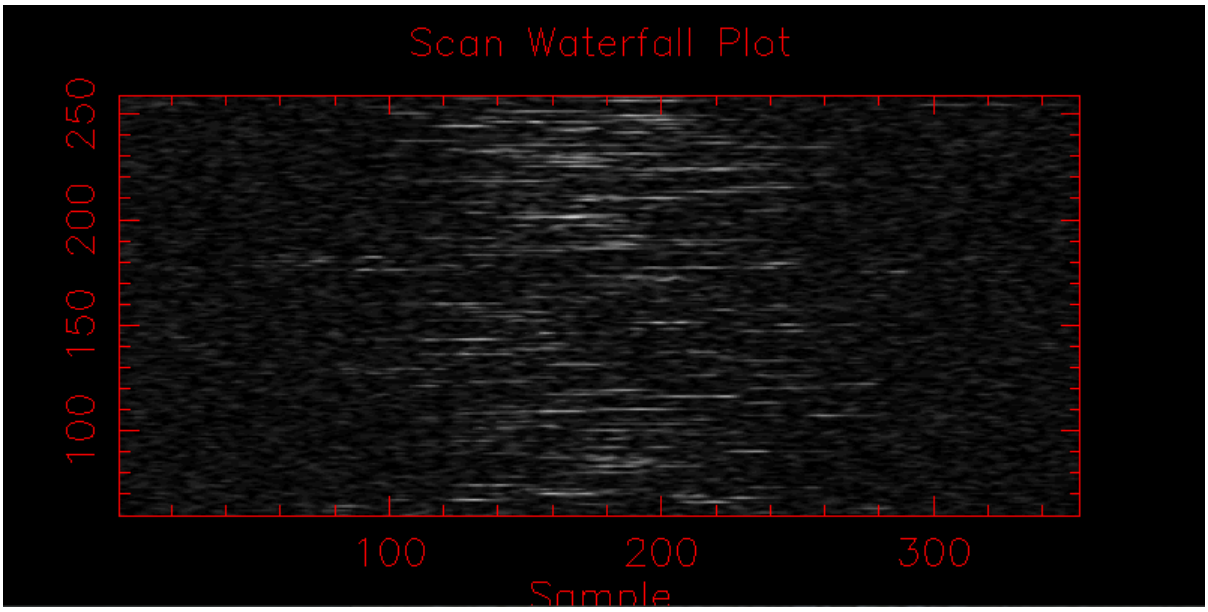

Figure B.19 The scan waterfall plot for the data file on HD 105881 taken on Mar 29, 2021, contained in the file 2021_04_29_HD_105881_ird_002.fit.

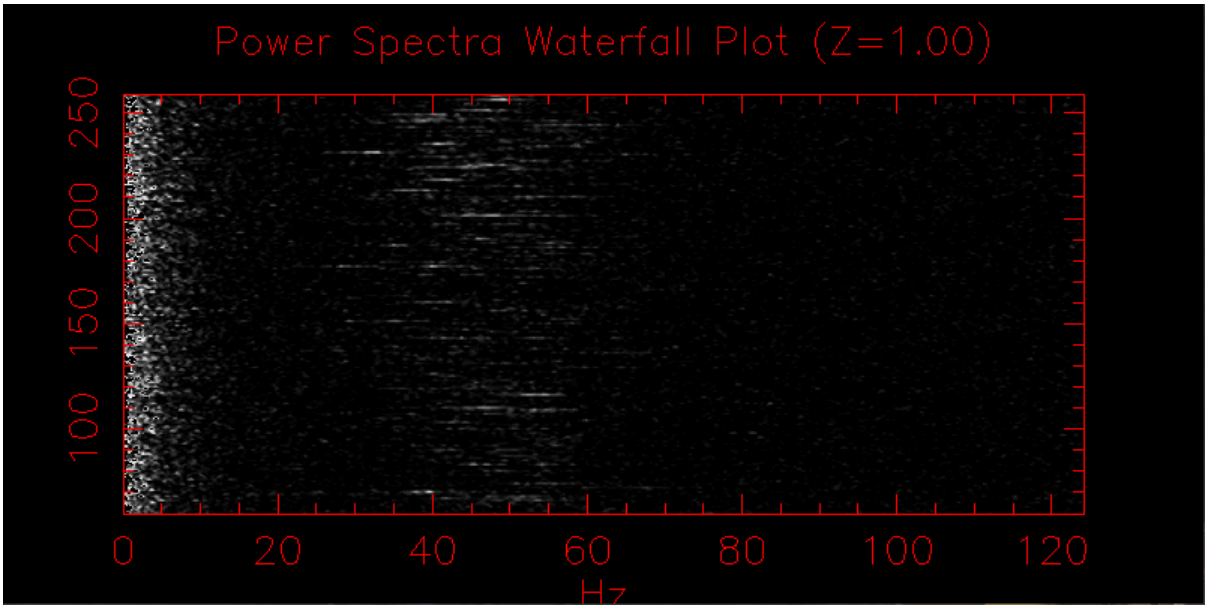

Figure B.20 The scan power spectra waterfall plot for the data file on HD 105881 taken on Mar 29, 2021, contained in the file 2021_04_29_HD_105881_ird_002.fit.

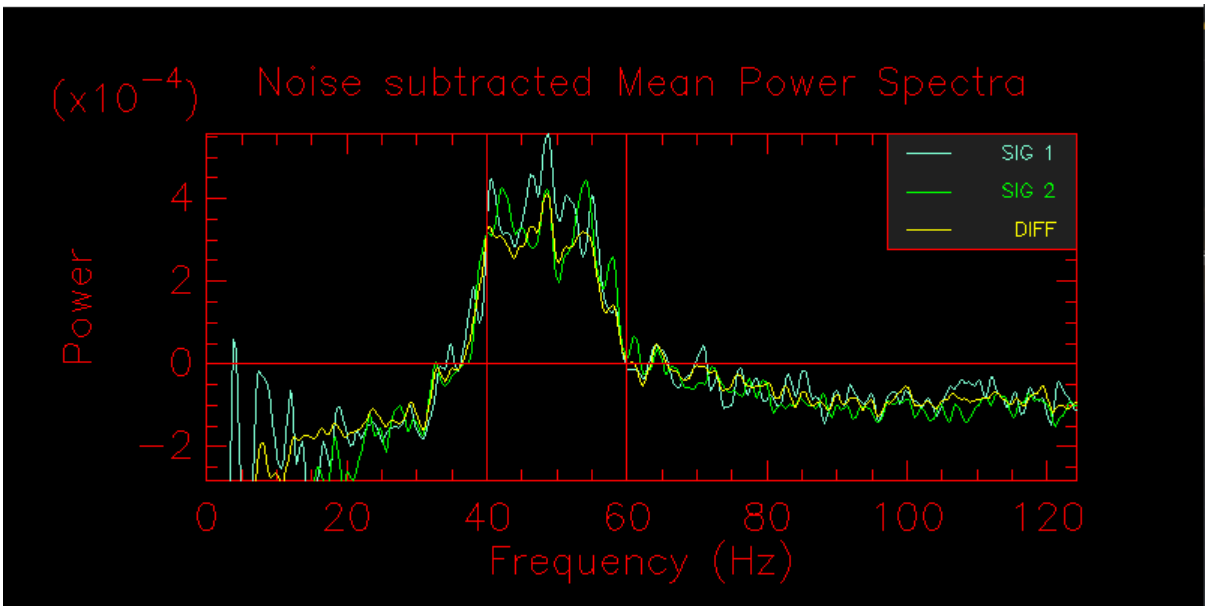

Figure B.21 The noise subtracted mean power spectra waterfall plot for the data file on HD 105881 taken on Mar 29, 2021, contained in the file 2021_04_29_SAO_HD105881_ird_002.fit.

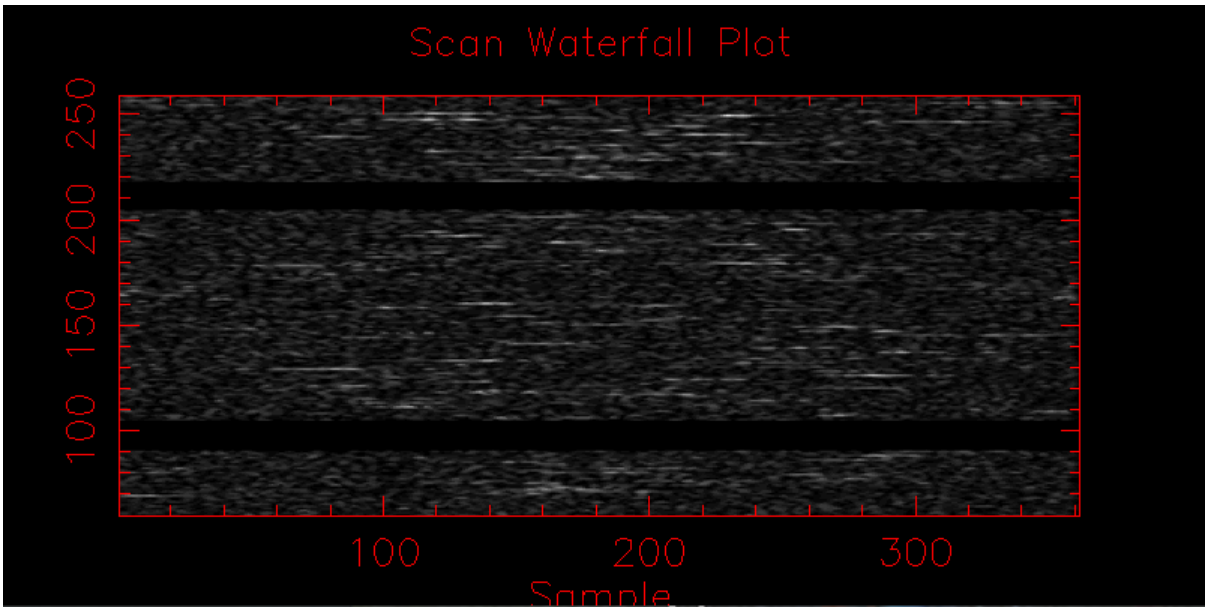

Figure B.22 The scan waterfall plot for the data file on HD 105881 taken on Mar 29, 2021, contained in the file 2021_04_29_HD_105881_ird_003.fit.

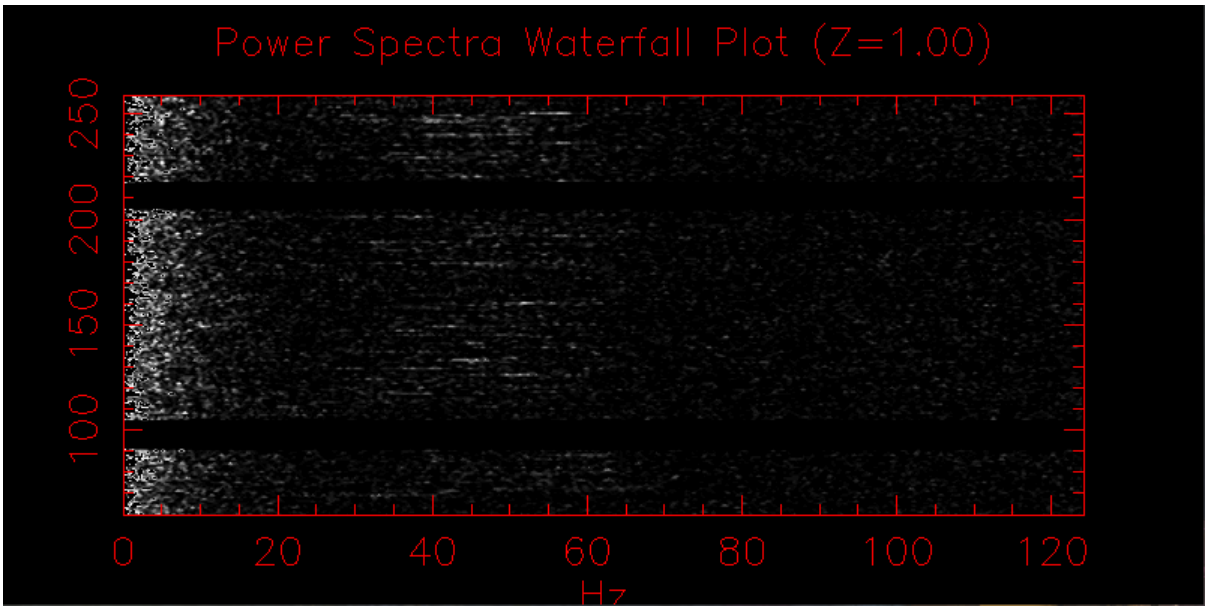

Figure B.23 The scan power spectra waterfall plot for the data file on HD 105881 taken on Apr 29, 2021, contained in the file 2021_04_29_HD_105881_ird_003.fit.

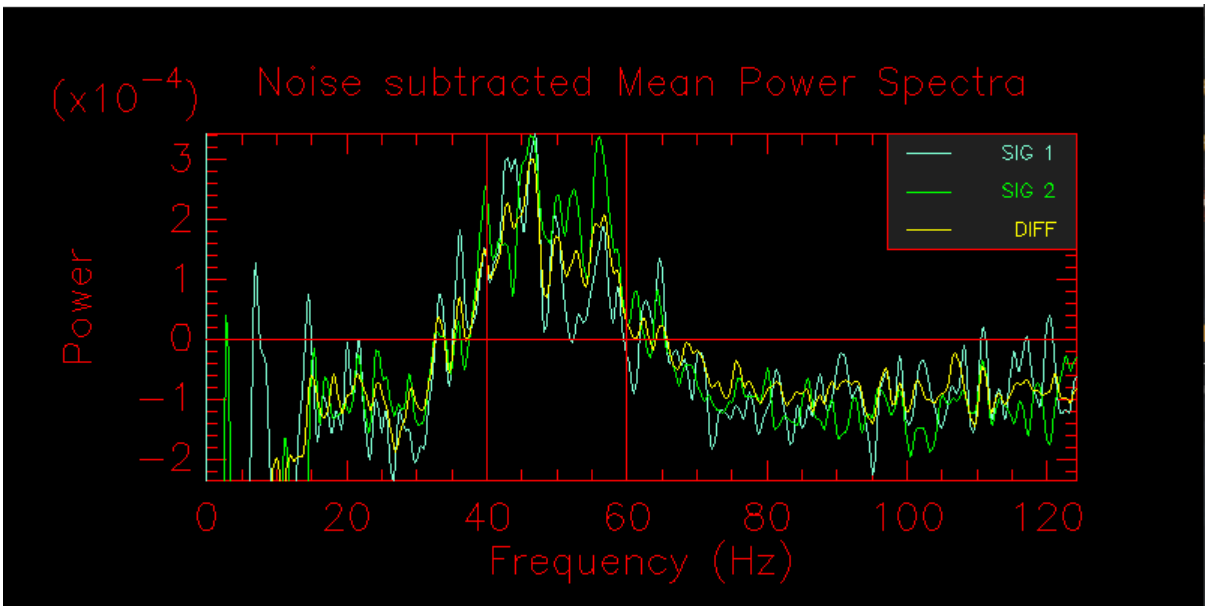

Figure B.24 The noise subtracted mean power spectra waterfall plot for the data file on HD 105881 taken on Apr 29, 2021, contained in the file 2021_04_29_SAO_HD105881_ird_003.fit.

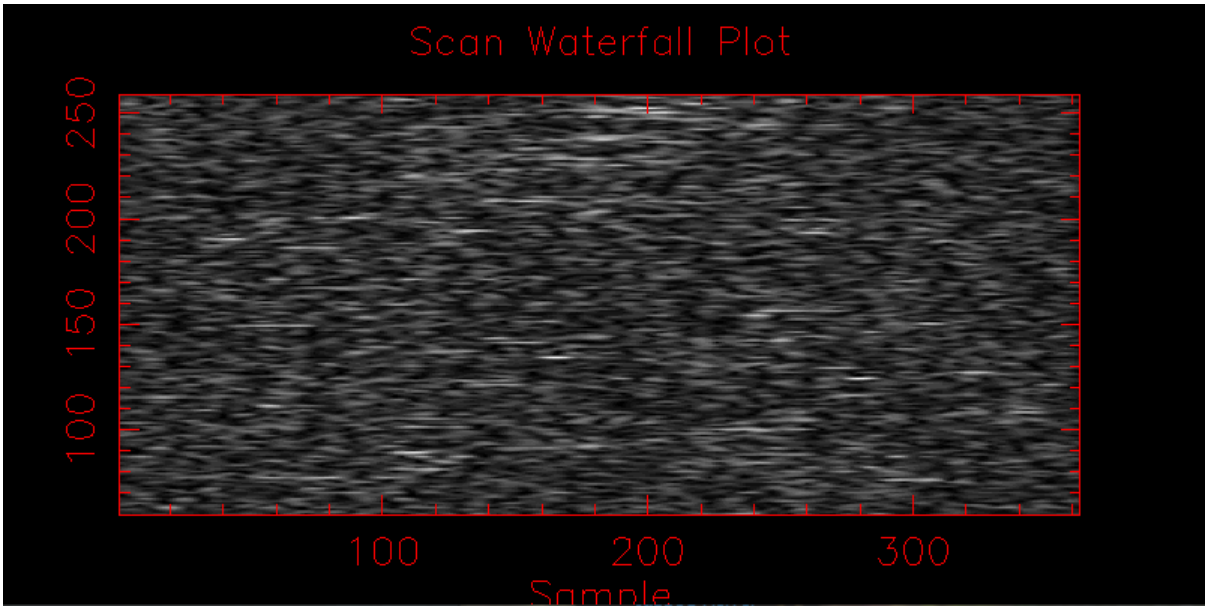

Figure B.25 The scan waterfall plot for the data file on TYC 3017-1666-1 taken on Apr 30, 2021, contained in the file 2021_04_30_2MASS_J12111971+3914148_ird_002.fit.

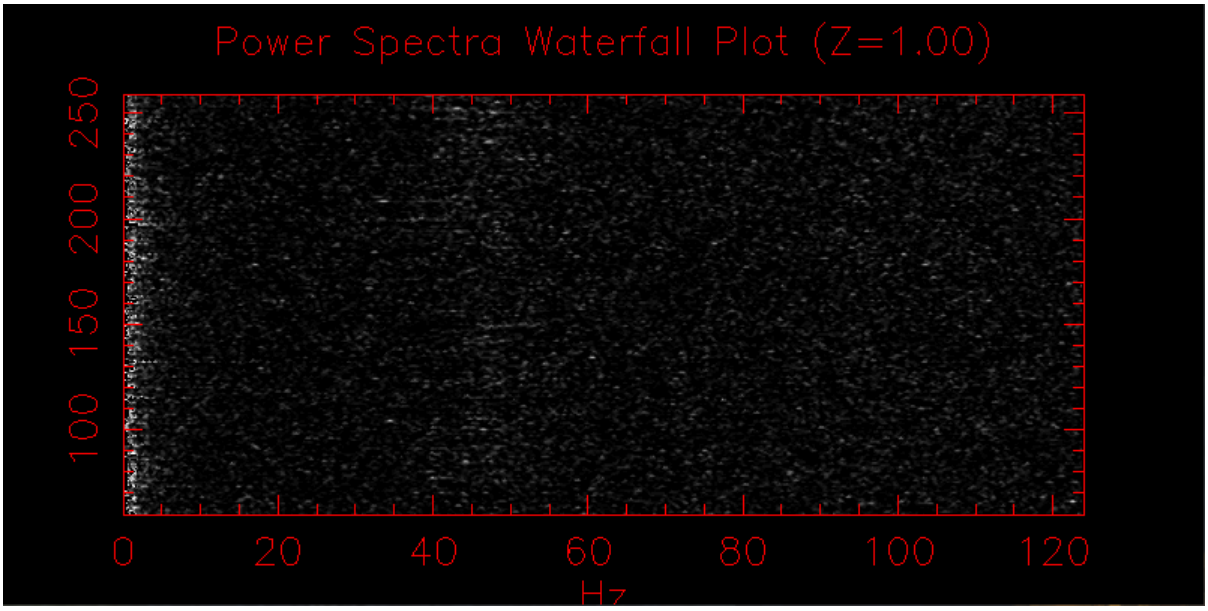

Figure B.26 The scan power spectra waterfall plot for the data file on TYC 3017-1666-1 taken on Apr 30, 2021, this data can be found in the CHARA archive contained in the file 2021_04_30_2MASS_J12111971+3914148_ird_002.fit.

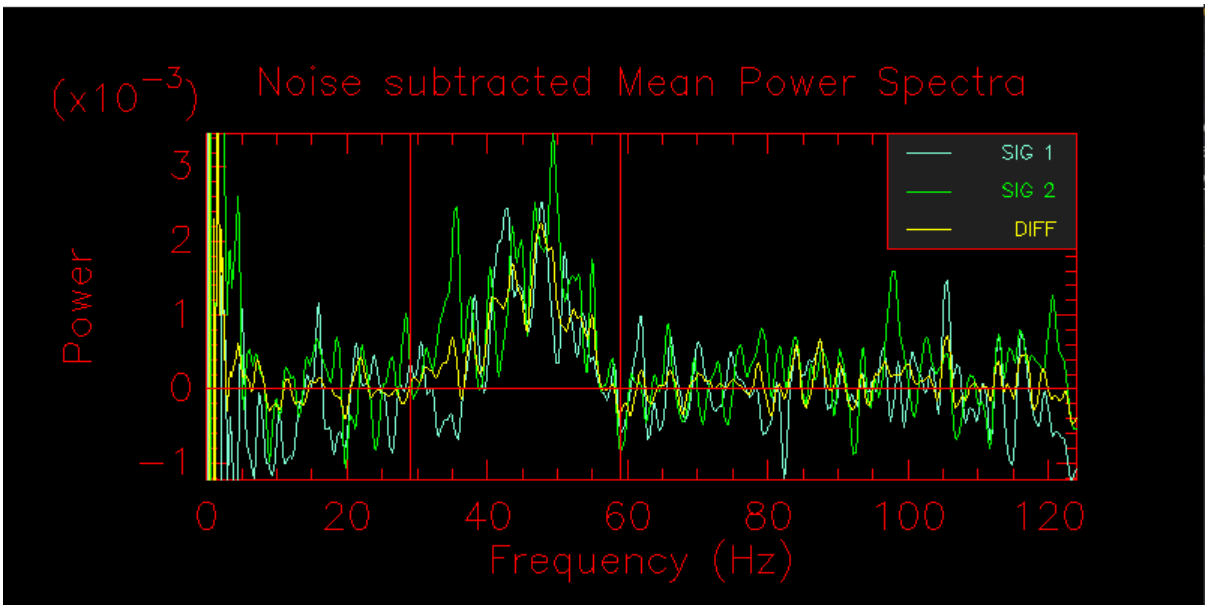

Figure B.27 The noise subtracted mean power spectra waterfall plot for the data file on TYC 3017-1666-1 taken on Apr 30, 2021, contained in the file 2021_04_30_2MASS_J12111971+3914148_ird_002.fit.

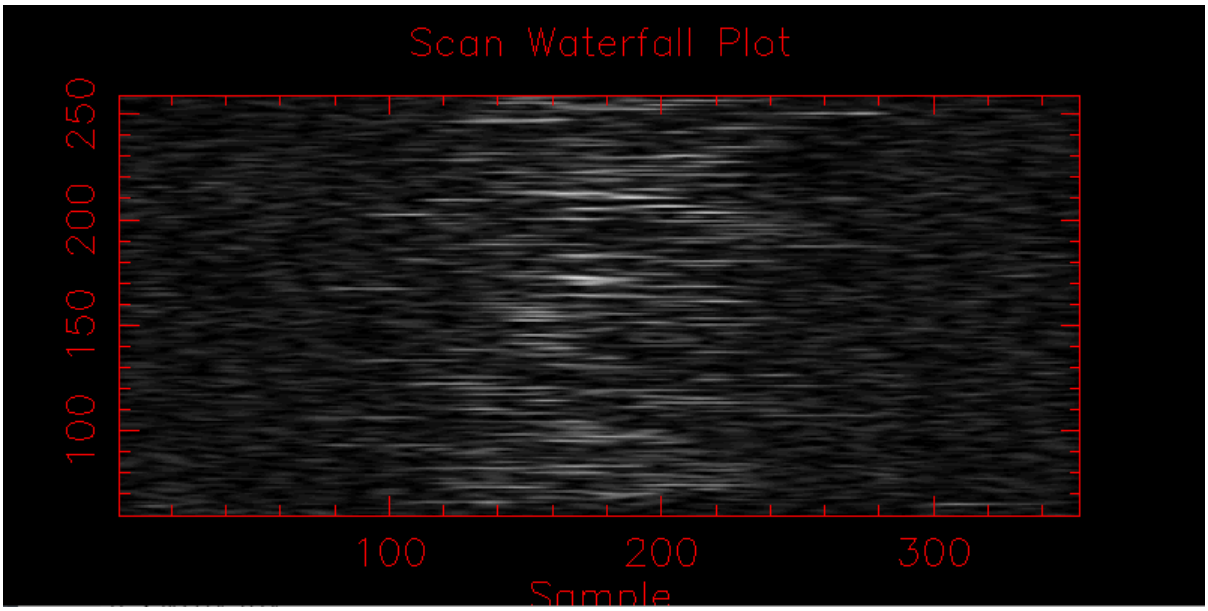

Figure B.28 The scan waterfall plot for the data file on SAO 62878 taken on Apr 30, 2021, contained in the file 2021_04_30_SAO_62878_ird_001.fit.

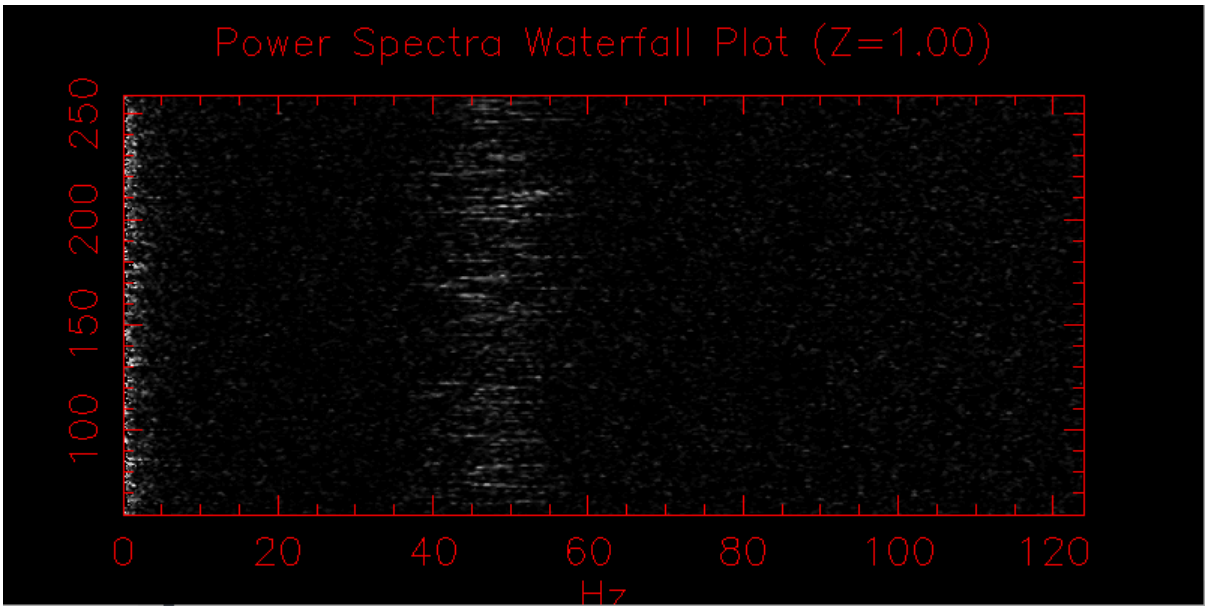

Figure B.29 The scan power spectra waterfall plot for the data file on SAO 62878 taken on Apr 30, 2021, contained in the file 2021_04_30_SAO_62878_ird_001.fit.

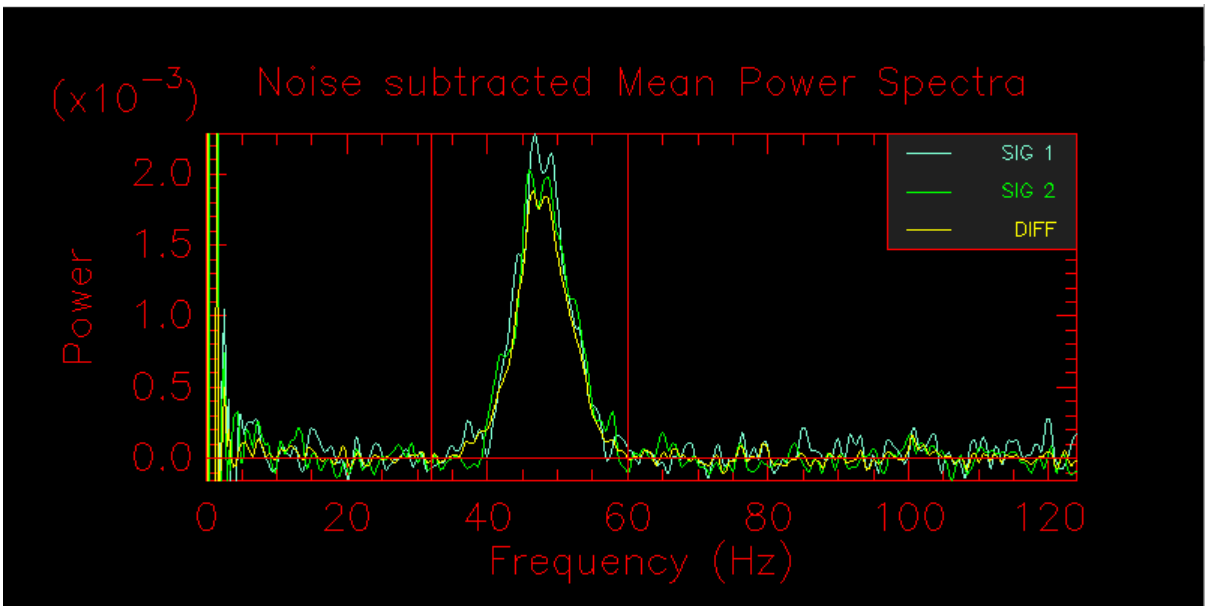

Figure B.30 The noise subtracted mean power spectra waterfall plot for the data file on SAO 62878 taken on Apr 30, 2021, contained in the file 2021_04_30_SAO_62878_ird_001.fit.

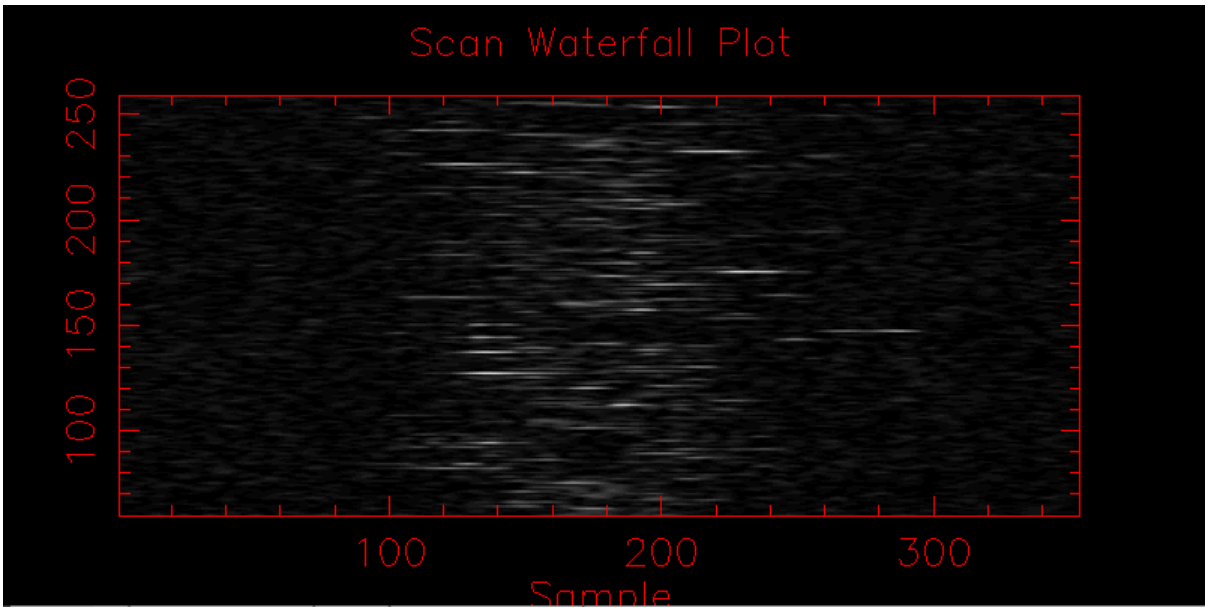

Figure B.31 The scan waterfall plot for the data file on HD 105881 taken on Apr 30, 2021, contained in the file 2021_04_30_HD_105881_ird_001.fit.

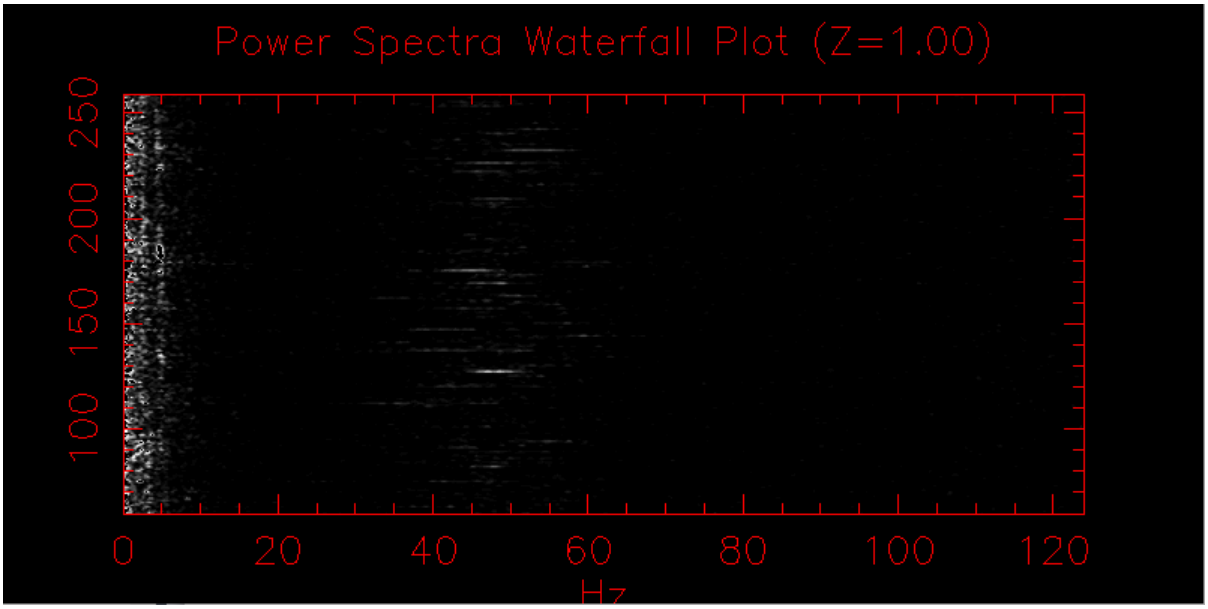

Figure B.32 The scan power spectra waterfall plot for the data file on HD 105881 taken on Apr 30, 2021, contained in the file 2021_04_30_HD_105881_ird_001.fit.

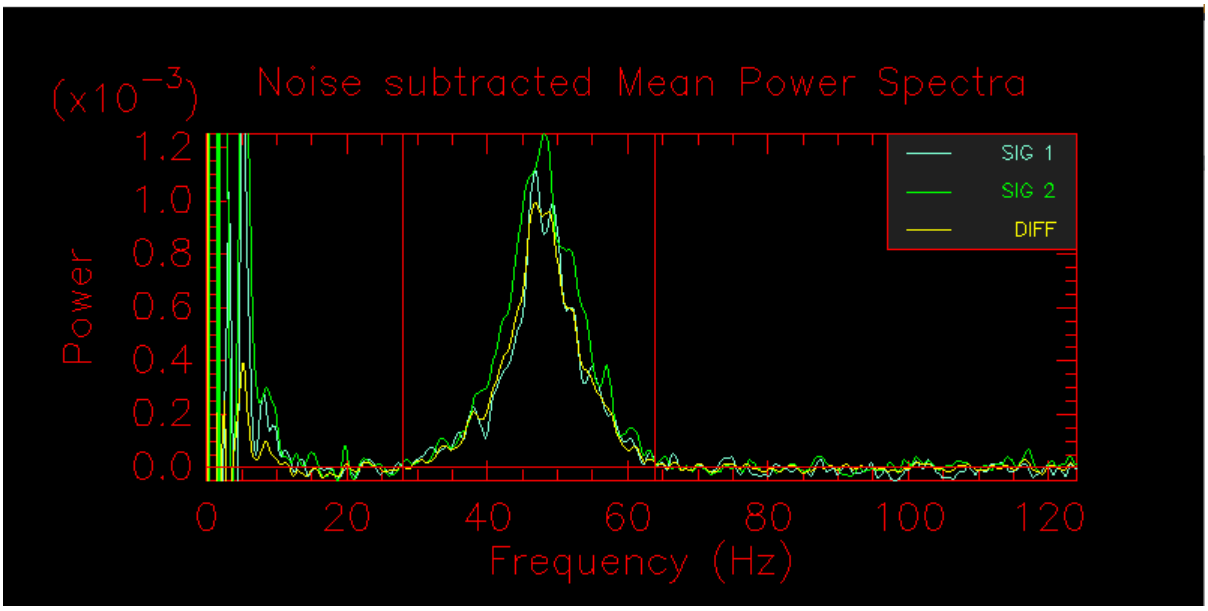

Figure B.33 The noise subtracted mean power spectra waterfall plot for the data file on HD 105881 taken on Apr 30, 2021, contained in the file 2021_04_30_HD_105881_ird_001.fit.

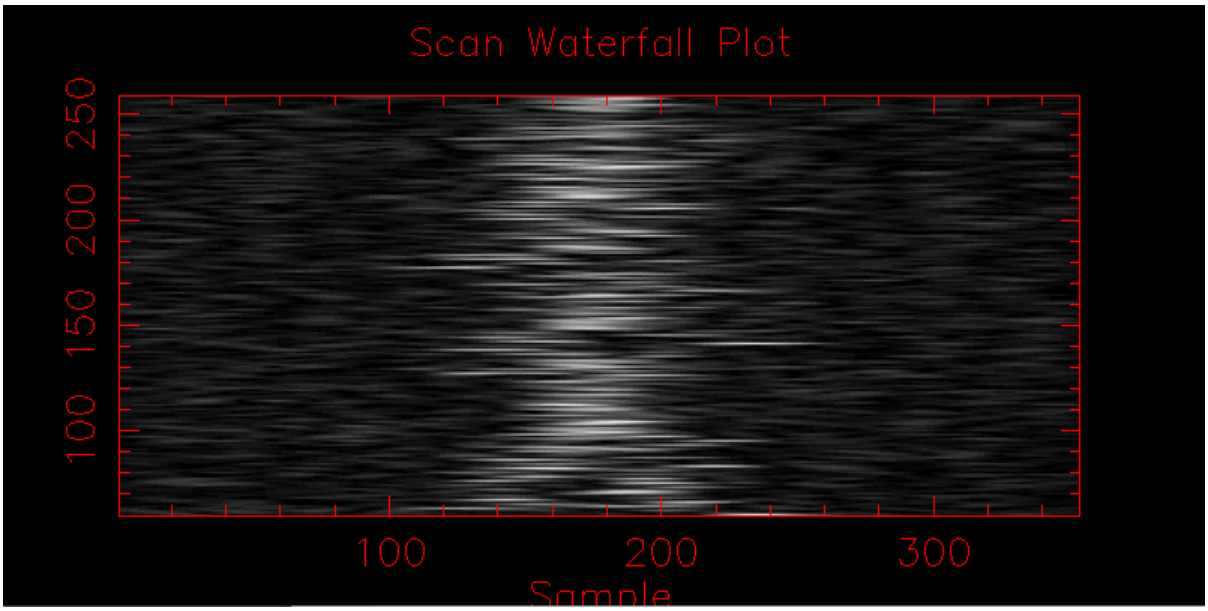

Figure B.34 The scan waterfall plot for the data file on SAO 62878 taken on Apr 30, 2021, contained in the file 2021_04_30_SAO_62878_ird_002.fit.

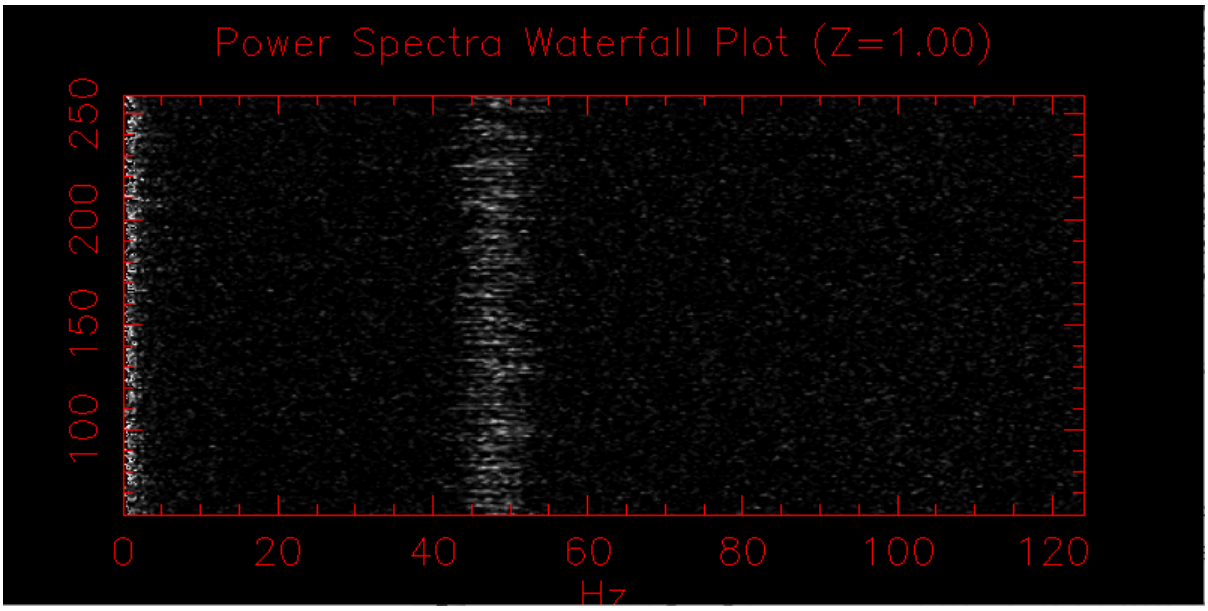

Figure B.35 The scan power spectra waterfall plot for the data file on SAO 62878 taken on Apr 30, 2021, contained in the file 2021_04_30_SAO_62878_ird_002.fit.

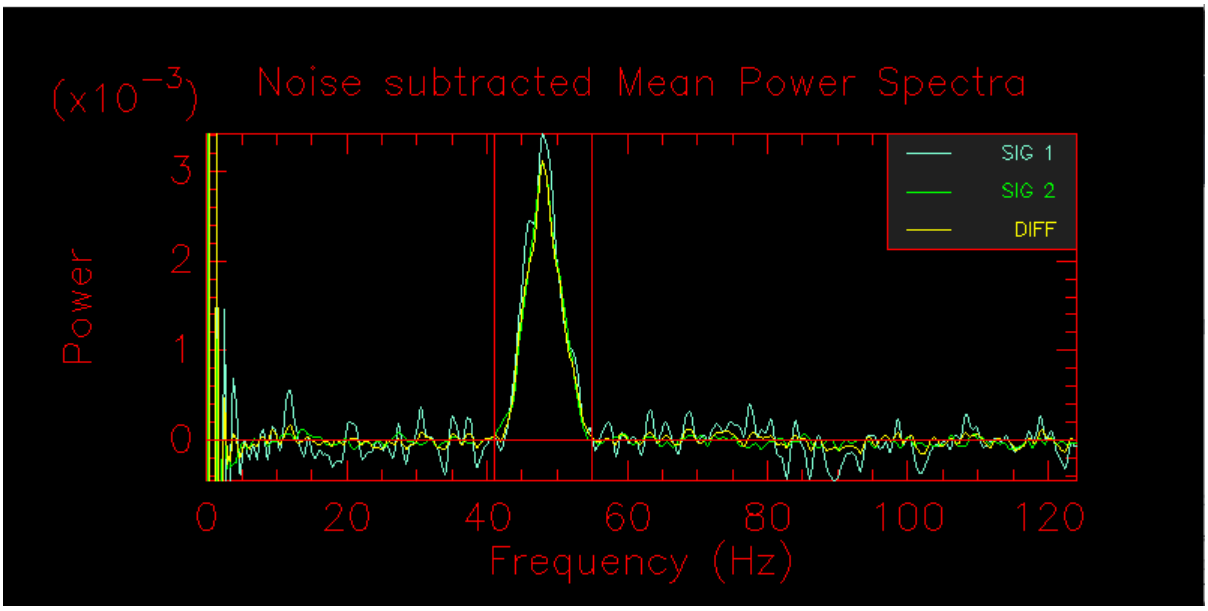

Figure B.36 The noise subtracted mean power spectra waterfall plot for the data file on SAO 62878 taken on Apr 30, 2021, contained in the file 2021_04_30_SAO_62878_ird_002.fit.

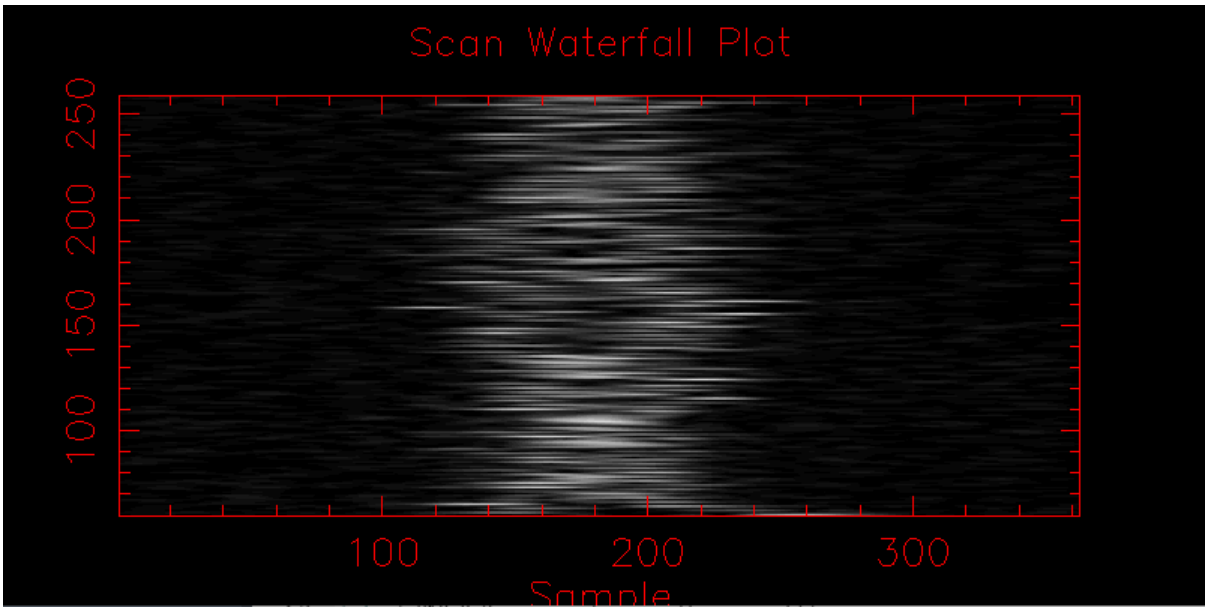

Figure B.37 The scan waterfall plot for the data file on HD 105881 taken on Apr 30, 2021, contained in the file 2021_04_30_HD_105881_ird_002.fit.

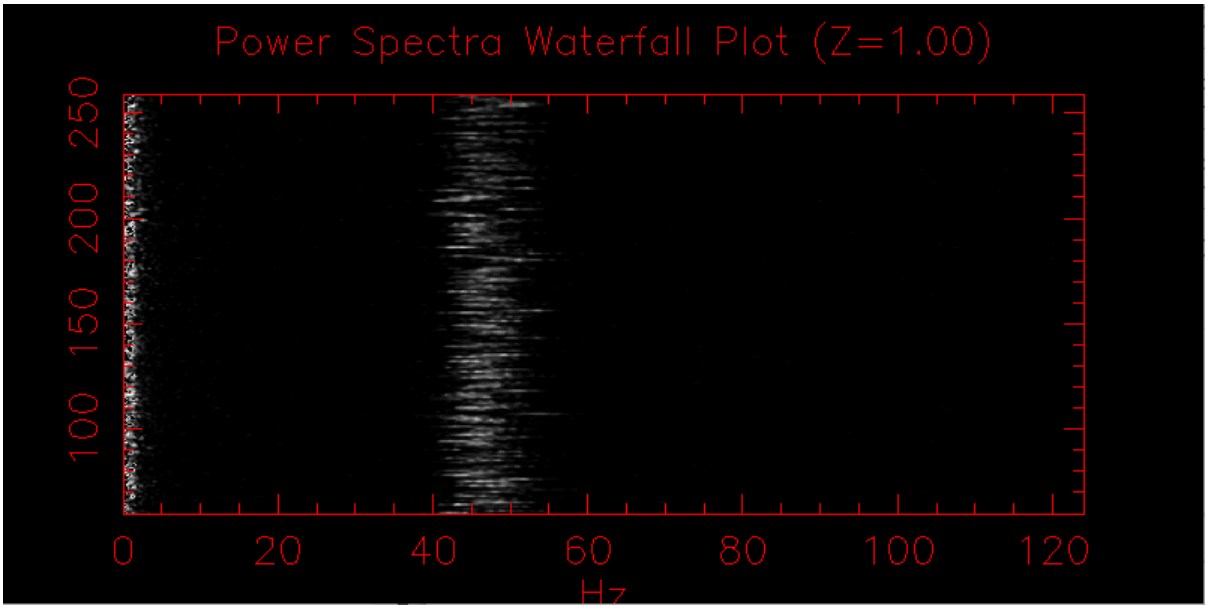

Figure B.38 The scan power spectra waterfall plot for the data file on HD 105881 taken on Apr 30, 2021, contained in the file 2021_04_30_HD_105881_ird_002.fit.

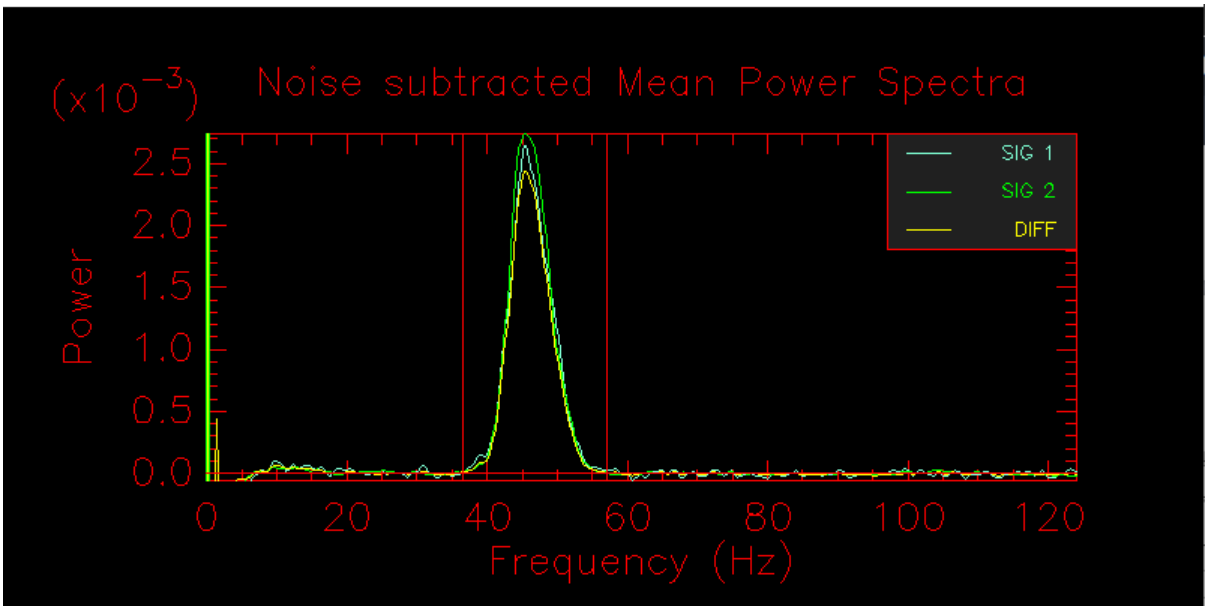

Figure B.39 The noise subtracted mean power spectra waterfall plot for the data file on HD 105881 taken on Apr 30, 2021, contained in the file 2021_04_30_HD_105881_ird_002.fit.

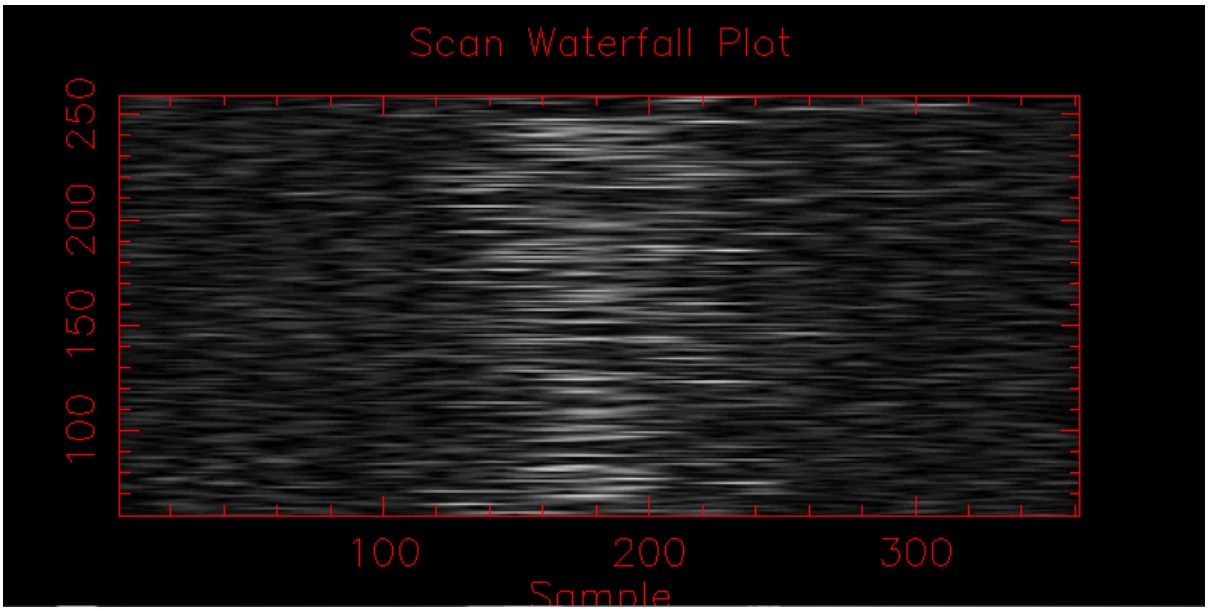

Figure B.40 The scan waterfall plot for the data file on SAO 62878 taken on Apr 30, 2021, contained in the file 2021_04_30_SAO_62878_ird_003.fit.

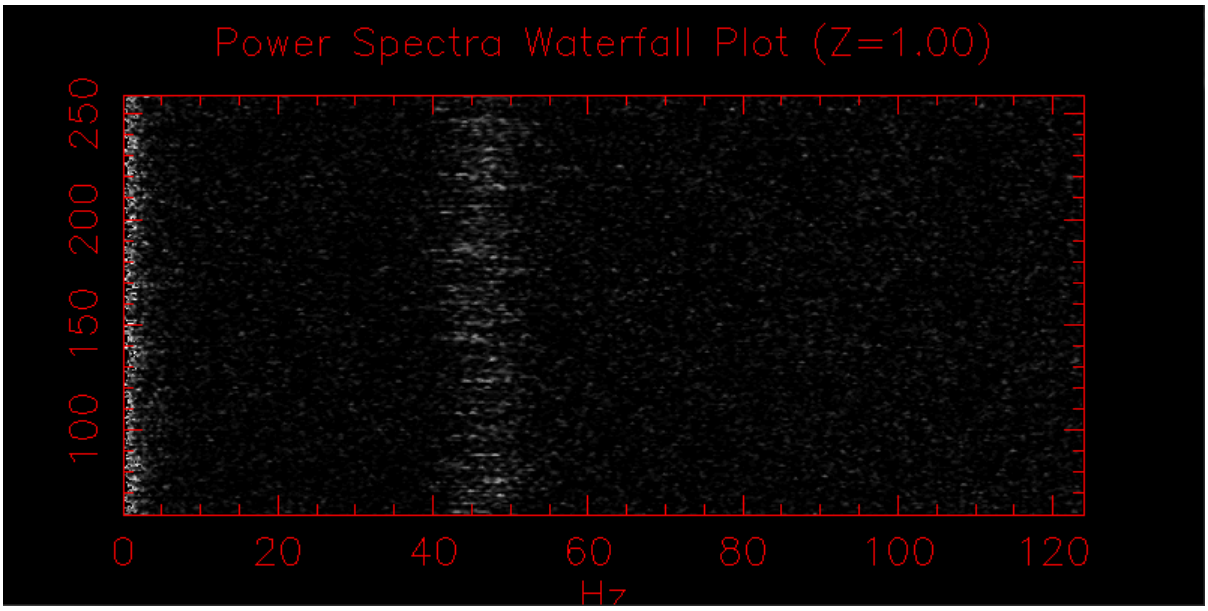

Figure B.41 The scan power spectra waterfall plot for the data file on SAO 62878 taken on Apr 30, 2021, contained in the file 2021_03_30_SAO_62878_ird_003.fit.

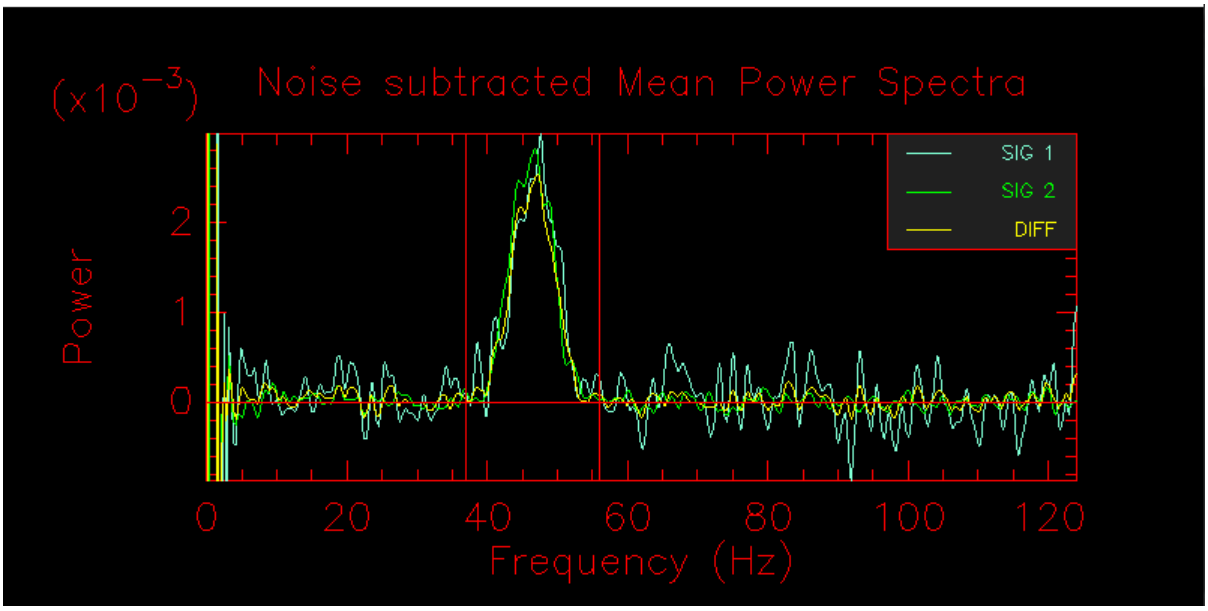

Figure B.42 The noise subtracted mean power spectra waterfall plot for the data file on SAO 62878 taken on Apr 30, 2021, contained in the file 2021_04_30_SAO_62878_ird_003.fit.